Imperial College London

The Imperial College of Science, Technology and Medicine
Department of Physics

Towards Laser Spectroscopy of Highly Charged Ions: Dynamics of ^{40}Ca^{+} Ions in a Penning Trap

Shailen Bharadia

Submitted in part fulfilment of the requirements for the degree of
Doctor of Philosophy in Physics of Imperial College, London,
30/08/2011

Abstract

To date, the most successful quantum field theory is quantum electrodynamics (QED) which offers a fully quantum mechanical description of the electromagnetic interaction between charged particles. Laboratory tests of the theory have been performed for a wide range of field strengths and no significant deviation from the predictions of the theory have been found. For heavy highly charged ions (HCI), the electric and magnetic fields around the nucleus can be orders of magnitude higher than those achievable by conventional means in a laboratory. Therefore, these ions offer a new regime in which the theory should be tested. For HCI above $Z > 60$, the ground state hyperfine structure splitting (HFS) shifts into the optical region, and becomes accessible to laser light sources. The aim of the SPECTRAP experiment at GSI in Germany, is to perform laser spectroscopy of the HFS in H-like and Li-like HCI, as a test of the corresponding bound-state QED calculations. In order for this to be successful, the weak magnetic HFS transitions need to be measured to a high precision. This will be accomplished in the SPECTRAP experiment by trapping and cooling bunches of HCI, such that the relative precision of the measured transition will be on the level of 10^{-7}, allowing bound-state high order QED calculations to be tested to the level of a few percent. As fluorescence rates will be low, a critical final part in preparing the ions in the trap will be the application of a rotating dipole ('rotating wall') about the magnetic field axis allowing for compression of the ion cloud in the trap, thereby increasing the fluorescence collection efficiency and signal to noise for detection.

In London, due to the availability of our own superconducting magnet, we have performed systematic measurements of the dynamics of laser cooled Ca^+ ions confined in a Penning trap driven by a rotating wall. With CCD camera imaging, we have measured the fluorescence from a cloud of ions, identified as being a strongly correlated non-neutral plasma, as a function of the rotating wall drive amplitude, frequency, sense of rotation and trap potential. We show that a cloud driven at sufficient amplitude reaches a low-slip regime within the time frame of a single CCD exposure ($\sim$ 1s), and that heating resonances are observed on scanning the rotation frequency. These resonances are identified as being associated with the axial motion of the ions in the trap potential, and the lowest order azimuthal plasma modes which are believed to be excited indirectly by a misalignment of the electric and magnetic fields.

By operating the rotating wall in the opposite sense of rotation to that used for cloud compression, the excitation of these plasma modes is shown to be a good diagnostic probe of the laser cooled rigid rotation frequency of the cloud, allowing the number density to be inferred from the measurement. These results will allow the SPECTRAP collaboration to define a procedure and set of optimum parameters for use of the rotating wall technique that offers maximum compression of ions needed for the precision spectroscopy of HCI. These results have been accepted for publication in Applied Physics B [1], and were presented at the European Conference for Trapped Ions in September 2010. The in-vacuum confocal fluorescence collection optical design proved valuable in alignment of the imaging system outside the magnet, and successful in increasing the detected fluorescence rates. As a result, the optical design and techniques employed here, have been successfully transferred to the GSI experiment.

We also present simulations conducted to optimise the transport and in-flight capture of HCI into the SPECTRAP ion trap from the HITRAP facility at GSI, and report on the first attempts at trapping singly charged Mg^+ and Ar^+ ions, testing the ability of the system to capture, localise and cool ions.

Acknowledgements

I would like to express my sincerest gratitude to my supervisors Professor Richard Thompson and Professor Danny Segal for giving me the opportunity to undertake this research, and for their continuous support throughout. I hope I will be fortunate to work with such people again. I would also like to especially thank Dr. Manuel Vogel for his supervisory role during my time at GSI.

During my studies, it has been my pleasure to work with Dan, Sean, Sandeep, Joseph, Brian, Zoran, Radu and Danyal. I also have great regard for all the members of the SPECTRAP collaboration.

I gratefully acknowledge financial support from the Engineering and Physical Sciences Research Council, and the Helmholtz Graduate School for Hadron and Ion Research.

Finally I would like to thank my parents for their unwavering support without which non of this would have been possible. This thesis is really dedicated to them.

Contents

List of Tables

List of Figures

Chapter 1

Motivation and Description of Thesis

The motivation behind this thesis comes from a desire to design and build an experiment which will be used to help improve our understanding of the physical world. Ion traps have proven to be amongst the most useful pieces of apparatus for conducting such experiments. An ion trap provides in vacuum, an isolated system to test our fundamental understanding of how our universe works. To this end, I began my Ph.D. studies on the SPECTRAP project with the initial goal of performing high resolution laser spectroscopy of H-like and Li-like heavy highly charged ions (HCI) at the GSI accelerator facility in Germany. With these electronically simple ions, it becomes possible to calculate the ground-state hyperfine splitting to high precision. As the electric and magnetic fields of electrons in orbit around such nuclei are orders of magnitude higher than those achievable by conventional means in the laboratory, they provide an new regime for testing the validity of quantum field theories. This thesis focuses on the preliminary trials of a prototype of the SPECTRAP ion trap, conducted at Imperial College London, to investigate the application of the rotating wall technique. It also includes ion optics simulations carried out for the SPECTRAP experiment at GSI, and a progress report on the work towards preparing this system for trapping and cooling of ions for the first time.

Chapter 2 describes how quantum field theories are tested, with emphasis on state-of-the-art experiments to probe bound-state quantum electrodynamics in HCI.

Chapter 3 provides the basic introductory theory of ion traps and describes the equilibrium state of a cold non-neutral plasma in a Penning trap. It is shown how the density and shape of such a plasma can be controlled by the application of a rotating wall, and where heating resonances may be expected.

Chapter 4 describes the main cooling methods employed in ion traps. Emphasis is placed on resistive and laser cooling as these are the two methods that are experimentally exploited in the SPECTRAP experiment at GSI.

In chapter 5, the Imperial College experimental setup to create, trap, laser cool and optically detect $^{40}\mathrm{Ca}^{+}$ ions in the SPECTRAP ion trap is presented in detail. As the laser system employed was built and setup by previous group members, only a brief description of the system in this area is given.

Chapter 6 presents the results obtained by operating the Imperial College SPECTRAP as an RF trap. The goal of running the trap in this configuration was to optimised the experimental setup without the physical constraints of a magnet, and the additional uncertainty in setting the (six) different wavelengths required for laser cooling in the Penning trap.

Chapter 7 provides the first results of fluorescence collected from $^{40}\mathrm{Ca}^{+}$ ions in a Penning trap using the group's superconducting magnet. The trap parameters are characterised and an estimate of the ion temperature is obtained.

Chapter 8 is a systematic investigation of the rotating wall technique carried out on laser cooled $^{40}\mathrm{Ca}^{+}$ ions. Results are presented showing how the fluorescence intensity of an ion cloud is affected by the rotating wall and trapping parameters. Compression of an ion cloud and heating resonances are observed on scanning the rotating wall drive frequency up to the Brillouin limit. These resonances are identified as the axial single particle trap motional frequency, and the lowest order azimuthal plasma mode. Measurements of the aspect ratio of an ion cloud as a function of the rotating wall drive frequency show good agreement with the theoretical expectations for a strongly correlated non-neutral plasma in a low-slip regime. The excitation of a plasma mode is shown to be a good diagnostic probe to determine the undriven cloud rotation frequency. The chapter is concluded by comparing the results to that found in the literature.

Chapter 9 introduces the SPECTRAP experiment at GSI and describes the various roles of the collaborators. Ion optics simulations are presented showing how HCI will be transported and captured in-flight into the SPECTRAP ion trap. An optimum set of voltages and beam parameters are identified for maximum kinetic energy removal and transport efficiency. Finally, the latest experimental progress obtained by 2 Ph.D. students (Z. Andjelkovic and R. Cazan) from the university of Mainz and the SPECTRAP collaboration, is reported.

1.1 The Author's Contributions

The author's contribution to this thesis starts from chapter 5 where the experimental setup of the prototype of the SPECTRAP ion trap at Imperial College London is presented. The trap itself was designed by Dr. M. Vogel and manufactured by B. Willey. I conducted my own analysis of the axial potential for the trap design both analytically and computationally. The pre-existing laser system for the cooling and spectroscopy of calcium ions was the work of previous group members. I was responsible for the design and build of the rest of the vacuum and imaging system around the trap vessel.

In chapter 6, I operated the SPECTRAP as a Paul trap to optimise the operation of the ion source and optical system. In chapter 7, I operated the SPECTRAP ion trap as a Penning trap and characterised the trapping parameters to calibrate the voltage applied to the trap electrodes, to the ion oscillation frequencies in the trap.

With the SPECTRAP operating as a Penning trap, I then carried out a systematic investigation of the rotating wall technique presented in chapter 8. These results have led to the publication [1].

In chapter 9, the work towards preparing the SPECTRAP experiment at GSI is discussed in detail. I conducted simulations for the transport and in-flight capture of ions into the SPECTRAP ion trap. The setup of the experiment at GSI has been a collaborative effort. The major contributors so far have been Dr. M. Vogel, Z. Andjelkovic, R. Cazan and myself. The latest results presented in this chapter showing laser cooling and optical spectroscopy of magnesium ions, were obtained by Z. Andjelkovic and R. Cazan.

Chapter 2

Tests of QED

Quantum electrodynamics, or QED, is a fully relativistic quantum mechanical theory of electromagnetism. Combing Dirac's equation for the electron and positron, with a quantised form of Maxwell's equations for the photon, it describes the interaction of charged particles via the exchange of virtual photons. As virtual particles, photons can violate energy and momentum conservation to the extent allowed by the uncertainty principle. Calculations of amplitudes and probabilities of events are based on perturbation theory, organised in terms of Feynman diagrams, which represent a systematic expansion in powers of the fine structure constant, α, given by

$$\alpha = \frac{e^2}{4\pi\varepsilon_0\hbar c} \approx \frac{1}{137} \tag{2.0.1}$$

where e is the elementary charge, $\hbar$ the reduced Planck constant, c is the speed of light in vacuum and ε_0 is the electric permittivity of free space. As α«1, the calculations converge very rapidly, and high accuracy can be obtained by taking into account only the first few lowest order terms. Theorists use this technique to make predictions of physical measurables e.g. transition rates, cross-sections, magnetic-moments etc.

The theory requires a value of α as an input. This can either come from measurements of the fundamental constituent constants, or trusting the theory is correct, α may be directly extracted from a measurable itself. In the latter case, verification of QED is then made by experimentally testing the theoretical predictions in other physical systems. To date, the most accurate value of α

comes from a measurement of the g-factor of a free electron [2]. The g-factor measures the magnetic moment μ in units of the Bohr magnetron μ_B according to

$$\frac{\mu}{\mu_B} = g\frac{|\vec{s}|}{\hbar} \tag{2.0.2}$$

where $|\vec{s}| = s.\hbar = \hbar/2$ is the spin of the electron. From Dirac theory, this g-factor should be exactly equal to two. However QED theory allows for two extra processes: Emission and absorption of a virtual photon by an electron, termed self energy; Creation and annihilation of a virtual electron-position pair by a photon, termed vacuum polarisation. These corrections in the presence of an external magnetic field are depicted by the Feynman diagrams in Fig. 2.1.

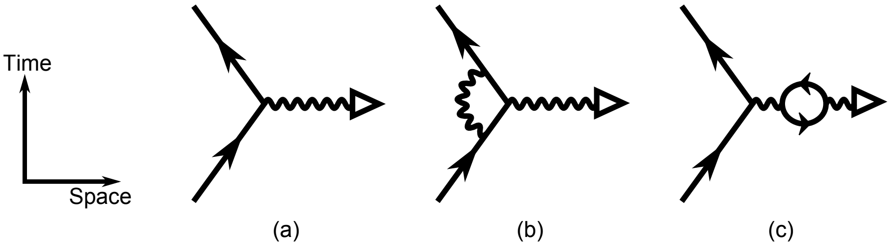

Figure 2.1: (a) Dirac equivalent, (b) self energy and (c) vacuum polarisation first-order Feynman diagrams of an electron (straight lines) interacting with an external magnetic field represented by a triangle via the exchange of a photon (wavy line). In (b) an electron emits and reabsorbs a photon temporarily changing its momentum and energy. In (c) an electron-positron pair is created that partially shields the external field. Hence the QED effects in (b) and (c) modify the amplitude or probability of the event (a).

Remarkable agreement is found between theory and experiments for light systems (e.g a free electron), and α is now known to of order 1 part per trillion [3]. For heavy simple atomic systems i.e. highly charged ions (HCI) and ions that have had all but one (or a few) electrons removed, $Z\alpha$ approaches unity and the interaction of the electron with the nuclear field must be considered to all orders in $Z\alpha$ (where Z is the charge on the nucleus). The electron self interaction can still be considered perturbatively, so QED contributions are ordered, as with light systems, according to this weaker interaction in powers of α. Hence, because of the nuclear field interaction, the scale of QED effects in such systems is much greater, and therefore this area offers a new regime in which the theory should be tested. The QED theory and contributions to corrections to the physical measureables specifically arising from these bound systems (e.g an electron bound to a nucleus in an atom or ion), is known as bound-state QED.

2.1 Highly Charged Ions

Highly charged few electron heavy ions offer the most intense electromagnetic fields available, and the opportunity to test high accuracy calculations of bound-state QED and nuclear parameters. Electric and magnetic field strengths up to 10^{16}V/m and 10^{4}T respectively can be found close to the nucleus in the ground-state of H-like Uranium U^{+91} [4], and steady-state fields of this order cannot be produced in the laboratory[1]. QED calculations for heavy ions are much more demanding than for light ions, as the nuclear field must be considered to all orders. However, the leading order QED contributions in terms of α and the Feynman diagrams will always dominate, and together with the larger overall scale of corrections, this makes for a stringent test of the theory against ever improving ongoing calculations.

2.1.1 Production of Highly Charged Ions

Highly charged ions (HCI), such as naked Uranium, can only be found in nature in the most active areas of the galaxy e.g. stellar corona, supernova remnants and accretion disks. To strip all but one electron from Uranium requires an energy of $\sim 13.6eV \times 92^2 = 10^5$eV, or an accelerating voltage of over 100kV. As difficult as this may appear, such exotic ions can readily be produced in an Electron Beam Ion Source (EBIS) or Trap (EBIT), and Heavy Ion Accelerators all over the world.

2.1.2 Electron Beam Ion Source

An EBIS is a compact efficient tool for producing HCI. A schematic layout is shown in Fig. 2.2. An EBIS provides radial confinement of positively charged ions by the electrostatic attraction to a tightly focused electron beam, and axial confinement by positive potentials on open endcap electrodes. The electrons are produced via an electron gun, and a strong axial magnetic field prevents the beam from diverging due to the space charge effect i.e. electrons are sent into cyclotron orbits. Lowly charged ions are successively ionised to high charge states by bombardment of electrons. Due to the high negative

---

[1] Huge transient fields can be made in the laboratory with high power short laser pulses.

charge densities along the electron beam, ions spend most of the time within its confines. Trapped ions continue to be ionised until the binding energy of the remaining charge state is greater than that of the incoming electrons. In this way, the final charge state is controlled by varying the acceleration voltage of the electron gun. The electron capture cross-section is reduced at the high energies of the beam that are necessary to overcome the binding energy. As a consequence, longer time scales are possible to achieve high charge states. The radiative recombination that does occur, allows the population of trapped ionisation states to be monitored by x-ray spectroscopy from this process.

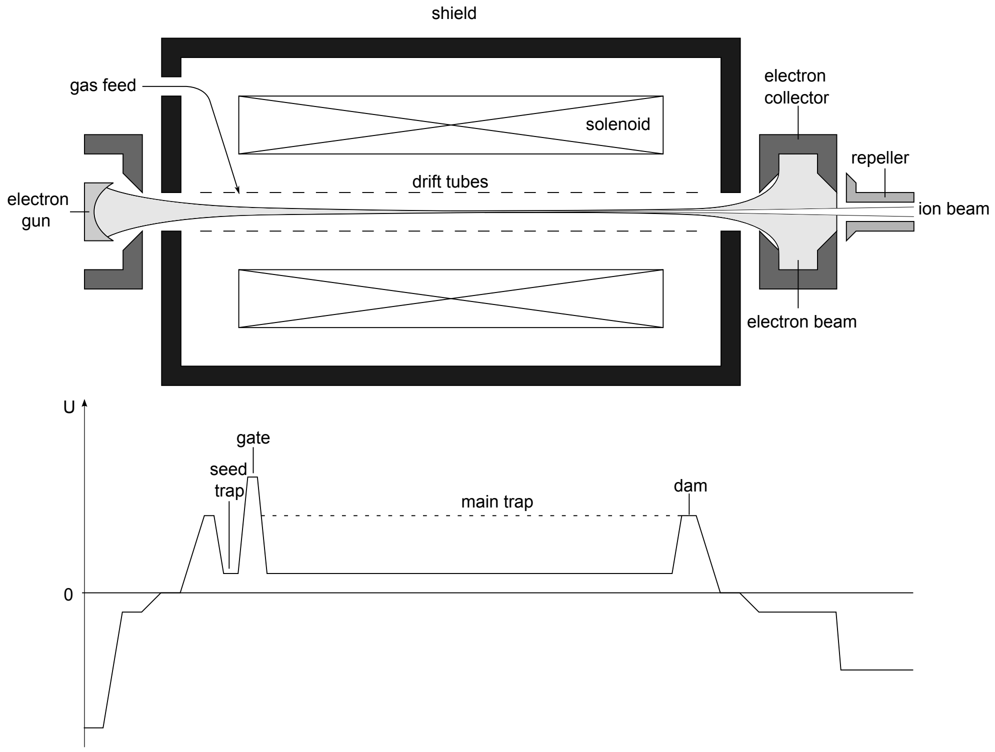

Figure 2.2: A schematic view of a cryogenic EBIS with typical electrical potentials applied along the electron beam. Application of DC voltages to the drift tubes allows the axial potential to be tailored. During the injection period, the gate is lowered and seed ions fill the main trap region where they continue to be ionised until the required charge state is reached. The base potential of the main trap is then increased to expel the ions over the dam [5].

An EBIT operates in essentially the same was as an EBIS, except it is designed to trap ions for long periods of time. Typically an EBIS has a trapping region of $\sim$ 1m, with beam transport and experiments downstream. An EBIT has at least one high precision, small trapping region of ∼ 2-4cm, and experiments are conducted with ions in situ. The EBIT is a predecessor of the EBIS, and has developed to the 'table-top' stage as there are no further infrastructure requirements. An EBIT can also be an effective EBIS if combined with a storage ring for ion accumulation.

A high energy version of the EBIT is called a Super EBIT which can operate over 100kV, sufficient to fully strip Uranium as the spectrum in Fig 2.3 shows.

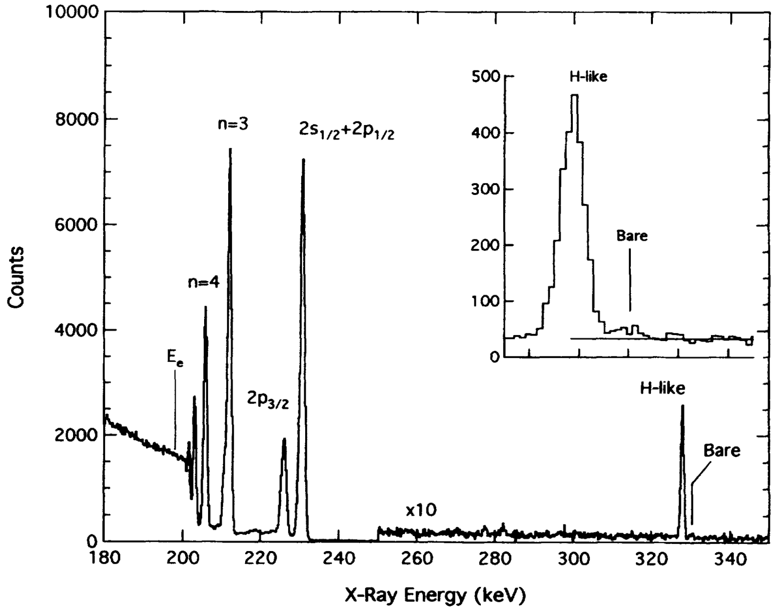

Figure 2.3: X-ray spectrum of the radiative recombination of He-like, H-like and bare Uranium at an electron energy of 198keV from the Super EBIT at Lawrence Livermore National Laboratory (LLNL) [6].

Cooling of ions in an EBIT is usually carried out by means of evaporative cooling by an admixture of ions in low charge states. These ions thermalise and boil off more rapidly as the effective potential scales with the ion charge i.e. shallower trap for lower charged ions. Compared to EBIS and EBIT HCI sources, heavy ion accelerators have the capability of abundantly providing ions of selected charge state up to U^{92+}.

2.1.3 Heavy Ion Accelerator

HCI can effectively be created by stripping ion beams in an accelerator. This is usually a two step process; ions of low charge state are first accelerated to intermediate energies and stripped on a target such as a gas or thin foil, then a fraction of these stripped ions are further accelerated to higher energies for the final stripping process. As the ion's energy is proportional to its charge, this two step process is more efficient as lower acceleration voltages are required.

There are two basic types of accelerators: those based solely on direct voltage or static potentials that use the applied voltages only once; and radio frequency or pulsed accelerators which make use of resonant acceleration and are not limited by the maximum voltage achievable. For this reason, all modern HCI accelerators use some form of RF acceleration.

Within these accelerator types, there are two basic geometries: a linear accelerator (LINAC) where the ions follow a straight line trajectory and the final energy is proportional the voltage integrated along this line; and a circular accelerator where the particles are bent by magnetic fields around a spiralling (cyclotron) or closed loop (synchrotron) path. In the latter case, the ions traverse many times around the device, and would return to the same potential if static electric fields alone were applied. For this reason, these accelerators use RF fields which allow the ions to gain up to GeV kinetic energies having travelled millions of kilometres over many cycles.

A good example of one such multistage facility that is of particular importance in this thesis, is the Gesellschaft für Schwerionenforschung (GSI) in Darmstadt, Germany. A schematic layout of this facility is presented in Fig. 2.4. It consists of a linear RF accelerator (UNILAC), a heavy ion synchrotron (SIS) and an experimental storage ring (ESR). The UNILAC serves two functions; it provides moderate to heavy ions for low energy experiments, and acts as a pre-accelerator for the SIS. The SIS then provides high energy beams to the fragment separator, FRS, the ESR or experiments in the target hall and adjoining cold spectroscopy facility, HITRAP [8]. There are stripping targets at the end of the UNILAC and SIS. The ESR provides the ability to cool ion beams (electron [9] and stochastic cooling [10] to reduced the velocity spread) and conduct experiments internal to the ring, as well as accumulation of ion current and feed through for the other sub-facilities. Ions in the ESR have a transport energy in the MeV range. The HITRAP sub-facility, where the SPECTRAP experiment is located, will provide further deceleration and cool-

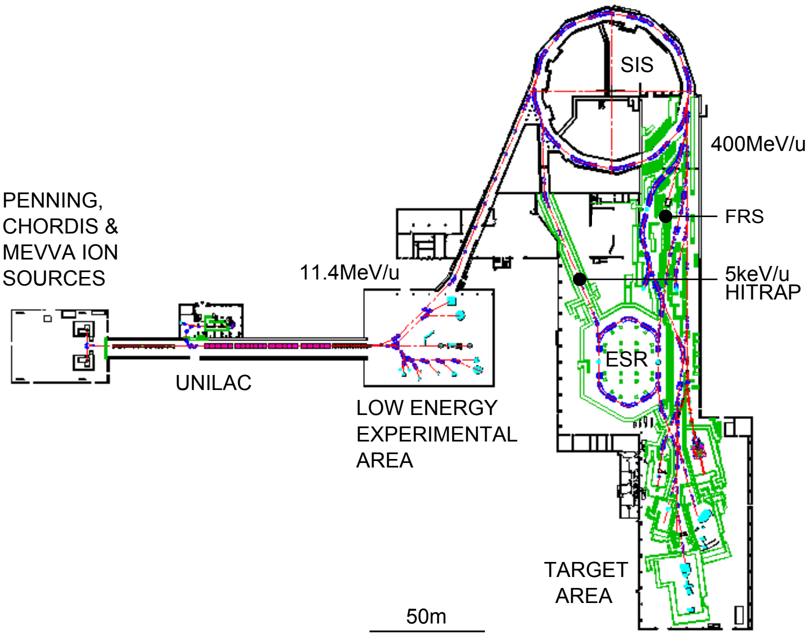

Figure 2.4: A schematic layout of GSI accelerator facility. Beam lines are outlined in red, radiation shields in green and magnetic deflectors in purple [7].

ing of ions to a temperature of 4K before transporting them with an energy of 5keV/u[2] to the experiments down stream.

For stable operation at high energies and currents, beam focusing and bunching are important. RF quadrupole accelerators rely on correctly matching the phase of ion bunches with the applied field. And due to the space charge effect, ions would be lost on the walls of the accelerator without focusing ion optics. For these reasons, along every few meters of beam line, there are devices such as magnetic quadrupole triplets, electrostatic and magnetic benders, as well as position sensitive detectors for optimisation. The repetitive use of equipment along the beam line to maintain a good vacuum of $< 10^{-10}$mbar is also required throughout the facility e.g. vacuum pumps, pressure gauges, and valves etc.

When the GSI ion accelerator is combined with the HITRAP facility, pulses of up to 10^5 HCI at cryogenic temperatures in the laboratory frame, will be

---

[2] This is the energy in units of electron volts per elementary charge on the ion u.

provided for investigation to experiments such as SPECTRAP (see section 9.2).

2.2 Experiments with HCI

QED effects manifest themselves in three main measurable quantities:

- Lamb shift
- g-factor
- Hyperfine structure

Currently there is an enormous effort being undertaken at GSI to investigate bound-state QED effects in the strong fields of highly charged few-electron ions for which accurate theoretical calculations are possible. A brief overview of the latest experimental undertakings to measure these quantities is now presented.

2.2.1 Lamb shift

The first great triumph of QED was the explanation of the $2S_{1/2} - 2P_{1/2}$ splitting in Hydrogen discovered by Lamb and Rutherford in 1947 [11]. From Dirac theory, these two energy levels should be degenerate as they share the same principal (n) and total angular momentum (j) quantum numbers. However due to the self interaction of the electron through the previously mentioned QED effects, which are stronger closer to the nucleus and hence for the S orbital, the electron attraction to the nucleus is weakened. This causes an electron to be less tightly bound and higher in energy when in the 2S state than the 2P. Today, apart from this specific splitting in hydrogen, the shift of any single atomic level from its Dirac value is termed the Lamb shift.

For H-like ions, the Lamb shift may be written as [12]

$$\Delta E = \frac{\alpha}{\pi}\frac{(\alpha Z)^4}{n^3} m_e c^2 F(\alpha Z) \tag{2.2.1}$$

where $F(\alpha Z)$ is a dimensionless slowly varying function describing the correction factors of self energy (SE), vacuum polarisation (VP) and nuclear finite size (FS)

$$F(\alpha Z) = F_{SE} + F_{VP} + F_{FS}. \tag{2.2.2}$$

For states with angular momentum, $l \neq 0$, this function is approximately equal to 1, whereas for S states, it increases logarithmically with Z. Therefore the Lamb shift is largest for the ground state, and strongly increases with at least Z^4. Hence the interest in ions such as H-like Uranium.

The Lamb shift contributions from leading order corrections are plotted as a function of Z in Fig. 2.5. It can be seen that self-energy is the main QED contribution, and nuclear finite size is important at high Z.

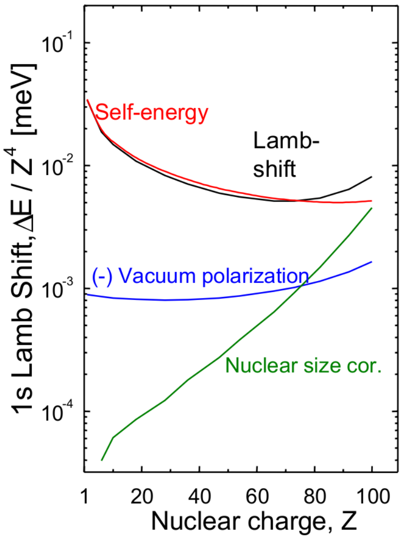

Figure 2.5: Individual contributions to the ground-state Lamb shift in H-like Uranium [13].

For the case of H-like Uranium, the 1S Lamb shift contributes some 464eV to the total ground-state energy of 131.816keV [14]. First and second-order QED effects amount to about 266eV and 1eV respectively. Experiments at GSI are being prepared to measure this Lamb shift to an absolute accuracy on the level of an electron volt in order to be sensitive to the higher-order QED contributions.

2.2.1.1 Experiment

To date, the most accurate measurement of the 1S Lamb shift in H-like Uranium was performed at GSI [14]. In essence, the experiment involved measuring transitions into the ground-state of U^{91+} via radiative recombination of bare ions. The Lamb shift value is deduced by comparison with Dirac energy eigenvalues for a point like nucleus, with the additional assumption that the energies of the excited states are known to a high accuracy. The energy levels of interest are shown in Fig. 2.6a.

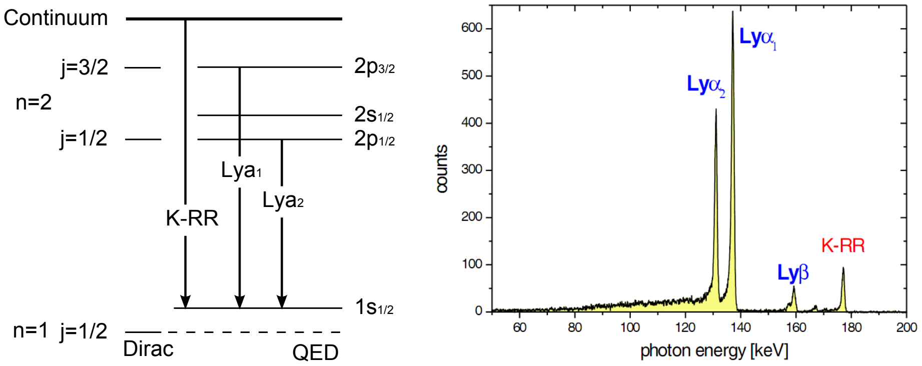

(a) (b)

Figure 2.6: (a) Level and decay scheme for low-lying states of U^{91+}, where K-RR and Ly denotes a K shell radiative recombination straight from the continuum and the Lyman series of transitions respectively. (b) shows the x-ray spectrum obtained from the latest experiment performed at the ESR [14].

The experiment is situated in the ESR and utilises the electron cooler [9]. This device reduces the temperature of ions by Coulomb interaction with a cold co-propagating electron beam. An electron gun produces cold electrons which are accelerated to match the velocity of ions without increasing their momentum spread. This electron current is then overlapped with the ions in a section of beam line, and hot electrons are collected off axis. The experimental arrangement used for the latest Lamb shift measurements in 2005 is shown in Fig. 2.7.

The experimental procedure follows Uranium (U^{92+}) ions that are produced after acceleration and stripping from the SIS, that are then injected into the ESR and decelerated from an energy above 300MeV/u to below 45MeV/u for measurement. This reduces the uncertainties introduced by the relativistic Doppler effect. Inside the electron cooler, radiative recombination to U^{91+} takes place producing x-rays which are detected with a solid-state detector. Coincidence detection with down-charged ions after the bending magnet allows

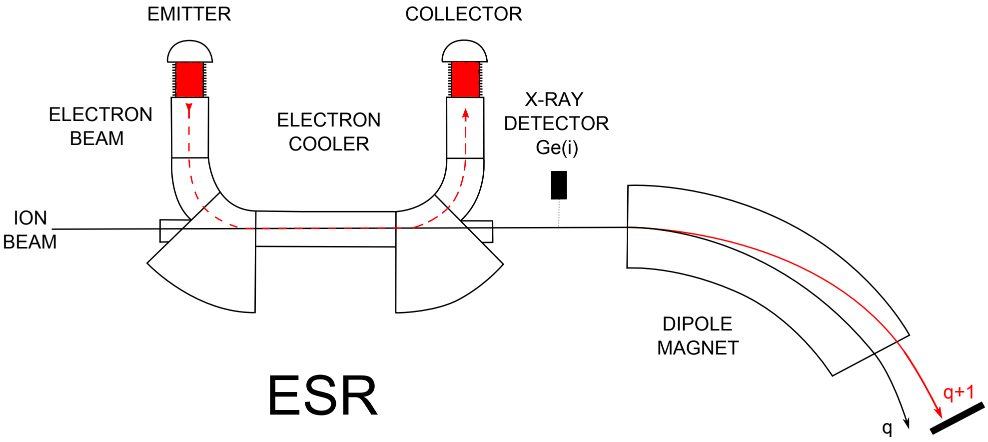

Figure 2.7: A schematic of the experimental setup at GSI to measure the ground state Lamb shift in HCI [15].

only the true events to be selected. The ions register in a gas filled multi-wire proportional counter (MWPC). The x-ray spectrum that was obtained from this setup is shown in Fig. 2.6b. The x-ray energies are Doppler shifted and require transformation into the rest frame of the ion. The relativistic Doppler shift is given by

$$E = E_{lab}\gamma(1 - \beta\cos\theta_{lab}) \tag{2.2.3}$$

where E and E_{lab} are the x-ray energies in the emitter and laboratory frame respectively, γ is the relativistic Lorentz factor, θ_{lab} denotes the observation angle and β is the velocity in units of the speed of light. From this it can be seen why detection close to 0 degrees is exploited as the sensitivity of the energy to the observation angle is at a minimum. Furthermore, with electron cooling, the error in phase $\Delta\beta$, is significantly reduced. The $1s$ Lamb shift is obtained from the Ly$_{\alpha1}$ and K lines. In the case of the K lines, Doppler transformation yields the $1s$ binding energy directly, however as the initial energy of the captured electron is not well known, there is a degree of uncertainty. For the Ly$_{\alpha1}$ line, the theoretical value of the well known binding energy of the 2P$_{3/2}$ state is added. After taking a weighted average, Stöhlker et al obtained a value of 460.2 ± 4.6eV from this experiment. It shows an improvement by a factor of 3 from previous experiments which were also conducted at the ESR, but with electron capture from a gas target [16]. The uncertainty is now on the level of one percent. This level of accuracy required theorists to calculate all second order QED corrections. This has been done and the results are compared below:

Finite nuclear size	198.81eV
1st order QED	266.45eV
2nd order QED	−1.26eV
Total Theory [17]	464.26 ± 0.5eV
Experiment [14]	460.2 ± 4.6eV

This table shows good agreement between theory and experiment. The experiment was sensitive to the level of 2% on first-order QED corrections. At present it shows that the calculations are more precise than experiment. However this gap will be addressed by the next iteration of this experiment.

2.2.2 Hyperfine Structure

Hyperfine structure results from the interaction of the nuclear magnetic moment, with the magnetic field of the bound electron. This leads to a hyperfine splitting of energy levels in atoms and ions, which is three orders of magnitude smaller than the fine structure splitting caused by spin orbit interaction. Nuclei with unpaired fermions have non-zero nuclear spin, and consequently a magnetic moment and hyperfine structure. The induced magnetic flux density on an electron in the ground state of a highly charged nucleus is about 10^4T [4], which is several orders of magnitude higher than the field provided by the most powerful superconducting magnets available today. This area offers one of the most stringent tests of the magnetic sector of bound-state non-perturbative QED.

The HFS in H-like ions is dominated by the Dirac contribution given by [18]

$$\Delta E^{1s}_{Dirac} = \frac{4}{3}\alpha(\alpha Z)^3 g_I \frac{m_e}{m_p}\frac{2I+1}{2} m_e c^2 A_s(1-\delta) \tag{2.2.4}$$

where g_I is the nuclear g-factor, I the nuclear spin, m_e and m_p are the electron and proton mass respectively, and the correction factors A_s and $(1-\delta)$ account for the relativistic energy of the s orbital electron and the 'Breit Schawlow' effect [19] [20] respectively. The ground-state HFS in most atoms and ions is typically in the microwave region e.g. the 21cm line in hydrogen. However from (2.2.4) and Fig. 2.8, it can be seen that for H-like ions with $Z > 60$, the Z^3 scaling shifts the transitions into the laser accessible optical region.

The transition between the ground-state HFS levels involves no change in the

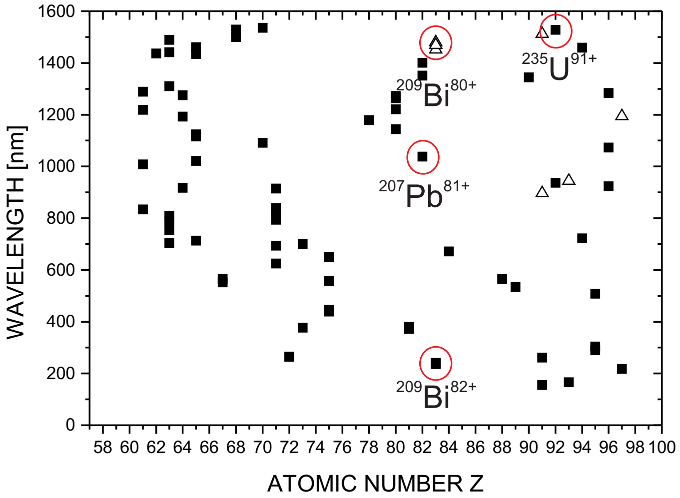

Figure 2.8: Transition wavelengths between the upper and lower hyperfine levels for different H-like (full symbols) and Li-like (open symbols) heavy highly charged ions [21].

Ion	Type	λ(nm)	t(ms)	I
^{207}Pb^{81+}	H-Like	1019.7	50	1/2
^{209}Bi^{82+}	H-Like	243.9	0.35	9/2
^{209}Bi^{80+}	Li-Like	1514	83	9/2
^{235}U^{91+}	H-Like	1538	110	7/2

Table 2.1: Table of the most interesting first HFS spectroscopy candidates [21].

principle quantum number (n) and the orbital angular momentum of the electron (l). Therefore the selection rules make the transition electric-dipole forbidden (E1), but magnetic dipole allowed (M1). In comparison to E1, M1 transitions only appear in the next higher order of the multipole expansion and so are relatively weak. Typically for low Z, these transitions would be very slow and not ideal for fluorescence spectroscopy. However, considering the lifetime τ, for a M1 transition between hyperfine states is given by [22]

$$A = \frac{1}{\tau} = \frac{4\alpha(2\pi\nu)^3\hbar^2 I(2\kappa+1)^2}{27m_e^2c^4(2I+1)} \tag{2.2.5}$$

where κ is related to the electron's angular momentum and ν is the frequency of the transition, as A is proportional to ν^3, and ν is proportional to Z^3, the transition lifetime scales as $\tau \propto Z^{-9}$. This implies for $Z \geq 70$, the typically weak HFS $M1$ transitions have acceptable lifetimes of the order of milliseconds as shown in table 2.1. With these two enhancements for high Z ions, it becomes possible to apply laser spectroscopy techniques to achieve high resolution measurements of the ground state HFS of HCI.

The main uncertainty in HFS calculations comes from the effect of the magnetic dipole distribution inside the nucleus (the Bohr Weisskopf effect) [23]. As QED corrections are of the same scale as this effect, it becomes impossible to test the theory without first understanding the nuclear structure in more detail. However, this limitation may be circumvented by a comparison of the ground-state HFS in both H-like (ΔE^{1S}) and Li-like (ΔE^{2S}) ions with the same nucleus through the difference

$$\Delta E' = \Delta E^{2S} - \zeta \Delta E^{1S} \tag{2.2.6}$$

where ζ is a numerical factor which has been shown to be calculable to high precision yielding the specific energy difference $\Delta E'$ that is almost independent of the nuclear structure [18]. Bismuth is the only element which has a stable isotope (^{209}Bi) with ground-state HFS transitions in both H- and Li-like ions in the range accessible to lasers. Isotopes of Lead are also of particular interest because their nuclear properties are known to even better precision due to the almost closed ‘doubly-magic’ structure [24], even though they do not meet this criterion. Hence the ions in table 2.1 are the first spectroscopic candidates of interest.

2.2.2.1 Experiment

The most precise measurement of the HFS of the heaviest HCI species to date was made at the ESR for H-like Bismuth in 1994 [25]. The experimental arrangement is shown in Fig. 2.9. The $^{209}\mathrm{Bi}^{82+}$ ions were injected into the ESR and accumulated over several cycles of the SIS. The velocity of the ions was ~ 0.6c with a relative velocity spread of $\sim 1 \times 10^{-4}$ measured via Schottky analysis [26][3]. The ion beam was overlapped in a field-free straight region of the ESR in a collinear counter-propagating geometry with a pulsed excita-

---

[3] A Schottky signal is the incoherent electrical signal from, for example, a pulsed ion bunch passing a pickup electrode. Via spectral analysis, information on the velocity spread of the ion bunch can be obtained.

tion laser. Because of the relatively low transition probability of the magnetic dipole transition, ions decayed along many entire cycles of the ESR. The fluorescence was collected along the laser-ion interaction region over a length of $\sim$ 1m using a cylindrical elliptical mirror system onto three photomultiplier tubes. Approximately 0.05% of the total fluorescence emitted in the ring was collected. The detection was also triggered to occur between laser pulses to reduce scatter i.e. detection in the dark.

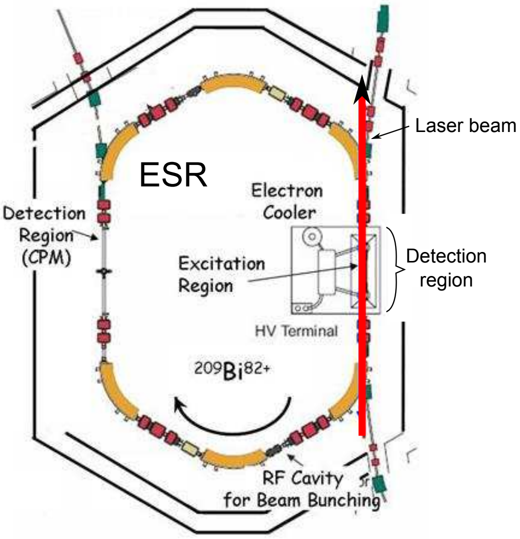

Figure 2.9: ESR ^{209}Bi^{82+} HFS experimental schematic diagram [27]. Note the illustration of the laser excitation and fluorescence detection region is enlarged and is not to scale.

In this geometry, the Doppler effect shifts the transition wavelength according to the relation

$$\lambda = \lambda_0 \frac{1}{\gamma(1 + \beta \cos\theta)} \tag{2.2.7}$$

where θ is the observation angle with respect to beam direction. This shifts the required laser excitation wavelength from λ_0 in the rest frame of the ion to λ in the laboratory frame. The main experimental uncertainty in determining the wavelength λ_0 did not come from the Doppler width of the transition, but instead the uncertainty associated in determining the absolute ion velocity (from Schottky analysis) required for the transformation from the laboratory to the ion's frame of reference.

Fig. 2.10 shows the resonance signal obtained for the ground-state HFS transition in $^{209}\mathrm{Bi}^{82+}$ from which a value of $\lambda_0 = 243.87 \pm 0.04$nm was obtained. Table 2.2 compares this experimental result with the theoretical expectations for the energy the HFS. There is a clear disagreement between theory and experiment, and this is believed to be due to inaccurate knowledge of the nuclear properties as mentioned before [24]. The next stage of investigation will be to measured the HFS in Li-like Bismuth to calculate the specific difference in equation (2.2.6). In the first instance, this will most likely be done by the similar experiment being prepared at the ESR by Nörtershäuser [28] which will use collinear co-propagating laser beams to shift the transition from ~ 1555nm to ~ 640nm at $v = 0.7$c in the laboratory frame. Already one unsuccessful attempt was made at the ESR where is it thought the signal to noise ratio was insufficient to see the weak fluorescence. Ultimately, the SPECTRAP experiment will have the highest resolution for such spectroscopy measurements as the HCI will be at cryogenic temperatures (see section 9.2).

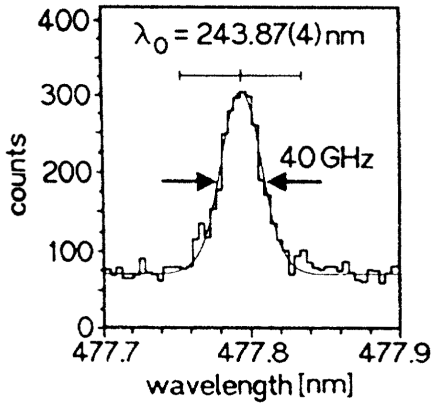

Figure 2.10: A fluorescence spectrum from a measurement of the ground-state HFS of $^{209}\mathrm{Bi}^{82+}$ in the ESR at GSI [25].

2.2.3 g-factor

For a free electron, the g-factor is modified from the Dirac value of exactly 2 by the aforementioned QED effects. For a bound electron, this value is further modified by the QED effects in the strong electric field of the nucleus. For H-like ions, there are contributions from the relativistic, QED and nuclear

Dirac value	5.839
Finite nuclear size	−0.649
Bohr-Weisskopf	−0.062
QED	−0.030
Total Theory [29]	5.098 ± 0.007eV
Experiment [25]	5.0840 ± 0.0008eV

Table 2.2: A table comparing the theoretical and experimental ground-state HFS of $^{209}\mathrm{Bi}^{82+}$.

corrections. Of these, the relativistic correction is the largest and for the ground-state of H-like ions is given by [30]

$$g = \frac{2}{3}(1 + 2\sqrt{1 - (\alpha Z)^2}). \tag{2.2.8}$$

For $^{235}\mathrm{U}^{91+}$, the g-factor already differs by as much as 15% from the Dirac value [31]. The QED corrections involve the sum of the free-electron and bound-state QED corrections of which the former is already known to the level of 10^{-12} [3]. The scale and hence sensitivity to which the remaining corrections test the g-factor as a function of Z is shown in Fig. 2.11. From the previous two sections, it has been shown that tests of QED via the Lamb shift and HFS in HCI suffer from large uncertainties associated with the nuclear structure. But as Fig. 2.11 shows, for medium heavy HCI, the g-factor is not sensitive to nuclear structure effects, and hence it represents a clean way to test pure bound-state QED in HCI.

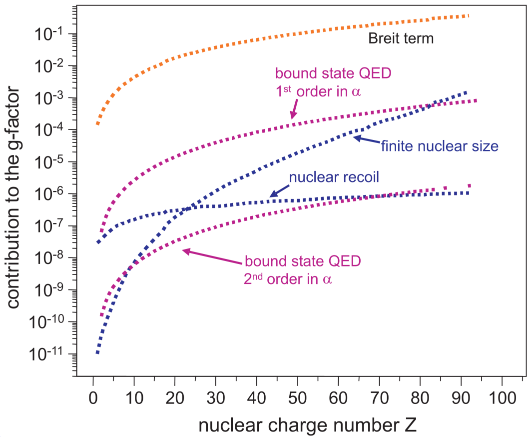

Figure 2.11: Contributions to the g-factor of an electron bound in the ground-state of a H-like ion as a function of nuclear charge Z [31].

In such an isolated environment as a Penning trap, the magnetic moment of an electron precesses in the presence of an external magnetic field at the Larmor frequency given by

$$\omega_l = g\mu_b \frac{B}{\hbar} = g\frac{eB}{2m_e} = \frac{g}{2}\omega_{c,e}. \tag{2.2.9}$$

where m_e is the mass of the electron, B the magnitude of the magnetic field and $\omega_{c,e}$ the electron's cyclotron frequency. The orientation of the spin may be parallel or anti-parallel with the magnetic field and hence leads to two states with an energy splitting of $\hbar\omega_l$. The g-factor of the free electron may be obtained by measuring the ratio of the (electron) Larmor to cyclotron frequency. For an ion with a zero nuclear spin, the magnetic moment of the ion is that of the electron. For a bound electron, since the cyclotron frequency of the ion $\omega_{c,ion}$ is measured instead of the electron's, the g-factor is obtained through the relation

$$g = 2\frac{\omega_l}{\omega_{c,ion}}\frac{\omega_{c,ion}}{\omega_{c,e}} = 2\frac{\omega_l}{\omega_{c,ion}}\frac{q_{ion}/m_{ion}}{q_e/m_e} \tag{2.2.10}$$

which requires an accurate measurement of the electron to ion charge to mass ratio.

2.2.3.1 Experiment

The most accurate measurement of the g-factor of the highest H-like ion has come from the group of W. Quint at the Johannes-Gutenberg-Universität in Mainz, Germany. The g-factor in H-like ^{28}Si^{13+} was measured with a single ion in the Penning trap setup shown in Fig. 2.12 [32].

The experiment consists of a stack a three connected cylindrical Penning traps placed along the magnetic field direction of a cryogenic solenoid type superconducting magnet. The electron gun, creation trap and reflector electrodes form what is essentially an EBIT for charge breeding by electron impact ionization. Electrons are emitted from the field emission point (FEP) and reflected by the hyperbolic reflector onto the target surface containing the sputtered atoms to be ionised. An electron beam energy of 4keV is used to charge bread silicon ions to ^{28}Si^{13+}. This is experimentally demanding and is almost at the limit of the heaviest H-like HCI that can be created in-situ. Hence the next generation of experiments will use the GSI accelerator.

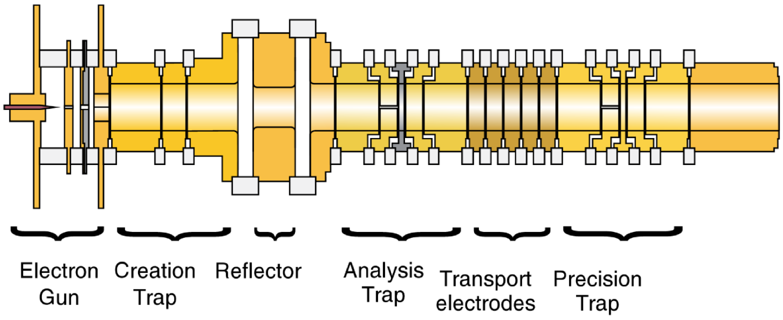

Figure 2.12: Experimental setup of the Mainz double trap g-factor experiment for hydrogen-like silicon [32]. The trap is located in a magnetic field of 3.76T.

The content of all the traps is monitored electronically by Fourier transforming the image currents induced on the trap electrodes. After the required ion is loaded into the creation trap, it is transported adiabatically to the analysis trap were a deliberately induced magnetic inhomogeneity (produced via a ferrous electrode), is used to couple the spin direction to the motional frequencies of the ion. By introducing a magnetic field proportional to the square of the displacement from the centre of the trap, the axial ion oscillation frequency is shifted in different directions for the two spin-states. Fig. 2.13(upper frame) shows a $^{28}\mathrm{Si}^{13+}$ ion in the analysis trap where a spin-flip is induced by microwave excitation at the Larmor frequency. In this way, the axial frequency can be calibrated to the direction of the spin. The magnetic field inhomogeneity in the analysis trap broadens all the motional (and Larmor) frequencies. Consequently the ion is transported to the precision trap which has the maximum magnetic homogeneity and electric harmonicity to measure the cyclotron frequency and induce spin-flip transitions at the Larmor frequency with the highest precision. To detect if a spin-flip has occurred, the ion is transported back to the analysis trap to detect the corresponding change in axial frequency. When this method is repeated several times, a probability for a spin-flip transition at a particular microwave frequency is obtained. The Larmor frequency is then obtained from the microwave frequency (ω_{MW}) which gives the maximum probability of a spin-flip transition as shown in Fig. 2.13(lower frame). Due to the presence of a residual magnetic inhomogeneity in the precision trap from the analysis trap, the cyclotron motional frequency becomes dependent on the energy of the ion. Therefore measurements of $\omega_l/\omega_{c,ion}$ are made at different cyclotron energies and extrapolated to zero field to give the g-factor and thus the magnetic moment of the bound-electron according to equation (2.2.10).

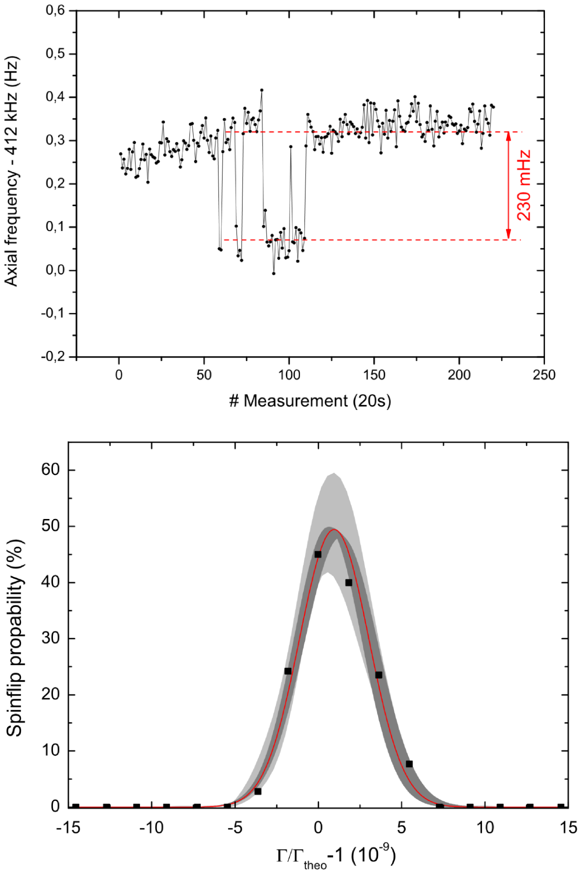

Figure 2.13: (upper frame) Axial frequency of a ^{28}Si^{13+} ion in the analysis trap irradiated by microwave radiated at ω_l showing the two spin directions [33] and (lower frame) the spin flip probability of the ion in the precision trap plotted as a function of $\Gamma = \omega_{MW}/\omega_c$ from the experiment to measure the bound electron g-factor in hydrogen-like silicon [32].

Table 2.3 below shows a comparison between the theoretical and experimentally determined g-factors of ^{28}Si^{13+}. The experiment was sensitive to the level of 0.001% of the bound-state QED contributions. To date, this is the most sensitive test of high order bound-state QED. The most experimentally challenging aspect of making such a measurement is the detection of spin-flip transitions via the relatively small frequency shift of the ion's axial resonance frequency $\delta\omega_z$which scales with $1/m$.

Dirac value	1.9930235716eV
Finite nuclear size	0.0000000205eV
Recoil	0.0000002061eV
Bound-state QED	0.0023251602eV
Free-electron QED	0.0023228195eV
Total Theory [34]	1.9953489580 ± 0.000000017eV
Experiment [35]	1.9953489587 ± 0.0000000010eV

Table 2.3: A comparison between the theoretically and experimentally determined values of the g-factor of $^{28}\mathrm{Si}^{13+}$.

2.3 Conclusion

In this review, the latest experimental efforts to measure the bound-state QED contributions to the Lamb shift, hyperfine structure splitting and bound-electron g-factor in hydrogen and lithium like highly charged ions have been presented. It has been shown that the three experimental approaches are sensitive to the various bound-state QED contributions to different degrees of accuracy. Therefore it may appear that the experiments are degenerate as quantitative tests of bound-state QED. This is not the case since the contributing Feynman diagrams and the mathematical and computational techniques used to evaluate the diagrams to make theoretical predictions of the QED contributions, are very different for the three experiments. Hence the experimental and theoretical motivation in the different areas.

The QED contributions have also been shown to scale with increasing nuclear charge, and therefore lead to more stringent tests of the corresponding theoretical calculations. By use of specific differences between isoelectronic systems, the main uncertainties from the nuclear effects can be removed and eventually better understood. Furthermore, by independent verifications in different systems and amongst different measurables, more accurate physical constants such as the fine structure constant and electron mass can be obtained.

Chapter 3

Ion Traps

The basic principles of ion trapping are described in this chapter. To trap ions, a restoring force is required. To lowest order, this force will be proportional to the displacement of ions from the trap centre, making the solutions to the equations of motion of the simplest form and analytically solvable. That is to say

$$F = -kx \tag{3.0.1}$$

where x is the displacement and k is the constant of proportionality. The potential ϕ, is related to the force on an ion of charge q by

$$F = -q\nabla\phi \tag{3.0.2}$$

which means the potential must have a harmonic or quadratic form

$$\phi = \phi_0(Ax^2 + By^2 + Cz^2). \tag{3.0.3}$$

Now ϕ must satisfy Laplace's equation

$$\nabla^2\phi = 0 \tag{3.0.4}$$

and hence requires the coefficients satisfy $A + B + C = 0$. This implies that a three dimensional potential minimum cannot be generated from static electric fields alone. If we assume radial symmetry, such as for the electrode configuration shown in Fig. 3.1, then $A = B = -1$ and $C = 2$. The radial electrode can be thought of as a ring surrounding the centre, and the axial electrodes as endcaps enclosing the volume. To generate such a potential, the electrodes must follow the contours of equipotential lines and therefore the endcaps must be hyperboloids of revolution, and the ring must have a hyperbolic cross section. With a potential U_0 applied between the endcaps and ring electrode, the quadrupole trap potential ϕ_t is generated

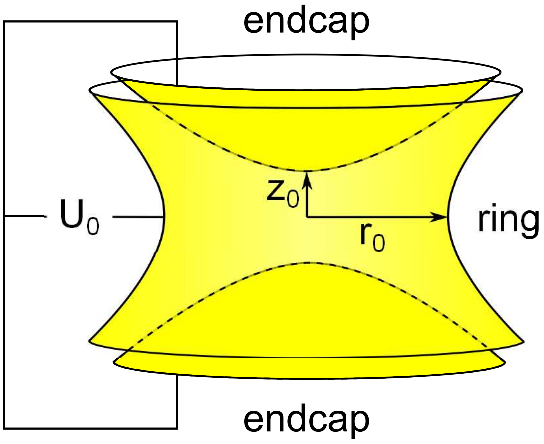

Figure 3.1: General electrode configuration for an ion trap.

$$\phi_t(r,z) = \frac{U_0}{4d_0^2}(2z^2 - r^2) \tag{3.0.5}$$

where $d_0 = \frac{1}{2}\sqrt{r_0^2 + 2z_0^2}$, and r_0 and z_0 are the distances from the origin along the axes to the ring and endcap electrodes respectively. As all real electrodes are finite in size, such a potential can never exactly be produced. However, near the origin, the potential can be well approximated by equation (3.0.5), and this is even true for flat or cylindrical shape electrodes. Using this general electrode structure creating a quadratic potential, a three dimensional ion trap can be made in two ways: time varying the electric potential (Paul trap), or superimposing a uniform magnetic field along one of the axis (Penning trap).

3.1 Paul Traps

The Paul or radio frequency trap operates by applying a time varying potential V_{rf}, at frequency Ω, in addition to a static potential U_0 (which is not strictly necessary) such that the potential at the centre of the trap is described by

$$\phi = \frac{(U_0 + V_{rf}\cos\Omega t)}{4d_0^2}(2z^2 - r^2). \tag{3.1.1}$$

Although the instantaneous potential ϕ leads to a divergent motion of an ion out of the trap, because the trapping field is inhomogenous, the time averaged force is convergent to the centre of the trap. For an ion of mass m and charge q, this gives the following equations of motion,

$$\ddot{r} + \frac{q}{m2d_0^2}(U_0 + V_{rf}\cos\Omega t)r = 0 \tag{3.1.2}$$

$$\ddot{z} - \frac{q}{md_0^2}(U_0 + V_{rf}\cos\Omega t)z = 0. \tag{3.1.3}$$

By making the following substitutions

$$a_z = -2a_r = \frac{-4qU_0}{md_0^2\Omega^2} \tag{3.1.4}$$

$$q_z = -2q_r = \frac{2qV_{rf}}{md_0^2\Omega^2} \tag{3.1.5}$$

$$2\zeta = \Omega t \tag{3.1.6}$$

the equations of motion can be rearranged into the familiar Mathieu type equations [36]

$$\frac{d^2r}{d\zeta^2} + (a_r - 2q_r cos2\zeta)r = 0 \tag{3.1.7}$$

$$\frac{d^2z}{d\zeta^2} + (a_z - 2q_z cos2\zeta)z = 0 \tag{3.1.8}$$

which have solutions with a periodicity given by

$$\omega_{n,i} = \frac{(2n \pm \beta_i)\Omega}{2} \tag{3.1.9}$$

where β_i is a continued fraction dependent on the a_i and q_i parameters

$$\beta_i^2 = a_i + \frac{q_i^2}{(2+\beta_i)^2 - a_i - \frac{q_i^2}{(4+\beta_i)^2 - a_i - \ldots}} - \frac{q_i^2}{(2-\beta_i)^2 - a_i - \frac{q_i^2}{(4-\beta_i)^2 - a_i - \ldots}} \tag{3.1.10}$$

and the index i denotes either a radial or axial set of terms. The β_i parameter defines the regions of stability in the a-q plane. Due to the negative factor relation between the axial and radial parameters, simultaneous stability or trapping is only obtained over the limited area of overlap of these regions, and due to the 2 factor, this stability region is asymmetric about the a_i axis. The first stability region with the smallest $|a_i|$ and $|q_i|$ is bound by $0 < \beta_r < 1$ and

$0 < \beta_z < 1$ and is shown in Fig. 3.2.

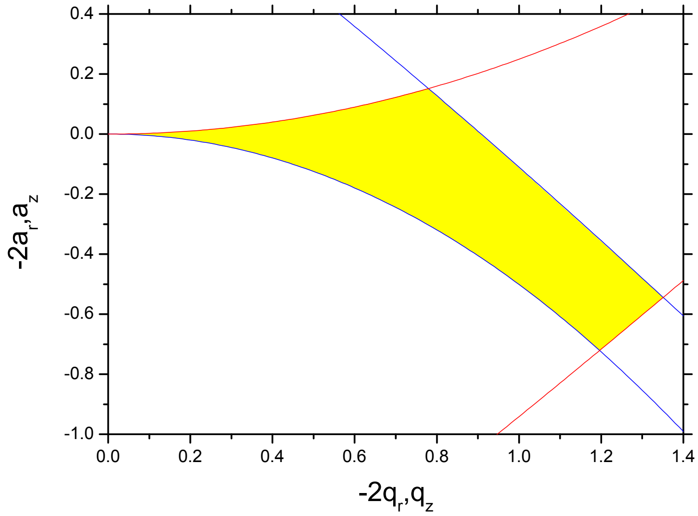

Figure 3.2: A plot of the Paul trap first stability region. The boundary of radial and axial stability is indicated by the red and blue lines respectively.

Although an ion in a Paul trap will have a whole spectrum of motional frequencies given by equation (3.1.9), the amplitude of each Fourier component decreases with increasing n [37]. For $|a_i|, |q_i| \ll 1$, β_i may be well approximated by

$$\beta_i^2 \approx a_i + \frac{q_i^2}{2} \tag{3.1.11}$$

and the amplitudes of successive Fourier components become factors of q smaller [37]. Hence the motion can well be described by considering only the first two terms in n in equation (3.1.9) giving

$$\omega_{o,i} = \frac{\beta_i \Omega}{2} \tag{3.1.12}$$

$$\omega_{1,i} = \frac{(2 \pm \beta_i)\Omega}{2}. \tag{3.1.13}$$

As $\beta_i \ll \Omega$, the fundamental motional frequency $\omega_{0,i}$ is well removed from the RF frequency applied and is called the macro-motion or secular-motion of the ion. The motion at $\omega_{1,i}$ is approximately at the RF frequency but because the amplitude of this motion is much smaller, it is known as the micromotion of the ion. Explicitly stated, in an ideal quadrupole Paul trap, there is an uncoupled macromotion and micromotion (at different frequencies) in the axial and radial directions.

For real ion traps, there will always be anharmonicities present to some degree due to errors in machining and aligning the trap electrodes. Furthermore, the electrodes themselves are a finite size approximation to the ideal trap described here, hence the potential will have high order spatial dependences. This leads to a coupling between the radial and axial degrees of freedom and instability in trapping for specific parameters that would otherwise give stable trapping. For the first stability region, the implication is that if an integer linear combination of the macromotion frequencies equals a multiple of the RF frequency

$$n_r\omega_{0,r} + n_z\omega_{0,z} + m\Omega = 0 \tag{3.1.14}$$

where n_r, n_z and m are all integers, then energy will be transferred from the field to the ions and an instability in trapping will occur. This produces lines of instability in the a-q plane not shown in Fig. 3.2.

The Paul trap has some advantages over the Penning trap. As the β stability parameter is dependent on the magnitude and not the sign of q, particles of opposite charge can be simultaneously trapped together in the same region of the trap. As no magnetic field is required, practically the system can be more compact, allowing for example, the traps to be used in devices such as portable mass spectrometers. With no magnetic field, there is also no Zeeman splitting and so laser cooling and spectroscopy is much simpler.

The main disadvantages of a Paul trap arise due to the oscillating RF potential. The micromotion in the trap fundamentally limits the lowest temperature to which a cloud of ions can be cooled to. This can have implications for example in studies with very large ion crystals where RF heating will be a limitation. Also as the effective depth of the trap scales with the square of the frequency and amplitude of the RF potential, but the stability scales with the ratio of the amplitude to frequency squared, a deep trap of typically less than several 10eV with hundreds of volts at megahertz frequencies is technically difficult to achieve. Hence Penning traps are usually needed for in-flight ion capture from an external source where ions are transported with a high kinetic energy to minimise the divergence angle.

3.2 Penning Traps

The Penning trap uses a static electric quadrupole potential as described in equation (3.0.5) with usually an axial superimposed homogeneous magnetic field. The force on an ion moving with velocity v in this combined field is given by

$$F = -q\nabla\phi_t + q(v \times B) \tag{3.2.1}$$

which in the axial direction is purely electrostatic and gives the equation of motion

$$\ddot{z} + \omega_z^2 z = 0 \tag{3.2.2}$$

where

$$\omega_z = \sqrt{\frac{qU_0}{md_0^2}} \tag{3.2.3}$$

and describes a simple harmonic motion at frequency ω_z. Hence axial confinement is provided by the electrode potential alone, and for condition the $qU_0 > 0$. In the radial direction, the magnetic field provides the confinement (via the Lorentz force) and the electrostatic potential acts to reduce this. By using the definition of the precession or cyclotron frequency of an ion in a magnetic field

$$\omega_c = \frac{qB}{m} \tag{3.2.4}$$

the radial equations of motion can be written in the form

$$\ddot{x} - \omega_c\dot{y} - \frac{\omega_z^2}{2}x = 0 \tag{3.2.5}$$

$$\ddot{y} + \omega_c\dot{x} - \frac{\omega_z^2}{2}y = 0 \tag{3.2.6}$$

which are coupled differential equations. These can be simplified via the substitution of the complex variable $u = x + iy$ to give

$$\ddot{u} + i\omega_c\dot{u} + \frac{\omega_z^2}{2}u = 0 \tag{3.2.7}$$

which via the general solution of $u = e^{-i\omega t}$ requires that

$$\omega^2 - \omega_c\omega + \frac{\omega_z^2}{2} = 0 \tag{3.2.8}$$

and hence yields the two solutions

$$\omega_c' = \frac{1}{2}\left(\omega_c + \sqrt{\omega_c^2 - 2\omega_z^2}\right). \tag{3.2.9}$$

$$\omega_m = \frac{1}{2}\left(\omega_c - \sqrt{\omega_c^2 - 2\omega_z^2}\right) \tag{3.2.10}$$

where ω_c' can be interpreted as the cyclotron frequency modified by the trap potential, and ω_m as a drift of the cyclotron motion along the radial equipotential lines of the trap potential (also known as the magnetron motion). Therefore in an ideal Penning trap, the motion of an ion is a superposition of three independent motions (or degrees of freedom) at frequencies ω_z, ω_m and ω_c'. An example of the trajectory of an ion in a Penning trap is shown in Fig. 3.3.

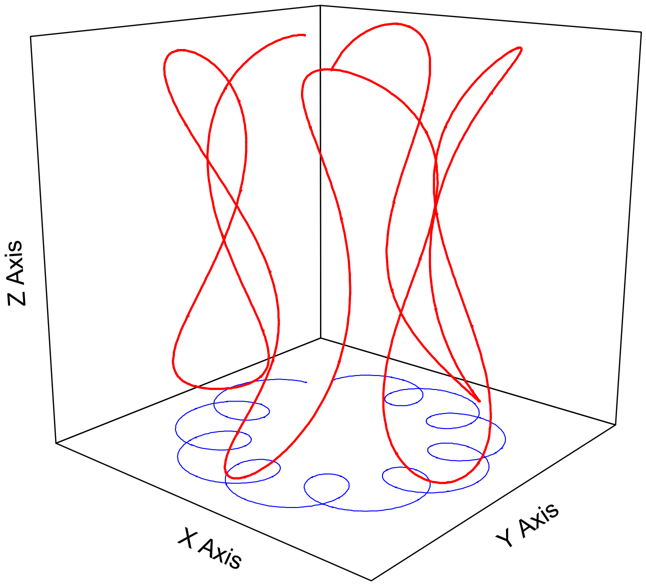

Figure 3.3: (red) A plot of the trajectory of an ion in a Penning trap with an axial magnetic field and (blue) the corresponding projection into the x-y plane.

The motional frequencies are linked together through the invariance theorem [38]

$$\omega_m^2 + \omega_z^2 + \omega_c'^2 = \omega_c^2. \tag{3.2.11}$$

For stable trapping, the solutions to the frequencies in equations (3.2.9) and (3.2.10) must be real, and therefore this sets the requirement for

$$2\omega_z^2 < \omega_c^2 \tag{3.2.12}$$

or in terms of the trap voltage

$$U_0 < \frac{qB^2 d_0^2}{2m}. \tag{3.2.13}$$

The left hand side of equations (3.2.12) and (3.2.13) is the effective strength of the repulsive radial electrostatic potential which of course must be less than the confinement provided by the magnetic field on the right hand side to constitute a trap.

As in the case for the Paul trap, anharmonicities in the quadrupole trap potential produce instabilities in the Penning trap. In this case, if an integer number of any one of, or sum of motional frequencies equals that of another

$$n_z \omega_z + n_m \omega_m + n_{c'} \omega_{c'} = 0 \tag{3.2.14}$$

where n_z, n_m and $n_{c'}$ are integers, energy can be exchanged between the degrees of freedom and ions can be lost. This is particularly important for the magnetron motion whose radius increases with decreasing energy i.e. the motion is inherently unstable. Therefore if energy is transferred out of the magnetron motion by resonant coupling, the radius of an ion's orbit could increases beyond the trap electrodes and the ion would be lost.

To first (even) order anharmonicity, magnetic and electric field misalignments, misshapen trap electrodes and space and image charge effects cause energy dependent shifts of the motional frequencies of single ions. For a cloud of ions, this effectively shifts and inhomogeneously broadens the collective motional frequencies of ions. For these reasons in practice, the stability of the trap is compromised well before the maximum voltage criteria set out by equation (3.2.13). For example, in one particular experiment [39], the maximum trap voltage is shown to be limited to $\lesssim 50\%$ of the theoretical maximum.

At the expense of additional complexity due to the axial magnetic field, the Penning trap has some specific advantages over the Paul trap which have not been discussed so far, that make is well suited to the SPECTRAP experiment at GSI. First, with radial confinement provided by the magnetic field, the potential on the endcaps can be switched fast ($<$ 500ns) to capture ions in-flight from an external source. And more generally, the trap size can be scaled to accommodate a large acceptance solid angle for in-flight ion capture while still maintaining high trapping fields i.e. the trap depth remains U_0 irrespective of the trap size and can easily be several 100eV. Secondly, high trapping fields support higher ion densities which can be dynamically controlled by the use of the rotating wall technqiue (see section 8). And lastly, electronic detection (or cooling) of ions is not swamped by the noise from the radio frequency trapping fields.

The biggest disadvantage of the Penning trap is the unstable magnetron motion. There must always be some form of torque applied to an ion (or cloud of ions) to balance the drag and eventual ion loss caused by collisions with residual gas particles or errors in the trapping fields causing coupling between degrees of freedom that transfers energy out of this motion. Hence this generally complicates the cooling schemes involved.

3.3 Non-Neutral Plasmas in Penning Traps

When there is more than one ion in a Penning trap, the total electrostatic potential ϕ is the sum of the trapping potential ϕ_T, the potential due to space-charge of the ions ϕ_{sc}, and the potential due to the image charges induced on the trap electrodes ϕ_{im}

$$\phi = \phi_T + \phi_{sc} + \phi_{im}. \tag{3.3.1}$$

The contribution to ϕ from ϕ_{im} may be estimated by considering the image charge from an ion trapped between a pair of infinite parallel plates separated by a distance $2z_0$ i.e loosely modelling the endcaps. Assuming the displacement of the ion is always much less than the distance between the plates, it can be shown that the shift in the axial frequency can be approximated by [40]

$$\Delta\omega_z \approx \frac{1}{\pi\varepsilon_0}\frac{q^2}{m\omega_z(2z_0)^3} \tag{3.3.2}$$

which implies for N ions, the fractional change to the axial trapping potential will be

$$\frac{\phi_{im}(0,z)}{\phi_T(0,z)} = N\left(\frac{\Delta\omega_z}{\omega_z}\right)^2. \tag{3.3.3}$$

For 10^5 trapped $^{40}\mathrm{Ca}^+$ ions in SPECTRAP with an axial frequency of $\omega_z = 2.\pi.50\mathrm{kHz}$, the above fraction is only 10^{-9}. Therefore, for what is considered a large cloud with a low axial frequency, this shows for singly charged calcium ions, that ϕ_{im} may be considered as a negligibly small term and hence is ignored hereafter.

For a large number of ions in a Penning trap at low temperature and high density, the Coulomb interaction between ions rotating at different frequencies drives the ion cloud to a thermal equilibrium in which all ions rotate at a global rigid rotation frequency, ω_r[1]. Under these conditions, the total effective electric potential of a ion in a Penning trap is given by

$$\phi(r,z) = \frac{m}{2q}\omega_r\omega_c r^2 - \frac{m}{2q}\omega_r^2 r^2 + \phi_t(r,z) + \phi_{sc}(r,z) \tag{3.3.4}$$

---

[1] Inside the ion cloud, the trapping fields are shielded by the space charge potential of the ions using the assumptions in this section. Therefore there is no cyclotron motion of individual ions in the interior of the cloud. Hence the entire ion cloud rotates as a rigid body about the centre of the trap and magnetic field axis, like the magnetron motion. For an undriven ion cloud, the value of ω_r depends on its initial conditions upon trapping.

where $\frac{m}{2q}\omega_r\omega_c r^2$ is the electric potential experienced by an ion rotating through a magnetic field (i.e that which provides radial trapping), $-\frac{m}{2q}\omega_r^2 r^2$ is the centrifugal potential, $\phi_t(r,z)$ is the potential produced by the trap electrodes, and $\phi_{sc}(r,z)$ the space charge potential.

The potential must obey Poisson's equation, and to be self consistent, we first require

$$\nabla^2\phi_{sc}(r,z) = -\frac{\rho(r,z)}{\epsilon_0} = -\frac{qn(r,z)}{\epsilon_0} \tag{3.3.5}$$

where $\rho(r,z)$ and $n(r,z)$ are the ion charge and number density respectively, with the boundary conditions of grounded trap electrodes. Since $\nabla^2\phi_t = 0$, and with azimuthal symmetry, it is simple to show that

$$\nabla^2\phi(r,z) = \frac{1}{r}\frac{\partial}{\partial r}\left(r\frac{\partial\phi}{\partial r}\right) + \frac{\partial^2\phi}{\partial z^2} \tag{3.3.6}$$

$$\nabla^2\phi(r,z) = -\frac{qn(r,z)}{\epsilon_0} + \frac{2m}{q}\omega_r(\omega_c - \omega_r). \tag{3.3.7}$$

In thermal equilibrium , the ion density distribution is given by [41]

$$n(r,z) = n_0 e^{-\frac{q\phi(r,z)}{k_B T}} \tag{3.3.8}$$

where n_0 is defined as the density at the centre of the trap. For low temperature and high density

$$k_B T \ll q\phi_{sc} < \frac{m}{2}\omega_r\omega_c r^2 - \frac{m}{2}\omega_r^2 r^2 + q\phi_t(r,z) \tag{3.3.9}$$

and in the limit of zero temperature, $k_B T \rightarrow 0$, the requirement for $n(r,z)$ to remain finite implies

$$\phi(r,z) = 0. \tag{3.3.10}$$

Hence,

$$\nabla^2\phi(r,z) = 0 \tag{3.3.11}$$

and therefore the space charge potential must exactly cancel out the total trap potential

$$\phi_{sc}(r,z) = -\left(\frac{m}{2q}\omega_r\omega_c r^2 - \frac{m}{2q}\omega_r^2 r^2 + \phi_t(r,z)\right) \tag{3.3.12}$$

and together with equation (3.3.7) yields the number density

$$n(r,z) = n_0 = \frac{2m\varepsilon_0}{q^2}\omega_r(\omega_c - \omega_r) \tag{3.3.13}$$

which is shown to be a constant inside the ion cloud and zero everywhere else. In this limit of zero temperature, the space charge neutralises the trap electrostatic field produced by the electrodes in the interior of the cloud. Therefore, along the axial direction, this means ions travel at near constant velocities and reflect specularly from the cloud boundary. In the radial direction, the electric field from the space charge balances the confinement provided by the rotation of the ions (ω_r) in the magnetic field (through ω_c), and hence the number density is only dependent on these two quantities for ions of a given q/m. In an analogy to the single particle axial frequency in a Penning trap, the so called plasma frequency can be introduced which can be interpreted as the equivalent simple harmonic motion frequency of a ion (of opposite sign) in the radial trapping field generated by the space charge potential

$$\omega_p^2 = 2\omega_r(\omega_c - \omega_r). \tag{3.3.14}$$

Inside the plasma, the radial motion has exactly the same form as that for a single ion in a Penning trap, except for the substitution of ω_p in place of ω_z. When $\omega_r = \omega_c/2$, $\omega_p = \omega_c/\sqrt{2}$, and the maximum density, n_B, or the Brillouin limit is reached where

$$n_B = \frac{m\varepsilon_0\omega_c}{q^2}. \tag{3.3.15}$$

At the Brillouin limit, in the frame rotating with the plasma, the motion of the ions is like that in a unmagnetised plasma where the ions travel in straight lines and reflect from the plasma boundary. For $\omega_r \geq \omega_c/2$, the radial confinement in the magnetic field is increasingly reduced by the centrifugal force, and a smaller space charge or plasma frequency is required to balance confinement. Hence the symmetry in the plasma frequency and number density about $\omega_c/2$ (see Fig. 3.4).

The requirements on the space charge potential described above allows the aspect ratio of the cloud to be calculated. We can expand and reorder equa-

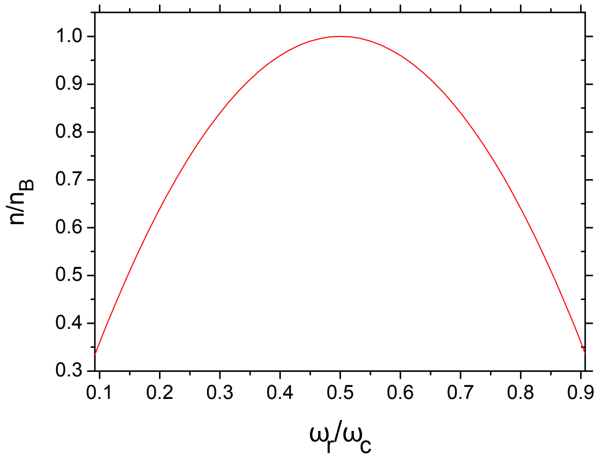

Figure 3.4: A universal plot of the number density as a function of the rotation frequency in units of the Brillouin density and cyclotron frequency respectively.

tion (3.3.12) as follows

$$\phi_{sc}(r,z) = -\frac{m}{2q}\left[\omega_r(\omega_c-\omega_r)+\omega_z^2\right]r^2 + \frac{m\omega_z^2}{q}z^2 \tag{3.3.16}$$

and by factoring out the number density using the relation in equation (3.3.13)

$$\phi_{sc}(r,z) = \frac{qn}{3\varepsilon_0}\left[-\left(\frac{3}{2}+\frac{3\omega_z^2}{2\omega_r(\omega_c-\omega_r)}\right)\frac{r^2}{2}+\left(\frac{3\omega_z^2}{2\omega_r(\omega_c-\omega_r)}\right)z^2\right] \tag{3.3.17}$$

$$\phi_{sc}(r,z) = -\frac{qn}{3\varepsilon_0}(ar^2+bz^2) \tag{3.3.18}$$

where

$$b = \frac{3\omega_z^2}{2\omega_r(\omega_c-\omega_r)} = \frac{3\omega_z^2}{\omega_p^2} \tag{3.3.19}$$

and $2a+b=3$ as required by Poisson's equation. This sets the bound of the global rotation frequency to the range $\omega_m < \omega_r < \omega_c - \omega_m$, where at either extreme, $\omega_p = \omega_z$ and $b = 3$ and $a = 0$ i.e. an infinitely thin radial disk. The coefficient b can be interpreted as the relative degree of axial to radial confinement and is determined by the ratio of the two frequencies. For a perfectly spherical cloud, $a = b = 1$.

Defining the aspect ratio, α, as the axial divided by the radial extent of the cloud, the parameter b can also be given by [41]

$$b = \left| \left(\frac{3}{\alpha^2 - 1} \right) \left[\left(\frac{\alpha}{\sqrt{1-\alpha^2}} \tan^{-1} \left(\frac{1-\alpha^2}{\alpha} \right) \right) - 1 \right] \right| \tag{3.3.20}$$

which can be numerically solved and equated to equation (3.3.19), to show how the ratio of axial to plasma frequency fully determines the aspect ratio of the cloud (see Fig. 3.5). Hence α is a function of the trap potential (U_0), the magnetic field (B) and the global rotation frequency (ω_r) for a low temperature, high density plasma of a single q/m spices.

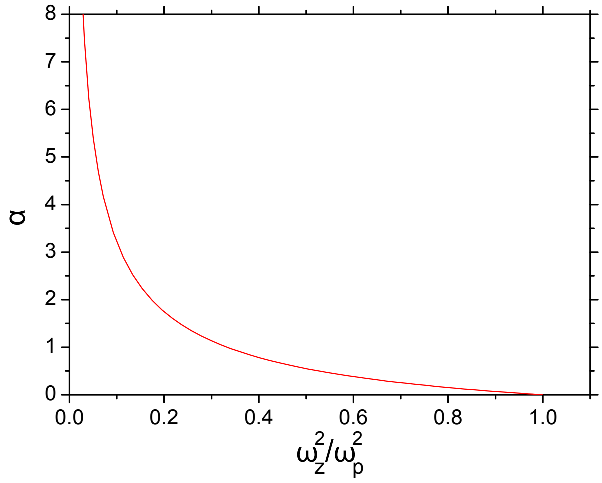

Figure 3.5: A plot to show how the aspect ratio of a cloud of ions is dependent on the trap parameters through ω_z and the magnetic field and rigid rotation frequency of the cloud through ω_p, via the ratio ω_z^2/ω_p^2.

For laser spectroscopy of the HFS in HCI, low fluorescence rates are expected. Compounded with this, for some species of ions, the wavelengths of the transitions are in the infra-red making the detection particularly noisy due to the high dark count of the available detectors in this region. Therefore low signal to noise is expected and this affects the precision to which the line centres can be determined. The signal to noise ratio can be increased by increasing the ion density as well as the overlap between the ion cloud and fluorescence collection imaging volume. Combining all the theory from above, this can be done by applying the maximum magnetic field available and setting the rotation frequency of the cloud to the Brillouin limit (achieving maximum density), and setting the aspect ratio, via the trap potential, approximately equal to one (achieving maximum fluorescence collection).

3.3.1 Rotating Wall

The rotation frequency of the ion cloud can be controlled by applying an external torque. This can come from radiation pressure from a resonant laser beam directed off axis in the radial plane, or an azimuthally asymmetric rotating electric field or ‘rotating wall’ [42]. The latter gives precise control over the rotation frequency of the cloud, and it is not limited to ions which have an accessible fast optical transition. Hence the rotating wall was chosen as a means of compression for ions in SPECTRAP.

To lowest order, the rotating wall is an electric dipole or quadrupole in the radial plane. Such fields can be realised by segmenting the radial or ring electrode as illustrated in Fig. 3.6, and applying a cosinusoidally varying voltage of the form $V = V_{rot}\cos(\theta - \omega_{rot}t)$. For a rotation of the electric field, a minimum of four or eight segments are needed for the dipole and quadrupole respectively. For the SPECTRAP trap, a rotating dipole was chosen due its simplicity of application both mechanically and electronically. Another disadvantage of a quadrupole field is that in the presence of anharmonicities in the trap potential, single ion or centre of mass motional frequencies can be parametrically coupled, and hence driven in a frequency scan or sweep of the rotating wall up to the Brillouin limit [43].

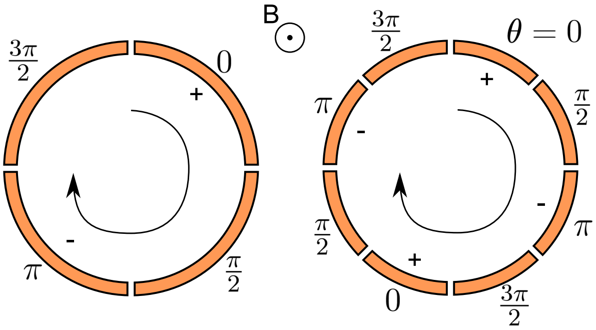

Figure 3.6: An diagram to show how a ring electrode in a Penning trap can be segmented to drive a dipole (left) or quadrupole (right) rotating wall. The direction of rotation has been chosen for compression of positive ions in an axial magnetic field out of the paper.

3.3.2 Plasma Modes

The previous section on the thermal equilibrium of a large number of ions at low temperature and high density neglected any effects due to the correlated motion of ions. At low temperatures and high densities, these correlations become important and the cloud behaves like a plasma, but as long as the inter-ion spacing is small compared to the plasma dimensions, the number density can still be considered a constant. Another way to quantify this condition is via the Debye length, λ_D, and the Coulomb coupling parameter, Γ_{Coul}

$$\lambda_D = \sqrt{\frac{\varepsilon_0 k_B T}{n_0 q^2}} \tag{3.3.21}$$

$$\Gamma_{Coul} = \frac{q^2}{4\pi\varepsilon_0 a_{ws} k_B T}. \tag{3.3.22}$$

where a_{ws} is the Wigner-Seitz radius defined by $4\pi a_{ws}^3/3 \equiv n_0^{-1}$. The Debye length can be thought of as an effective penetration depth into the plasma, inside which ions are screened from external electric fields. In this case if $\lambda_D \ll$ plasma dimensions, the ion number density can be considered constant in the interior of the cloud, then dropping to zero over a length of λ_D at the plasma boundary. The Coulomb coupling parameter is simply the ratio of energy of two neighbouring ions to the average thermal energy. For $\Gamma_{Coul} \ll 1$ the ion-ion correlations are small and the plasma is said to be weakly correlated, and for $\Gamma_{Coul} \geq 1$ the opposite is true and plasma is strongly correlated. In the latter case, the ions effectively lose their individuality and the plasma can have fluid and solid like characteristics.

For a strongly correlated plasma, a multitude of electrostatic modes of oscillation exist. These modes can be described in spherical coordinates by two integers, l and m, with $l \geq 1$ and $m \geq 1$ [44]. The index m denotes an azimuthal dependance of the form $e^{im\phi}$, and l denotes a dependence along a spherical surface in the axial direction of the plasma mode potential [44]. The lowest order (1,0) and (1,1) modes are the centre of mass modes at ω_z, ω_m and $\omega_c^{'}$ respectively. The next highest are the (2,0) and (2,1) modes. Of these, the (2,1) are of most interest as they can be driven by an azimuthally asymmetric potential, such as static electric trapping field errors[2]. In this case, if

---

[2] In the frame of reference rotating with the rigid rotation frequency of the ion cloud, a static field error in the laboratory frame, is seen to rotate in the ion's frame of reference at

the plasma rotation (or rotating wall) frequency matches one of these plasma mode frequencies, energy from the field can be coupled into the plasma causing heating. This requires a misalignment between the magnetic field and the electric trap potential, where the magnetic field can then provide the coupling to transfer energy from the static field errors into the plasma [45].

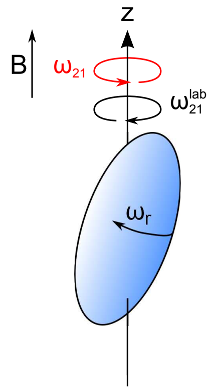

Figure 3.7: An illustration to show how the (2,1) plasma modes cause a tilt and precession of a spheroidal plasma about the z-axis of a radially symmetric Penning trap [44]. In the frame of reference rotating with the ion cloud, the positive sense of rotation of the plasma mode ω_{21}, is taken to be in the opposite sense of rotation to that in the laboratory frame ω_{21}^{lab}.

The (2,1) modes can be interpreted as a precession of a tilted spheroidal plasma about the axial direction, as shown in Fig. (3.7). There are three modes with the dependence prescribed by (2,1) and their frequencies in the frame rotating with the plasma, ω_{21}, must simultaneously satisfy [44]

$$-\omega_{21}^2 - \Omega_v \omega_{21} - \frac{\omega_p^2}{2} f(\alpha)(\alpha^2 + \eta) = 0 \tag{3.3.23}$$

$$-\omega_{21}^2 - \frac{\omega_p^2}{2} f(\alpha)\left(\frac{\alpha^2}{\eta} + 1\right) = 0 \tag{3.3.24}$$

where $\Omega_v = (\omega_c - 2\omega_r)$ and $f(\alpha) = [1 - b(\alpha)]/(1 - \alpha^2)$. These equations arise from solving the equations of motion for ions displaced from their equilibrium position inside the plasma with the addition of an azimuthally asymmetric quadrupole potential. As these mode frequencies are dependent on the aspect ratio, they are functions of B, V and ω_r for a single q/m component plasma. When equations (3.3.23) and (3.3.24) are simultaneously solved for η, a cubic

---

$-\omega_r$.

equation is obtained

$$\Omega_v^2\eta + \frac{\omega_p^2}{2} f(\alpha)(\alpha^2+\eta)(\eta-1)^2 = 0 \tag{3.3.25}$$

which can be numerically solved and the solutions substituted back into equations (3.3.23) and (3.3.24) to yield the mode frequencies. Fig. 3.8 shows a plot of these mode frequencies as a function of ω_r for $\omega_z/\omega_c = 0.15$ and $\omega_z/\omega_c = 0.41$.

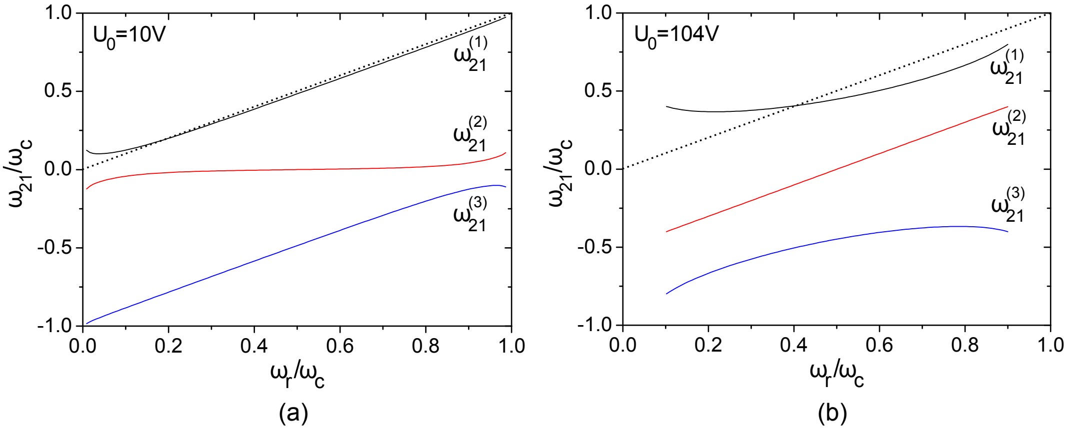

Figure 3.8: A plot of the (2,1) mode frequencies as a function of the plasma rotation frequency in the frame rotating with the plasma for (a) $\omega_z/\omega_c = 0.15$ and (b) $\omega_z/\omega_c = 0.41$. The dashed lines show where $\omega_{21} = \omega_r$. For $^{40}\text{Ca}^+$ ions in SPECTRAP with $B = 1.75$T and $C_2 = 0.54$, (a) and (b) correspond to the plots for trap voltages 10V and 104V respectively.

With a strongly driven rotating wall, in equilibrium, a plasma should reach a low-slip regime where the rotation frequency of the plasma and the rotating wall are approximately equal [46]. To evolve the plasma to the Brillouin limit, the rotating wall frequency can be swept from $\sim \omega_m$ to $\omega_c/2$. If at any point in the frequency scan $\omega_{21} = \omega_r$, then a static electric field error in the laboratory frame, will appear with the correct periodicity in the rotating frame of the plasma to resonantly excite a (2,1) mode and heating can occur. It has been shown that such excitations of the $\omega_{21}^{(1)}$ mode can limit the value of ω_r to less than where $\omega_r = \omega_{21}^{(1)}$ [44]. From Fig. 3.8, it can be seen why this is the case as typically a (2,1) mode resonances exist below the Brillouin limit. For a low trap potential such as that in Fig. 3.8a, after the crossing of $\omega_r = \omega_{21}^{(1)}$,

$\omega_r \approx \omega_{21}^{(1)}$ and hence a static field error is likely to drive the $\omega_{21}^{(1)}$ plasma mode all the way to the Brillouin limit in a rotating wall frequency scan.

This analysis of the plasma mode frequencies can be applied to the SPECTRAP experiment to avoid (possible) heating resonances limiting the density and compression of ion clouds to values below the Brillouin limit. This may be done in three ways; The trap potential may be abruptly switched during a rotating wall frequency scan to avoid a (2,1) mode resonance; The rotating wall frequency may be abruptly switched over a (2,1) mode resonance; The trap potential may be chosen to make a rotating wall frequency scan up to the Brillouin limit free of all (2,1) mode resonances. It has also been shown how the trap potential affects the (2,1) modes and suggested that heating may well continue past the resonance condition (with respect to the rotation frequency of the plasma) for low trap frequencies. Hence in this case, a higher trap potential should yield sharper heating resonances which can be avoided as suggested above. It should be remembered that the trap potential is not a completely free parameter as it controls the aspect ratio of the ion cloud which ideally should remain close to spherical for a high fluorescence collection efficiency. Hence a compromise may be necessary.

Chapter 4

Cooling Methods in Ion Traps

The aim in cooling ions in our trap is to reduce the average kinetic energy and increase the number density of ions. This cannot be accomplished by just adiabatically reducing the trap potential. The definition of the temperature refers to the width of the velocity distribution for a cloud of ions, or in the case of a few ions, the average vibrational quantum number. For single ions and small ensembles of ions, the quantum regime of the vibrational motion has been accessed for a range of Paul traps [47][48]. This is not the case for larger clouds of ions in Paul traps where RF heating becomes a limiting process, or for Penning traps where the cooling scheme becomes very complicated due to the proliferation of Zeeman sub-levels. As this thesis only deals with clouds of ions, the motion and cooling of ions in a trap is treated purely classically i.e. the motional vibrational quanta are unresolved by the cooling methods.

Even without cooling, the trap depth can be several eV, which translates to over 10000K. This is much greater than the temperature of ions created from an atomic oven. Hence this seems to suggest that ions would be trapped indefinitely. However, collisions with residual gas particles and anharmonicities in the trap potential reduce the lifetime of ions in a trap. Hence the immediate benefit from some level of cooling, even just to balance the ion loss mechanisms, is to trap ions for an extended period of time in a controlled environment.

Cooling ions in a trap provides long storage times, reduced Doppler broadening and increased localisation, hence this is advantageous for experiments in high resolution spectroscopy and metrology where the precision of the measurements is increased. Laser cooling is arguably the most efficient way to cool ions in a trap, but as it requires a suitable energy level structure, it is not applicable in the general sense to all types of ions in traps e.g. HCI in the SPECTRAP experiment at GSI. Therefore in this section, an overview of the most common cooling methods for ion clouds is discussed.

To set the scene, first some fundamentals about cooling ions in Paul and Penning traps are considered. In the Paul trap, the micromotion of the ions cannot be cooled directly as it is a motion driven by the applied RF trapping fields and is dependent only on the amplitude of these fields at the position of the ion. That is, the trapping field and amplitude of this motion go to zero at the centre of the trap. However, cooling the secular motion confines ions closer to the centre of the trap where the micromotion is minimised. Hence in this way, the overall motion is cooled. In a Penning trap, cooling is more complicated as energy must be removed from the axial and cyclotron motions but put into the magnetron motion to cool ions and localise them to the centre of the trap. If energy is removed from the unstable magnetron motion, ions will evolve into larger orbits, eventually hitting the trap walls. This complication or hindrance to direct cooling of ions in the Penning trap can be overcome by coupling the magnetron motion to the (modified) cyclotron motion by the application of a radial oscillating quadrupole field (via a split ring electrode) at the sum frequencies of the motions i.e. $\omega_m + \omega_c^{'} = \omega_c$. This technique is known as Axialisation and extends the efficient cooling of the cyclotron motion to the magnetron motion [49].

4.1 Buffer Gas Cooling

When ions are created in a trap, they have energies that are much higher than room temperature thermal energies. Thus, any scheme to bring these ions into thermal equilibrium with the laboratory environment would constitute considerable cooling. When an inert gas is introduced inside a vacuum system containing trapped ions, elastic collisions between the ions and the gas molecules eventually bring the system to thermal equilibrium with a final temperature close to that of the walls of the vacuum system. The buffer gas particles must be lighter than the trapped ions for efficient cooling and the pressure of the gas must not be too high such that the mean free time between collisions remains much longer than the oscillation periods in the trap for trapping stability [37] [50]. Hence helium is a good choice for cooling at pressures in the range $10^{-6} - 10^{-5}$mbar [51].

One advantage of buffer gas cooling over laser and resistive cooling is that it works with ions with a wide range of energies and oscillation frequencies. It is in principle also very simple to employ as it requires just a leak valve attached to a pressurised gas cylinder. In the Penning trap the magnetron motion would have to be coupled using Axialisation.

There are however a number of drawbacks. First the collisions with the trapped ions results in broadening of the motional frequencies and atomic transitions and this reduces the precision to which these values can be measured. Second, the lowest temperature to which the ions can be cooled, is limited by that to which the whole system can be taken down to i.e. $>$3K below which all gasses condense. Cryogenic operation of a trap to reach very low temperatures entails a great overhead in effort and expense. And third, charge exchange can occur with the trapped ions and this poses a severe limitation to the use of buffer gas cooling for HCI down to low energies.

4.2 Resistive Cooling

Ions in a trap induce image charges on the electrodes. If the electrodes are connected together via a resistive load, the movement of the ions in the trap causes an image current to flow through the circuit. Hence the energy of the ions is dissipated into ohmic heating of the resistor into the environment (usually at cryogenic temperatures). This is the basic principle of electronic detection and resistive cooling [52].

Consider an ion in a trap with a resistor connected between the endcap electrodes (as shown in Fig. 4.1). The axial oscillation of the ion causes a current I to flow through the resistor R. Hence there will be an associated voltage drop across the resistor of IR. This voltage creates an electric field in the trap E, which creates a force on the ion F, in the opposite direction to the motion. Hence this damping force can be written as

$$F(t) = -qE(t) = -q\frac{I(t)R}{2z_0} \tag{4.2.1}$$

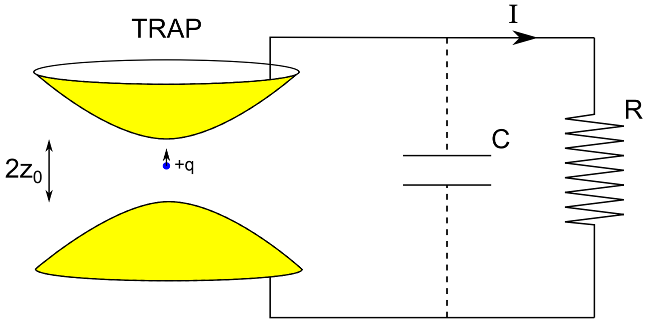

Figure 4.1: A circuit diagram showing how the electrodes of an ion trap can be connected together for resistive cooling. The trap is equivalently modelled as the virtual capacitor in this diagram.

where the endcap electrodes are modelled as two infinitely long parallel plates a distance $2z_0$ apart. Therefore the power or the rate of energy dissipation in the resistor is given by

$$\frac{dE_{KE}}{dt}(t) = v_z(t)F(t) = -I(t)^2 R \tag{4.2.2}$$

where $\frac{dE_{KE}}{dt}(t)$ is the rate of loss of the ion's kinetic energy and $v_z(t)$ the velocity of the ion at time t. This can be solved for I to give

$$I(t) = \frac{qv_z(t)}{2z_0} \tag{4.2.3}$$

which gives the instantaneous current flowing through the resistor at time t where the velocity of the ion is $v_z(t)$. To get the average rate of energy loss, a time average over equation (4.2.2) must be taken

$$\frac{dE_{KE}}{dt} = - < I^2 R > = -\frac{q^2 R}{4z_0^2} < v_z(t)^2 > \tag{4.2.4}$$

which, by factoring in a mass dependence m, gives

$$\frac{dE_{KE}}{dt} = -\frac{q^2 R}{4z_0^2 m} m < v_z(t)^2 > . \tag{4.2.5}$$

If the ion's axial oscillation frequency is ω_z, then the velocity of the ion at time t, with respect to the velocity at $z = 0$, $v_{z,0}$, is given by

$$v_z(t) = v_{z,0} \cos \omega_z t. \tag{4.2.6}$$

Hence using the identity

$$< mv_z^2 >= m < v_z^2 >= mv_{z,0} < \cos^2 \omega_z t >= \frac{1}{2} mv_{z,0}^2 = E_{KE} \qquad (4.2.7)$$

where E_{KE} is the average kinetic energy at time t, equation (4.2.5) may be written as

$$\frac{dE_{KE}}{dt} = -\frac{q^2 R}{4z_0^2 m} E_{KE} \qquad (4.2.8)$$

which can be integrated from time t_0 to t to give the fraction of kinetic energy remaining after a time $(t - t_0)$ by

$$\frac{E_{KE}(t)}{E_{KE}(t_0)} = e^{-\frac{q^2 R}{4z_0^2 m}(t-t_0)} = E_{KE}(t_0) e^{-\frac{(t-t_0)}{t_{res}}}. \qquad (4.2.9)$$

The final energy or temperature of the ion is determined by the electronic noise present in the cooling circuit i.e. thermal or other fluctuations in the current. The parameter t_{res} may be identified as a characteristic cooling time constant over which the kinetic energy of an ion is reduced by a factor of e^{-1}

$$t_{res} = \frac{4z_0^2 m}{q^2 R}. \qquad (4.2.10)$$

This shows that the rate of resistive cooling, or $1/t_{res}$, will be higher the smaller the trap size (z_0^{-2}), the higher the ion charge to mass ratio (q^2/m), and the higher the resistive load (R). Hence this method is particularly effective for HCI.

For a large resistance of 10MΩ, and a typical trap capacitance of around 10pF, essentially no current would flow through the resistor for frequencies much greater than $1/RC$ or $\approx$ 2kHz. As trap frequencies are typically in the 100KHz to 10MHz range, it is clear that the capacitance of the trap needs to be 'tuned out'. This can be done by using an inductor in place of the resistor, to form an LCR circuit. Hence the practical realisation of the cooling circuit is that shown in Fig. 4.2, where R is now the effective lumped ohmic resistance of the inductor coil (and connecting wires).

This circuit acts as a resonator with a resonance frequency ω_{LC} given by

$$\omega_{LC} = \sqrt{\frac{1}{LC}} \qquad (4.2.11)$$

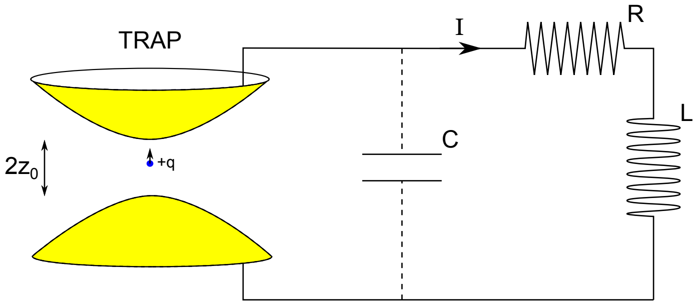

Figure 4.2: A circuit diagram showing how an inductor connected to an ion trap forms an LCR circuit for resistive cooling of ions. The trap can be modelled as a capacitor, and the resistance of the inductor as the series resistor R.

at which point the impedance Z is maximised and is purely resistive and is given by

$$Z = \frac{L}{RC}. \tag{4.2.12}$$

Hence by adding an inductor of high inductance L, and low resistance R, the resistive load can be maximised. However, the frequency of the resonance must match the oscillation frequency of the ions. Therefore this puts a restriction on the value of the inductance. For example for cooling between the endcaps of a trap, this resonance must match the axial frequency of oscillation

$$\omega_{LC} = \omega_z = \sqrt{1/LC} \tag{4.2.13}$$

and therefore the resistance is the only remaining free parameter to maximise the cooling rate (which scales with the resistive load). Hence it is a common choice to make an inductor from a wire of low resistance, and place it in a cryogenic environment.

A disadvantage of this type of (LCR) cooling circuit is that it has a limited frequency response range or bandwidth. This is characterised by the quality factor or Q_{LC} given by

$$Q_{LC} = \frac{1}{R}\sqrt{\frac{L}{C}} = \frac{\omega_{LC}}{\Delta\omega_{LC}} \tag{4.2.14}$$

where $\Delta\omega_{LC}$ is defined as the frequency range over which the power spectrum of the circuit is within -3dB of the maximum about resonance. Hence the disadvantage of maximising the impedance in equation (4.2.12) and the cooling rate, is to limit the bandwidth of the circuit. After ions are initially loaded into a trap, their amplitude of oscillation will be large such that anharomicities will shift and broaden the oscillation frequencies. This shift in frequency can be corrected for by adjusting the trap potential to keep the ions resonant with the cooling circuit. However if the width of the ion oscillation frequency is larger than the bandwidth of the circuit, the initial cooling rate will be lower. Furthermore, once the ions are cold, space charge potentials also have a broadening effect on the motional frequencies and therefore for efficient cooling for a cloud of ions, a compromise is necessary between the Q_{LC} and the effective resistive load at resonance Z or cooling rate. Hence typically Q values of around 500 are used in experiments involving clouds of ions, where extra capacitance may be added to the circuit to broaden the resonance.

So far, the electrodes of the trap have been modelled as infinitely long parallel plates. In practice of course, this is only an approximation so the cooling time constant will be increased by some factor β^{-2}, where $\beta < 1$, to account for the electrode geometry. Hence the true time constant for a single ion with an LCR resistive cooling circuit will be given by

$$t_{res} = \frac{4z_0^2 mR}{\beta^2 q^2}\sqrt{\frac{C}{L}}. \tag{4.2.15}$$

In an ideal trap, for a cloud of ions only the centre of mass (CM) motion is cooled. As the cooling time constant scales with m/q^2, for N ions, the cooling rate is N times faster compared to that for a single ion. Non-CM motions can be cooled if the resistive cooling circuit is connected asymmetrically across the trap (i.e. from the ring to one endcap only), but any motion that is not resonant with the tuned circuit will see a much reduced cooling rate. In a real trap, trapping field imperfections and contaminant ions will lead to slower exponential and non-exponential energy dissipation in the circuit.

The main advantages of resistive cooling are: It is applicable to any ion species as the dissipation of energy requires only a charged particle with a certain frequency of oscillation; It is non destructive to the trap contents as no collisions or charge exchange can occur with buffer gas molecules or sympathetically cooled ions; The voltage fluctuations across the resistive load can be amplified, and via spectral analysis around the resonance frequency, a detection signal for the ions can be obtained. The main disadvantage of this cooling method is the required complexity to reach ultra-cold temperatures where both the trap and cooling circuit have to be put into a cryogenic environment where the electronic noise on the circuit needs to be kept to a minimum to prevent substantial heating of the ions above the ambient temperature. Also, the cooling time to reach an equilibrium with the (effective) temperature of the circuit may be much longer than expected if the frequency of the ions' oscillation is not optimally set to that of the circuit. In the Paul trap, resonant cooling of the secular motion is possible, but RF pick-up on the circuit makes cooling to low temperatures difficult. In the Penning trap, the axial and cyclotron (via a split ring electrode) motions can be directly resistively cooled, but the magnetron motion requires the aforementioned coupling technique.

4.3 Laser Cooling

Fundamentally laser cooling relies on the use of resonant radiation pressure to cool ions (or atoms). It requires the linewidth of the resonant radiation source to be narrower than the Doppler broadening of an internal ionic (or atomic) transition. For transitions in the optical spectrum with temperatures around 100K, the broadening of the natural line profiles are in the GHz region. Hence for high power in a narrower linewidth, ideally as narrow as the natural linewidth of the transition (typically MHz), lasers are the preferred sources of radiation especially to cool down to cryogenic temperatures.

Consider an ion confined in a trap. If the linewidth of the cooling transition is much greater than the ions oscillation frequency, $\omega_{z,m,c'} \ll \Gamma$, the scattering of a photon takes places in a time frame much shorter than the motional period of oscillation. Hence to a good approximation, the velocity of the ion can be treated as a constant during the absorption and re-emission processes. Therefore the Doppler effect can be treated like that for a free particle (i.e. classically), and this is known as the weak-binding or Doppler regime. This criterion is typically fulfilled by fast electric-dipole transitions which have linewidths orders of magnitude greater than the trap frequencies. In this regime, the lowest temperature that can be reached is the so-called Doppler limit (see section 4.3.1).

Conversely, if $\omega_{z,m,c'} \gg \Gamma$, the frequency of the radiation as seen by the ion appears strongly modulated at the trap frequency, and this is known as the strong-binding regime. Thus the ions absorption spectrum consists of well resolved sidebands. This allows schemes in which phonons of vibrational energy (e.g. $\hbar\omega_z$) are removed and the ion can be cooled to the motional ground-state of the ion-trap system. This usually requires long lived transitions (e.g. electric-quadrupole) which have much narrower linewidths to fulfil the above criteria.

For the experiments discussed in this thesis, cooling down to the motional ground-state was not required. Hence the focus now lies on laser cooling in the Doppler regime.

4.3.1 Doppler Cooling

In the Doppler cooling regime, consider an ion with velocity v travelling towards a laser beam with wave vector k_l and frequency ω_l. The frequency of the light as seen by the ion ω_{ion} will be first order Doppler shifted, assuming non-relativistic velocities, by

$$\omega_{ion} = \omega_l - k_l v. \tag{4.3.1}$$

If ω_{ion} is made resonant with an internal transition, the ion will scatter photons. In the case where the laser frequency is (red) detuned below resonance, and even accounting for the spectral width of the transition and source, photons will have a greater probability to be scattered for ions moving towards the laser beam then away from it.

The absorption of a photon ($k_l \approx k_{ion} = k$) transfers a momentum of $\hbar k$ to the ion in the direction of the laser beam. Assuming the energy level structure of the ion can be modelled as a two level system, the ion can relax back to the ground state via spontaneous or stimulated emission. If stimulated emission occurs, the photon is re-emitted back in the same direction as the incident photon and therefore the net momentum transfer is zero. However if spontaneous emission occurs where a photon is emitted in a random direction, the average net momentum transferred over many absorption-re-emission cycles is $\hbar k$, in the direction of the laser beam propagation. Therefore on average a photon transfers a momentum of $\hbar k$ to the ion which causes it to change its velocity by the recoil velocity $v_r = \frac{\hbar k}{m_{ion}}$.

Consider $^{40}\mathrm{Ca}^+$ as an example, the typical thermal velocity in one degree of freedom is $v_t = \sqrt{2k_BT/m_{ion}} = 350\mathrm{m/s}$, and the recoil velocity from absorbing one photon on the Doppler cooling transition (see section 5.1) is 0.03m/s. Therefore it would take approximately 11000 photons to bring such an ion (ideally) to rest. To estimate how long this would take, i.e. the cooling rate, the number of photons that can be scattered on the transition needs to be worked out. It can be shown that this scattering rate (γ) is a function of the spontaneous decay rate (Γ) and the steady state population of the excited state under laser irradiation, which for a two level ion is given by [53]

$$\gamma = \frac{\Gamma}{2} \frac{I/I_{sat}}{(\frac{2(\Delta\omega - kv)}{\Gamma})^2 + I/I_{sat} + 1} \tag{4.3.2}$$

where the first term in the denominator accounts for the detuning from resonance ($\Delta\omega$), and the second for power broadening of the transition due to the intensity of the laser light I, where I_{sat} is defined as the saturation intensity at which the average population of the excited state is half that of the ground state and is given by the relation [53]

$$I_{sat} = \frac{\hbar\Gamma\omega_{ion}^3}{12\pi c^2}. \tag{4.3.3}$$

For the Doppler cooling transition in $^{40}\mathrm{Ca}^+$, $I_{sat} = 466\mu\mathrm{Wmm}^{-2}$. On resonance and assuming saturation ($I = I_{sat}$), the scattering rate tends to $\Gamma/4$ or $3.5 \times 10^7\mathrm{s}^{-1}$. Assuming the laser is red detuned such that the scattering rate is further reduced by a factor of 2, this implies the thermal velocity is removed in a time $v_t/(v_r \times \Gamma/8) \approx 1\mathrm{ms}$. In reality, the initial Doppler width will reduce the scattering rate considerably, but once the ion is cold, this order of magnitude estimate gives the effective Doppler cooling rate. This cooling rate is the fastest out of all the methods discussed.

At the limit of cooling, the ion's velocity is dominated by the cumulative effect of the momentum kicks of the ion absorbing and re-emitting photons. At this stage, isolating the spontaneous emission process, the ion can be seen as executing a random walk in momentum space in units of $\hbar k$. Hence the lowest temperature of a single ion in a trap is a balance between absorbing red detuned photons that cool the ion, and heating from spontaneous emission. These two processes are balanced out for a laser detuning of $\Gamma/2$ from line centre, and under these circumstances the temperature is minimised to [54]

$$T = \frac{\hbar\Gamma}{2k_B} \tag{4.3.4}$$

which for $^{40}\mathrm{Ca}^+$ is $\sim$ 1mK. This simplistic model assumes that an ion is always resonant with the laser and scattering photons. In reality in an experiment, the laser beam will have a Gaussian intensity profile and an ion may move out of the laser beam for a fraction of the time, especially when it is 'hot' and not well confined. Hence the cooling time, laser intensity and lowest temperature calculated here are just lower bound estimates to this idealised case. If a laser beam is directed along the axial direction, then the axial degree of freedom is cooled. However if the beam can be directed such that there is a non-zero component of the wave-vector in the axial and radial plane, all degrees of freedom can be cooled. This is the principle of cooling the secular motions (directly) and micromotions (indirectly) in the Paul trap[1]. In the Penning trap, as energy needs to be put into the magnetron motion, the laser beam has to be radially offset as illustrated in Fig. 4.3. This allows more photons to be absorbed in the direction of the magnetron motion than opposing it, putting torque or energy into the unstable motion [55]. This way all the degrees of motion (CM and internal) can be cooled. The disadvantages of this technique are that the width of the laser beam (or intensity gradient across the cloud) determines the degree to which the magnetron motion can be cooled, and it fundamentally requires careful positioning of the beam with respect to the trap centre. By applying the Axialisation technique described above, these constraints are removed and the cooling efficiency in the Penning trap can be improved by just using a laser beam directed at the centre of the trap [49].

For a large cloud of ions over 1000 ions for example, there may only be at best partial overlap of the cloud with the laser beam. In addition, ions in a cloud will be more prone to heating effects from the micromotion in the Paul trap, or to static field errors in the Penning trap driving internal plasma modes. In the Penning trap, there is also typically poor magnetron motion cooling using the scheme set out in Fig. 4.3. Hence a large cloud is likely not

---

[1] Cooling reduces the secular motion so that the ion resides near to the centre of the trap where the micromotion is smaller.

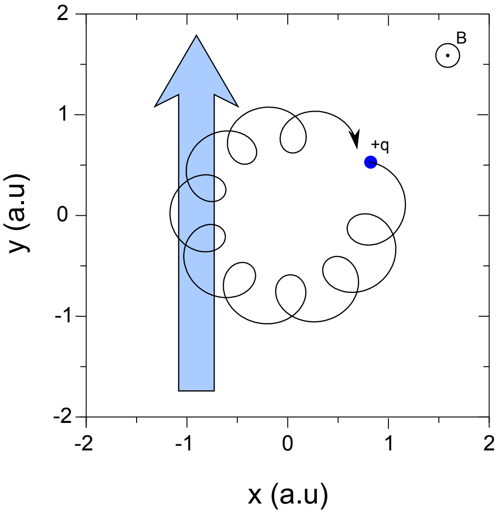

Figure 4.3: An illustration of how a radially off-centre laser beam (blue arrow) can be used to cool both of an ion's radial degrees of freedom in a Penning trap.

to cool to the Doppler limit, and may maintain a Doppler broadening many times the natural and laser linewidths. For these reasons, only a faction of the ions in equilibrium at optimised laser detuning, are likely to scatter photons and be directly cooled. Therefore, for larger clouds of ions, longer cooling times, higher temperatures and lower fluorescence rates per ion are expected. The cooling time to reach equilibrium may be reduced by scanning the laser frequency repetitively from a large to small red-detuning to interact with a greater fraction of ions.

Doppler cooling has a number of advantages. First, the lowest temperatures are possible without the need to cool the entire vacuum system. Second, the cooling is not dependent on the frequency or harmonicity of the ion's motion in the trap as it is for resistive cooling. Third, the photons that are scattered (i.e. the fluorescence) can be collected and provide a non-destructive means for detection of ions. And last, the cooling rate can be fast - of the order milliseconds.

The main disadvantage of Doppler cooling is the requirement for a closed cycle fast optical transition for efficient cooling. Also as optical access is required to the ions, this may require additional holes in trap electrodes compromising the harmonicity for frequency (metrology) measurements in the trap.

4.4 Sympathetic Cooling

The cooling of one ion species by another through thermalisation is called sympathetic cooling. Ions can be cooled via this method even when they have no other means of direct cooling. In this way, many of the benefits of laser cooling can be transferred to the sympathetically cooled ions.

In a Penning trap, only multiple ion species of the same sign of charge can be simultaneously trapped over the same volume[2]. In equilibrium, as has already been discussed, at low temperatures ions undergo a global rigid rotation about the centre of the trap. Therefore by cooling one species accounting for the need to put energy into the magnetron motion, this requirement is assured for the sympathetically cooled ions. As the rotation frequency of the ions will be the same, there is a difference in the centrifugal force between two ion species of a different mass, and assuming these ions have the same charge, there is a radial separation of the ion species [56]. For ions of the same mass but different charge, the trap potential is more binding for the higher q/m species which will then be found at the centre of the trap, and via Coulomb repulsion, will be surrounded by the lower q/m ion species. Hence in general different species of ions will spatially separate at low temperatures in the Penning trap.

Assuming the ions are sympathetically laser cooled, the advantages of this method are simply the advantages of laser cooling except that the internal energy level structure of the sympathetically cooled ions is not disturbed. In addition, this method is applicable to any type of ion that can be simultaneously trapped in either a Paul or Penning trap. For example, HCI have been sympathetically cooled in the Penning trap with laser cooled lower charge state ions [57]. The Coulomb barrier between these species prevents them from coming in close proximity at low energies and so reduces charge exchange. Although Paul traps in principle can trap multiple ion species, a combined (Paul-Penning) trap can provide a better compromise for tight confinement of trapped ions with radically different q/m ratios e.g. for the creation of anti-hydrogen involving trapping positrons and anti-protons.

There are some potential disadvantages to this cooling method that may make it unfavourable to use. First, although there is fluorescence signal from the

---

[2] Penning traps with nested electric fields can trap ions of opposite sign.

laser cooled ions, there is no direct signal from the sympathetically cooled ions. Second, the larger volume of the trap occupied by ions implies greater anharmonicities and potentially a more unstable trap. Finally, the trap has to be loaded twice, which for ions not created in situ, implies a greater complexity.

Chapter 5

Experimental Setup

This chapter describes the complete experimental setup of the preliminary SPECTRAP experiments at Imperial College London. The Ion Trapping group at Imperial College has research interests primarily in quantum information processing (QIP) with trapped ions. For the last several years, the group has been working with $^{40}\mathrm{Ca}^+$ which has the required energy level structure for laser cooling and provides a qubit for QIP. As there is only one system of lasers available, the experiments with the SPECTRAP ion trap in London were performed with the same ion species. Hence the laser light for cooling and spectroscopy of calcium was prepared using the pre-existing setup on an optical table, but fed via optical fibres to an isolated (SPECTRAP) platform under a superconducting magnet where the trap was located (see Appendix B).

5.1 $^{40}\mathrm{Ca}^+$ Ions

Calcium 40 has a natural abundance of just over 96% and has first and second ionisation energies of 6.1eV and 11.8eV respectively [58]. $^{40}\mathrm{Ca}^+$ ions were created in SPECTRAP by electron impact ionisation of a weak atomic beam (see section 5.3.3). This method is not isotope selective but the high abundance of calcium 40 ensures the fraction of contaminant ions is small (assuming a good vacuum). The first ionisation cross section peaks at 25eV [59], but in this case to avoid creating doubly ionised calcium, the electron energy should be kept below 11.8eV particularly in the region near the centre of the trap.

An energy level diagram of $^{40}\mathrm{Ca}^+$ is shown in Fig. 5.1. The strongly allowed electric-dipole $4^2S_{1/2} \rightarrow 4^2P_{1/2}$ transition at 397nm is used for Doppler cooling and the subsequent decay is detected as fluorescence. The $4^2P_{1/2}$ state has a natural lifetime of 7.1ns , a scattering rate (Γ) of 1.4×10^8s^{-1} and a natural linewidth of 22MHz [58]. However, there is a 1/13 chance the excited electron will decay into the metastable $3^2D_{3/2}$ state which has a lifetime of 1.1s since the ground state can only be reached via an electric-quadrupole transition. Hence this would essentially switch off laser cooling and fluorescence emission. Therefore repumping is required on the $3^2D_{3/2} \rightarrow 4^2P_{1/2}$ transition at 866nm. Hence in a Paul trap in the absence of a magnetic field, only two lasers are required for cooling and inducing fluorescence; One at 397nm and one at 866nm of an arbitrary polarisation.

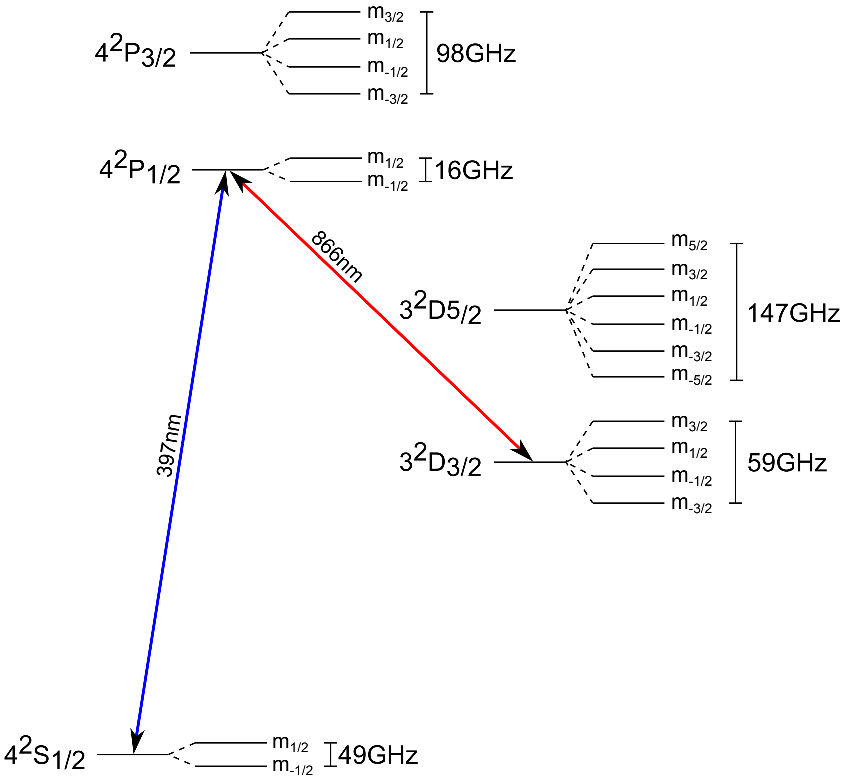

Figure 5.1: The lowest lying energy levels of ^{40}Ca^{+} with transition wavelengths. The Zeeman splitting in a 1.75tesla magnetic field is also shown.

In a Penning trap in the presence of a magnetic field, there is Zeeman splitting of the energy levels according to

$$\Delta E = g_J \mu_B m_j B \tag{5.1.1}$$

where g_J is the Lande$'$ g-factor, μ_B the Bohr magnetron, and m_j the projection of the total angular momentum along the magnetic field direction. This splitting at a trapping magnetic field of 1.75T (see Fig. 5.1) is of the order GHz compared to the transition and laser linewidths of MHz. Therefore each m_j component of the $4^2S_{1/2}$ and $3^2D_{3/2}$ states must be addressed seperately to prevent electrons from being shelved into non-fluorescent or dark states. In the laser system at the time of this experiment, this was accomplished with two 397nm and four 866nm lasers. Fig. 5.2 shows the spectrum of Zeeman transitions corresponding to the splitting in Fig. 5.1 calculated using equation (5.1.1). For the reasons of practical simplicity for beam steering it is preferable to have the same polarisation for all the lasers. And for adjusting wavelengths between Paul and Penning trap operation, laser frequencies closer to those in zero magnetic field are favourable. Therefore the 397nm lasers were set to the π ($\Delta m_j = 0$) transitions, and the 866nm lasers were set to the σ ($\Delta m_j = \pm 1$) transitions.

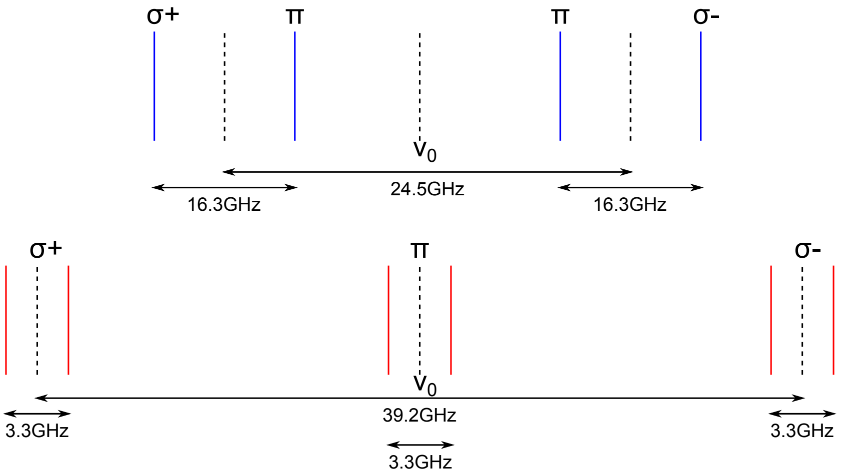

Figure 5.2: Spectrum of Zeeman transitions in ^{40}Ca^{+} between the (upper frame) $4^2S_{1/2} - 4^2P_{1/2}$ and (lower frame) $3^2D_{3/2} - 4^2P_{1/2}$ states in a 1.75T magnetic field about the line centres ν_0.

5.2 Laser System

In this section of the thesis, only a brief description of the laser system is given as it has already been well documented by previous group members who designed and built the system [60][61][62]. Some fundamental operating principles are included which are required to be understood for daily setup of the system from a user's perspective.

5.2.1 Diode Lasers

A schematic diagram of the laser system is shown in Fig. 5.3. The 397nm and 866nm lasers are all tunable external cavity laser diodes in a Littrow configuration. This consists of a laser diode followed by a collimating lens after which the light is incident on a diffraction grating that provides the frequency selective feedback (as shown in Fig. 5.4). The angle of the grating is such that the first order of diffraction is sent back to the diode and the zeroth order to the experiment. This provides strong frequency selective feedback for wavelength tunability and stability, and high power laser output respectively. The external cavity gives a smaller emission linewidth compared to that for the single mode of a free running laser. The degree of linewidth narrowing is roughly given by the ratio of lengths of the diode-cavity over the diode-grating extended cavity. The emission wavelength can be coarsely adjusted by the angle of the grating over the broad gain profiles of the laser diodes typically of the order of 10nm. Adjusting the temperature and length of the cavity provides the finer level of wavelength tunability required to set the lasers to the ionic transition. The gain or mode profile of such a laser is shown in Fig. 5.5. The extended cavity mode that lases must be at a frequency inside the grating feedback profile and inside a mode of the diode cavity to see gain.

The two 397nm lasers are TuiOptics (now Toptica) DL100 commerical devices with a typical power output of 5mW and linewidths around 10MHz [63]. The four 866nm lasers are home built devices with laser diodes sourced from a range of manufacturers, but all have power outputs in excess of 5mW and linewidths of around 1MHz [63]. Each laser head is mounted on top of a thermoelectric cooler or TEC (Peltier) to control the temperature of the diode-grating cavity. Each grating is suspended horizontally by a piezoelectric transducer to control the cavity length.

Each laser requires a current driver for the laser diode, a TEC controller and a piezo controller. The temperature of each laser is monitored via a thermistor and the signal is feed into the TEC controller via locking electronics to stabilise the temperature about a defined set point. The current to the laser diodes not only provides control of the laser power output, but also the temperature and hence wavelength of emission through ohmic heating of the diode. By increasing the temperature of the diode (current) or cavity (Peltier), the effective optical length of the diode and diode-grating cavities is increased and hence the comb of cavity modes shifts to longer wavelengths or lower frequencies. This gives the ability to maximise the mode-hop-free scan range of the laser around the resonance. This then gives the largest range over which the ionic transition can be searched for using fine control of the piezoelectric transducer, or to perform a fast repetitive frequency scan of the laser. The cavity temperature also affects the grating feedback which must also shift to longer wavelengths to maintain the order of diffraction. Therefore in this way, the whole gain profile of the diode-grating can be manually moved allowing the wavelength to be tuned over a much larger range than would otherwise be possible without adjusting the grating angle.

The laser diodes are orientated such that their major axis of polarisation is along the vertical direction and perpendicular to the blaze on the grating. The grating has a higher diffraction efficiency for this (sagittal) polarisation and hence the laser output is well linearly polarised along the vertical direction. The horizontal divergence from the output of the laser diodes is much greater than that of the vertical due to the cross-sectional profile of the active region. For this reason, after the collimating lens, the laser spots have an aspect ratio such that the horizontal length is ~ 3 times larger than the vertical i.e. a horizontal stripe $\sim 3\text{mm}\times 1\text{mm}$. Such a beam does not couple well in into an optical fibre and so for this reason, beam shaping is employed. For the 397nm lasers a pair of cylindrical lenses are used, and for the 866nm lasers, an anamorphic prism pair. This gives the beams a nearly square profile which leads to a fibre coupling efficiency of up to 70% c.f. $< 40\%$ without reshaping.

5.2.2 Wavemeter

Before ions are loaded into the trap, the lasers must first be tuned to the ionic transitions. This requires determination of the laser wavelengths to within a Doppler broadened linewidth or typically a few parts in 10^7. In the present system, this is achieved using a travelling Michelson interferometer. The interferometer simultaneously measures the interference fringes of two co-propagating overlapping laser beams. The relative length of the interferometer arms is then varied, whilst the interference fringes are counted. The ratio of the number of fringes between the two beams then gives the corresponding ratio of wavelengths. Hence if one wavelength is known, the other can be derived from the measurement.

The reference laser for the wavemeter is a frequency stabilised Helium Neon laser (HeNe) stable to $\sim$ 1MHz [63]. The mirrors of the interferometer are actually retro-reflectors (cube corners) on opposite sides of a cart which travels on a cushion of air (for mirror stability) and shuttle repetitively at a constant speed between two actuators along a straight rail. The benefit of coupling the two arms of the interferometer is that the relative distance of travel between the arms is doubled, hence more fringes can be counted and the wavelength determined to a greater precision. The fringes are detected on photodiodes and counted on specially designed electronics provided by R. Blatt's group (Innsbruck). The counting process starts and stops on coincidences between the fringe patterns from the two lasers, hence counting an integer number of fringes. This is done once for each traverse of the cart along the track and a conversion to wavelength is displayed in real time on an LCD screen. With this wavemeter, repeatable measurements are obtained with a precision of 0.0003nm (0.5GHz@397nm). The accuracy (absolute value uncertainty) is highly dependent on the alignment of the laser beams through the interferometer. Therefore usually, the wavelength can be set to within at most 0.0005nm (1GHz@397nm) of the transition. This is verified by monitoring the fluorescence level from ions.

5.2.3 Scanning Cavity

A scanning cavity Fabry-Perot interferometer (SFPI) is used to view the mode structure of the 866nm lasers. The SFPI uses the optical transmission characteristics of a Fabry-Perot cavity as a frequency selective filter to scan across an optical spectrum of a laser (or multiple lasers). The transmission is maximised when the cavity length is an integer number of half wavelengths of the laser.

The SFPI is a TecOptic SA7.5 confocal cavity with a free spectral range (FSR) of 7.5GHz. One of the mirrors of the cavity is scanned via a piezoelectric transducer in a saw tooth fashion, and the transmission is monitored on a photodiode in real time. A small fraction of each 866nm laser beam is picked off via an optical flat after they are combined (on beam splitters) and sent into the SFPI. In this way all the lasers can be monitored together during trapping for correction of laser drift (as all four lasers are unlikely to drift together in the same direction by the same amount) and potential multimode behaviour without being sent to the wavemeter and stopping laser cooling altogether. Each laser can of course be independently reviewed by blocking the other beams as well. And even though multiple lasers may be larger than a SFPI FSR apart in frequency, a peak from a different order will appear in the same FSR scan. The actual SFPI cavity scan amplitude (and DC offset) is chosen to encompass all four lasers and may be less than the maximum supported SFPI FSR to avoid multiple peaks from the same laser.

5.2.4 Tuning to the Atomic Transitions

To set up the lasers for Doppler cooling of $^{40}\mathrm{Ca}^{+}$, the wavelengths for all the lasers initially need to be within a Doppler broadened linewidth of their respective target transitions (see Fig. 5.2). After switching the lasers on, and allowing several hours for the temperature to stabilise, each laser beam in turn is sent to the wavemeter by use of the flipping mirrors (see Fig. 5.3). The piezo voltage that controls the length of the cavity is then adjusted to set the correct wavelength. If there is a mode-hop to another frequency at the voltage required for the wavelength, or within a red-detuned scan range of 1GHz for the 397nm lasers, the current of the diode is adjusted to shift the diode modes and make the range mode hop free. Multimode operation of the lasers can be observed on the wavemeter as a beating of the fringe pattern as observed on an oscilloscope. If the wavelength cannot be pulled far enough to reach the required value, the temperature of the cavity or the grating angle may be adjusted. As the 397nm laser diodes are not readily available, these lasers are turned off at the end of each day for longevity. The 866nm lasers however are readily available and so these are usually left on over night. Several months usually elapse without requiring a grating angle adjustment or major TEC temperature adjustment.

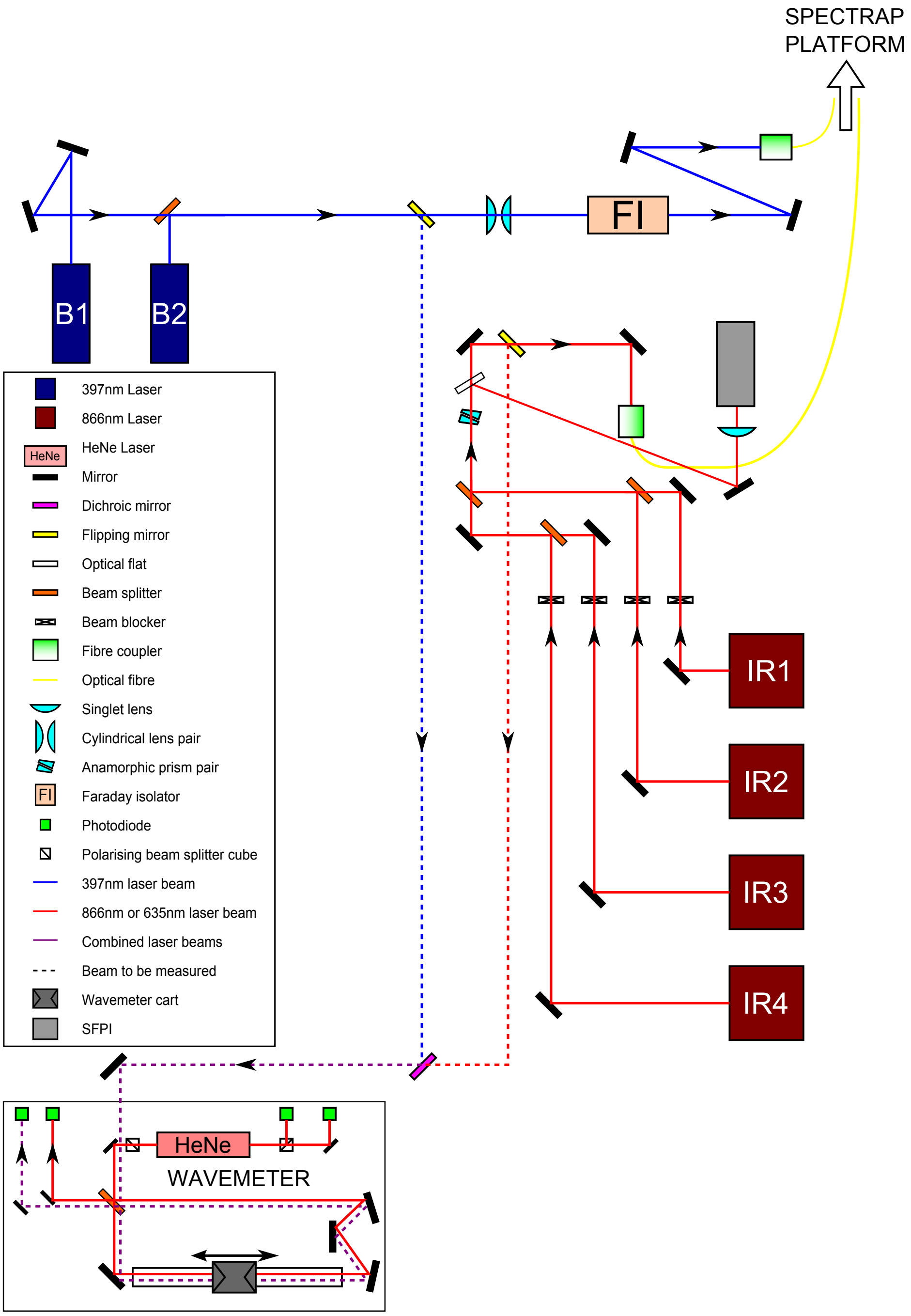

Figure 5.3: A schematic of the laser system for Doppler cooling and spectroscopy of ^{40}Ca$^+$ ions. The laser beams are combined on beam splitters and therefore this results in large losses of laser power. Typically about 100μW from each 397nm laser, and 200μW from each 866nm laser is coupled into the optical fibres for spatial overlap and transportation of the light to the ion traps in the group.

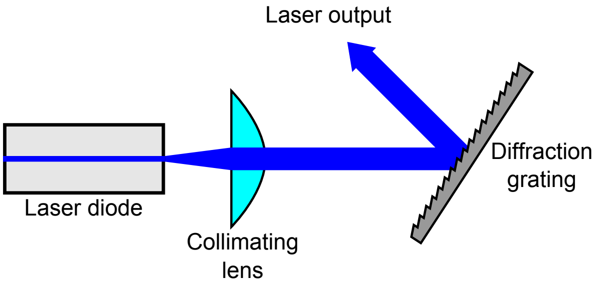

Figure 5.4: A schematic diagram of a laser diode in a Littrow configuration creating a tunable extended cavity laser diode.

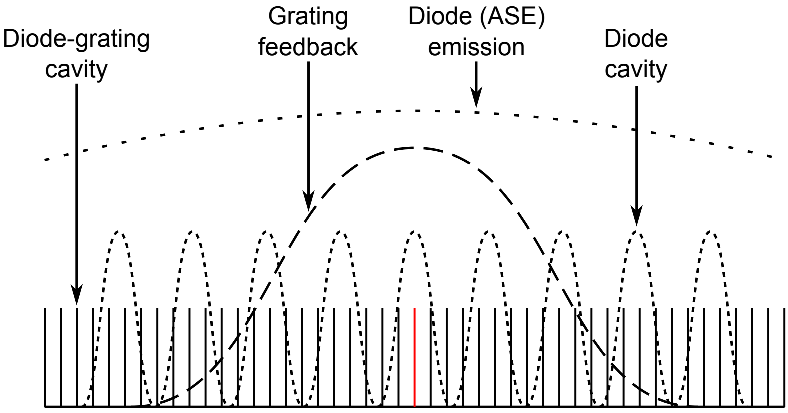

Figure 5.5: An spectrum of the constituent modes of a laser in the Littrow configuration. The mode which is most likely to lase is highlighted in red.

5.3 London SPECTRAP

The SPECTRAP ion trap is a cylindrical electrode open endcap Penning trap. The internal structure of the trap was designed for the spectroscopy measurements at GSI, but the outer dimensions of the trap were constrained so that an identical trap could be installed in the superconducting magnet at Imperial College. For practicality, two identical traps were made, where one was installed in the London setup and the other in Germany. This has allowed both experiments to be worked on independently. Although there have been minor modifications to both traps, they are still essentially identical to each other. The traps and associated vacuum vessel were designed by Dr. Manuel Vogel and manufactured before I joined the group. In this chapter, the London variant of the trap is described in detail.

5.3.1 Electrode Design

The trap is manufactured from oxygen free high conductivity copper which is non-magnetic and of high purity to minimise the in-vacuum outgassing. The basic electrode structure can be seen in Fig. 5.6. The main trapping region is composed of a segmented ring electrode and a pair of endcaps. As the electrodes do not follow contours of hyperbole, the potential is not purely quadratic and anharmonicities are present. However, with the addition of the compensation electrodes inserted between the ring and the endcap electrodes, the potential can be 'tuned' to remove these higher order terms in the potential, and the non-ideal electrode structure can be compensated for. In the GSI experiment, HCI must be loaded into the trap from an external source, whereas in the London experiment the ions are created 'in situ' in the trap. Extra electrodes are required to capture externally generated ions and these are known as the capture electrodes. These capture electrodes shown in Fig. 5.6 played no role in the London experiment and were connected together with the support flanges to ground.

Cylindrical electrode ion traps have three main advantages over other trap designs. Firstly, the electrodes can be machined to a greater accuracy and in less time than hyperbolic electrodes. Secondly, the potential can be calculated analytically, in turn allowing the motional frequencies and anharmonicities to be calculated without requiring computer simulations. Thirdly, the open access

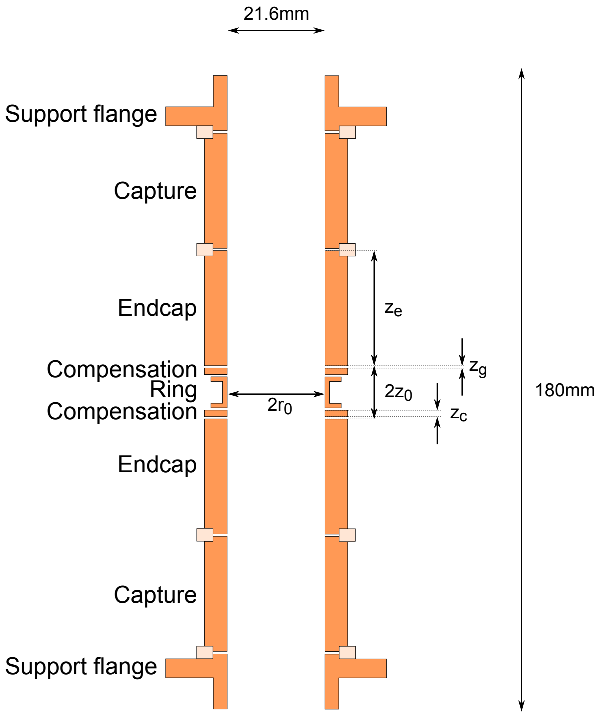

Figure 5.6: Schematic view of the SPECTRAP electrode structure.

to the interior of the trap allows for easy loading of ions, as well as throughput for fluorescence, laser beams and microwave radiation. The following part of this sub-section details the method to design a cylindrical electrode Penning trap, and uses this to discuss the features of the SPECTRAP ion trap.

A potential with azimuthal symmetry can be expressed in spherical polar coordinates (r,θ) by an expansion in Legendre polynomials [64][1]

$$\phi = \frac{1}{2}U_0 \sum_{k=0}^{\infty} C_k \left(\frac{r}{d_0}\right)^k P_k(\cos\theta) \qquad (5.3.1)$$

where $P_k(\cos\theta)$ denotes a Legendre polynomial of order k, and where only the even order C_k coefficients are present due the reflection symmetry about the Cartesian $z = 0$ plane. For ions near the centre of the trap, $(\frac{r}{d_0}) << 1$, only the lowest order terms are important. The first term, C_0, is a constant and can be ignored for the following discussion. The next lowest order term, C_2,

---

[1] A more modern approach for solving the potential for a cylindrical electrode trap is available in [65]. This method uses cylindrical coordinates and gives exact results for finite electrodes sizes and gaps between electrodes.

defines the axial frequency of oscillation

$$\omega_z = \sqrt{\frac{qU_0}{md_0^2}C_2}. \tag{5.3.2}$$

For an ideal hyperbolic trap with a perfect symmetrical quadrupole potential, $C_2 = 1$, and all other terms are zero. Therefore, the coefficient C_2 can be thought of as an efficiency factor since typically $C_2 < 1$ for a real cylindrical electrode trap, the axial confinement is less than it would be for the same voltage applied to a perfect hyperbolic electrode trap.

For a non-zero C_4 coefficient, the potential will be anharmonic and this leads to a shift in the axial frequency [64]

$$\frac{\Delta\omega_z}{\omega_z} = \frac{3}{2}\left(\frac{C_4}{C_2}\right)\frac{E_z}{qU_0C_2} \tag{5.3.3}$$

that is dependent on the energy of the ion's axial motion, E_z. Such shifts in frequency are undesirable when wanting to measure small changes in ω_z, or resistively cool ions with high quality factors.

The next anharmonic term is C_6 which is a factor $(\frac{r}{d_0})^2$ less important than C_4. This of course produces a shift in ω_z proportional to the square of the energy

$$\frac{\Delta\omega_z}{\omega_z} = \frac{15}{4}\left(\frac{C_6}{C_2}\right)\left(\frac{E_z}{qU_0C_2}\right)^2. \tag{5.3.4}$$

By adding extra electrodes between the endcaps and ring electrode, these anharmonicities can be tuned out. This is the purpose of the compensation electrodes in the present trap. The total potential in the trap, with compensation electrodes, maybe be written as a simple superposition

$$\phi_{total} = U_0\phi_0 + U_c\phi_c \tag{5.3.5}$$

where ϕ_0 and ϕ_c are solutions to Laplace's equation with orthogonal boundary conditions i.e. $U_0 = 1$ when $U_c = 0$ and vice versa. As in equation (5.3.1), these solutions can be expanded to give

$$\phi_0 = \frac{1}{2}\sum_{k=0}^{\infty} C_k^0 (\frac{r}{d_0})^k P_k(\cos\theta) \tag{5.3.6}$$

and

$$\phi_c = \frac{1}{2}\sum_{k=0}^{\infty} C_k^c (\frac{r}{d_0})^k P_k(\cos\theta) \tag{5.3.7}$$

which, with the aid of Bessel functions of the first kind and zero order (J_0), can be shown to give the expansion coefficients [64]

$$C_k^0 = \frac{(-1)^k/2}{k!}\frac{\pi^{k-1}}{2^{k-3}}\left(\frac{d_0}{z_0+z_e}\right)^k \sum_{n=0}^{\infty}(2n+1)^{k-1}\frac{A_n^0}{J_0(ik_n r_0)} \tag{5.3.8}$$

with

$$A_n^0 = \frac{1}{2}\{(-1)^n - \sin(k_n z_0) - \sin[k_n(z_0 - z_c)]\} \tag{5.3.9}$$

and

$$C_k^c = \frac{(-1)^k/2}{k!}\frac{\pi^{k-1}}{2^{k-3}}\left(\frac{d_0}{z_0+z_e}\right)^k \sum_{n=0}^{\infty}(2n+1)^{k-1}\frac{A_n^c}{J_0(ik_n r_0)} \tag{5.3.10}$$

with

$$A_n^c = \sin(k_n z_0) - \sin[k_n(z_0 - z_c)]\} \tag{5.3.11}$$

where with reference to Fig. 5.6 for the definitions of z_0 and z_e

$$k_n = \frac{(n+\frac{1}{2})\pi}{z_0+z_e}. \tag{5.3.12}$$

The coefficients of the trap potential are now given by

$$C_k = C_k^0 + \frac{U_c}{U_0}C_k^c. \tag{5.3.13}$$

Hence the potential on the compensation electrodes, U_c, can be adjusted to cancel out any particular anharmonicity. However, in general, adjusting U_c will involve changes to C_2 causing unwanted changes to the oscillation frequencies requiring the trap potential U_0 to be readjusted. As these coefficients are functions of the relative size of the electrodes, r_0/z_0 and z_c/z_0, there is an extra degree of freedom that can be exploited to make the trap "orthogonal" to changes in U_c such that there is no effect on C_2. That is, for a given trap size, r_0/z_0, there is a specific size for the compensation electrodes, z_c/z_0, which makes $C_2^c = 0$ (see Fig. 5.7).

If the ratio of the sizes of the ring and compensation electrodes are both un-

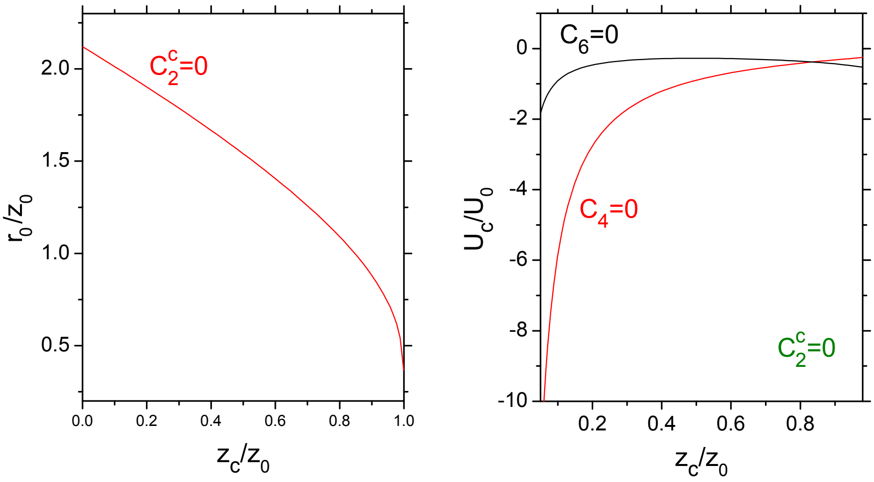

Figure 5.7: (left) relative size of compensation electrodes required to orthogonalise a cylindrical electrode trap, and (right) voltage required for compensation of low order anharmonicities in an orthogonalised trap.

constrained parameter, there is a specific value of r_0/z_0 and z_c/z_0, where the potential of the compensation electrodes can be made to simultaneously cancel out all lowest order anharmonicities. From Fig. 5.7, it can be seen that this occurs for a trap of size $r_0/z_0 = 1.01$ and $z_c/z_0 = 0.835$ making $C_2^c = 0$, with the potential ratio $U_c/U_0 = -0.38$ making $C_4 = C_6 = 0$.

These calculations were considered in the design of the SPECTRAP ion trap. As the aperture of the trap had to be large for acceptance of ions from the HITRAP facility ($r_0 \geq 10$mm), and the overall length of the trap had to be limited to fit inside the magnet ($z_0 \leq 200$mm), the condition described in the previous paragraph could not be fulfilled. Therefore the trap was designed to be orthogonal, with the ability to compensate for only one particular anharmonicity i.e. C_4.

A summary of the SPECTRAP geometry and expansion coefficients can be seen in table 5.1. These equations (5.3.8-5.3.10) assume infinitely long endcaps and zero gaps between electrodes[2]. Hence accordingly, the electrode lengths

---

[2] A recently developed method to analytically calculate the trap potential with arbitrary electrode geometries, that includes the effects of the gaps between electrodes, can be found in [65].

are extended into the gaps, which changes in particular z_0 from 5.9mm to 5.65mm. In all other calculations in this thesis, the real physical distances in the trap of $r_0 = 10.6$mm and $z_0 = 5.9$mm are used which give a characteristic trap dimension of $d_0 = 6.75$ mm. A fully detailed model of the SPECTRAP ion trap was also simulated in SIMION[3]. From table 5.1 is can be seen that the expansion coefficients derived analytically appear to be inaccurate when compared with the coefficients derived from a polynomial fit of the axial potentials, ϕ_0 and ϕ_c, from SIMION (see table 5.1 and Fig. 5.8). The is because of the effects of the compensation and ring electrodes being smaller than theoretically assumed due to the truncation to allow for the insertion of the 0.5mm gaps, and this reduction in size is significant for the smaller electrodes.

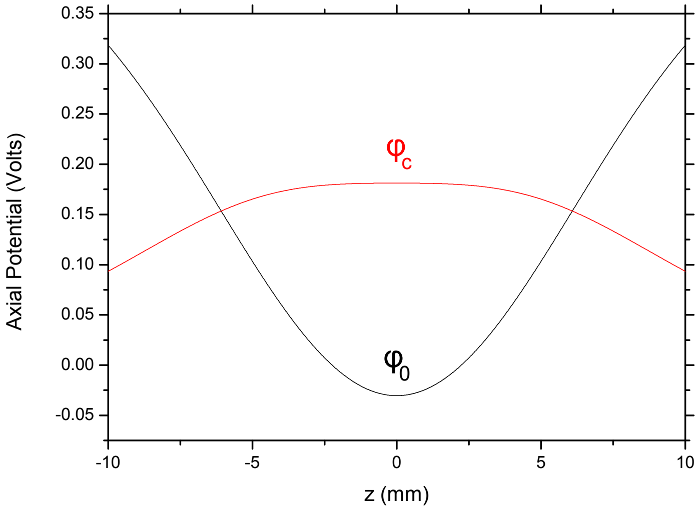

Figure 5.8: Simulated SPECTRAP ion trap axial potentials of ϕ_0 (endcaps= 0.5V, ring= -0.5V and compensation= 0V) and ϕ_c (endcaps=ring= 0V and compensation= 1V).

These simulations were conducted after the trap was manufactured but show that the orthogonality may actually be better than expected. Therefore theoretically, the effect of the compensation electrodes on the axial frequency should be, $\frac{\Delta\omega_z}{\omega_z} < 2.5\%$ for $\left|\frac{U_c}{U_0}\right| < 2$ and hence is within acceptable limits.

---

[3] SIMION is a commercial software package for performing charged particle optics simulations [66].

Analytical model trap parameters	
Length,	$z_0 = 5.65\text{mm}$
Radius,	$r_0/z_0 = 1.88$
Endcap electrodes,	$z_e/z_0 = 4.51$
Compensation electrodes,	$z_c/z_0 = 0.35$
Ring electrodes,	$z_r/z_0 = 1.29$
Gaps between electrodes,	$z_g/z_0 = 0$

Expansion Coefficients	Analytical Solution	SIMION
C_2^0	0.509	0.578
C_2^c	-0.030	-0.018
C_4^0	-0.140	-0.234
C_4^c	-0.074	-0.214
C_6^0	0.021	0.383
C_6^c	0.045	0.031
Voltage required for $C_4 = 0$		
$\frac{U_c}{U_0} = -\frac{C_4^0}{C_4^c}$	-1.89	-1.09

Table 5.1: Geometry and expansion coefficients of the SPECTRAP ion trap. SIMION coefficients are derived from a 6^{th} order polynomial fit of the axial potentials ϕ_0 and ϕ_c (see Fig. 5.8) between the range $-1 \leq z \leq +1$ mm.

5.3.2 Construction

A schematic of the SPECTRAP trap mechanical structure can be seen in Fig. 5.9. All inner surfaces of electrodes were separated by ~ 0.5mm along z. Between the support flanges, capture and endcap electrodes, this spacing was provided by macor rings which also radially locked the electrodes into position. Between the endcaps and ring electrodes, sapphire balls were used which located into drilled sockets. This approach minimised the surface area of insulator that could be charged up by the deposition of ions (particularly HCI at GSI) lost from the trap. Copper rods with threaded ends provided a connection between the support flanges which allowed the trap to be clamped together, making the structure rigid. These rods also horizontally supported a pair of optics holders which ensured good alignment between them, and with the axis of the trap. The holders rested on spacers which went around the rods and set the vertical position to the centre of the trap. Due to the radial symmetry, there was no need for x-y translation adjustments (tilt) for the optics, and it was assumed that the optical axis would be well overlapped along the geometric centre of the trap. This assumption was justified as all trap components were machined to tolerances less than 0.01mm. With an imaging magnification of unity, the smallest feature from a large ion cloud would be an order of magnitude larger than this i.e. the ≈ 0.2mm axial extent of fluorescence set by the laser beam waist.

All components of the trap discussed and shown so far were made of OHFC copper unless otherwise stated. The trap was suspended from the top by three screws which held the trap support flange to a steel tripod assembly welded to the main vacuum vessel flange as shown in Fig. 5.10. These screws along with the rest of the vacuum system were made from type 304 and 316 stainless steel which have a particularly low magnetic permeability. This was important as anything that could become magnetised, would affect the magnitude and homogeneity of the magnetic field at the centre of the trap.

Electrical connections to the outside were made using three sets of four copper feedthroughs on the top flange (see Appendix A). This gave a total of 12 connections which were all necessary to operate the trap. Four connections were used for the ring electrode to produce the rotating wall, and a further four were used for independently addressing the compensation and endcap

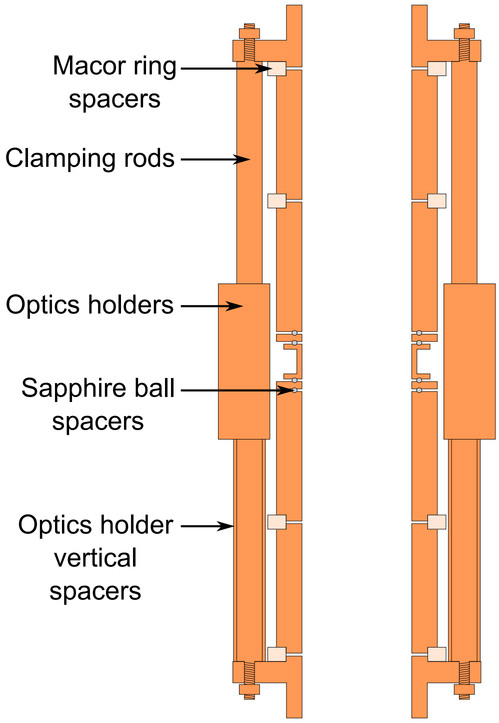

Figure 5.9: The Imperial College SPECTRAP ion trap schematic showing the major elements of construction.

electrodes. This gave the ability to shift the electric centre of the trap along the axis to overlap the ions with the fluorescence collection optical axis, and also to drive dipole and quadrupole radio frequency excitations to determine the ion motional frequencies. The four remaining feedthroughs were used for connections to the electron filament and atomic oven for the ion source.

The electrical connections from the feedthrough inside the vacuum were made using Kapton coated copper wires. Kapton provides good electrical insulation (typically $>$ 1kV for usual insulator thicknesses) and ultra high vacuum compatibility (low outgassing). The wires were connected to the outer surfaces of the electrodes by solder and the feedthrough pins via barrel crimp connectors. Solder is not particularly good under UHV, so an absolute minimum amount had to be used. This was accomplished by creating a contact point on each electrode by use of a blind drilled hole only fractionally larger than the wire to be inserted. Filling this hole with solder created a good anchor point for the wires as the surface area with electrodes was maximised and only a small volume of solder was used.

As copper has a high thermal conductivity, a soldering iron could not be used to melt the solder on the electrodes. Instead each electrode had to be heated under a flame. This caused the surfaces to become oxidised, but using a soft solder with a melting point around 280 degrees helped minimise the surface contamination. The electrodes were then cleaned with acid, acetone and ethanol successively to recover their previous condition (more details regarding cleaning are presented in the final paragraph below).

There were three different thickness of wires used in vacuum. As the oven and filament required high current (> 1A), the thickest and most rigid wire was used here (conductor diameter, $A_{cc} = 0.94\text{mm}^2$). For the endcaps and capture electrodes, a medium thickness semi-flexible wire was used ($A_{cc} = 0.61\text{mm}^2$). And due to the physical constraints around the compensation and ring electrodes with the surrounding optical mounts, a much thinner fully flexible wire was used ($A_{cc} = 0.25\text{mm}^2$).

A photograph of the Imperial College SPECTRAP superstructure is provided in Fig. 5.10.

An important final stage in the assembly of the trap and vacuum system was the cleaning of the components to reduce outgassing. Collisions with residual gas particles can transfer energy to trapped ions and at the very least, limit the lowest temperature that can be reached with cooling. If the collision rate is too high, it can result in ion loss particularly in Penning traps where the magnetron motion is unstable. Charge exchange can also occur and ions can be lost via this mechanism as well. Hence the importance of a good a vacuum. To this end, all copper components received an acid, acetone and ethanol clean in an ultrasonic bath to remove oxidation, grease and any remaining surface residue respectively. All other components to be inserted in the vacuum enclosure were cleaned with acetone and ethanol. With this method, the system was able to reach a base pressure in the range $10^{-10} - 10^{-9}$mbar limited by the conductance of the vacuum system i.e. pumping speed (see section 5.3.5).

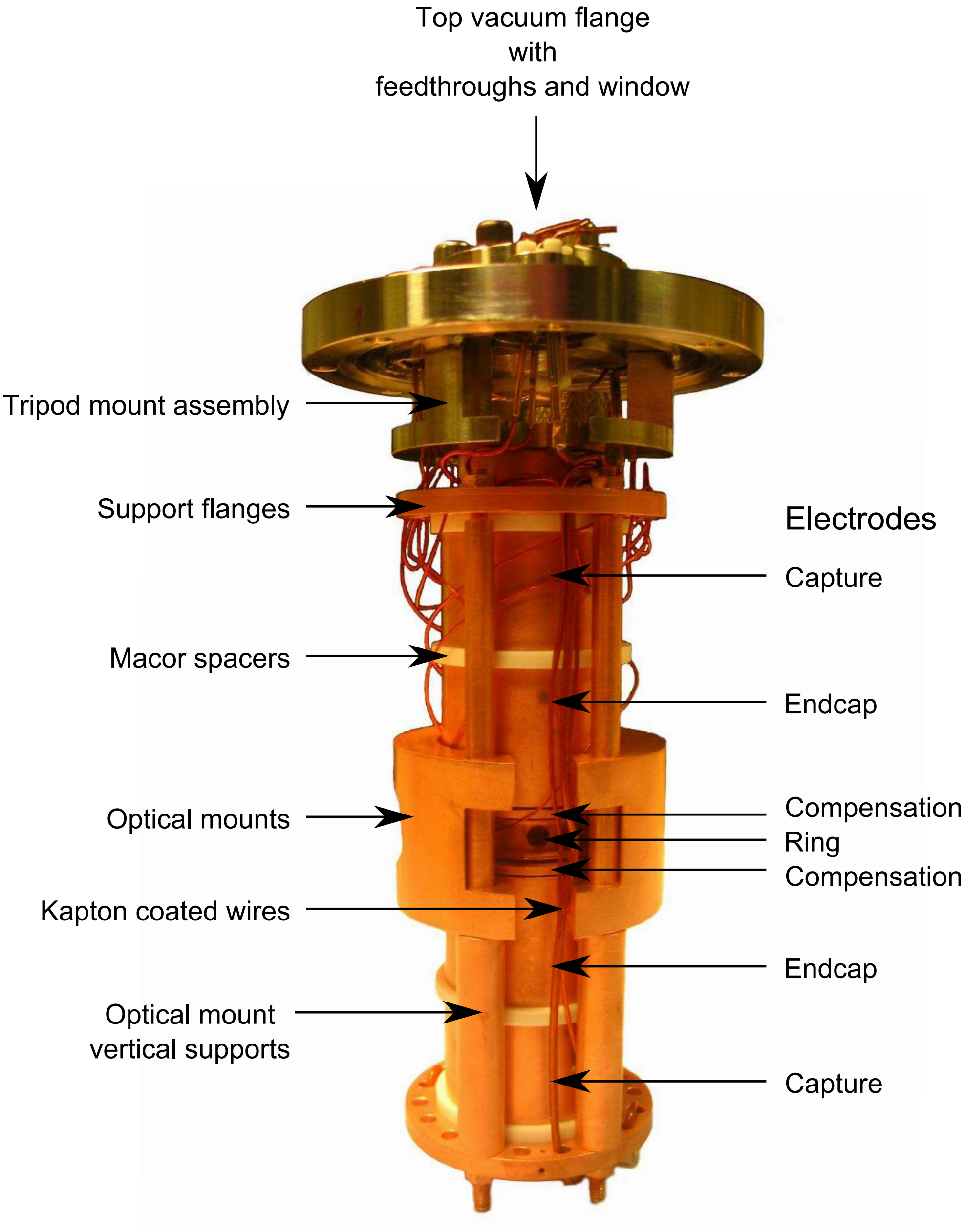

Figure 5.10: Photograph of the Imperial College SPECTRAP in vacuum superstructure without the filament and oven attached.

5.3.3 Ion Source

Ions in the SPECTRAP experiment at Imperial College were created by electron impact ionisation of a weak atomic beam, 'in situ' at the centre of the trapping potential. Electrons were produced by thermionic emission from a hot filament, and calcium atoms were produced by evaporation from an atomic oven. The filament emission current density is described by the Richardson equation [67] [68]

$$J = A_m T^2 e^{-\frac{(W-\Delta W)}{k_B T}} \tag{5.3.14}$$

$$\Delta W = \sqrt{\frac{e^3|E|}{4\pi\epsilon_0}} \tag{5.3.15}$$

where J is the current density, A_m is a constant depending on the metal, T is the temperature, k_B is the Boltzmann constant, W is the work function of the metal and ΔW is the reduction in the work function by the presence of an external electric field E at the surface of the metal. By passing a current through a wire, the ohmic resistance causes a metal to heat up. If the current is high enough, this heat can provide enough energy for free electrons in the metal to overcome the work function (W) and be liberated from the surface. The emission can be enhanced if the wire is biased negative relative to its surrounding, such that an electric field is created that reduces the barrier to emission ($W - \Delta W$).

The filament for the ion source was made from thoriated tungsten wire ($A_{cc} = 0.012\text{mm}^2$). Tungsten is a common choice for filaments due to its high melting point and resistance to breaking. In general for UHV systems, the highest emission for the lowest current (temperature) is wanted since heating inside the vacuum causes an unwanted increase in pressure due to outgassing. This is the purpose of the thorium oxide which provides a reduced work function for electron emission.

The filament had to be placed outside the electrodes of the trap, to avoid disturbing the trap potential. It also had to be placed along the axis of the trap for the electrons to traverse to the centre of the trap in the presence of the high axial trapping magnetic field i.e the electrons travel only along the magnetic field lines. Therefore the filament was positioned diametrically, and under the trap (see Fig. 5.11). It was also coiled to increase the total surface area for emission and to help achieve a high temperature for a low current i.e. higher resistance. This also ensures that the maximum current rating of the vacuum electrical feedthrough of 5A is not exceeded.

The oven consisted of a tantalum tube (outer diameter of 2mm and inner diameter of 0.5mm) filled with calcium cuttings, pinched closed at both ends, with a small hole (diameter 0.25mm) drilled into the wall for emission. The oven was spot welded to tantalum wire ($A_c = 0.05\text{mm}^2$), which provided the heating element. Tantalum was used because it is mechanically hard, has a high melting point ($\sim 3000°\text{C}$) and is chemically inert such that is will not react with calcium. The trapping fields have virtually no effect on the neutral atoms, so in theory, an oven could be placed anywhere with line of sight to the centre of the trap. However emission from the oven is broad, and coating on electrodes producing contact potentials cannot be avoided. If the oven was displaced radially, the electrodes would receive an asymmetric coating of calcium resulting in static field errors that would be driven by the rotating wall. Therefore, in order to preserve the radial potential symmetry, the oven was positioned axially in the same manner as the filament, at the opposite end of the trap.

Fig. 5.11 shows the complete layout of the ion source around the trap. The oven was mounted between a pair of copper feedthroughs, and the filament was mounted between a pair of Kapton wires wound around the lower support flange. The thickness of the wires ensured they would stay in place, and the simplicity of installation greatly reduced the time to install the source at the end of the build. This was important since the time after cleaning the trap and filling the oven needed to be minimised to reduced oxidation before the vacuum system was evacuated.

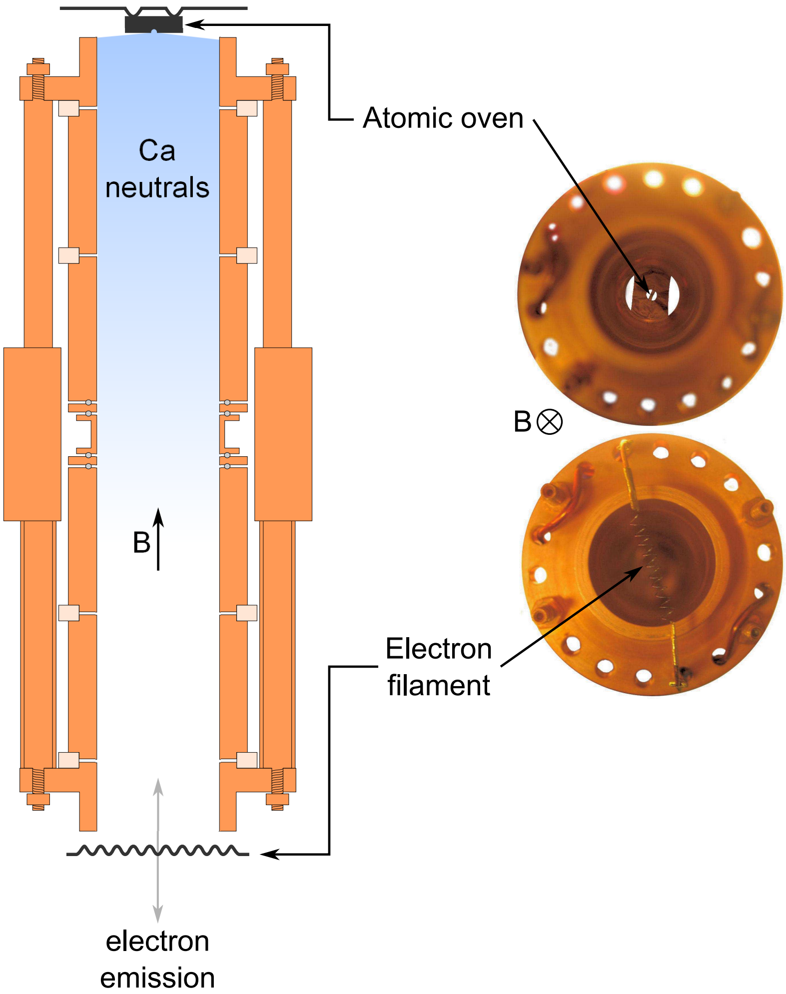

Figure 5.11: (left) Schematic and (right) photos of the Imperial College SPECTRAP showing the positions of the calcium oven and electron filament for creating ions 'in situ'.

5.3.4 Magnetic Field

The magnetic field for the SPECTRAP experiment at Imperial College was provided by a solenoid type superconducting magnet manufactured by Magnex Scientific Ltd.. A superconducting magnet provides an efficient way of generating a large volume of high homogeneity, high strength (> 1T) magnetic field without the resistive losses of conventional electromagnets. The field stability of superconducting magnets can also be orders of magnitude better than that of conventional electromagnets as they are isolated from noise on power supplies when in a persistent mode of operation. A solenoid type configuration also provides an excellent ambient field shield (through the Meissner effect) at the cost of reduced radial access. A diagram and table of the main specifications of this magnet is provided below in Fig. 5.12.

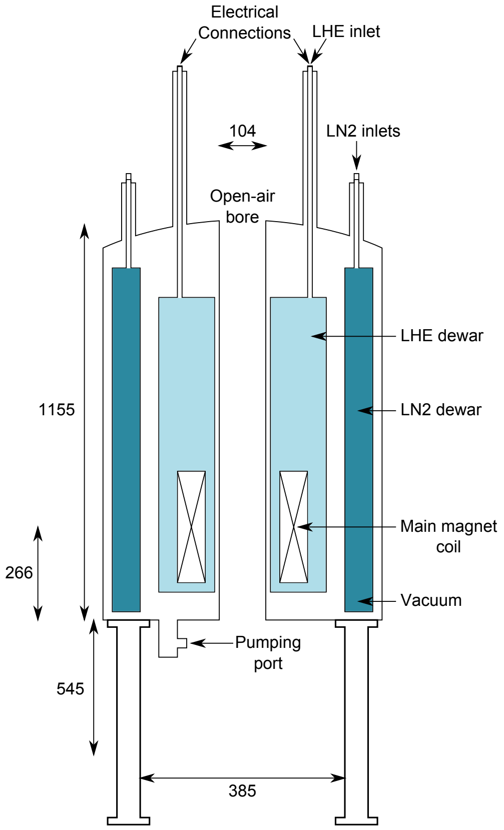

Centre Field calibration	$\sim 40A$@1T
Field stability	< 10ppm/hr
Operating range	< 2.5T
Vert. Field homogeneity	$< 1 \times 10^{-4}$ over 5mm
Open-bore diameter	104mm
LHe boil-off rate	< 4mm/day
Volume of LHe dewar	100litres
Volume of LN2 dewar	85litres

Figure 5.12: (left) Diagram and (right) specification of the custom made Magnex Scientific superconducting magnet at Imperial College London.

For the London experiments, the room temperature open-air bore provided ready access to the interior of the magnet with no additional thermal loading on the cryostat i.e. conserving the cost of cryogens.

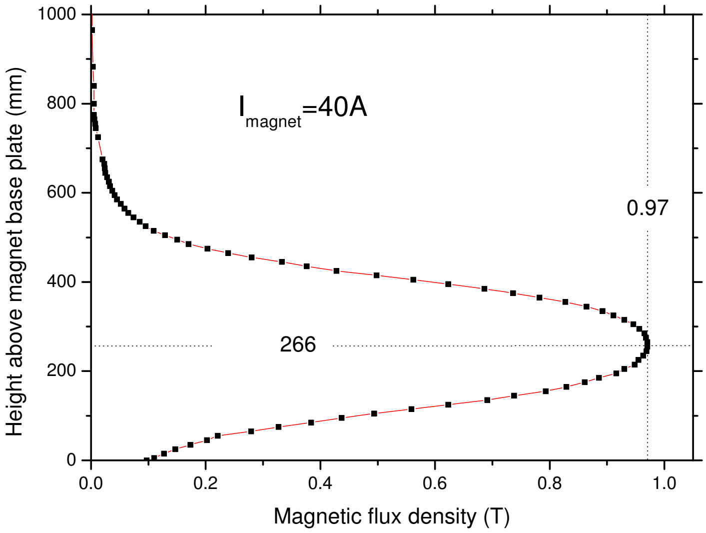

Figure 5.13: Measured axial magnetic field along the centre of the bore of the superconducting magnet. The errors in the height are ±5mm which come from using a 10mm axial hall probe, and the errors in the magnetic field are ±0.01tesla limited by the sensitivity of the probe on this measurement scale. Both of these error bars have been omitted from the above plot as they would be too small to be seen.

As fluorescence was the only means of detection of ions in the trap, for first Penning trap operation, it was necessary to know the magnitude and direction of the magnetic field to set the laser wavelengths and beam position correctly. Hence a calibration of the magnet plus power supply was made with a current of 40A. The results can be seen in Fig. 5.13 which were obtained from measurements of the axial magnetic field along the centre of the bore using a Hall probe. This gives a calibration of 41A per tesla at peak field with the magnetic field vector pointing vertically upwards.

5.3.5 Vacuum System

The SPECTRAP vacuum system shown in Fig. 5.14 was constructed from type 304 and 316 stainless steel, for the aforementioned reasons. The trap was suspended in a custom made vacuum vessel at the top of the system. There were four radial (90 degrees apart) and one axial (top) quartz windows around the trap for optical access. Quartz was used because it has particularity low scattering losses in the ultraviolet due to its crystalline structure, and would therefore minimise the background laser scatter in the trap. The outer diameter of the trap vessel was 75mm which left only 14.5mm radially to the walls of the magnet bore. In this space, external optics had to be fitted for laser excitation and fluorescence detection (see section 5.3.6). To reduce RF pick-up on the connecting wires to the electrodes outside the vacuum, coaxial cables were used. Due to their physical size, and the constraints around the bore, all connections to the trap flange were made from the top of the magnet. A 40ls^{-1} Varion ion pump maintained the vacuum, and an ion gauge provided pressure measurements. Both of these are affected by magnetic fields. As the ion pump had to remain functional in the fringe fields of the superconducting magnetic, it was placed at the extremity, far away from the magnet[4]. The vacuum system (and optical breadboard) rested on top of an aluminium platform attached to a crane that was used to raise the trap into the magnet (see photo Appendix B). The height of this system was dictated by the requirement to place the centre of the trap at the centre of the homogeneous region of the magnetic field. With the platform lowered to the floor, less than 5mm of height remained from the top of the vacuum system to the base of the magnet. Electrical connections to the top flange were made by dropping a bundle of wires down the bore, when the trap was located on the floor before it was inserted into the magnet. The magnet could not be raised due to limitations set by the ceiling height.

All flanges in the system were sealed using a knife edge pressed into a copper gasket, except the radial optical ports which used an indium wire loop. This is because the ports were recessed into the vacuum vessel to improve access inside the bore, making it difficult to turn a knife edge into the port. All vacuum components were cleaned with acetone and ethanol before the system

---

[4] An ion pump uses electrons produced via field emission from a cathode, that are contained by a magnetic field, to ionise residual gas atoms which are attracted by a strong electric field to an anode getter. Hence any strong external magnetic fields can affect an ion pumps own magnetic field (axis) and operation.

was assembled. To reach the required UHV, the system was baked on a turbo molecular pump, to efficiently outgas, for a period of one week. The soft indium seals limited the bake-out temperature to 110°C, so a pre-bake was first carried out of the vacuum system without the trap vessel at 300°C for a period of 4 days before venting with dry nitrogen. During bake-out, pressure measurements were made using the ion gauge to determine if a plateau had been reached indicating the bake-out was complete. After the final bake, a pressure of 10^{-9}mbar was reached before the ion pump was turned on, and the system valved off.

The vacuum system is based on standard CF40 hardware, except for the CF16 adapter connecting to the trap vessel. The conductance at room temperature for Nitrogen in the molecular flow regime is only 6.7ls^{-1} for the CF40 system at the position of this adapter due to its long length. The adapter itself only has a conductance of 7.1ls^{-1}, which implies the pump speed at the trap vessel is reduced from 40ls^{-1} to 3.1ls^{-1} for Nitrogen at room temperature[5].

---

[5] These calculations assume the molecular flow regime with the vacuum system modelled as a long straight uniform diameter pipe, followed by the CF16 adapter as a long smaller diameter pipe in the formulae provided in [69].

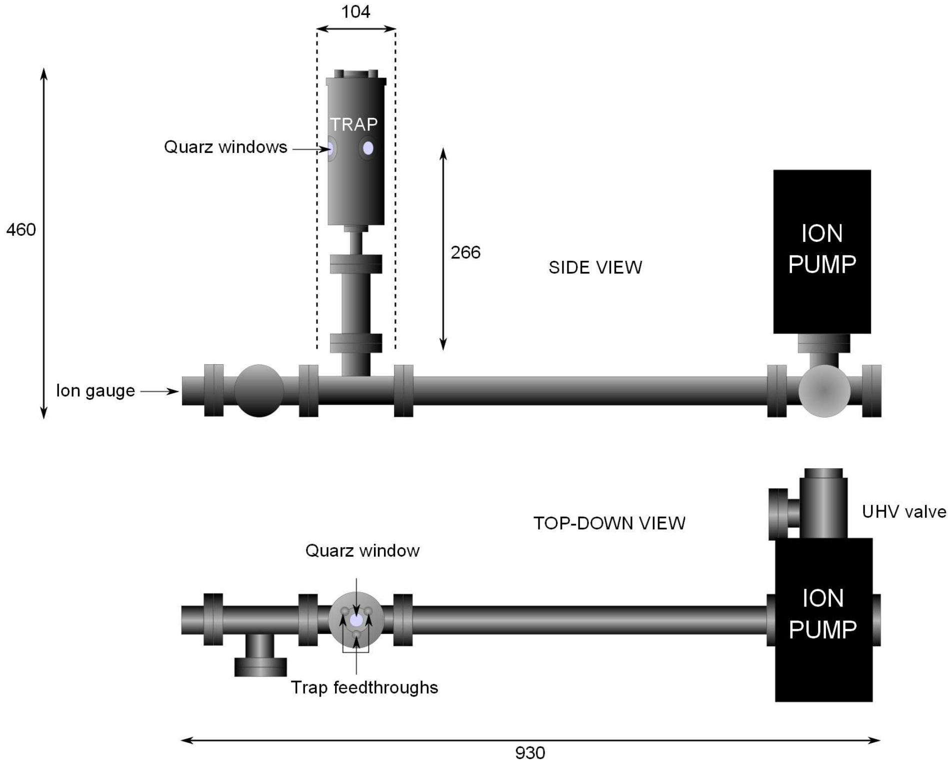

Figure 5.14: A schematic diagram showing the major elements of the vacuum system.

5.3.6 Optics

The SPECTRAP vacuum system was mounted on top of a custom made optical breadboard. This allowed optics to be mounted such that it could remain fixed relative to the trap. This was essential as the system could be aligned and tested (in Paul trap operation) outside of the magnet, and then inserted into the magnet bore (for Penning trap operation). With such a physically constrained system, particularly inside the bore of the magnet, standard mounts and translation stages were not an option. Compounded with this, a large field of view was required to capture the complete cross-sectional profile of an ion cloud, onto a CCD camera outside the bore of the magnet. The most practical solution was to have laser excitation and fluorescence detection in the radial plane. For this reason, four holes were made in the ring electrode segments allowing perpendicular laser excitation and fluorescence collection, minimising laser scatter along the collection axis (see Fig. 5.15). The holes drilled in the ring were made as large as possible without compromising the structural integrity of the ring electrode. These were of diameter 4mm and SIMION simulations of the axial potential showed that these holes, in a symmetric arrangement, did not modify the expansion coefficients of the trap potential shown in table 5.1 to the accuracy considered i.e. to the level of 3 significant figures.

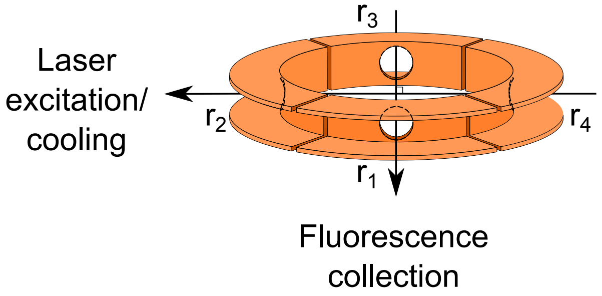

Figure 5.15: Schematic diagram showing the SPECTRAP ring electrode with a radially symmetric arrangement of 4mm diameter holes in each ring segment 90 degrees apart for optical access.

5.3.6.1 Laser Excitation and Cooling

The optical setup on the SPECTRAP platform in plan view is shown in Fig. 5.16. The lasers were transported to the optical breadboard by use of optical fibres. Light from both 397nm (blue) and all four 866nm (infra-red) lasers was coupled into two single mode fibres, ensuring good spatial overlap and a good quality Gaussian beam profile thereafter. On the SPECTRAP breadboard, the light from these fibres was recollimated and combined on a dichroic mirror. To have a large range for beam steering at the centre of the trap, a focusing lens was positioned outside the magnet bore. If a lens (of diameter < 16mm) had been placed just outside the ring electrode, a sufficient angle could not be imparted from an actuated mirror on the breadboard, such that the waist at the centre of the trap could be moved by up to 1mm without missing the lens completely. Furthermore, if a large lens could physically fit inside the trap or bore, the off-axis use of the lens would result in aberrations in the focused laser beam. Hence a singlet lens with a focal length of $f' = 1000$mm was positioned immediately after the dichroic mirror, and before the computer-controlled actuated mirror, to focus the lasers at the centre of the trap. Singlet lenses suffer from chromatic aberration, but the focus of the infra-red fibre collimator was adjusted to overlap the foci correctly at the centre of the trap. As both the infra-red and blue fibres had the same numerical aperture of 0.15, and the same focal length of collimating lens ($f' = 18.4$mm), the waist and Rayleigh range of the infra-red laser beam was over 2 times greater than that for the blue. This meant that the infra-red lasers were more likely to overlap the entire blue laser beam waist, and ensure repumping and fluorescence over the full laser-ion interaction region.

The optical fibres were polarisation maintaining and the output ends were adjusted to give the blue lasers a vertical and the infra-red lasers a horizontal polarisation for the π and σ Zeeman transitions (see section 5.1) respectively. To maintain the degree (and orientation) of linear polarisation, the laser beams were kept in a horizontal plane on the breadboard, and a vertical plane along the periscope. This meant that the polarisations of the lasers were correct at the trap, and so no $\frac{\lambda}{2}$ waveplates were necessary for rotation. A second periscope was used to guide the laser light out of the bore to reduce the level of scatter in the trap that would have resulted if the beam had been dumped near the trap, and to use this output beam as a visual diagnostic for pointing of the beam in the trap. To aid in the latter, a second lens ($f' = 150$mm) was positioned after the trap and used to form a focus, where an adjustable iris was installed, before a screen for observations. In this way, it could be known if the beam position had moved relative to the trap once the system was inserted into the magnet.

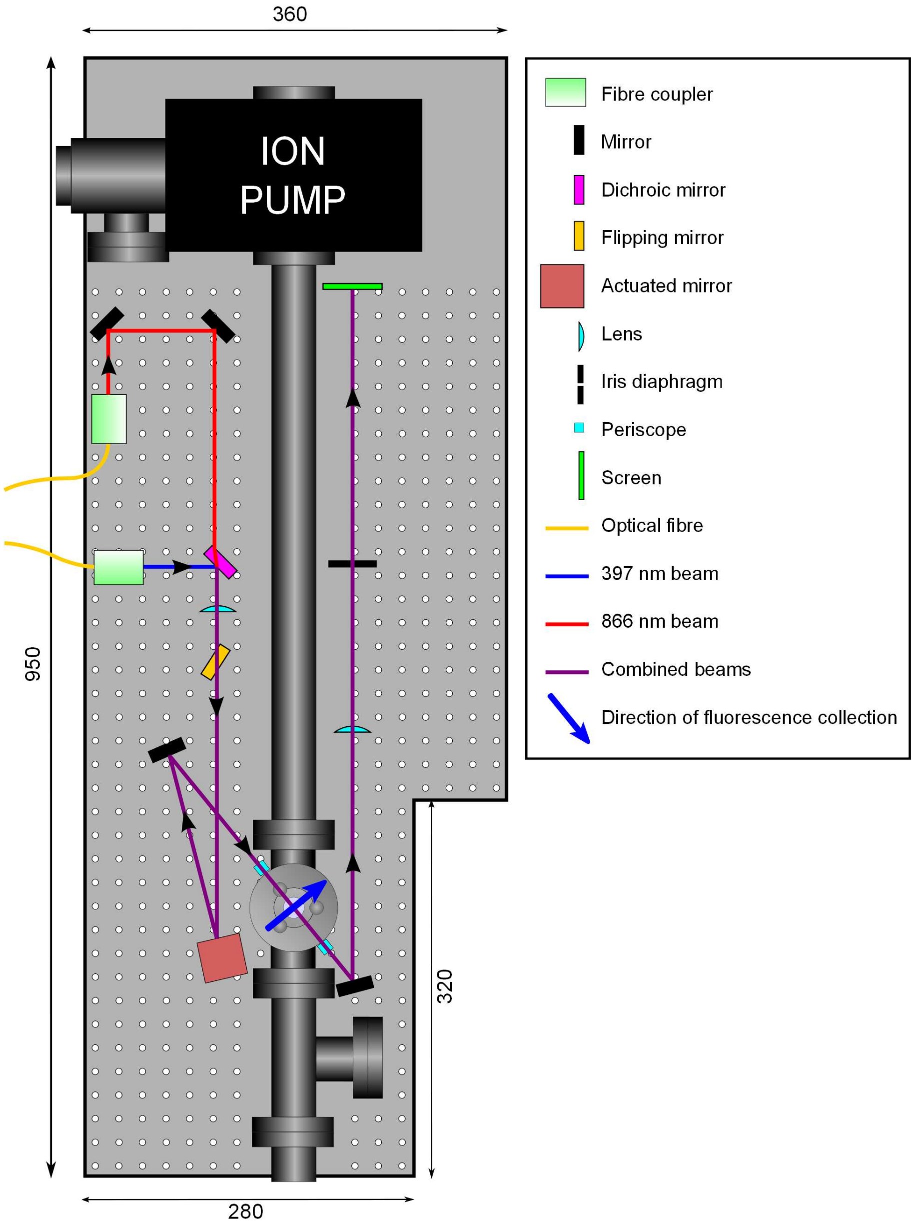

Figure 5.16: A plan view schematic diagram showing the layout of the SPECTRAP optical system for laser induced fluorescence excitation. All lengths are in units of mm.

A flip up mirror was installed after the dichroic mirror to reflect the laser beams out of the setup and into free space in the laboratory where the overlap between the blue and infra-red laser beams could be optimised. Typically a minimum power of 100μW and 200μW from each blue and infra-red laser respectively was output immediately after the fibre couplers. Approximately 50% of this power was delivered to the trap. The large losses were mainly due to the accumulation of Fresnel reflections and the reflectivity of the many mirrors which could not all be very high reflectivity dielectric mirrors due to the two different wavelengths[6].

5.3.6.2 Fluorescence Collection

The maximum solid angle (0.11sr) for fluorescence collection was set by the holes or apertures in the ring electrode. Optics were installed in-vacuum around the trap for fluorescence collection only, due to the high numerical aperture requirements, and consisted of a singlet lens ($f' = 20$mm) and spherical mirror ($f' = 10$mm) in a confocal arrangement (see Appendix D). The focal length of the lens was chosen to collimate the light from the centre of the trap. This confocal arrangement with a mirror acting as a retro-reflector was chosen primarily to double the amount of fluorescence collected. It also gave the system an unforeseen advantage which was the ability for the imaging outside the vacuum system to be aligned by sending light in from an object, and reimaging back onto the same plane, even with an arbitrary number of optical elements.

The alignment of the internal optics was therefore critical in this confocal arrangement. If the centre of curvature of the mirror and the rear focal plane of the lens were not made to overlap at the centre of the trap, this would result in a superimposed image of an in-focus and out-of-focus ion cloud. Such a setup cannot be corrected for outside the vacuum for an extended source i.e. by spatial filtering. Therefore particular attention was paid to developing a method for aligning the internal optics. The method that was used employed a knife edge test to first set the lens at the correct distance from the centre of the trap[7]. This setup can be seen in Fig. 5.17. The trap electrodes obstructed a knife edge from being inserted directly into the centre. However, due to the

---

[6] Aluminium and silver mirrors were used after the blue and infra-red laser beams were combined.

[7] The radial position of the optical mounts was fixed by machining. Therefore the only degree of freedom to set was the position of the lens and mirror in and out of their mounts to adjust the focus along the optical axis.

radial symmetry, the electrodes could be removed and the test carried out on a bare trap consisting of only the optical mounts resting on the base of the lower support flange. The test consisted of illuminating the trap lens with an expanded collimated laser beam propagating across the centre of the trap. A knife edge was then repeatedly translated across the geometric centre of the trap until the focus of the lens was set to this position. The mirror was then installed and a beam splitter cube was positioned in front of the lens to isolate the retro-reflected beam. The mirror was then translated until this reflection was collimated, setting the centre of curvature of the mirror onto the back focal plane of the lens. With good parallelism and radial symmetry between the optical mounts and the trap, the optical axis of the lens and mirror was assumed to be well overlapped in the radial plane across the centre of the trap.

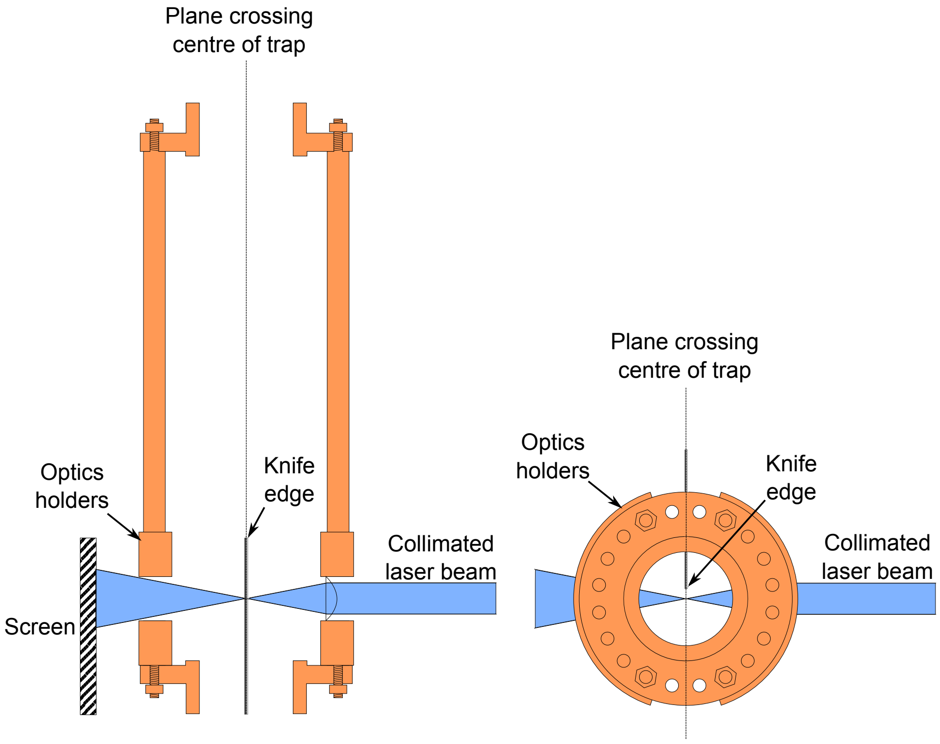

Figure 5.17: Schematic showing the SPECTRAP ion trap setup for setting the focal position of the fluorescence collection lens before the mirror is installed. (left) shows an axial and (right) shows a radial cross-sectional view of the trap.

In order to capture fluorescence from a large cloud at the periphery, and relay this image outside of the magnet, a single lens pair could not be used. With the aid of Fig. 5.18, consider a cone of light originating from the edge of a cloud only 1mm away from the optical axis, that is collimated and folded inside the bore of the magnet i.e. as the fluorescence would be imaged outside the bore of the magnet using a single lens pair. This would be cropped by the walls of the magnet itself before exiting the bore, resulting in a complete loss of fluorescence at this edge of the cloud. Compounded with this, outside the magnet, off-axis imaging would result in astigmatism and coma aberrations. Both these factors would give a false aspect ratio of the cloud and impair an investigation into the effects of the rotating wall on the shape of the cloud. Therefore the only solution was to re-image inside the bore. This was most conveniently done by use of a rigid multimode optical fibre bundle that maintains the individual relative spatial locations of the fibres. That is to say, it relays an image formed on one face to the other. Although such a glass fibre has large coupling losses due to the lossy cladding surrounding each individual core of the fibre bundle, it is easier to align and more robust than a series of lenses down the bore of the magnet. The resolution of the fibre bundle was required to be much less than the smallest feature of the images from the cloud. Namely, for large clouds, this would be the axial extent of fluorescence given by the blue laser beam waist ($\omega_0 \sim 0.125$mm). The length of the fibre was also required to be greater than 266mm to come out of the bore. The only stock fibre bundle that fulfilled these requirements was one produced by Edmund Optics and had a resolution of 12μm, a length of 305mm and a diameter of 3.2mm. This was the fibre that was installed and the rest of the imaging was setup around it.

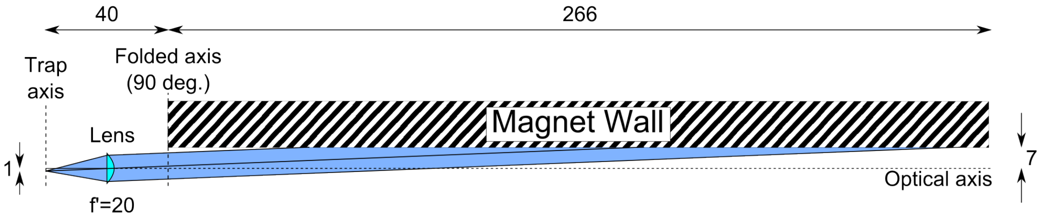

Figure 5.18: Ray trace of the marginal rays from a cloud of radius 1mm at the centre of the trap, down the bore of the magnet.

A schematic of the SPECTRAP fluorescence imaging system can be seen in Fig. 5.19. The fluorescence from the centre of the trap is collimated by the first lens (L_1) and exits the window (W) of the vacuum system. It is then folded vertically downwards by a prism (P) and another identical lens is used to form an image on the fibre bundle (F_{bundle}). This makes the magnification of this subsystem or intermediate image equal to unity, and the diameter of the fibre sets the real scale limit on the observable cloud diameter to 3.2mm. The fibre relays this image to its opposite face underneath the bore of the magnet. As the fibre has a large numerical aperture of 0.55, suitably high F number lenses have to be used thereafter. Hence, an aspheric pair (L_2) is used to reimage from the fibre. The focal length of these lenses is specifically chosen to form an image at least 40mm below the breadboard, but physically for the lenses to remain above the SPECTRAP platform allowing this entire system to stay fixed and attached, particularly during the installation procedure into the magnet which involved first lowing the platform to the floor.

With this arrangement, a CCD camera could then be installed at the correct distance below the platform where an image of the ions and the fibre bundle would be formed. Alternatively the image could be picked up by a relay system consisting of another aspheric lens pair (L_3) and a folding mirror (M_2) to image onto a photomultiplier tube (PMT). The PMT had to be placed well outside the fringe field of the magnet to operate properly, whereas this was not such a strong requirement for the CCD camera. A filter package was placed in front of both detectors in a light tight fashion to isolate the fluorescence from the stray laboratory light. This package consisted of a bandpass (Comar 435IK25) coloured glass filter, and a short pass (Comar 395GB25) dielectric filter with transmissions of 70% and 80% respectively. The fluorescence was focused through a pinhole of diameter $\sim$ 0.7mm in front of the PMT to act as a spatial filter.

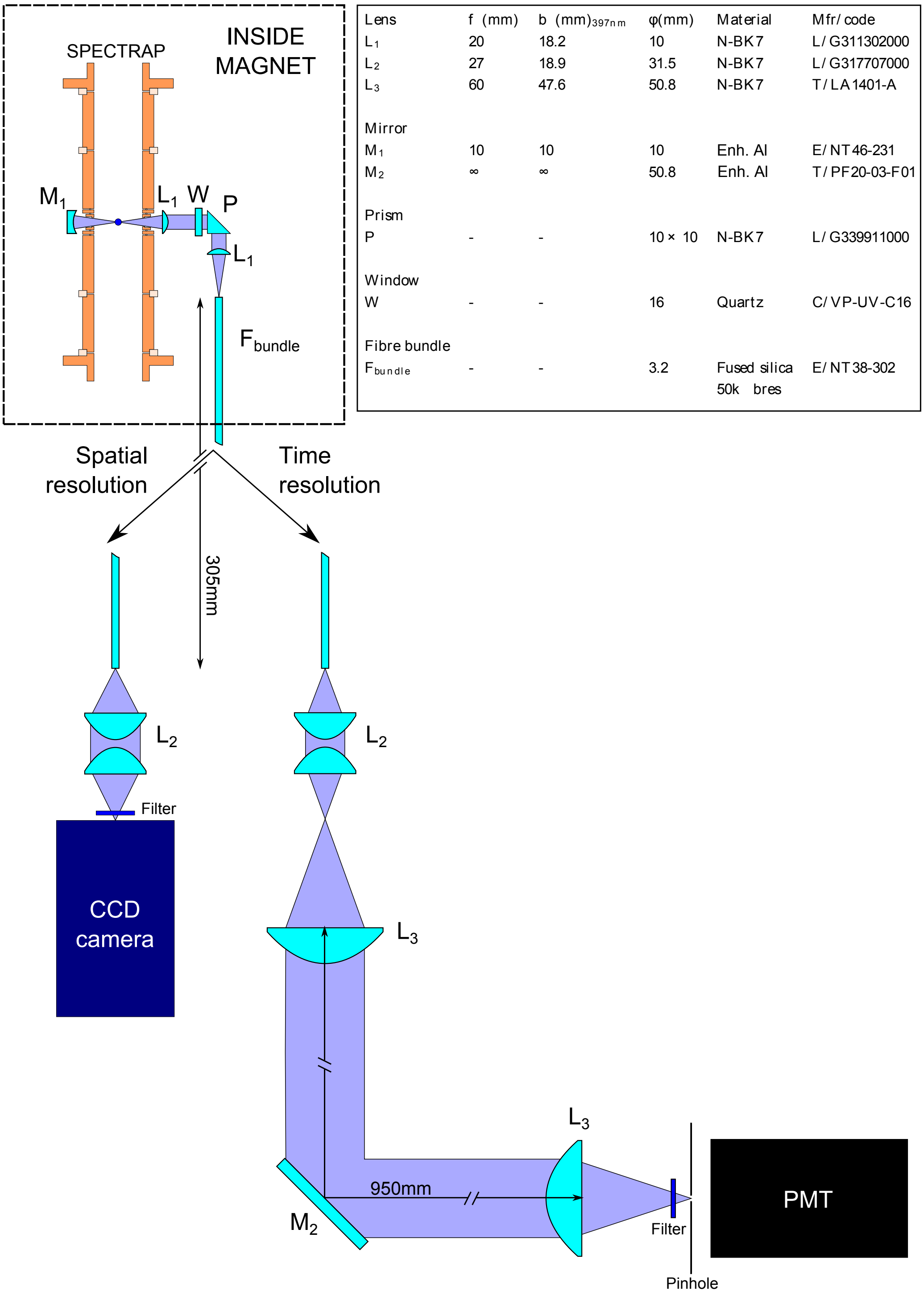

Lens	f (mm)	b (mm)$_{397nm}$	φ(mm)	Material	Mfr/ code
L_1	20	18.2	10	N-BK7	L/ G311302000
L_2	27	18.9	31.5	N-BK7	L/ G317707000
L_3	60	47.6	50.8	N-BK7	T/ LA1401-A
Mirror					
M_1	10	10	10	Enh. Al	E/ NT46-231
M_2	∞	∞	50.8	Enh. Al	T/ PF20-03-F01
Prism					
P	-	-	10 × 10	N-BK7	L/ G339911000
Window					
W	-	-	16	Quartz	C/ VP-UV-C16
Fibre bundle					
F_{bundle}	-	-	3.2	Fused silica 50k fibres	E/ NT38-302

Figure 5.19: An approximately to scale schematic of the SPECTRAP fluorescence imaging system. All lenses are used in their designed infinite conjugate setup.

The fluorescence collection efficiency for a single ion at the centre of the trap is limited by the fraction of the solid angle captured through the 4mm hole in the ring electrode before the lens L_1. This fraction is given by

$$\frac{\pi \times 2^2}{4\pi r_0^2} = 0.0090. \tag{5.3.16}$$

Due to symmetry of the system, this same fraction is incident on the mirror M_1 which has a reflectivity of 90% at 400nm. Therefore the effective fraction of fluorescence incident on L_1 is

$$0.009(1.9) = 0.0017 \tag{5.3.17}$$

The transmittance factors due to the Fresnel reflection losses from each of the optic surfaces (up to and including L_2) can be compounded together to give

$$0.96^{14} = 0.56 \tag{5.3.18}$$

The internal transmittance of quartz and N-BK7 glass at 400nm over a length of 10mm is over 99%, so the absorption and scattering losses in the lenses, prisms and windows may be neglected. The transmittance of the fibre optic bundle is substantially more complicated to effectively calculate. To this end, the manufacturer has provided an estimate of 30% internal transmittance at $\sim$ 400nm with up to an error of 5%. The large loses are predominately due to the coupling efficiency into the individual fibre cores which have a packing ratio of about 50% with respect to the lossy cladding. Combining all these factors with the filter transmissions, the fluorescence collection efficiency to the CCD camera is

$$0.0017 \times 0.56 \times 0.30 \times 0.7 \times 0.8 = 0.00016 \pm 0.00003 \text{ or } 0.016\%. \tag{5.3.19}$$

A $^{40}\mathrm{Ca}^+$ ion at most will scatter $\sim 1.7 \times 10^7$ $(\Gamma/4)$ photons per second on the $4^2S_{1/2} - 4^2P_{1/2}$ transition optimised for Doppler cooling in a Penning trap (see section 5.1), and therefore with the above collection efficiency, a maximum of $\sim$ 2700 photons per second per ion can be expected in front of the CCD camera.

5.3.7 Fluorescence Detection

Fluorescence was detected with either an intensified CCD camera (Andor DH-534-18S-03) or a PMT (Thorn-EMI 9893QB). The camera provided the spatial resolution for 2D images of the ion cloud, and the PMT gave fast time resolution for frequency scans of the blue lasers to measure the Doppler broadened $2S_{1/2} - 2P_{1/2}$ line profile i.e to determine temperature.

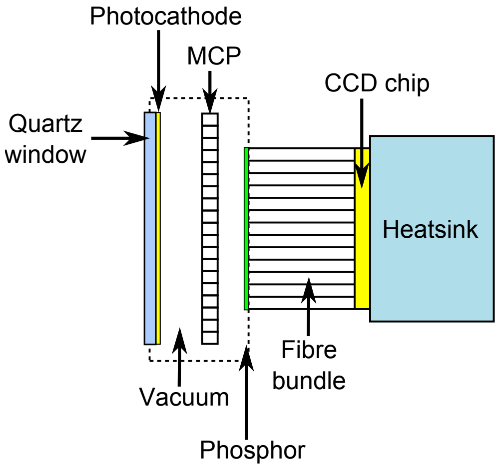

Figure 5.20: A diagram showing the main elements of the Andor iCCD camera. All components inside the dashed lines are in vacuum, and the window is UV transmissive.

The basic internal structure of the CDD camera is shown in Fig. 5.20. The camera is capable of detecting single photons and for this, a very high gain (to lower readout noise) is required. The camera converts a photon to a photoelectron (via the photocathode), which is then multiplied (via a microchannel plate or MCP) to create a more intense image (via a phosphor screen) that is fed into a fibre bundle backing onto a CCD chip. This chip has a matrix of (1024×1024) square pixels of width 13μm, and the optical resolution of the camera is 22μm. This is approximately 10 times the minimum optical resolution set by the numerical aperture of the in-vacuum trap lens. The gain on the camera can be adjusted with a setting of 0-9 which controls the voltage across the MCP. The response to the setting is non-linear and reaches a plateau at 8. The MCP or intensifier can be used as a very effective fast optical gate ($\sim$ 10ns). The camera was exclusively used on a gain setting of 8 with a typical exposure time of > 1s. From the Andor camera test data sheet, the measured actual gain (g_{CCD}) on this setting is 3780 counts per photoelectron. And with a photocathode quantum efficiency of 14%, and 96% transmission through the window at 400nm, this gives a photon detection efficiency μ_{CCD} of 13%.

For good rotating wall compression and a generally deeper and more stable Penning trap, the higher the magnetic field the better. The superconducting magnet was capable of providing up to a 2.5T magnetic field but the camera operating range was the limiting factor. The camera was positioned almost directly under the magnet bore and so was approximately along the strongest magnetic field lines of the magnetic fringe field. In this configuration, the magnetic field was found to actually increase the gain, but only up to a field of 1.85T where it dropped off sharply. A possible explanation for this could be due to electrons undergoing more collisions with the walls of the MCP (generating more electrons) as they are sent into a cyclotron motion by the magnetic field. Once the magnetic field becomes high enough, the cyclotron orbit radius could become smaller than the MCP channel radius causing the gain (and signal) to drop off sharply. For this reason, the magnetic field was limited to a conservative 1.75T, which gave an enhancement in the gain of ×2.44 with no noticeable image distortions (i.e. cross talk). Hence with an enhanced gain of 9223 counts per photoelectron, and a detection efficiency of 13%, this gives a calibration of 1240 counts per photon incident on the camera at 1.75T at 400nm.

The PMT was of the standard type with an operating voltage of 1.8kV and a quantum efficiency of 20% at 400nm. This voltage is essentially shared via a resistor chain to the various dynodes in the vacuum tube to generate an accelerating electric field to produce ever more electrons from a single photoelectron. In this way, each photon produces a current pulse, which is discriminated and converted into a TTL pulse that is counted by a multichannel scaler (MCP). It was found that the fringe fields around the magnet had a very detrimental effect on the performance of the PMT. This was the reason for the $\sim$ 1m extension in the distance to the PMT compared to the camera. Even in this configuration, several layers of encompassing μ-metal[8] shielding were required around the PMT to operate the magnet up to 1.75T. With this extension, fluorescence would only be captured from ions on-axis, but this would be sufficient to get an estimate of the temperature of the ions. Hence a calculation

---

[8] μ-metal is a nickel-iron alloy with a very high magnetic permeability which makes it very effective at channelling magnetic field lines around shielded areas.

of the fluorescence collection efficiency is not meaningful for the PMT where the effective pinhole size is not the actual cross-section imaged at the trap (due to aberrations and vignetting). The PMT was not an essential detector for this investigation of the rotating wall technique with large clouds, but was very valuable in characterising and optimising the setup. In previous experiments of Mg^+ ions in a Penning trap in the superconducting magnet, the PMT was placed axially at the top of the magnet, but this was impossible in the SPECTRAP setup due to several practical limitations.

5.3.8 Data Acquisition and Image Analysis

The PMT and MCS could be used in two detection modes. The first is just an integrator of the number of photons or counts per time bin (∼ms), and the other (with the addition of a time to amplitude converter) is a register to display a histogram of the number of photons vs the time delay between photons. The latter once Fourier transformed, can yield the frequency of oscillations in the trap, but this only works for small clouds or single ions where the modulation in the fluorescence from an ion moving in the beam is not washed out by the random phases of photons emitted by all the other ions in the trap. Hence only the former mode was useful in this investigation of the rotating wall with large ion clouds, and an example of a fluorescence trace is shown below in Fig. 5.21.

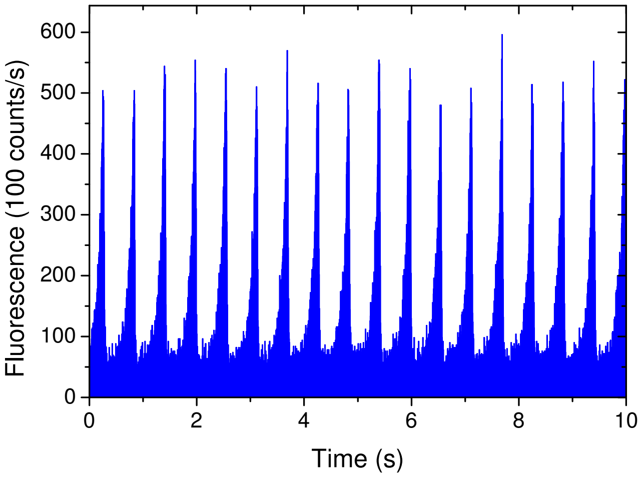

Figure 5.21: A fluorescence trace from a cloud of Ca^+ ions in the SPECTRAP ion trap as one of the Doppler cooling lasers is scanned in frequency in a saw tooth fashion over 1GHz.

The CCD camera images could be read via a frame grabber card and the software provided by the manufacturer. Pixels could be grouped together to reduce the spatial resolution, but improve the signal to noise ratio and the frequency of acquisition i.e. reduce exposure time. For a typical exposure time of 1s, the level of background laser scatter was of order 10^3counts/s/pixel with a dark count rate of 10^2counts/s/pixel. The CCD camera also saturates with of order 10^4counts per exposure per (grouped or single) pixel. Hence for grouped pixel acquisitions, this reduced the sensitivity of the images and often led to small hints of the first fluorescence signal being missed or saturation across parts of the cloud. Therefore no grouping was used in practice but instead, the (AC) noise on the captured images was effectively reduced by accumulation of images (up to 10). To reduce the read out time (1μs/pixel) and image post-processing time, only pixels around the fibre bundle were captured ($\sim [350 \times 350]$ pixels^2). Typically the exposure times were between $(0.5-3)$s, and the software allowed real time statistics to be calculated on regions of interest on the images for monitoring purposes i.e. average and standard deviation of counts per pixel.

To make measurements from the captured images post-processing was involved. This was aided by the camera software which saved the images with a record of the camera setup (e.g. exposure time) to a structured text file (.sif). This could then be uploaded into Matlab where a program was written (see Appendix E) to allow the automation of: the removal of background laser scatter; the extraction of radial and axial lengths and line profiles; calculation of integrated fluorescence; images to be formatted and plotted.

Below is a step-by-step description of how the programme performs these functions:

1) An image of (just) the background laser scatter is loaded into the array M_S[9]. The counts in a region of high scatter and what should always be an ion free region of the trap (or fibre bundle) are integrated to give the scaler b_S. An image of M_S can be seen in Fig. 5.22a where the integrated scatter area is highlighted in red.

2) The image data, now with ion fluorescence, is loaded from a sif file into the array M_I. As the camera position was constrained by the space available under the SPECTRAP platform, the x-y axis of the CCD chip was not aligned with the axis of the trap. Hence the rotated image of the ion cloud in M_I shown in Fig. 5.22b.

---

[9] The saved scatter image (or array) is already rotated so that the radial and axial axis of the trap are aligned with the horizontal and vertical axis of the image. This angle was identified by recording two successive images with a trapped ion cloud: one with fluorescence to measure the rotation; one with the infra-red repumpers blocked to stop fluorescence and display only the background laser scatter.

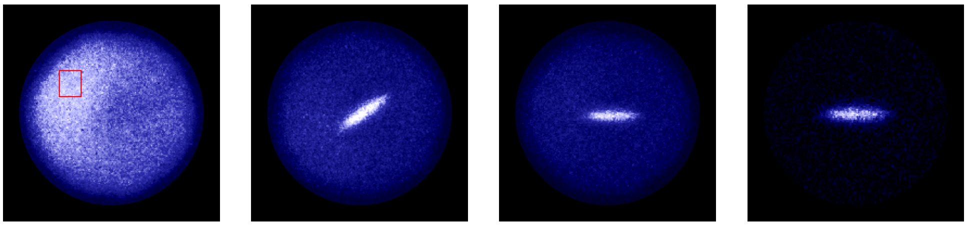

Figure 5.22: (a) An image of background laser scatter, (b) fluorescence from a cloud of ions as they would appear live from the camera, (c) a rotated image of the cloud and (d) a background scatter removed rotated image of the cloud. The full scale of each image is approximately 3.5mm.

3) M_I is rotated 37 degrees clockwise so that the radial axis of the trap becomes aligned with the x-axis of the image array (as shown in Fig. 5.22c). The orientations of both M_I and M_S should now be the same.

4) The laser scatter is then integrated in the same area of the fibre bundle in M_I as it was for M_S to give b_I. The background scatter array is then scaled by b_I/b_S and removed from the image array (visually about their estimated centres) to give a background scatter removed image M_I' where $M_I' = |M_I - (b_I/b_S)M_S|$. M_I' is then cropped about the centre to give a 220×220 pixel background scatter removed image (as shown in Fig. 5.22d) for making measurements. Scaling of the scatter image M_S is required in this way because the level of background scatter depends on laser powers at the time of acquiring the images. Therefore generally $b_I \neq b_s$.

5) The exact centre x-y coordinates of the cloud are found by finding the M_I' index values of the row (y_0) and column (x_0) with the maximum integrated counts.

6) About the centre of the cloud $M_I'(x_0, y_0)$, an x and y line profile is taken to give the lists L_r and L_z respectively. Every element of L_i (where $i = z$ or r) is an average over 3 perpendicular adjacent pixels to reduce the noise on the line profiles. Via the scaling $L_i/(\mu_{CCD} \times g_{CCD} \times t_{expo})$, a new set of line profiles L_i' are obtained with values corresponding to the fluorescence intensity (I_γ) which has units of photons/s/pixel. Each index of L_i' corresponds to a pixel and hence a physical distance of 13μm (l_{pixel}). To plot the line profiles,

a further two lists of x_r and x_z are created with the index values of the line profiles multiplied by the length of a pixel and centred at the position of the median of the integrated fluorescence along L_i'. A plot of (L_r,x_r) and (L_z,x_z) is then created for the radial and axial line profiles as shown in Fig. 5.23.

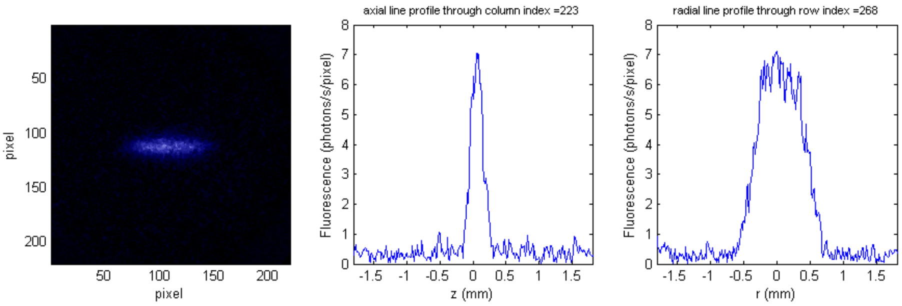

Figure 5.23: (left) An image of an ion cloud with a low aspect ratio with the corresponding plots of the axial (middle) and radial (right) line profiles from Matlab. This image is obtained from a single exposure of the camera and hence no averaging is occurring to reduce the noise fluctuations in intensity.

There are three different methods to measure the integrated fluorescence from an ion cloud on the CCD camera. These are:

(a) Integrate all the pixels inside a fixed area about the centre of the cloud.
(b) Integrate all the pixels inside the cloud.
(c) Integrate all the pixels inside the cloud and divide by the corresponding area.

From these three methods, (a) will give the poorest signal to noise because the aspect ratio of the cloud is changing as a function of rotation frequency of the ion cloud. If the cloud is larger than the area of integration, signal is thrown away, and if it is smaller, there is more scatter and increased noise. This leaves (b) and (c) which are similar except that (c) will have a stronger dependence on the ion number density by a factor of the cross sectional area of the cloud. For comparison between measurements on different ions clouds, (c) will also be independent of the cloud size. Hence method (c) was chosen for fluorescence measurements from the camera images as calculated by the Matlab programme in the last step below.

7) All pixel counts and number of pixels above 50% of the maximum counts

are integrated to give F_{FWHM} and N_{FWHM} respectively. A measure of the fluorescence intensity I_γ, is then calculated from $I_\gamma = F_{FWHM}/(N_{FWHM} \times \mu_{CCD} \times g_{CCD} \times t_{expo})$ which again has units of photons/s/pixel.

Chapter 6

Paul Trap Operation

The purpose of running the SPECTRAP as a Paul trap at Imperial College was to test various aspects of the system, leaving a smaller experimental parameter space to search through in order to see the very first fluorescence signal from ions in the Penning trap. In the Paul trap the position and overlap of the laser beams, operation of the ion source and alignment of the imaging and detectors could all be tested and optimised. This would then leave the main uncertainty in operating the Penning trap to come from setting the (six) laser wavelengths on the wavemeter which also implicitly depends on knowing the amplitude of the magnetic field at the centre of the trap.

For ion clouds, space charge effects shift the first stability region away from low q_z values [70]. Hence the most stable trap for the lowest q_z is, for $|a_z| \ll 1$, where q_z is approximately in the range $0.4 - 0.8$, as seen in Fig. 3.2. In the SPECTRAP trap, the RF potential was applied to the endcaps (V_{rf}) and the DC to the compensation and ring electrodes (i.e $-U_0$). The RF trapping voltage was produced by a function generator (HP 3325B) connected to an RF power amplifier (ENI 300L) and a home made $\approx \times 10$ step-up transformer. Co-axial cables [1] of length 2.5m had to be used to connect to the trap electrodes inside the bore of the magnet, adding a relatively large amount of capacitance (30pF) in addition to the trap itself ($\sim$ 35pF). This reduced the resonance frequency of the transformer from 2.5MHz to 0.515MHz when connected to the trap. At this lower frequency, the q_z range above could easily be accessed with V_{rf} between $(70 - 145)V$. In the Paul trap pseudo-potential

---

[1] The co-axial cables were type RG58C/U with a nominal impedance of 50Ω.

approximation [70], the trap depth scales with the frequency and amplitude of the RF potential squared, hence high frequency and high amplitudes are usually desired. In this setup, increasing the resonance frequency to 1MHz led to substantial ohmic heating of the transfer coil for the voltage required for q_z. Hence for this reason, the RF frequency of $\Omega = 2\pi \times 0.515$MHz was used in trapping throughout.

Ions were loaded into the trap with the trapping potentials applied. For the first test of the trap, the PMT detector was set up to capture fluorescence directly in front of the trap vacuum vessel outside the magnet (i.e. the PMT was closer to the trap than it would be for Penning trap operation), bypassing the fibre bundle relay system, with a large 2mm pinhole providing spatial filtering. The wavelengths of the Doppler cooling and repumping lasers were set to 396.3847nm and 866.2145nm respectively[2], with the maximum possible power going through the trap of approximately 200μW and 400μW from a single 397nm and 866nm laser respectively. A sinusoidal RF voltage at frequency $\Omega = 2\pi \times 0.515$MHz and peak amplitude of 75V was applied to the endcaps, with the compensation and ring electrodes grounded. The source was operated by heating the oven with a current $I_{ov} = 3.25$A for a period of 1 minutes. The filament was switched on for the last 10s of the oven heating period, with a current of $I_{fil} = 1.05A$ and a bias of $U_{fil} = -10$V. The fluorescence and background scatter recorded on the PMT during this loading process is shown in Fig. 6.1, where the Doppler cooling laser is linearly scanned repetitively from 1.5GHz red-detuned to approximately line centre. With the oven and filament on together for 10s, the trap detection volume reached a full capacity (or maximum density) as indicated by the saturation in fluorescence level. Since the oven and filament were run at high currents for these initial test, they outgassed heavily meaning that the ions were produced under conditions of elevated background pressure. As such, the ions were prevented from cooling to a half Doppler width less than the scan amplitude (or $\approx$ 1200K) as the pressure took a couple of hours to recover back to 10^{-9}mbar.

Having optimised all the parameters based on the fluorescence level and temperature of the ions, the trap could then be loaded with lower filament and oven currents allowing the pressure in the system to stay at the level of 10^{-9}mbar.

---

[2] These wavelengths were obtained from fluorescence measurements with a recently run (different) Paul trap with the same wavemeter.

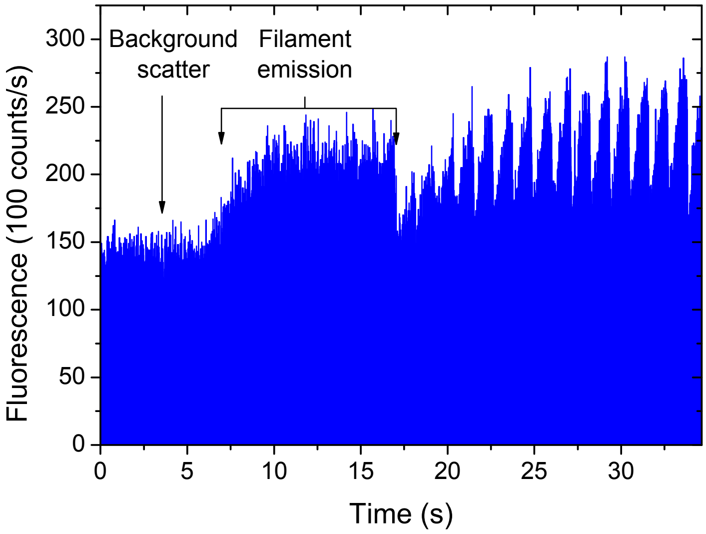

Figure 6.1: A PMT trace showing loading of ^{40}Ca^{+} ions in the Paul trap for an early unoptimised setup. The Doppler cooling laser is scanned 1.5GHz below and up to line centre in a saw-tooth like fashion. After the filament is switched off, the fluorescence increases as ions begin to cool, but the pressure in the system prevents cooling to the point where the Doppler width can be seen to be narrowing.

With laser cooling, the ion lifetime in the trap was at least several hours. Hence the trap only required loading once, unless ions were intentionally driven out by applying external driving fields. At this stage, the trap was then installed into the magnet and run as a Paul trap just before the field was ramped up. The final set of optimum parameters were: $\Omega = 2\pi \times 0.515$MHz, $V_{rf} = 85V$, $U_0 = 1$ $I_{ov} = 2.85$A, $I_{fil} = 0.95$A and $U_{fil} = -8V$. An optimised fluorescence trace for the Paul trap is shown in Fig. 6.2a. As the source was run with lower currents, the filament and oven were on together for a longer duration of 30s. The optimum laser beam position was found using the CCD camera detector. For a symmetric (trap) potential setup, the integrated fluorescence was maximised when the laser beam was at a position that produced an axially mirrored double image. This can be seen in Fig. 6.2b, which shows the fluorescence with the beam at this position. A split or double image is recorded because the electric centre of the trap, and therefore the cloud, is offset from the imaging axis resulting in a separation between the locations of the direct image from the lens, and the indirect retro-reflected image of reduced intensity ($\approx 40\%$) from the mirror. This misalignment is examined in detail in section 8.1.5, but here, just by visual inspection of Fig. 6.2b is it clear that the imaging axis is approximately a beam waist lower than the centre of the trap. By applying an asymmetric potential with 3V on the upper compensation electrode and 2.5V on the lower, the cloud could be overlapped with the optical axis. With this optimised setup, the fluorescence shown in Fig. 6.2a and Fig. 6.2c was recorded on the PMT and CCD camera respectively, with the trap inside the bore of the magnet, and with the PMT pinhole size reduced to 0.7mm. For the CCD camera images in Fig. 6.2, the laser frequency is fixed and optimised to give maximum fluorescence. From the PMT trace, the half width of the Doppler broadened line profile is now clearly much narrower than the 1.5GHz frequency scan of the cooling laser. The resolution of this scan is not adequate to obtain an accurate estimate of the half width of the Doppler broadened transition, but a conservative estimate gives 200MHz, implying an upper bound to the temperature of the ion cloud of about 20K (ignoring the contribution from the natural linewidth and power broadening of the transition). This value is most likely limited by the micromotion which is made stronger by (DC) offsetting the cloud from the centre of the AC trapping fields in order to optimise the imaging.

An estimate of the trap efficiency or C_2 coefficient was obtained by measuring the axial secular motion frequency. This was done by applying and scanning the frequency of an excitation voltage to the upper compensation electrode. With $V_{rf} = 82$V (i.e $q_z = 0.352$) and $U_0 = 1$V (i.e $a_z = -0.011$), a reduction in fluorescence was observed at (75.0 ± 0.5)kHz with a 1mV drive amplitude, indicating heating via resonance with the secular motion $\omega_{0,z}$. With a suitable approximation to β found in [36], accurate to approximately 3% in the range $|a_z|$,$q_z < 0.5$, this implies $C_2 = 0.507 \pm 0.004$[3] which agrees within errors with the analytical solution (0.52), but strongly disagrees with the numerical SIMION solution (0.59) expected for this electrode setup (i.e. grouped compensation and ring electrodes) from section 5.3.1. The latter should have provided a more accurate solution from the detailed SPECTRAP model. If the computer simulations are trusted, then this discrepancy can only be explained through a combination of the following factors:

- the characteristic trap dimension d_0 is smaller than expected.
- a lower RF voltage was arriving at the trap through the coaxial trans-

---

[3] Including the uncertainty in the approximation of β used.

mission lines.

- a larger positive DC voltage was on the ring and compensations electrodes with respect to the endcaps.
- anharomicities were larger than expected in the extent of the cloud shifting the axial frequency.

This measurement of the trap efficiency provided an initial calibration for the effective trap voltage (C_2U_0) and motional frequencies to be expected in the Penning trap.

In conclusion, Paul trap operation of the SPECTRAP ion trap was extremely useful in optimising the system. It allowed the trap to be run outside the magnet and the position of the laser beams and detection system to be optimised without the physical constraints of the magnet. During the installation procedure of the trap into the magnet, there was potential for the imaging optics to be misaligned if contact was made with the walls of the bore. Operating the Paul trap before the magnetic field was raised gave great confidence in the final setup before the magnetic field was ramped up and the lasers were adjusted for Penning trap operation. This stepped (cautious) approach was necessary because no fluorescence had been observed from the previous and only other calcium ion superconducting magnet trap in the group.

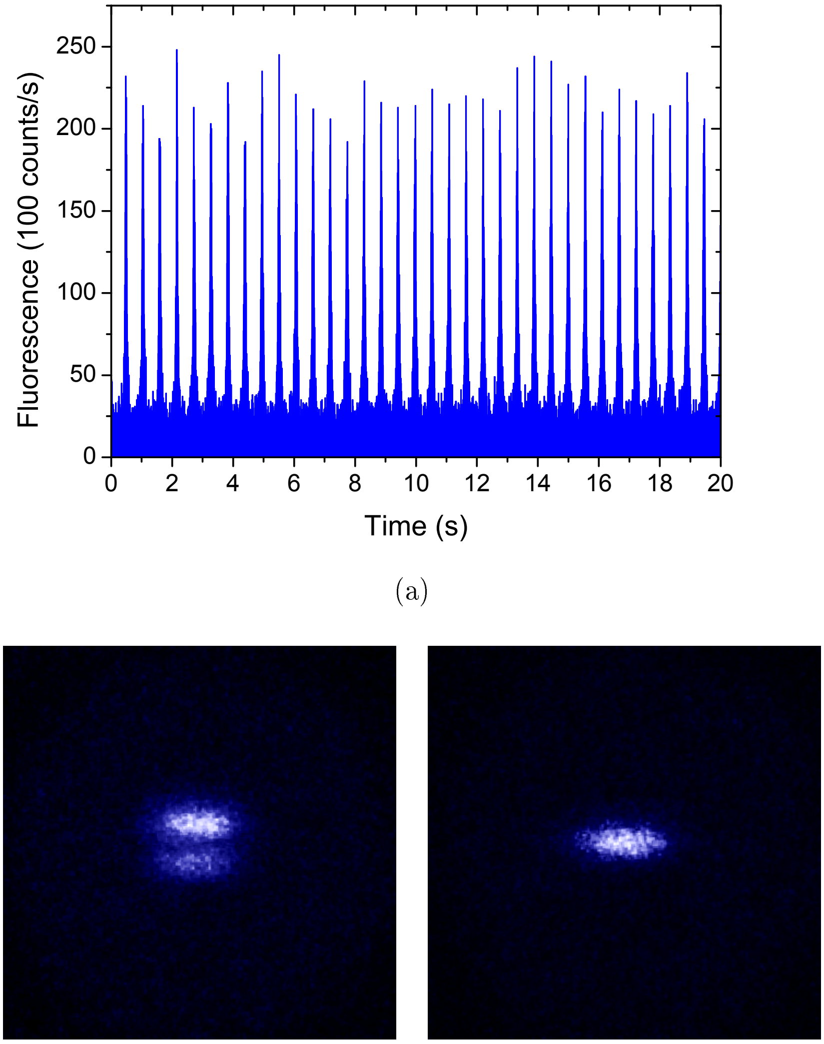

(a)

(b)

(c)

Figure 6.2: Optimised fluorescence measurements from an ion cloud in the SPECTRAP ion trap operating as a Paul trap. (a) shows a PMT trace where one of the Doppler cooling lasers is scanned repetitively from 1.5GHz below resonance to line centre. (b) and (c) show CCD camera images where the laser beam is overlapped with the cloud. In (a), the variation in peak height is due to under-sampling. In (b), there is a double image of the same ion cloud as the imaging axis is lower than the electrostatic centre of the trap. And in (c), the cloud is offset from the trap centre to overlap with the confocal imaging axis.

Chapter 7

Penning Trap Operation

To load ions into the SPECTRAP operating as a Penning trap, the electric potential landscape of the trap first had to be considered. In general, as ions born near the centre of a trap have the smallest magnetron motion amplitude, they are more likely to stay confined until cooling is optimised. The kinetic energy of the electrons used for ionising the atoms at the centre of the SPECTRAP trap could be controlled by the potential difference between the filament and the potential found at the centre of the trap. SIMION simulations of the axial potential have shown that the centre of the trap floats at approximately $0.4U_0$ above the grouped ring and compensation electrode potentials, and that the potential U_0 is shielded from the filament by the grounded trap support flange and capture electrode. Therefore this sets a requirement for the filament to be at a negative potential to accelerate electrons towards the trap. Hence in order to load ions into a deep and stable trap, the filament bias was set to a low voltage of $U_{fil} = -1$V, and the trap potential to a relatively high voltage of $U_0 = 18$V. This would give the electrons an energy of about 8eV for ionisation at the centre of trap[1].

The current in the superconducting magnet was set to 72A giving a trapping magnetic field of 1.76T estimated from the calibration in section 5.3.4. The wavelengths of the lasers were set to those shown in table 7.1, and the typical power of each Doppler cooling and repumper laser going through the trap was about 50μW and 200μW respectively. The source was run with the same

---

[1] The electron energy is kept below 12eV at the centre of the trap to avoid ionising and contaminating the loaded trap with a greater fraction of Ca^{2+}.

Laser	Wavelength(nm)
B1	396.8386
B2	396.8556
IR1	866.1614
IR2	866.1694
IR3	866.2593
IR4	866.2675

Table 7.1: Optimised wavelengths for laser cooling a cloud of ions in the SPECTRAP operating as a Penning trap.

currents as before, except the oven and filament were on together for a longer duration of 1 minute to fill the trap to capacity (as observed on the CCD camera by the maximum radial extent of the cloud after optimised laser cooling). In contrast to the Paul trap operation, fluorescence was not observed immediately after a load. This is because the radial laser beam position (along with the Doppler cooling laser frequencies) had to be manually scanned-in towards the trap centre to cool the initially large (average) magnetron motion (amplitude) of a cloud in as short a time frame as possible to try and prevent ions from being lost. Hence it took of the order of 30s to see fluorescence after a load. It should be noted that the first Penning trap fluorescence signal was detected using the CCD camera and not the PMT. This might seem counter-intuitive because the camera suffered more from the effects of shot noise due to the lower number of photons arriving per pixel than that for the PMT through the larger pinhole detection area. However per pixel, the camera was still more sensitive to fluorescence above the level of background laser scatter than the PMT i.e. higher SNR. Fluorescence on the camera also only appeared in a specific area (a stripe) across the centre of the image where the laser beam was overlapped with the cloud. By looking for this fluorescence pattern in the images, it was easier to differentiate between changes in fluorescence and changes in background laser scatter. With this method, calcium ions were first identified in the Penning trap. With electrostatic fields, it was relatively easy to adjust the endcap potentials independently to alter the axial position of the cloud. It was found that with U_0 on the lower endcap, and $1.05U_0$ on the upper endcap, the cloud overlapped with the imaging axis. Once the trap was loaded, the potentials could be adjusted. The maximum trap potential above which ions appeared to be lost was around 270V, where $2\omega_m \approx \omega_z$. This is the lowest order (in ω_m) trap instability, with increasing higher orders at lower trap frequencies. Misalignments of the electric and magnetic fields could potentially cause higher order instabilities to appear at lower trap frequencies. Hence as no other instabilities were observed at lower trap voltages, this suggests that the trapping fields were well aligned [37].

7.1 Characterising the Trap Parameters

For an investigation of the rotating wall technique, the motional frequencies of the ions must be known. This required a measurement of the amplitude of the magnetic field and the effective trap potential or efficiency. This was accomplished by driving the motional frequencies (via excitations to an endcap or two adjacent ring electrode segments) and looking for heating resonances or minima in fluorescence intensity at a fixed trap potential of $U_0 = 104\text{V}$. The motional frequencies were identified with the resonances at

$$\begin{aligned} \omega_m &= 2\pi(61.28 \pm 0.03)\text{kHz} \\ \omega_z &= 2\pi(275.0 \pm 0.5)\text{kHz} \\ \omega_{c'} &= 2\pi(607.5 \pm 0.5)\text{kHz} \end{aligned}$$

which via the cyclotron frequency from the invariance theorem (equation 3.2.11), gives a magnetic field of $B = (1.745 \pm 0.002)\text{T}$ independent of the physical trap parameters. This agrees with the value expected from the axial Hall probe calibration of the magnetic field, and with the frequency separation between the two π Doppler cooling transitions[2]. From the axial frequency, the efficiency of the trap is calculated to be $C_2 = 0.541 \pm 0.002$. This disagrees as before with the numerical SIMION solution $C_2 = 0.59$, but by a smaller fraction. If this discrepancy is solely attributed to a smaller characteristic trap dimension $d_0 = \frac{1}{2}\sqrt{r_0^2 + 2z_0^2}$, then with the accuracy of machining limiting the error in r_0 to 0.01mm, this would require a change in $2z_0$ from a nominal 11.8mm to 10.4mm. The size of $2z_0$ is the distance between the endcap electrodes which is set by the sapphire ball bearing spacers. These sapphire balls are much harder than the softer copper electrodes and compression could have occurred

---

[2] The error in estimating the magnetic field from the wavelengths of the Doppler cooling lasers is an order of magnitude less precise compared to that obtained from driving ion motional frequencies in the trap due to the limited precision of the wavemeter. For the experiments at GSI where the value of the magnetic field must be known to a high precision to account for the Zeeman shift in the transitions between $m_F = 0$ states in a test of QED, the detection of motional frequencies via the image current will provide more precise trap frequencies rather than the optical detection method used in London.

here under the influence of the clamping pressure that holds the trap together. Hence a reduction in $2z_0$ of up to 1.4mm is plausible. For the Paul trap measurement of C_2, $2z_0$ would have to be reduced to 9.4mm which would result in zero gaps between electrodes, and this would have been electrically and visually detected. Therefore such a large change in d_0 could not have been the sole factor affecting the larger discrepancy in the Paul trap measurement in section 6. The trapping (constant) parameters of $B = 1.75$T and $C_2 = 0.54$ are henceforth used to calculate all trap motional frequencies and plasma modes.

Throughout the operation of SPECTRAP in London, the compensation electrodes were not used to orthogonalise the trap. The quality of the harmonicity of the trap potential was not an important parameter for efficient laser cooling to localise ions to the centre of the trap. In addition, with the axial asymmetric potential applied to overlap the cloud with the imaging axis, further (odd) anharmonicities would be introduced complicating the investigation.

7.2 Ion Temperature and Laser Drift

For ions moving randomly in a cloud in a Paul trap, one can estimate the temperature of ions by assuming that the width of the peaks shown in Fig. 6.2a, is simply given by half the Doppler broadening (since the laser is only scanned over half the lineshape), assuming other broadening mechanisms are negligible. The situation is more complicated for ions in a Penning trap and such an analysis would give a significant overestimate of the ion temperature.

The physical restrictions around the superconducting magnet limited the laser cooling and fluorescence detection to the radial plane as illustrated in Fig. 7.1. In section 3.3, it was shown that the equilibrium state of a cold non-neutral plasma with $\lambda_D \ll$ plasma dimensions, is a rigid uniform rotation at frequency ω_r about the magnetic field axis. Assuming this condition is reached in the experiments, this implies that along the direction of the laser beam, using the co-ordinate system in Fig. 7.1, the velocity component will be $v.\underline{\hat{y}} = \omega_r.x$ i.e. a constant for a given value of x. Therefore along and in the direction of an infinitesimally thin line in the radial plane, the transition (for all the ions) in the laboratory frame (ν_0') will have an identical Doppler shift. However, for ions across the width of the laser beam, the transition will be blue Doppler shifted by increasing amounts with increasing distance away from the centre of the trap. Hence the laser frequency must also be blue detuned from the frequency of the transition for an ion at rest in the laboratory frame in order to interact strongly with the ions. This Doppler shift scales according to

$$\nu_0'(\omega_r, x) = \nu_0 \left(1 + \frac{\omega_r.x}{c}\right) \tag{7.2.1}$$

and in order to have a net effect of cooling the (modified) cyclotron motion for all the ions across the beam width, with a symmetric laser beam intensity profile, the laser detuning must remain below that of the frequency of the transition for the ions along the centre of the laser beam. If the laser beam is directed as shown in Fig. 7.1, the maximum Doppler shift in scanning the laser frequency up to the position of maximum fluorescence will be that across the half width of the laser beam given by

$$\Delta\nu_0' = \frac{1}{2}\frac{\omega_r \times \omega_{FWHM}^{laser}}{\hat{\lambda}} \tag{7.2.2}$$

where $\hat{\lambda}$ is the wavelength of the transition at the centre of the beam. As a result of this Doppler shift, the laser detuning is measured relative to the position of maximum fluorescence, which is not the frequency of the transition for an ion at rest in the laboratory frame.

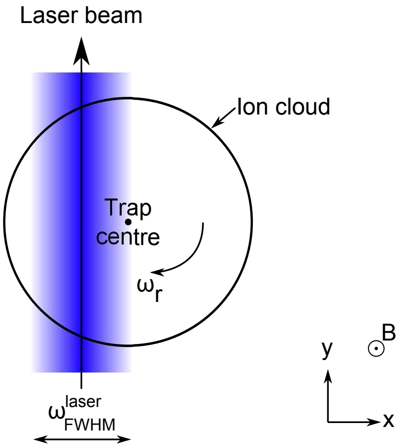

Figure 7.1: A diagram showing the laser cooling scheme in the experiment. The origin of the co-ordinate system is the centre of the cloud at the centre of the trap.

In the present setup, the FWHM diameter of the laser beam ω_{FWHM}^{laser} is $\sim$ 0.15mm. If we assume for a trap potential of $U_0 = 104$V, the laser drives the cloud to $\omega_r \approx 2\pi \times 90$kHz (measured in section 8.1.8), the half Doppler shift expected across the beam is $\sim$ 110MHz. The fluorescence was measured in the trap at this potential as a function of one of the Doppler cooling laser frequencies, whilst the other was at a fixed frequency and optimised for maximum fluorescence. The laser was repetitively scanned over 1GHz up to the position of maximum fluorescence and the corresponding averaged scan trace is shown in Fig. 7.2. This plot yields a relative red-detuned fluorescence half width of approximately 130MHz. To obtain an estimate of the temperature of the ions, the expected Doppler shift of 110MHz is subtracted giving a HWHM Doppler broadened linewidth of approximately 20MHz (assuming no power broadening). Using an approximation to the width of the Vogit profile [71], the natural linewidth is removed leaving a HWHM Doppler broadening of approximately 13MHz and a corresponding temperature of $\sim$ 0.1K. This temperature is higher than the Doppler cooling limit of $\sim$ 1mK. This is most likely a result of the inefficient purely radial cooling scheme. However, as the main purpose of laser cooling in this experiment was to increase ion lifetime in the trap and to provide fluorescence to image an ion cloud, cooling to the absolute minimum in temperature was not necessary.

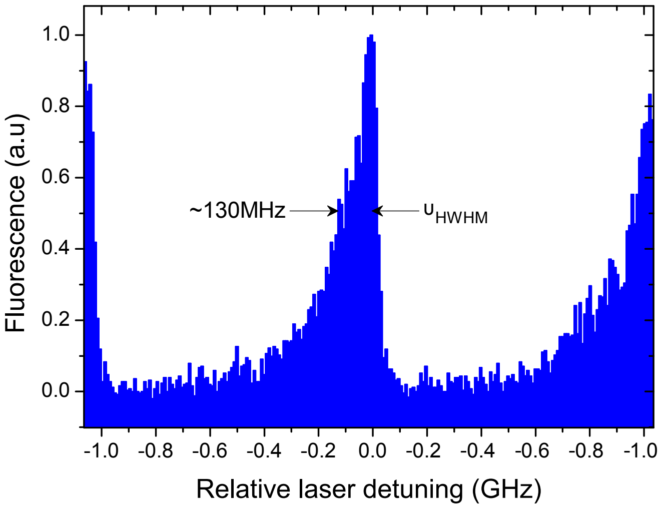

Figure 7.2: An averaged PMT trace as one of the Doppler cooling lasers is scanned from 1GHz below and up to the frequency of maximum fluorescence, while the other is fixed and optimised for maximum fluorescence. The major contribution to the width of this fluorescence profile is the Doppler shift across the width of the laser beam.

This Doppler shift is also a function of the cloud rotation frequency. Under the action of the rotating wall at frequencies of $\omega_{rot} \approx \omega_m$ and $\omega_{rot} = \omega_c/2$, with a drive amplitude above 0.5V and a trap potential of $U_0 = 104$V, in steady-state the fluorescence as a function of the frequency of one of the Doppler cooling lasers was again measured, but this time using the CCD camera[3]. These results are presented in Fig. 7.3. Assuming the cloud rotation frequency is equal to the rotating wall frequency, the expected Doppler shift in the fluorescence profiles is $\sim$ 90MHz and $\sim$ 400MHz for the low (Fig. 7.3a) and high (Fig. 7.3b) rotating wall frequency respectively. In both cases, accounting for the natural linewidth, the width of the fluorescence peak is $100-200$MHz larger than these estimates. This is not surprising considering the heating effects of the rotating wall are not well known. However, the scaling is in the right direction and hence lends support to this theory.

---

[3] The justification for the amplitude applied and the assumption of rigid rotation at frequency $\omega \approx \omega_r$ in the measurements in Fig. 7.3 are made in the section 8.

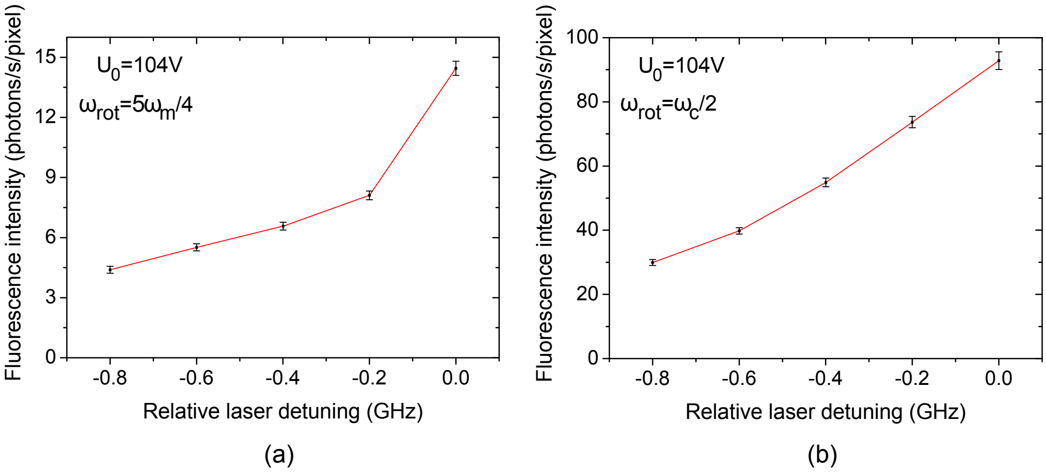

Figure 7.3: Measured fluorescence intensity from the CCD camera images of an ion cloud driven by the rotating wall at (a) $\omega_{rot} = 5\omega_m/4$ and (b) $\omega_{rot} = \omega_c/2$ with a drive amplitude of 0.9V and 1.5V respectively, as a function of the laser relative red-detuning of one of the Doppler cooling lasers in steady-state i.e. a manual discrete slow frequency scan. The frequency of the other 397nm laser is fixed at that which gives maximum fluorescence. It can be seen that the width of the fluorescence peak is broader in (b) than in (a). For a description of the errors in fluorescence intensity, see Appendix C.

The requirement to lock the laser frequencies has been overlooked so far. However, as the above results show, the fluorescence is not a strong function of the relative red-detuning of the Doppler cooling lasers compared to the natural linewidth. The origin of this has been shown to be due to the spatial width of the laser beam which was constrained to be 150μm.

The effects of temporal drift of the laser frequencies are now examined. Considering the 866nm lasers first, due to the lower branching ratio into the $D_{3/2}$ states and the power broadening of the transitions, the repumpers could drift by up to approximately 500MHz without any noticeable effects on the fluorescence. Via the scanning cavity transmission peaks, it was observed that this level of drift took at least an hour to manifest itself, and this could easily be manually corrected to avoid any reduction in fluorescence. The 397nm Doppler cooling lasers each have a typical drift of $\approx$ 200MHz per hour after allowing a few hours for stabilisation (estimated by Koo [72] by manually correcting for the laser drift via the piezo to maintain the level of fluorescence for a cloud of ions in a different Penning trap in the group). Each Doppler cooling laser was also relatively red-detuned about 200MHz to keep it on the cooling side of the fluorescence profile. If the effective fluorescence rate when both Doppler cooling lasers are relatively red-detuned by 200MHz is approximated by that of one detuned by 400MHz, then at most, at the low end of the rotating wall frequency spectrum, Fig. 7.3a indicates that up to a 20% change in fluorescence rate is expected per 397nm laser over a drift of ≈ 200MHz. Therefore, accounting for the drift rate from both 397nm lasers, up to a 40% change in the fluorecence rate is expected per hour. As most measurement sets in this thesis were conducted in less than 5 minutes, only about up to a 3% change in fluorescence rate was expected[4]. As this was on the level of the shot noise on the captured CCD camera images, the laser drift was within acceptable limits without stabilisation. For the very limited number of measurements that took of order 5 minutes, the average fluorescence across the ion clouds was monitored in real time using the Andor camera software for a fixed set of trapping parameters. Then if the fluorescence at this operating point could not be reproduced during or at the end of a measurement set within the level of the (averaged) shot noise, the lasers had drifted beyond acceptable limits. In this case the process of re-optimising the frequencies was repeated and the results retaken. Hence locking of the laser frequencies, to for example temperature stabilised reference cavities, was not strictly required or employed. For a single ion, this argument would not hold and locking would be necessary.

---

[4] The effects of laser drift on the fluorescence rate has been shown to become even smaller the higher the rotation frequency of the cloud i.e. during a rotating wall frequency scan up to the Brillouin limit.

Chapter 8

Rotating Wall

Images of ^{40}Ca$^+$ ions were recorded on the CCD camera for various rotating wall and trapping parameters in the SPECTRAP ion trap at Imperial College London[1]. The aim of this investigation was to show compression of ion clouds and manipulation of their aspect ratio with the application of the rotating wall drive in order to understand how best to set the trapping and rotating wall parameters to achieve maximum fluorescence intensity in the SPECTRAP experiment at GSI. One of the open questions prior to this work was whether or not it would be necessary to sweep the rotating wall drive frequency up from low values to $\omega_c/2$ to ensure that the cloud would lock on to the drive. Due to time constraints, and the requirement to keep the camera at the same focal position for all the recorded images for comparison purposes, the PMT could only be attached for the single measurement in section 7.2 during Penning trap operation. A discussion of the errors associated with all of the figures present in this chapter is given in Appendix C. A systematic investigation of the rotating wall technique now follows.

8.1 Rotating Wall Results and Discussion

8.1.1 Drive Amplitude Scan

The first parameter that needed to be investigated and optimised was the amplitude of the rotating wall drive V_{rot} that was required to give the max-

---

[1] The results in this section have been submitted for publication [1], and a few paragraphs in the following discussion have been reproduced (in part) from this source. This reproduced text was solely written by the author of this thesis, as a co-author of the paper itself.

imum fluorescence and perceived compression. Fig. 8.1 shows the effects of the rotating wall drive amplitude on the fluorescence intensity of an ion cloud in steady-state at fixed a drive frequency of $\omega_{rot} = \omega_c/2$ and trap potential $U_0 = 104$V. Fig. 8.1a and b show that the fluorescence increases linearly with small drive amplitudes and saturates above approximately $V_{rot} = 300$mV, where the fluorescence is a factor of 2 higher than the purely laser driven cloud. Above this saturation amplitude, the frequencies of the rotating wall and ion cloud must be in a low-slip regime. Only in such a regime, would any further increase in amplitude of the rotating wall apply no additional torque to the ion cloud, and no subsequent increases in fluorescence. As the fluorescence remains constant within errors up to a relatively large amplitude of $V_{rot} = 2$V, the application of the drive must have a minimal effect on the temperature of the cloud in the presence of laser cooling. If substantial heating was occurring due to the applied rotating wall drive (i.e. a Doppler broadening greater than the Doppler shift across the laser beam), once maximum compression was reached, the fluorescence would be expected to fall at larger amplitudes. This is not observed within this amplitude scan range. To ensure a strongly driven ion cloud in a low-slip regime with the rotating wall, and hence precise control of the rotation frequency of the ion cloud, an amplitude of $V_{rot} = 1.5$V was used in all subsequent experiments unless otherwise stated. From Fig. 8.1, a hypothesis can be made that the Brillouin density was reached.

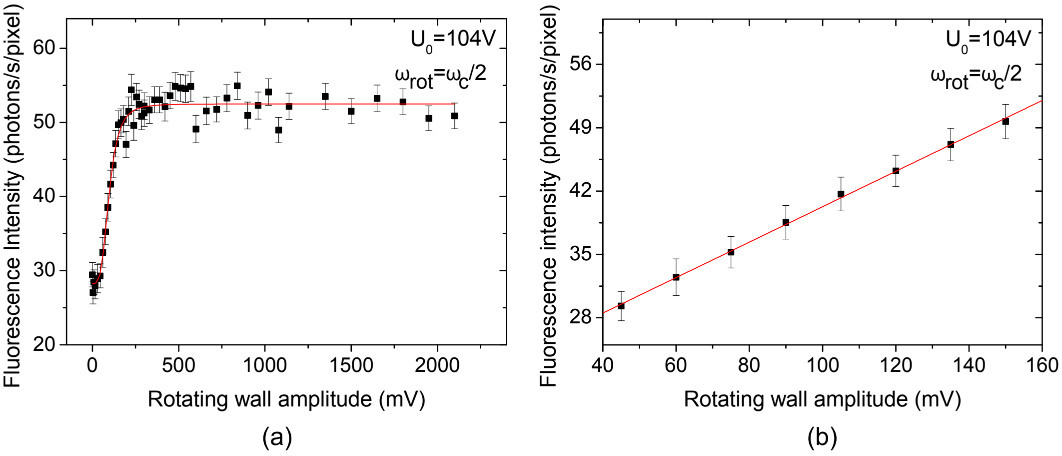

Figure 8.1: (a) graph showing how the fluorescence intensity of an ion cloud varies as a function of the rotating wall drive amplitude and (b) shows the linear increase at small amplitudes. The rotating wall frequency and trap potential are fixed at $\omega_c/2$ and 104V respectively. The relatively large amount of noise reflects the use of only single exposures of the camera in constituting each image for each data point i.e. $N_{accum} = 1$.

8.1.2 Dynamic Response

Fig. 8.1 involved taking measurements typically several seconds apart, where a steady-state or equilibrium was assumed to have been reached. However, now with a fixed amplitude, this assumption could be tested and the time to reach steady-state quantified. Fig. 8.2a shows the results of the variation in fluorescence intensity of an ion cloud as the frequency of the rotating wall drive was suddenly switched at time $t = 5$s from 80kHz to 335kHz or $\sim \omega_c/8$ to $\omega_c/2$ at $U_0 = 104$V. The fluorescence reaches its maximum and saturation level within a single CCD exposure of 0.5s, and shows that steady-state or a low-slip regime must have been reached within this short time. Hence no additional time was required between changing the rotating wall parameters and recording data. At the two extremes in frequency, the images in Fig. 8.2b and radial line-profiles in Fig. 8.2c were recorded and show compression of the ion cloud as expected. For various loading times longer than the usual 1 minute, the subsequent laser cooled clouds at a rotating wall frequency of $\omega_c/2$ were always approximately of the same radial extent of about 0.3mm. This seems to suggest some limit to the cloud size was reached. This may be caused by a resonance limiting the number density at the lower trap loading voltage.

Alternatively it may be that the trap was full to the walls of the ring electrode as the ion cloud would have the shape of an oblate pancake like spheroid at $\omega_r \approx \omega_m$ before cooling.

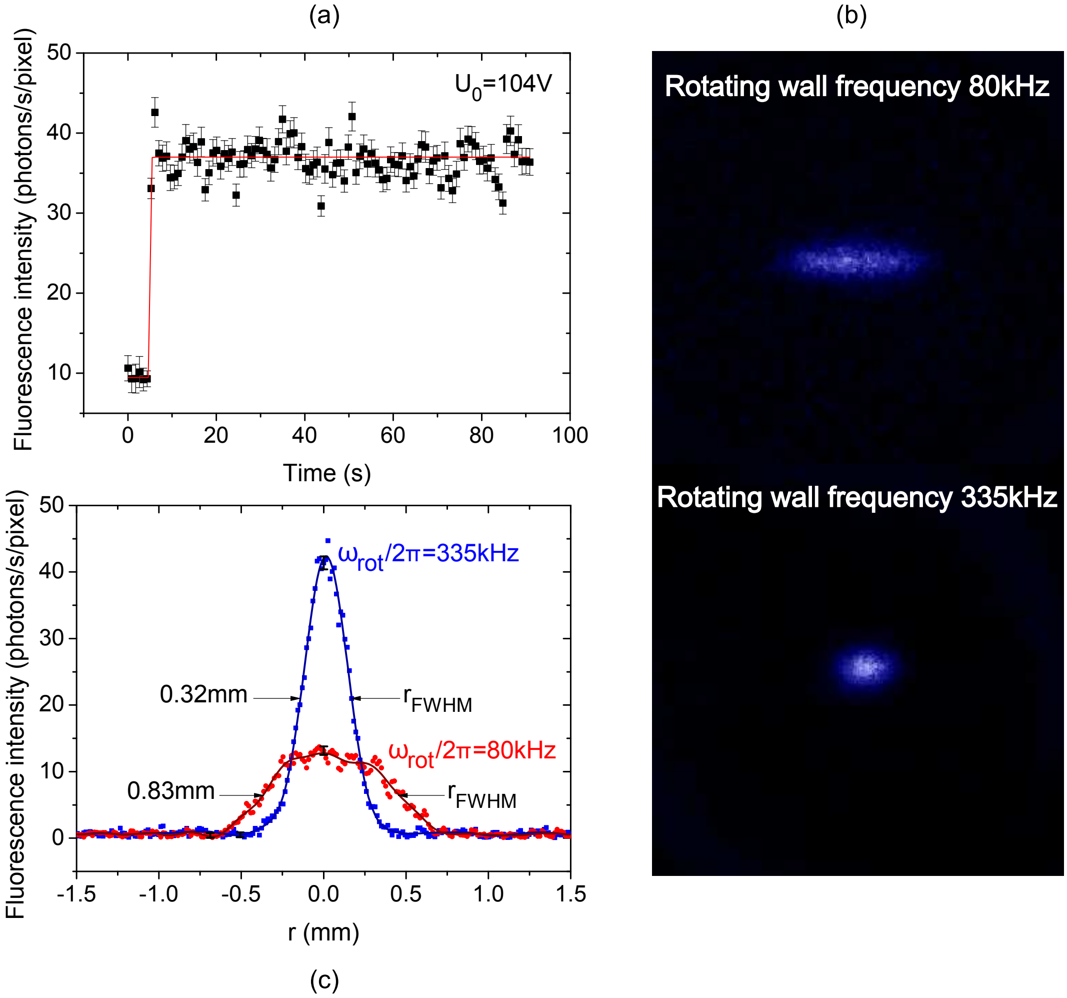

Figure 8.2: (a) graph showing how the fluorescence intensity from an ion cloud varies dynamically in time as the frequency of the rotating wall drive is abruptly changed from 80kHz to 335kHz at time t≈ 5s. (b) and (c) show the corresponding images and radial line-profiles for the cloud at the two extremes in rotating wall frequency. The line of best fit in (a) is created just to guide the eye.

8.1.3 Laser Detuning

The effects of laser detuning (or slow frequency drift) on the fluorescence intensity of these ion clouds has already been discussed in section 7.2. However, as aspect ratio measurements were required, the effects of laser detuning (or cooling) on the ion cloud size had to be investigated. The results are shown in Fig 8.3, which compares the radial line-profiles of the two extreme cases (i) both Doppler cooling lasers optimised for maximum fluorescence, and (ii) one cooling laser is 0.8GHz red-detuned from this frequency at fixed trap and rotating wall parameters (i.e $U_0 = 104\text{V}$ and $\omega_{rot} = \omega_c/2$). Case (ii) mimics a situation in which one of the lasers has drifted significantly away from the optimum detuning. The line-profiles are normalised for comparison. The results show within errors, that the FWHM of the radial fluorescence intensity distributions agree for the two cases indicating that the heating rate of the cloud under the influence of the rotating wall, from the rotating wall itself and other sources such as collisional with residual gas atoms, is small compared to the laser cooling rate even at large detuning. This also lends support to the hypothesis made from other observations that the rotating wall drive does not significantly heat the ion cloud. Hence aspect ratio measurements or comparisons of line-profiles did not need to be carried out with specific Doppler cooling laser frequencies or level of cooling.

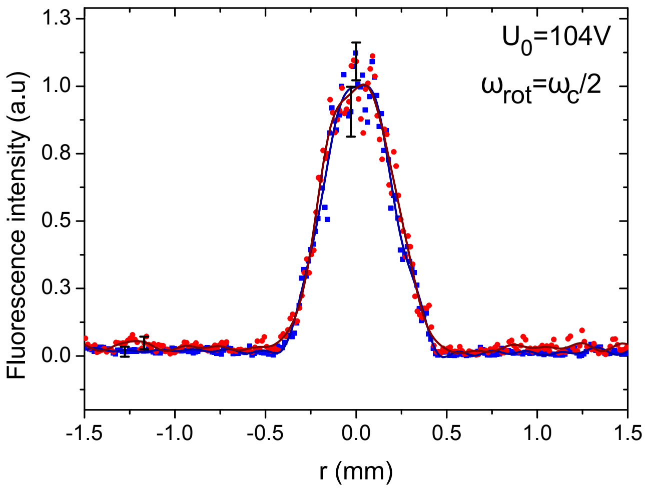

Figure 8.3: A graph comparing the normalised radial line-profiles of a cloud under the action of the rotating wall at frequency $\omega_{rot} = \omega_c/2$ and $U_0 = 104\text{V}$ for (blue) optimised laser cooling and (red) with one Doppler cooling laser red-detuned 0.8GHz from this optimum frequency.

8.1.4 Drive Frequency Scan

From the results so far, it has been shown that a frequency scan of the rotating wall drive (ω_{rot}) over the rotation frequency of the cloud (ω_r) is not necessary to reach a dissimilar cloud rotation frequency in steady-state in a short time interval of < 1s. However such a frequency scan from $\sim \omega_m$ to $\omega_c/2$ provides a further insight into where maximum compression is actually reached. The results in Fig 8.4a, b and c show how the fluorescence intensity of an ion cloud varies as a function of ω_{rot} in steady-state i.e. in a discrete manual frequency scan. Depending on the choice of trapping parameters, resonances at the axial and $\omega_{21}^{(1)}$ plasma mode frequencies occur within the scan range. These resonances occur due to a residual misalignment of the trap axis with respect to the magnetic field axis. This misalignment is estimated to be up to 0.1 degrees from the geometry of the trap and its mounting inside the magnet bore.

The $\omega_{21}^{(1)}$ plasma mode is driven by an asymmetric azimuthal potential (see section 3.3.2). Under the action of the rotating wall frequency scan, the plasma modes will be driven when the rotation frequency of the cloud matches that of the plasma mode i.e. $\omega_r = \omega_{21}^{(1)}$. Under this condition, static field errors in the laboratory frame are approximately resonant with the plasma mode and heating occurs. Although static field errors in principle cannot change the total energy of the ensemble of ions, potential energy can be converted to thermal energy by an expansion of the cloud [44].

The axial motion is driven because in the presence of misaligned trapping fields, the rotating wall has a oscillating dipole component along the axial direction. This can be further exaggerated if the ring electrode segments are not all exactly axially aligned. Hence this motion is seen to be strongly driven.

Fig. 8.4a shows that for a low trap potential of 10V, both the axial and the (2,1) plasma resonance (which is very broad and asymmetrical) are observed. If the rotating wall frequency is set to the axial or plasma mode resonance, and the amplitude of the rotating wall is ramped up, the fluorescence simply decreases. Hence these heating effects cannot be avoided with a smaller drive amplitude than the nominal 1.5V. If the rotating wall frequency were ramped from $\sim \omega_m$ up to $\omega_c/2$, these heating resonances would have a significant transient effect on the cloud. A feature of the (2,1) resonance is a sharp onset followed by a slower recovery in fluorescence as the scan continues upwards in frequency. The higher the trap potential, the faster this recovery. At $U_0 = 104$V, the axial and (2,1) resonances are degenerate as Fig. 8.4b shows. Above this potential, no evidence of driving the (2,1) modes is found. If the trap potential is sufficiently high, as in Fig. 8.4c where $U_0 = 180$V, both resonances are shifted above $\omega_c/2$ and can be completely avoided. Both Fig. 8.4b and c show that the fluorescence steadily increases and reaches a maximum around $\omega_{rot} = \omega_c/2$ consistent with reaching the Brillouin limit.

A summary of the observed heating resonances is shown in Fig. 8.4d for a range of trap frequencies. The trap efficiency and magnetic field measured in section 7.1 were used to plot the theoretical curves, and good agreement is found between the axial heating resonances measured directly using the rotating wall, and those expected from theoretical predictions from the trap voltages using $C_2 = 0.54$. The error bars reflect the effective width of the resonances by indicating the -3dB range in fluorescence intensity from the onset of heating. The (2,1) heating resonances are highly asymmetrical, and their widths decrease with increasing axial frequency. This is expected from theoretical considerations as Fig. 3.8a shows how the (2,1) plasma modes vary with ω_r for a low trap potential ($U_0 = 10$V). Resonance occurs when $\omega_{21}^{(1)} = \omega_r \approx \omega_{rot}$, and in this case $\omega_{21}^{(1)}$ remains close to ω_r all the way to the Brillouin limit. The higher the potential, the higher the rate of separation of $\omega_{21}^{(1)}$ from ω_r just above the resonance. Hence the width of the measured $\omega_{21}^{(1)}$ heating response decreases with increasing trap potential. For a trap potential greater than 40V, the resonances cannot be separated, and above 104V or an axial frequency of 275kHz where they cross, no further evidence is found of driving $\omega_{21}^{(1)}$. This implies, at least in this experimental setup, that the plasma modes are only driven if their rate of separation from ω_r (and hence ω_{rot}) from resonance is low, and this is only true for the $\omega_{21}^{(1)}$ mode. Hence a plot such as Fig. 8.4d shows which frequencies need to be avoided if the drive frequency is swept from a small value up to $\omega_c/2$.

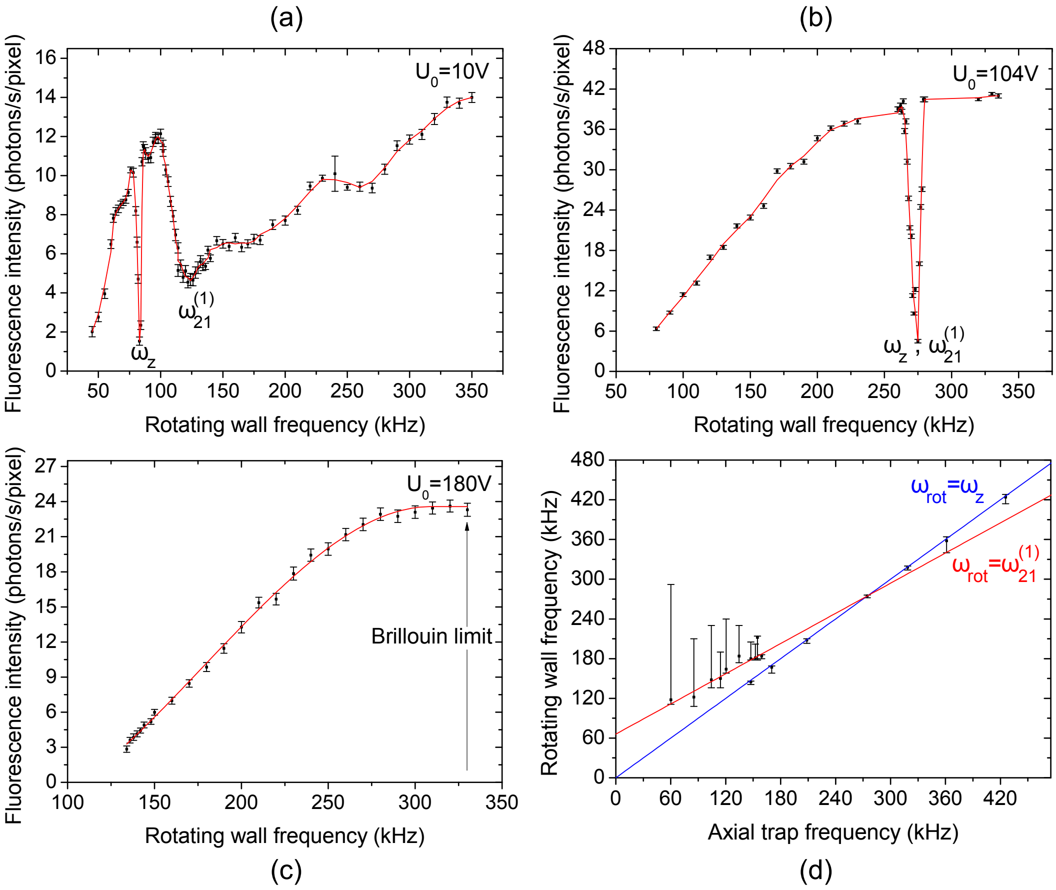

Figure 8.4: Graphs (a), (b) and (c) show how the fluorescence intensity of an ion cloud varies as a function of the rotating wall drive frequency at trap voltages of 10V, 104V and 180V respectively. In (a) the ω_z resonance is sharp but the $\omega_{21}^{(1)}$ resonance is very broad and asymmetrical with its effect persisting to large values of ω_{rot}. An overview of all the heating resonances measured at various trap axial frequencies is shown in (d). The error bars in (d) reflect the -3dB width in fluorescence intensity of the heating response, and the straight lines are the theoretical predictions assuming $C_2 = 0.54$ and $\omega_r = \omega_{rot}$.

8.1.5 Imaging Analysis

To make measurements of the aspect ratio of ion clouds, it is necessary to understand the peculiarities of the imaging system. Although the spherical mirror provided the ability to align the imaging system before seeing fluorescence from ions, if the foci of the mirror and lens were not exactly at the same location in the trap, the direct and retro-reflected images could never be made to precisely overlap. This would lead to incorrect aspect ratio measurements.

To separate out the direct and retro-reflected fluorescence, the trap potential was lowered to 5V and the rotating wall frequency was set to $\omega_c/2$ (as illustrated in Appendix D). This produced a prolate spheroidal cloud along the trap axis. With an axially extended cloud, a CCD image was recorded with the laser beam vertically offset to separate out the fluorescence, as shown in Fig. 8.5a (upper frame). The fluorescence image looks circular because the Gaussian laser beam waist only interacts with a small radial slice of the pencil shaped cloud. An axial line-profile through the centre of the direct image of the cloud is shown in Fig 8.5b. The ratio between the two peak fluorescence intensities gives a measure of the mirror reflectivity of approximately 45%. This is much lower than the manufacturer's specification of $> 90\%$ at 400nm. This discrepancy is too large to be accountable to vignetting, and therefore must be due to a damaged mirror coating which may have resulted from the high temperature bake-out processes. With hindsight, and further information from the manufacturer, the bakeout temperature (110°C) was higher than the recommended maximum temperature for the mirror (50°C).

From Fig. 8.5b, the FWHM of the two fluorescence distributions (z_{FWHM}) agree within errors, indicating that the foci of the lens and mirror are in the same plane. This measured width of about 0.2mm is larger than the corresponding 0.15mm width of the laser beam theoretically expected at the centre of the trap. Assuming the density of the prolate cloud is fairly flat across the width of the laser beam, this apparent broadening could be due to several factors, namely spherical aberration, defocus and saturation of the transition near the waist where $I > 2I_{sat}$ is expected for the laser powers used. The alignment of the mirror and lens axis can be tested by comparing the axial and radial line-profiles of the direct but separated image with that of the overlapped image shown in Fig. 8.5a (lower frame). From Fig. 8.5c and Fig. 8.5d, the width of the overlapped and direct fluorescence distributions agree within errors and shows that the mirror and lens were well aligned i.e. there is negligible tilt between the lens and mirror. If the fluorescence from the lens and that reflected from the mirror did not overlap well due to poor alignment, the width of the overlapped fluorescence distributions would be broader than that due to the fluorescence only from the lens.

This analysis shows that the imaging setup was sufficiently well aligned to measure the aspect ratios of ion clouds. Even though the system likely suffered from spherical aberrations, its effects are uniform across the image and hence should not affect the aspect ratio. Defocus however would affect the width of the cloud as a function of its size. However, if required, this could be removed by post-processing the images with a deconvolution algorithm. As the Rayleigh range of the Doppler cooling lasers is around 250mm about the centre of the trap, the radial laser beam intensity can be taken as a constant across the typical ion cloud dimension of 0.3mm. Hence the radial fluorescence intensity distribution is dependent only on the characteristics of the cloud.

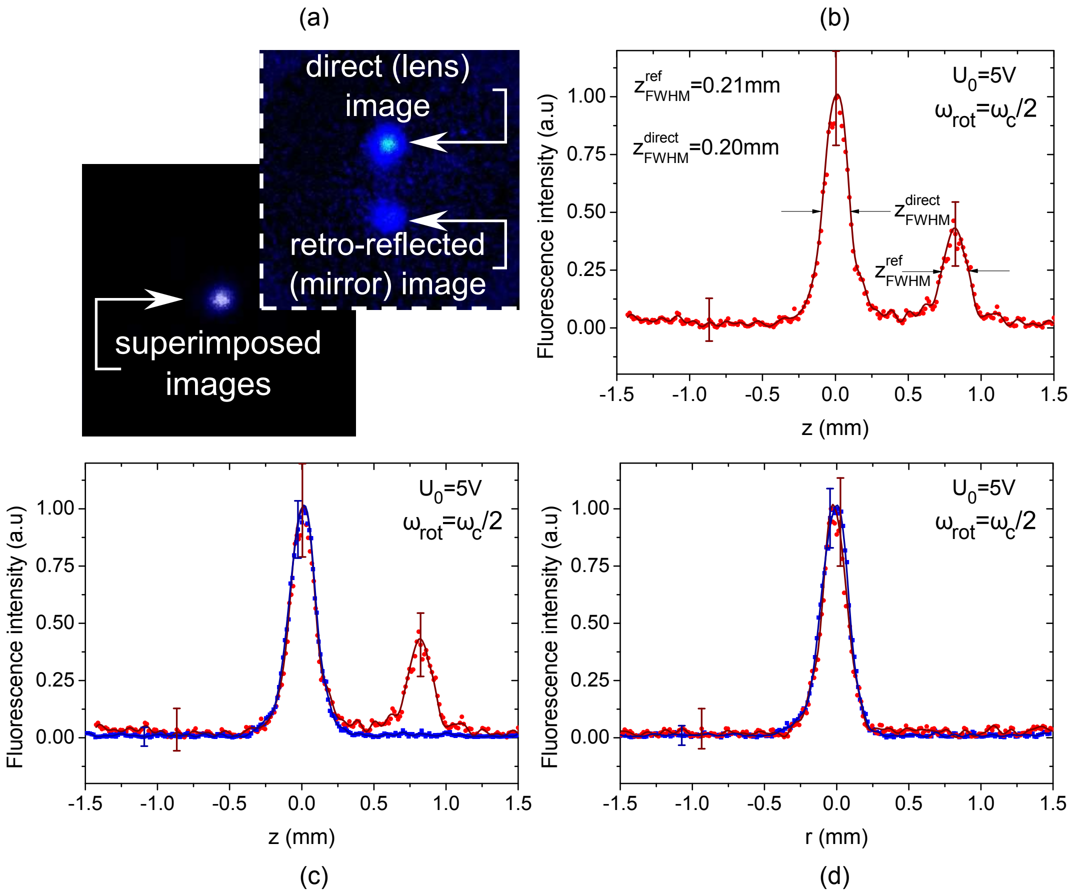

Figure 8.5: (a) shows two images recorded from the camera where (lower frame) the ion cloud and laser beam are centred on the imaging axis, and (upper frame) where the laser beam is vertically offset above this position. For comparison between the direct and retro-reflected images of the cloud, an axial line-profile of the latter image is provided in (b). For analysis of the optical alignment between the mirror and lens, superimposed axial and radial line-profiles of the direct but separated (red data points and line) and the fully overlapped (blue data points and line) imaging setups are shown in (c) and (d) respectively. These line-profiles are all taken through the centre of the same ion cloud in the two images in (a) under the operating parameters $U_0 = 5V$ and $\omega_{rot} = \omega_c/2$ i.e. an axially narrow pencil shaped cloud.

8.1.6 Aspect Ratio

The aspect ratio of an ion cloud in a Penning trap depends on the trapping parameters (B, ω_z) and the cloud rotation frequency (ω_r). To maximise the fluorescence collection from spherical optics, a near spherical dense cloud at the centre of the trap is desired. Maximum density is obtained at the Brillouin limit where $\omega_r = \omega_c/2$. Hence with a fixed magnetic field and trap efficiency of $B = 1.75$T and $C_2 = 0.54$ respectively, this defines a specific voltage of $U_0 = 104$V to obtain a spherical cloud with an aspect ratio equal to one.

As the present setup was restricted to a radially directed laser beam, this required the beam to be axially scanned in position, and images to be recorded at the extremes of an ion cloud[2]. By maintaining the spatial position of the captured images, the axial extent of the cloud could then be determined by superimposing these images and measuring the relative distance between the edges of the cloud. Fig. 8.6a and b shows this composite axial profile and radial line-profile respectively, of an ion cloud under these operating parameters. The axial extent of the cloud is measured between the outer half maxima of the direct (lens) fluorescence profiles and is estimated to be $z_{FWHM} = 0.38 \pm 0.02$mm. Likewise, the radial extent of the cloud is estimated from the FWHM of the overlapped radial profile giving $r_{FWHM} = 0.37 \pm 0.01$mm. This gives an aspect ratio of $\alpha = 1.02 \pm 0.06$. Hence the cloud is determined to be (within errors) spherical and implies the Brillouin limit was reached as theoretically expected. At this operating point, assuming the number density is $\approx 2 \times 10^5 \text{mm}^{-3}$ (n_B) and the temperature of the cloud is around 0.1K (see section 7.2), $\lambda_D \approx 2\mu$m and $\Gamma_{Coul} \approx 16$. Since $\lambda_D \ll$ cloud dimensions, the criteria for a rigid cloud rotation frequency is fulfilled. The value of Γ_{Coul} indicates that the plasma is strongly correlated but not a crystal. This is likely due to the lack of axial cooling.

If the parameters at this operating point where $U_0 = 104$V and $\omega_r = \omega_c/2$ are denoted by a subscript B, the ratio between the radii of the same ion cloud can be shown to be given by

$$\frac{r(\omega, U_0)}{r_B} = \sqrt[3]{\frac{n_B \alpha_B}{n(\omega)\alpha(\omega, U_0)}} \tag{8.1.1}$$

which gives a more convenient relation to test how the shape of the cloud varies with the cloud rotation frequency and trap potential. Fig. 8.7a shows how the cloud radius in units of r_B varies with the rotating wall frequency at fixed $U_0 = 104$V. The radii from these images are measured directly from

---

[2] The cloud is expected to have a flat density profile with a sharp edge assuming the Debye length is much smaller than the cloud dimensions. Hence the size of the cloud can be determined with the laser beam at the extremities in position.

the distance between the FWHM of the radial fluorescence intensity distributions without any smoothing or fitting functions applied. The cloud is oblate about the Brillouin limit at this trap potential, and a section of the scan between 215kHz and 320kHz is avoided due to heating resonances. The data points show a general agreement with theory where symmetry is expected about $\omega_r = \omega_c/2$. Fig. 8.7b shows how the trap potential influences the cloud radius at a fixed rotating wall frequency of $\omega_{rot} = \omega_c/2$. Above $U_0 = 104$V, the cloud is oblate and again good agreement is found with theory. However below this voltage, heating resonances influence the measurements and the results show greater scatter about the theoretical prediction.

The fact that the measured radius of the cloud matches the theoretical expectations for different values of the rotating wall frequency and trap voltage, lends support to the hypothesis that the ion cloud was in a strongly driven low-slip regime with the rotating wall drive i.e. $\omega_r \approx \omega_{rot}$. With a typical ion cloud radius of 0.15mm at the Brillouin density of $n_B \approx 2 \times 10^5\text{mm}^{-3}$, this implies ≈ 3000 ions were trapped.

A comparison can be made between the theoretical and detected fluorescence rates by using the inferred number density. The measured fluorescence intensity represents the average fluorescence per pixel per second over the FWHM region of the ion cloud. With an optical magnification of one and ignoring aberrations, each pixel on the CCD chip collects fluorescence from an effective cross-sectional area[3] of l_{pixel}^2 and a volume of $l_{pixel}^2 \times \delta x$ at the centre of the trap, where δx is the width of the laser beam that induces fluorescence. Only a fraction of the full width of the laser beam induces fluorescence because of the Doppler shift of the ions in the radial plane (see section 7.2). Assuming fluorescence is only induced if ions have the correct velocity for the transition to be Doppler shifted within a half Doppler broadened natural linewidth of approximately 20MHz from the laser detuning[4], $\delta x = 0.008$mm which is much less than the 0.15mm FWHM waist of the laser beam. Hence the effective number

---

[3] The use of an optical fibre bundle to relay an image of an ion cloud outside the bore of the magnet, and an MCP inside the CCD camera, sets the minimum optical resolution to approximately 24μm or a 2×2pixel area. Therefore a single pixel does not represent a real imaged area across the trap. However the average fluorescence intensity per pixel is effectively identical whether calculated from a group of 2×2pixels or a single pixel alone.

[4] Using the Doppler broadening estimated in section 7.2, and assuming the linewidth of the laser is negligible in comparison.

of ions fluorescing per pixel is $n_B \times l_{pixel}^2 \times \delta x \approx 0.3$. At saturation intensity, the average photon scattering rate per ion is $\Gamma/8 = 1.7 \times 10^7$ photons per second. Therefore with a 0.007% fluorescence collection efficiency to the CCD camera corrected for the reduced mirror reflectivity, the expected fluorescence intensity is ≈ 350 photons/s/pixel. With the lasers optimised for maximum fluorescence at the Brillouin limit, Fig. 7.3b shows that the measured fluorescence intensity is ≈ 100 photons/s/pixel. This measurement agrees within an order of magnitude which is all that can be expected given the number of assumptions made.

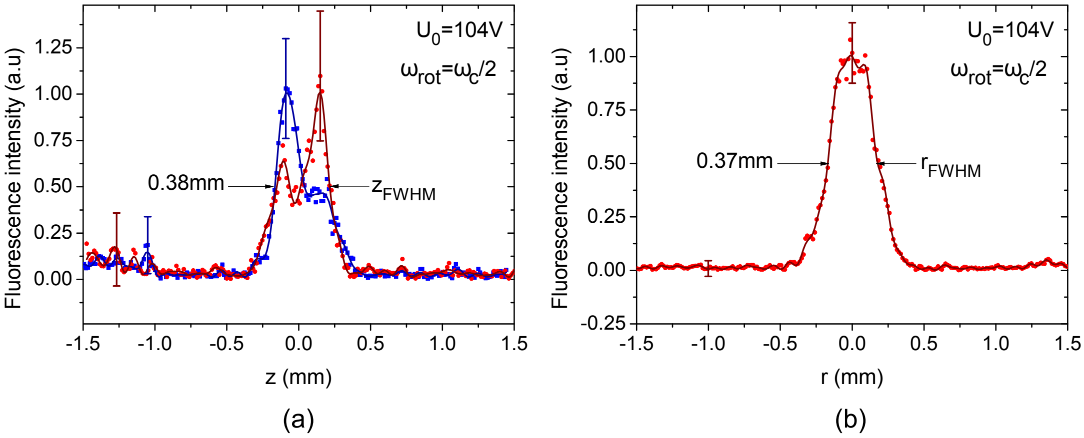

Figure 8.6: (a) superimposed axial line-profiles of an ion cloud with the laser beam at the axial extremes of the cloud and (b) the corresponding radial line-profile of the cloud with a centred laser beam when $U_0 = 104$V and $\omega_{rot} = \omega_c/2$. In (a) the fluorescence from the lens and mirror are separated out as the laser beam is not directed along the confocal imaging axis.

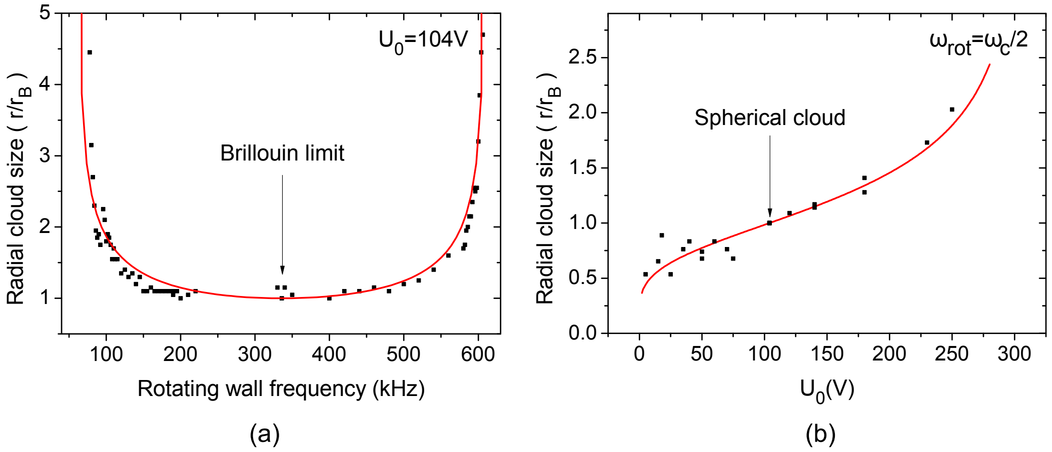

Figure 8.7: (a) data points showing the measured cloud radius in units r_B (the radius at $\omega_{rot} = \omega_c/2$) as a function of the rotation wall frequency at $U_0 = 104$V, and (b) this radius measured as a function of the trapping potential at fixed $\omega_{rot} = \omega_c/2$. The red lines indicate the theoretical expectations assuming $\omega_r = \omega_{rot}$ and $C_2 = 0.54$.

8.1.7 Sense of Rotation

The rotating wall drive electronics unit had four outputs 1, 2, 3 and 4 incrementally out of phase by $\pi/2$ (see section 3.3.1). When connected to the segmented ring electrode in a clockwise fashion when viewed from above, this formed the sequence (1-2-3-4) for the configuration of the rotating wall technique. However there were several other possible permutations of connections to the ring electrode. Of greatest interest was the (4-3-2-1) configuration which formed a rotating wall in the opposite sense of rotation to an ion's magnetron motion. Fig. 8.8 shows how the fluorescence intensity of an ion cloud varies as a function of the rotating wall drive amplitude for three difference rotating wall configurations at $U_0 = 104$V and $\omega_{rot} = \omega_c/2$. In the positive sense of rotation (1-2-3-4), the cloud is compressed to the Brillouin limit and the fluorescence intensity saturates at its maximum value. In the negative sense of rotation (4-3-2-1), the fluorescence remains flat at the level of the laser driven cloud because the frequencies of the drive and cloud are so far removed from each other. Even in this strongly driven regime, the cloud rotation frequency is seen not to couple to the drive in the negative sense of rotation. The (1-2-4-3) configuration can be thought of as a combination of positive and negative senses of rotation. Hence it is termed an inter-mixture, and accordingly the fluorescence intensity increases but saturates at a level lower then the maximum. The only configuration of voltages applied to the ring segments that is predicted to give no compression is (4-3-2-1). The null result therefore allows an independent check that the electrodes have been connected and labeled correctly without having to break the vacuum.

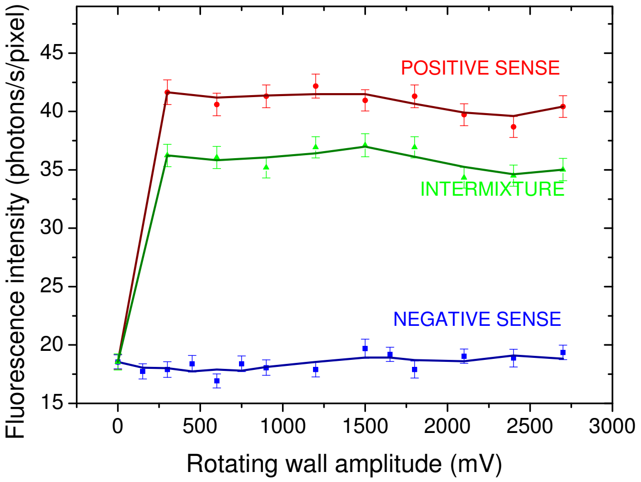

Figure 8.8: A graph showing how the fluorescence from an ion cloud varies as the rotating wall drive amplitude is scanned for three different configurations of the rotating wall drive with respect to the segmented ring electrode for a fixed drive frequency of $\omega_c/2$.

8.1.8 Plasma Mode Probe

The ability to apply the rotating wall drive in the negative sense of rotation without driving compression, gives access to the $\omega_{21}^{(2)}$ and $\omega_{21}^{(3)}$ modes allowing a more direct determination of the actual (unperturbed) laser driven cloud rotation frequency. In this mode of operation, the rotating azimuthally asymmetric electric field of the rotating wall provides the mechanism to drive the plasma modes, as opposed to the static field errors in the positive sense of rotation. If the rotating wall drive is scanned over $\omega_{21}^{(2)}$ or $\omega_{21}^{(3)}$, either mode frequency can be used to infer the cloud rotation frequency through the theoretical framework in section 3.3.2. As it is of interest to determine the cloud rotation frequency, the relation of the plasma modes to the rotation frequency of the cloud in the laboratory frame of reference is used. From rotating wall compression frequency scans, the cloud rotation frequency is expected to be around 100kHz in the absence of the rotating wall. The greatest sensitivity at this rotation frequency is given by the $\omega_{21}^{(2)}$ mode at a low trap potential which changes rapidly with the cloud rotation frequency, as shown in Fig. 8.9.

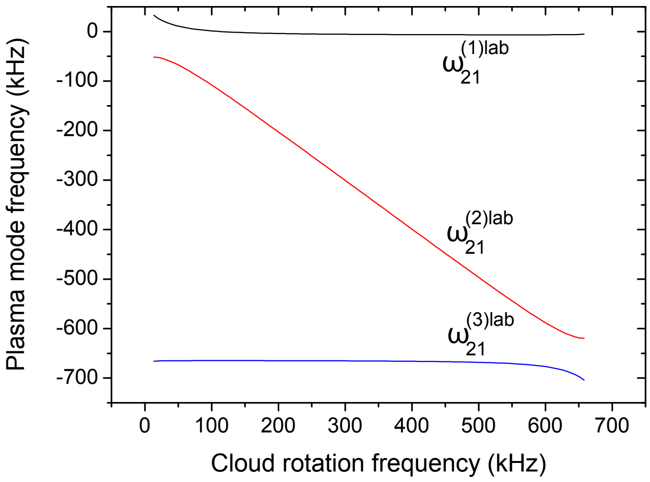

Figure 8.9: Calculated laboratory frame (2,1) plasma mode frequencies for an axial frequency of 60kHz (i.e. $U_0 = 5\text{V}$ with $C_2 = 0.54$).

Fig. 8.10a shows the results of a rotating wall scan in the negative sense of rotation for a trap potential of 5V. Only a single heating response is observed at 103kHz in scanning across the range 80kHz to 335kHz. Using Fig. 8.9, a cloud rotation frequency of 96kHz can be inferred and a rotating wall amplitude scan in the positive sense of rotation at this frequency can be performed to test this hypothesis. The Fig. 8.10b shows that at 96kHz, the fluorescence intensity is unaffected by the application of the rotating wall drive, and confirms the drive is locked on to the cloud rotation frequency as expected.

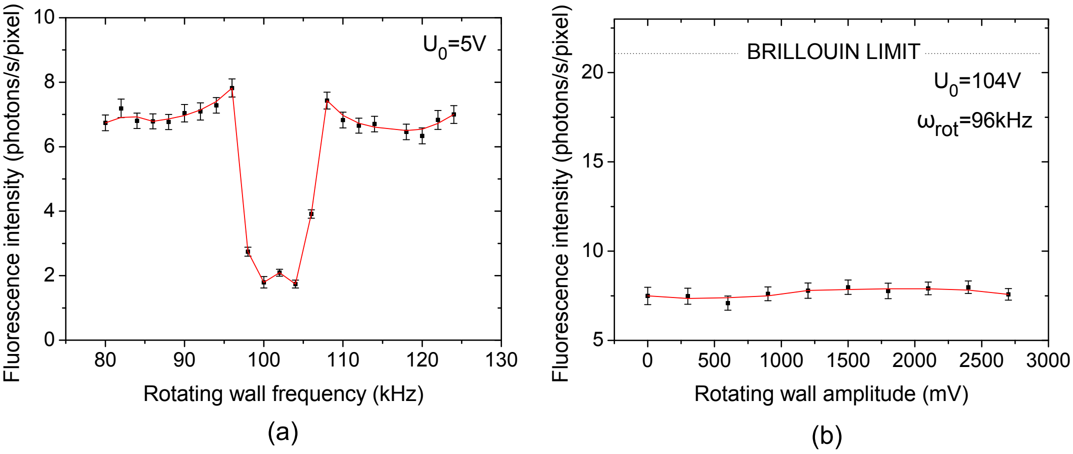

Figure 8.10: (a) graph showing how the fluorescence intensity varies as the rotating wall frequency is scanned in the negative sense of rotation over the suspected $\omega_{21}^{(2)}$ plasma mode resonance. (b) graph showing the variation in fluorescence as the rotating wall amplitude is scanned at the suspected laser driven cloud rotation frequency of 96kHz in the positive sense of rotation. For comparison, the maximum level of fluorescence at the Brillouin limit is shown. At 96kHz, the rotating wall drive does not affect the cloud since it is already rotating at this frequency.

8.1.9 Conclusion

A systematic investigation of the rotating wall technique has been carried out on a cloud of laser cooled $^{40}\mathrm{Ca}^{+}$ ions in the SPECTRAP ion trap. It was found that a drive amplitude above $V_{rot} = 0.3\mathrm{V}$ was sufficient to reach a low-slip steady-state equilibrium within a time of $< 1\mathrm{s}$ for a rotation frequency in the range $\omega_m < \omega_{rot} < \omega_c'$. On scanning the frequency up to the Brillouin limit, heating resonances were observed at ω_z and $\omega_{21}^{(1)}$. With careful choice of trapping parameters, such resonances are shown to be avoided. Measurements of the aspect ratio at a drive frequency of $\omega_{rot} = \omega_c/2$ have confirmed that the Brillouin density limit was reached. The manipulation of the radial extent of the cloud as a function of the drive frequency and trap potential has been shown to agree well with the theoretical expectations across the complete frequency range above, demonstrating the level of control obtained.

The application of the rotating wall in the negative sense of rotation is shown not to couple to the rigid rotation of the cloud. The azimuthal perturbation is henceforth used to drive the $\omega_{21}^{(2)}$ mode which is used to infer the laser driven cloud rotation frequency. When the phases of the rotating wall are applied incorrectly to the ring electrode, the resulting admixture of positive and negative senses of rotation is shown to give only partial compression.

Such a systematic investigation of the rotating wall technique for ions is not available in the published literature. A similar study does exist for an electron plasma [73], but the frequency range of the drive in such cases is limited to well below the Brillouin limit due to the much higher cyclotron frequencies involved (i.e. as $\omega_c = 2\pi \times 28\text{GHz/T}$). The experiments by O'Neil [42] on a cloud of up to 10^9 Mg^+ ions found that the torque applied to the cloud was only non-zero when the rotating wall frequency was within approximately 1% of ω_r/ω_c. This range was observed to become even narrower the higher the temperature of the ions. Hence this suggests that the rotating wall frequency would have to be scanned over the cloud rotation frequency to impart control and compress the ions. This was the expectation from the outset of this investigation (see first paragraph section 8.). The experiments in this thesis have found this not to be the case. This may be a result of the smaller number of ions trapped, a larger amplitude of rotating dipole field at the position of the ions or a greater fraction of impurity ions (e.g. CaH^+) making the dipole drive in particular more effective [46][5].

Extensive studies on the electrostatic modes of non-neutral ion plasmas exist in the literature [44] [74] [75]. One such example with experimental measurements of the (2,1) plasma modes is [44] where torque from a laser beam was used to control the rigid rotation frequency of a cloud of Be^+ ions. It was found that the cloud rotation frequency could only be increased beyond the point of the (2,1) heating resonance if the angle between the trap axis and magnetic field was less than 0.1 degrees. Compression of an ion cloud by a rotating dipole field has been shown to be limited by the (2,1) plasma modes in [75]. However in all these cases either just the frequency of the heating resonance is identified or the ω_r scan is terminated at resonance. In this thesis, the entire (fluorescence intensity) heating response of the cloud is measured all the way up to $\omega_{rot} = \omega_c/2$, showing essentially the full signature or spectral profile of the (2,1) mode resonance under the action of the rotating wall. The width of the measured resonance is seen to narrow with increasing axial frequency and

---

[5] Other non-ideal effects such as different radial ring segment positions can also provide coupling for the dipole drive to control the cloud rotation frequency.

this feature is explained as a result of the (2,1) mode structure as a function of the cloud rotation frequency.

In a Penning trap, the single ion motion frequencies are ordered according to $\omega_m \leq \omega_z \leq \omega_c'$ and it is usually the case that the trap is operated with $\omega_z < \omega_c/2$. In the Imperial College SPECTRAP ion trap, the rotating wall is found to drive the axial resonance very strongly and this phenomenon has not been reported in other traps. This is most likely a result of the alignment of the split-ring electrode, and hence this unexpected resonance may also be present in the GSI trap and should be avoided, in addition to the $\omega_{21}^{(1)}$ plasma mode. If the axes in Fig. 8.4d are converted into units of the cyclotron frequency, the plot becomes universal and hence can be used to avoid heating resonances for any ion species, magnetic field and trap potential in the SPECTRAP experiment at GSI.

Chapter 9

SPECTRAP Experiment at GSI

9.1 Introduction

The SPECTRAP experiment currently being prepared at GSI is a collaborative effort to perform high-resolution laser spectroscopy of the hyperfine structure of highly charged ions as a test of the corresponding bound-state QED calculations. Fig. 9.1 shows a spider digram of the various collaborators and their main roles in the SPECTRAP experiment. The experimental system originated from the Lawrence Berkeley National Laboratory (LBNL) in the USA where it consisted of a cryogenic Penning trap setup (RETRAP) which was attached to an EBIT for experiments with medium heavy HCI. Studies were conducted on strongly coupled single and multi- species non-neutral plasmas, as well as electron transfer between HCI and neutrals [76] [57]. In 2007, RETRAP was relocated to GSI. A new ion trap (SPECTRAP see section 5.3) was designed by Dr. M. Vogel for the system with a greater solid angle and axial length for capturing ions in-flight from the HITRAP facility. Two identical such traps were made at Imperial College London, and one of these was taken to GSI. The trap at GSI was gold plated to prevent an oxide layer from forming on the electrode surfaces when outside the vacuum thereby maintaining the electrical purity of the trapping potential. The axial spacing either side of the capture electrodes was also increased from 0.5mm to 1.5mm to reduce the likelihood of dielectric break down at the high voltages required for in-flight ion capture. Hence with respect to the main trapping region between the endcap electrodes, the Imperial College and GSI traps are still essentially identical.

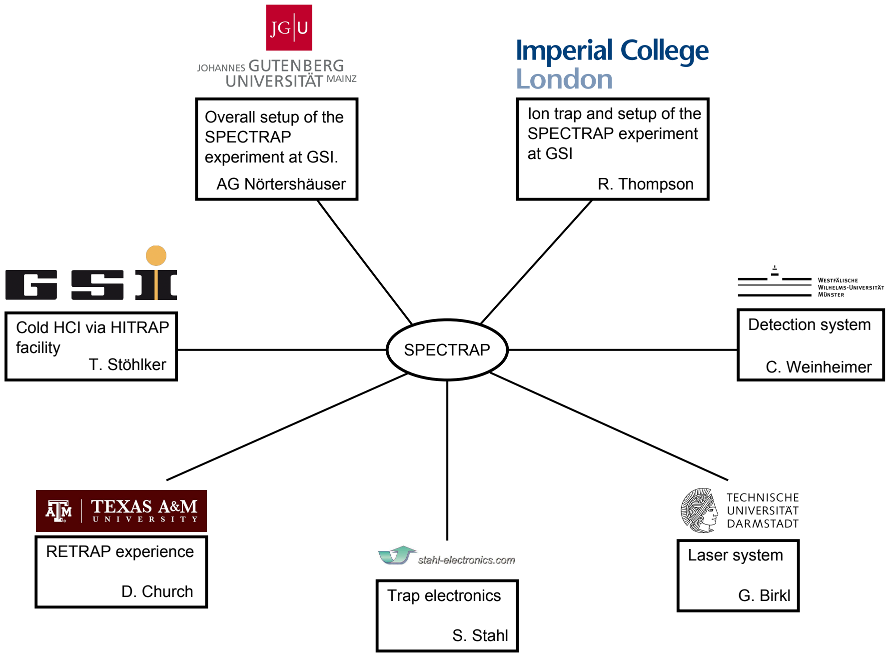

Figure 9.1: Members and their main roles in the SPECTRAP collaboration. The principle heads of group are also noted for each institution and organisation.

The experimental setup at GSI has mainly been the work of the Ph.D. student Z. Andjelkovic (of Mainz) and Dr. M. Vogel (of GSI) from 2007. In Early 2010, the Ph.D. student R. Cazan who worked on the Mg^+ Doppler cooling laser for the SPECTRAP in Mainz joined the effort at GSI to help prepare the system for preliminary trails at the end of 2010. Although I made visits to GSI to help at critical phases of the build, it was only after the experiments in London were completed and the trap at GSI was close to being operated for the first time, that I relocated to GSI from October 2010 to February 2011 to help full time in this effort. Hence most of the experimental work (and decision making) discussed here has been done by these other individuals and I report here to give a general overview and progress update. I also present simulations I conducted for the transport and in-flight injection of ions in the SPECTRAP ion trap at GSI.

9.2 Experimental Overview

An experimental schematic diagram of the SPECTRAP setup, which is still being prepared at GSI, is shown in Fig. 9.2(lower frame). The SPECTRAP trap is situated at the centre of a Helmholtz coil type cold-bore superconducting magnet. This configuration provides easy radial optical access for fluorescence collection unlike the Imperial College solenoid type magnet. The laser beam used for exciting the transitions will be directed axially along the magnetic field direction to give minimum background laser scatter. HCI from the HITRAP facility will be captured in-flight by switching the potentials on the capture electrodes of the trap (Fig. 9.2a), followed by similarly raising the endcap electrodes to localise the ions to the central harmonic trap (Fig. 9.2b), where resistive cooling will bring the ions to thermal equilibrium with the surroundings at cryogenic temperatures (Fig. 9.2c). At this stage, the rotating wall technique will be applied to compress the ion cloud and improve the signal to noise ratio for fluorescence detection perpendicular to the laser excitation axis. It should be noted that in the presence of the magnetic field, there is Zeeman splitting of the hyperfine structure according to the projection of the total atomic angular momentum ($\vec{F} = \vec{I} + \vec{J}$), along the direction of the magnetic field (m_F). This splitting is in the low field regime and typically tens of gigahertz per tesla, so can easily be resolved by lasers with linewidths in the megahertz region. The magnetic dipole transitions between $m_F = 0$ sublevels in $\Delta F = 1$ are not affected by the magnetic field and hence yield the HFS directly. For the transitions induced between $m_F = \pm 1$ in $\Delta F = 1$, they additionally provide information on the g-factor of the bound electron (g_F).

The relative precision of the HFS measurements will be limited by the Doppler broadened linewidth of the transitions given by

$$\frac{\Delta\nu_{FWHM}}{\nu} = \frac{\Delta\lambda_{FWHM}}{\lambda} = \frac{2\sqrt{2\ln 2}}{c}\sqrt{\frac{k_B T}{m_{ion}}}. \tag{9.2.1}$$

A conservative estimate of $T = 10$K has been made by Dr. S. Stahl for the lowest temperature achievable by resistive cooling in the presence of the expected electrical noise in the system. Hence the anticipated precision of the measurements according to equation (9.2.1) will be $\sim 10^{-7}$ which is three orders of magnitude greater than for example the ^{209}Bi^{82+} measurements in the ESR reported in section 2.2.2.1. This is on the level of one hundredth of a percent of the first order QED contributions, and hence the validity of the test of bound-state QED will only be limited (at the present time) by the precision of the calculations themselves. Via the specific difference between H- and Li-like HCI (see section 2.2.2), the main uncertainties from the nuclear effects can be reduced and QED may be tested to the level of a few percent.

To emphasise the requirement for the rotating wall technique, the spectroscopy of the ground-state HFS of $^{207}\mathrm{Pb}^{81+}$ is taken as an example. This ion has a transition wavelength of $\sim$ 1020nm and an upper-state lifetime of $\sim$ 50ms (see section 2.2.2). This gives a natural limewidth of 3Hz and a saturation intensity of $24\mu\mathrm{Wm}^{-2}$. At 10K the transition is Doppler broadened to approximately 110MHz, and therefore the intensity required to saturate all the ions in the in-homogeneous linewidth scales to $\approx 900\mathrm{Wm}^{-2}$. For a typical ion cloud of diameter of 0.5mm, this requires a laser power of approximately 180μW which is easily achievable with current laser technology e.g. Ti:Sapphire lasers. If the transition is heavily saturated ($I \gg I_{sat}$), the maximum fluorescence rate per ion is approximately $10\mathrm{s}^{-1}$ ($\Gamma/2$). This implies for a cloud of 10^5 ions, up to 10^6photons/s will be emitted. From the SPECTRAP ion trap at GSI, only 0.17% of this total emission will be collected giving approximately 2000photons/s for detection[1]. Using the avalanche photodiodes diode (APD) system developed by the Münster collaboration [28], the detection efficiency is expected to be around 50% with a dark count of $100\mathrm{s}^{-1}$ (LN2 cooled APD). Therefore this gives a signal to noise ratio (SNR) of approximately 10 which is sufficient for a measurement. This is only achievable if all the photons from the cloud can be collected onto the small 2mm$\times$2mm square detector area which will be located up to 2m away from the centre of the trap. This essentially requires a point source and this is (approximately) the case for a spherical cloud at the Brillouin limit in a high magnetic field i.e. that which is driven by the rotating wall. This calculation could be repeated for Li-like Bi, however, detectors have not yet been developed with a low enough dark count, even when the signal is integrated over several hours, to provide a SNR≥ 1 at the required wavelength of 1514nm. This will be the next task of the Münster collaboration.

---

[1] The in-trap optical design for fluorescence collection using a lens and mirror in a confocal arrangement has been replicated from the Imperial College trap.

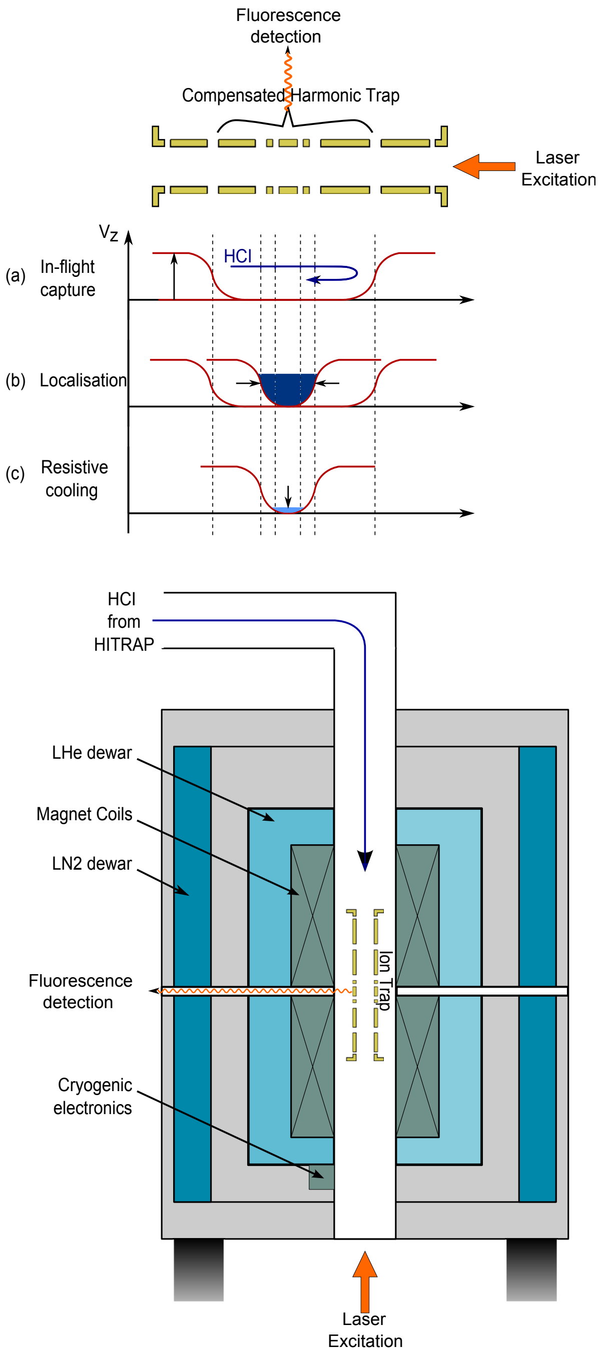

Figure 9.2: (lower frame) diagram showing the layout of the SPECTRAP experiment and (upper frame) experimental procedure for trapping and cooling HCI from HITRAP. (a), (b) and (c) show the on-axis axial potential V_z for the latter.

9.3 Simulations of SPECTRAP Ion Transport and In-Flight Capture

9.3.1 Introduction

The main aims of these simulations were to investigate the injection of ions into the trapping magnetic field, pulsing of the drift tubes to remove ion kinetic energy, to set up-stream requirements for ions from the HITRAP facility and ultimately to have a smaller experimental parameter space to search through (in the actual experiment) for optimum ion transport into the SPECTRAP ion trap at GSI. This should expedite the time-line when the limited HITRAP beam time is available.

Simulations were conducted in SIMION using a detailed scale model of the SPECTRAP ion optics. A program was written to scan through various parameters of each of the ion optics elements in turm. This report first provides an overview of the system followed by a systematic optimisation as ions are transported to the trap.

9.3.1.1 The Ions

A good first candidate for study in SPECTRAP will be H-like lead, or $^{207}\mathrm{Pb}^{81+}$. Assuming HITRAP can cool up to 10^5 such HCI to a temperature of 4K, and that they will be transported without appreciable heating with an energy of 5keV/u, the total kinetic energy (KE) of each ion will be

$$KE = 5 \times 81 = 405\mathrm{keV}$$

which gives a non-relativistic longitudinal velocity v of

$$v = \sqrt{\frac{2KE}{m_{ion}}} = 614\mathrm{kms}^{-1}.$$

The high transport energy is crucial in keeping the relative energy spread of the ion bunch low through the various ion optics elements. As the ions will be cooled to 4K via thermalisation with cold trapped electrons in the HITRAP facility, a Boltzmann velocity distribution is assumed. This implies the velocity spread σ_v will be

$$\sigma_v = \sqrt{\frac{k_B T}{m}} = 13\text{ms}^1.$$

This is a negligible fraction of v. If the angular spread is derived from this value alone, it would also be negligible. However space charge effects will cause the bunch to diverge when densities become high i.e. on focusing and bunching. To this end, HITRAP has provided an estimate of the beam emittance ϵ of

$$\epsilon = 10\text{mm.mrad}.$$

For a Gaussian beam profile, the emittance is given by the area in the $(x - \theta_x)$ plane

$$\epsilon = 4\sigma_x \sigma_{\theta_x} \tag{9.3.1}$$

where σ_x and σ_{θ_x} are the root mean squared half spatial width and divergence angle respectively. Upon rearranging, the divergence angle can be estimated from

$$\sigma_{\theta_x} = \frac{\epsilon}{4\sigma_x}. \tag{9.3.2}$$

For an ion bunch radius of 2.5mm, the divergence will be 1mrad or 0.1 degrees (1.d.p). A 2.5mm radius is chosen such that over 90% of the ions in the tangential plane lie within a radius of 5mm or $2\sigma_x$. If the radius is too small, space charge will cause the bunch to rapidly expand, and if it is too large, this increases the chance of losing ions to the walls and electrode surfaces. This parameter can be easily adjusted by HITRAP-SPECTRAP via a pair of einzel lenses in a telescopic arrangement.

The maximum acceptable ion bunch length is a parameter that this simulation will investigate and feed-back to HITRAP. The maximum acceptable bunch length at the position of the SPECTRAP ion trap is approximately equal to the round trip between the capture electrodes, 160mm. To be inside this, the initial bunch length is set to $\sigma_z = 25$mm at the start of the simulations. This implies as before, over 90% of the ions will be contained inside a longitudinal length of 100mm. To actually simulate 10^5 individual ions is computationally intensive and not strictly necessary. It is only the ion-ion interactions or space charge effects that are not simulated correctly if a smaller number of ions are flown. To this end, SIMION provides an alternative method where (just) the Coulomb interaction between ions is calculated from an effective total charge of, in this case, 10^5 ions or $10^5 \times 81 \times e = 1.3 \times 10^{-12}$C, distributed equally between the actual smaller number of ions flown e.g. 100. This method is employed in these simulations and each simulation run or flight for a set of parameters through the system takes of order 10 minutes.

To summarise, ions from HITRAP are modelled as a bunch of 10^5 mono-energetic ions with a 3D Gaussian spatial distribution of width $\sigma_z = 25$mm and $\sigma_x = \sigma_y = 2.5$mm, a forwards longitudinal kinetic energy of 405keV (5keV/u) and a tangential divergence half angle spread of 0.1 degrees. The Gaussian profile is preferable over the alternative of a uniformly filled hard edge cylinder as space charge effects will be more realistic. Fig. 9.3 shows a screen-shot of this ion bunch created in SIMION.

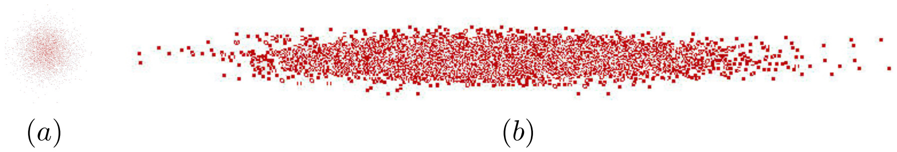

Figure 9.3: Ion bunch created in SIMION. (a) shows an (x-y) and (b) shows an (x-z) cross-sectional slice of 5000 ^{207}Pb^{81+} ions filling the distribution described in section 9.3.1.1 for illustrative purposes.

9.3.1.2 The Beamline

The SPECTRAP experiment has its own local ion transport system derived from RETRAP. This includes a short horizontal and vertical beamline section which connects HITRAP to the SPECTRAP ion trap. Successful operation of this section of beamline is the responsibility of the SPECTRAP team and not the HITRAP facility. The pressure in the beamline will be kept below 10^{-10}mbar via ion and cryogenic pumping, implying that collisions with residual gas particles will be low. For the case of HCI, these collisions can result in charge exchange and loss of the ion species desired. As the goal of this investigation is to optimise essentially voltages on the transport system, these collisions are ignored in the simulations i.e. a perfect vacuum is assumed. An overview of the layout of the ion optics is shown in Fig.9.4. It is this transport and capture system that is investigated. The beam path and the various ion optics are now discussed in more detail.

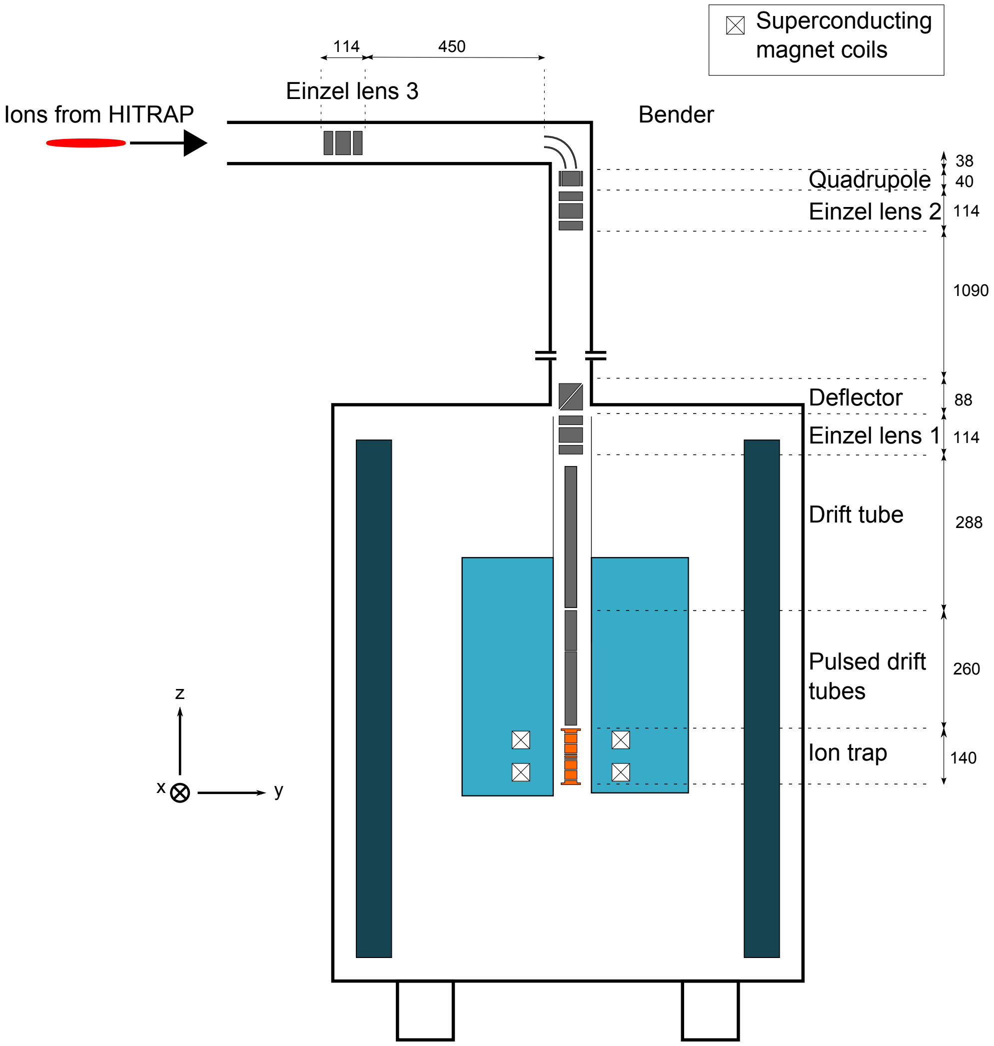

Figure 9.4: A schematic diagram of the SPECTRAP ion transport system. The discontinuity between the deflector and einzel lens #2 illustrates the height has been significantly compacted in this area. Lengths are in millimetres and the light and dark blue colours show the positions of the liquid helium and nitrogen dewars respectively.

Starting from the HITRAP ion feed to the horizontal beamline, the ions first pass through an einzel lens (#3). This is one of three identical einzel lenses in the system, each made from three cylindrical electrodes (Fig. 9.5).These lenses are axially symmetric about the centre, and only the central electrode is addressable. The outer two electrodes are grounded internally. The optical analogue for this component is a singlet lens. The purpose of this first lens is to collimate the beam for the next element, the bender.

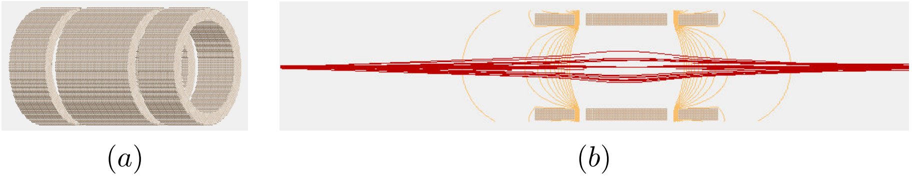
(a) (b)

Figure 9.5: (a) an isometric and (b) cross-sectional view of the einzel lenses present in the SPECTRAP experiment. Potential contour lines (orange) and ion flight trajectories (red) can be seen in (b) for typical experimental parameters.

The electrostatic bender deflects the ions by 90° towards the ion trap. It is constructed from a wire mesh so it can be made transparent if grounded. In the simulation however, it is equivalently modelled by two solid parallel plate electrodes bent around a radius as shown in Fig. 9.6a. The optical analogue in this case is a mirror with curvature along the reflecting axis. This component introduces aberrations because ions that enter off-axis still experience the same bending radius since the electric field is approximately constant between the plates. Therefore ions that enter closer to one electrode, leave closer to the other i.e. they are focused inside, as shown in Fig. 9.6b. In the plane perpendicular to the bender's curvature, there are no electric field components and hence no effects on the beam as shown in Fig. 9.6c.

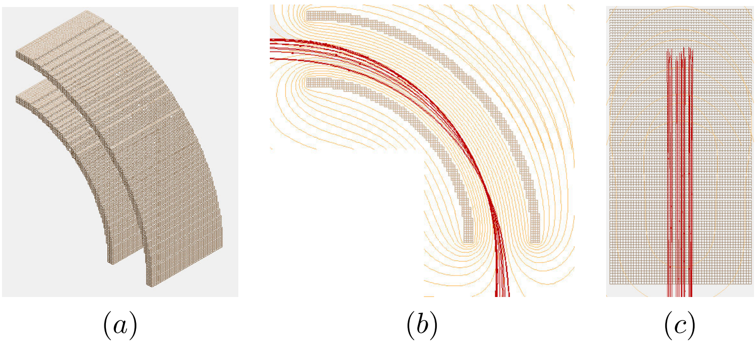
(a) (b) (c)

Figure 9.6: (a) an isometric, (b) cross-sectional and (c) top-down view of the 90 degree "bender" deflector present in the SPECTRAP system. Potential contours lines (orange) and ion flight trajectories (red) show the typical optimised behaviour of this device.

On leaving the bender, the ion propagation is collimated in one axis but diverging in the other. To correct this asymmetry a quadrupole is used. This has four similar electrodes with circular cross sections in the tangential plane as shown in Fig. 9.7a,b. In this case, like potentials are applied to opposing electrodes in the direction of the bender deflection. The optical analogue is a pair of cylindrical lenses, one negative and one positive lens aligned along the collimated and diverging axis of a beam respectively. This way the lens(es) can create an equally diverging beam in both directions. The potentials on quadrupoles are typically much lower than those required on einzel lenses due to the electrode configuration being more efficient at producing transverse electric potential gradients. An einzel lens (#2) is located immediately after the quadrupole to recollimate the bunch. The aspect ratio is now likely to be different, but not substantially greater than 1:1.

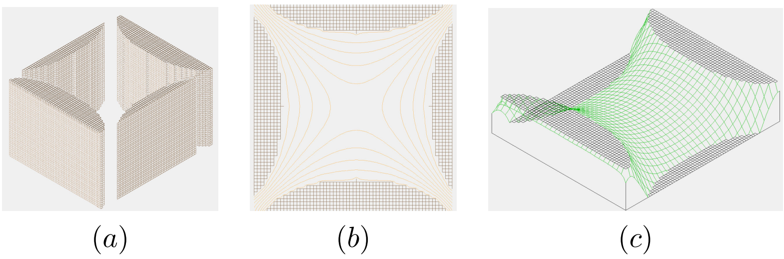
(*a*) (*b*) (*c*)

Figure 9.7: (a) an isometric, (b) cross-sectional and (c) potential energy surface view of the electro-static quadrupole element. Potential contours lines (orange) and surfaces (green) are shown for typical operating voltages.

The ions then travel into a deflector which is made by two half cylindrical electrodes that intersect at 60 degrees. The plane of this intersection or cut, is perpendicular to the bender deflection. This generates a voltage step or sideways deflection of the beam in parallel with the bender deflection. Thus if the ions are not exactly deflected by 90 degrees by the bender, they can be repointed towards the trap with the help of this second deflector.

The ions then pass through a final einzel lens (#1) which focuses at the centre of the trap. Between this einzel lens and trap, there are a pair of pulsed drift tubes which remove most of the ion transport energy. This is done by rapidly lowering the tube potentials whilst the ions are inside, such that they do not reclaim all their KE on exiting the tube. The ion trap (and electronics) is designed for the Penning configuration hence requires the magnetic field. The fringe fields of this magnet will affect ion injection into the trap. As charged

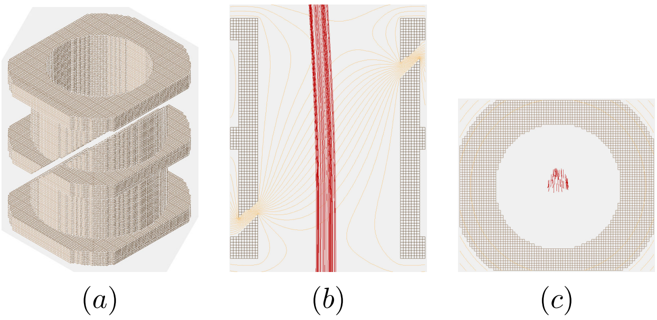

Figure 9.8: (a) an isometric and (b,c) cross-sectional views of the 1D deflector. Potential contours lines (orange) and ion flight trajectories (red) show the typical optimised behaviour of this device.

particles follow magnetic field lines, this should help guide the ions in the vertical beamline into the centre of the trap. However in the horizontal beam line, ions will be deflected laterally which is not desired as this introduces aberrations further on. If the magnetic field is a problem in this area, shielding can be used around this section of beamline.

The in-flight ion capture process works by first having the trap open on one side, that is the top-most capture electrode is grounded, and the other is at a high enough voltage to reflect all the ions (typically in the keV range for HITRAP). Once the ions have passed the upper capture electrode, the potential is raised so that the ions are trapped between these electrodes. The origin of the co-ordinate system is at the centre of the trap.

9.3.2 Optimisation of Static Ion Optics

The ion optics components that use only static (conservative) electric fields are responsible for transporting ions to the trap. This section goes through the optimisation of these components, namely the einzel lenses, deflectors and quadrupole elements.

9.3.2.1 Horizontal Beamline

The ion bunch as defined in section 9.3.1.1 has a small angular spread of 0.1 degrees. Therefore a mere 500V on einzel lens #3 is enough to collimate the propagation of the ions as observed in the far field. The RETRAP magnet provides a maximum magnetic field of 5.8tesla. A similar Helmholtz coil was simulated in SIMION and shown to produce approximately the same on-axis axial dependence. This maximum magnetic field is used in the simulations and shows here that the ion bunch is deflected by approximately 3mm on travelling up to the bender. Given that the range of inner electrode radii is $10-26$mm, this is not a negligible fraction. Furthermore the transverse velocity imparted to the ions will remain and this offset will increase and be magnified upon lensing towards the trap. Therefore it is desirable to cancel this field by use of magnetic shielding (e.g μ-metal) in the horizontal beamline section. Fig. 9.9 shows the simulated axial magnetic field responsible for the lateral force on the ions in the horizontal beamline. Although the magnitude of the field is small, the velocity is large and the track length is long. For comparison, the field is approximately a factor 10 times higher than the typical Earth's magnetic field.

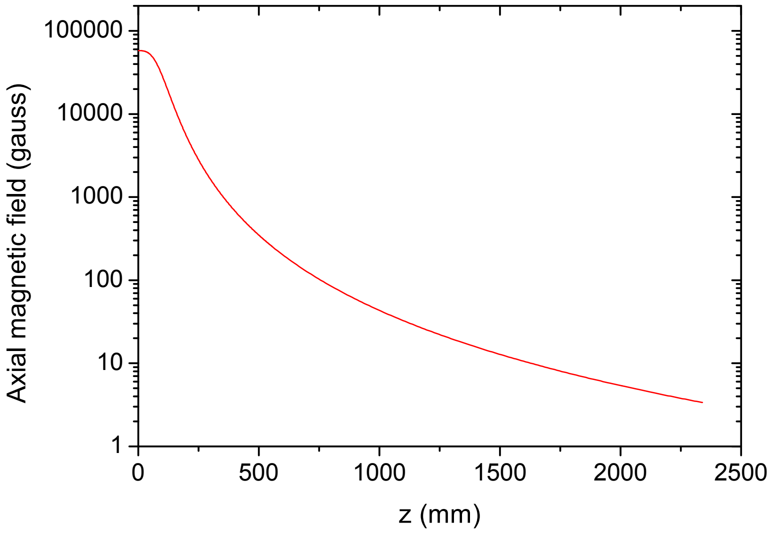

Figure 9.9: Axial magnetic field plot from the centre of the trap (z = 0mm) up to the position of the horizontal beamline (z = 2231mm). The magnitude of the field at these positions is 58000Gauss and 5Gauss respectively.

A 0.1mm thickness μ-metal single layer cylindrical shield can attenuate the field by a factor of 100 [77]. For a double layer shield with air spacing, the attenuation factor is proportional to the product of the individual layer factors [77]. Since the field is small enough at the position of the horizontal beamline such that the saturation induction of the material will not be a concern, it is envisaged this type of shielding will make the field negligible in this section. Hence it will now be assumed the magnetic field only permeates out to the boundary of the bender electrodes.

9.3.2.2 90 Degree Deflector

The 90 degree deflector has a bending radius of 87.5mm. Theoretically the electric field required to produce a centripetal force to turn the $KE = 5\text{keV/u}$ and u=81 Pb ions around this radius is 114kVm^{-1}. For an electrode separation of 25mm, the potential difference between the electrodes should be of the order 2.9kV. In the simulation, the setup to optimise the bender includes using the succeeding einzel lens (#2) to focus the ions towards the trap. This allows an accurate determination of the 90 degree deflection point as otherwise the ions would be diverging (as seen in Fig. 9.6).

Defining the potential on the radially situated outer bender electrode as V^{+}_{bender} and that on the inner as V^{-}_{bender}, the graph in Fig. 9.10 shows the potential difference that must be applied between the bender electrodes ($\Delta V_{bender} = V^{+}_{bender} - V^{-}_{bender}$) to deflect the ions by 90 degrees as a function of V^{+}_{bender}, and the corresponding kinetic energy of the ions inside the bender.

It is found that the value of ΔV_{bender} required to deflect the ions towards the trap decreases with increasing V^{+}_{bender}. This happens because the ion energy is changed by an asymmetric potential setup. For example, for $KE = 5\text{keV/u}$ ions, the ion energy inside the bender remains unchanged for the $V^{+}_{bender}/V^{-}_{bender}$ electrode setup of $1405\text{V}/-1405\text{V}$. For a 2200V/0V setup, the ions are decelerated to $KE = 4.5\text{keV/u}$ before entering the bender and hence with a smaller velocity, a smaller electric field or potential difference is required for the same bending radius. Conversely for a $0\text{V}/-3500\text{V}$ setup, the ions are accelerated to $KE = 7\text{keV/u}$ and a greater electrode potential difference is required. The relationship is linear because the centripetal force is proportional to the kinetic energy of the ions, which in turn is linearly affected by the potential on the electrodes. When observing in the plane perpendicular to the deflection ($x-z$), the ions remain collimated for the symmetric setup (Fig. 9.11a), but converge for a more negative (Fig. 9.11b) and diverge for a more positive (Fig. 9.11c) overall electrical setup i.e. $V^{+}_{bender} + V^{-}_{bender} > 0$. Neither asymmetric setup is suitable for the experiment. Either the ions are focusing too sharply for the quadrupole to have an effect, or diverging too quickly such that the ions impact electrodes before the quadrupole can make an equally diverging beam. Thus

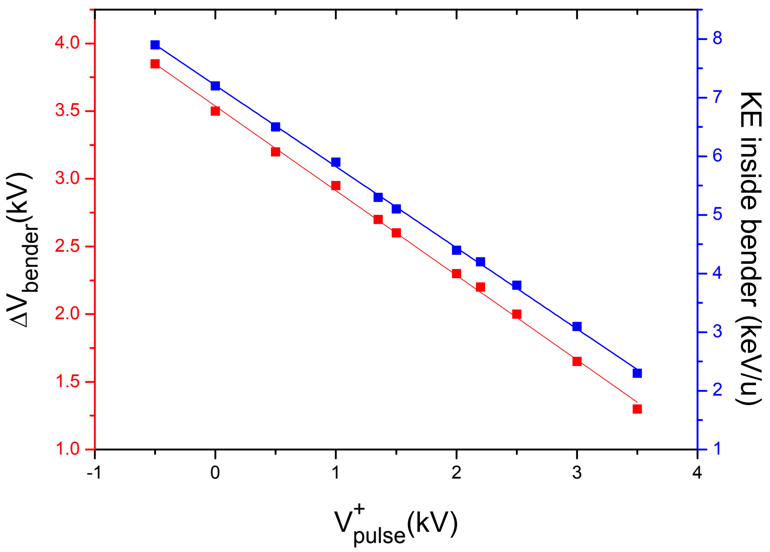

Figure 9.10: A double plot showing how the potential difference between the electrodes of the bender and the kinetic energy of the ions inside the device, changes with increasing potential on the positive (outermost) electrode of the bender for a 90 degree deflection towards the trap.

the optimum configuration is at (or near) the symmetric potential electrode setup ($|V^+_{bender}| \approx |V^-_{bender}|$) and that is what is selected from here on as the optimum.

9.3.2.3 Quadrupole

The quadrupole is now setup such that an equally diverging beam is created. By inspection, this occurs for a potential of 500 ± 50V. With the succeeding einzel lens (#2) at a potential of 2950 ± 50V, the ions are successfully recollimated. The aspect ratio in the plane perpendicular to the direction of propagation is now measured to be about $1 : 1.2$. As the bender and quadrupole are separated by only 40mm, the bender deflection is affected by use of the quadrupole. Upon recollimation, the ions are deflected just under 90 degrees. Therefore a small correction to the symmetric bender setup is made. The potential difference between the electrodes is increased and the symmetry is maintained for $V^+_{bender} = 1340$V and $V^-_{bender} = -1340$V. An ion flight through this new configuration is shown in Fig. 9.12.

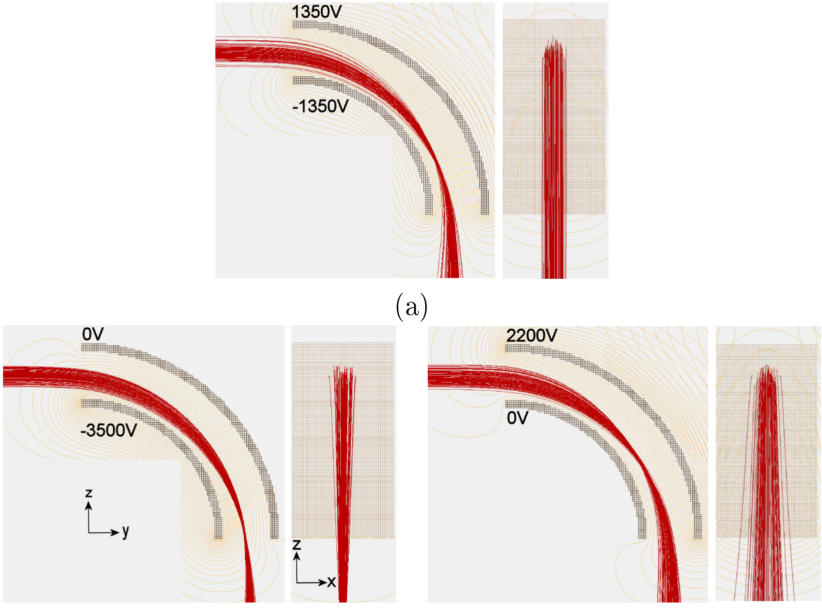

(a)

(b)

(c)

Figure 9.11: (b) Ion flight trajectories for the symmetric and (a,c) asymmetric setups required for a 90 deflection. Ion flight trajectories (red) are shown in the plane $(y-z)$ and perpendicular to the plane $(x-z)$ of deflection. These particular asymmetric setups are chosen for their practical implementation simplicity.

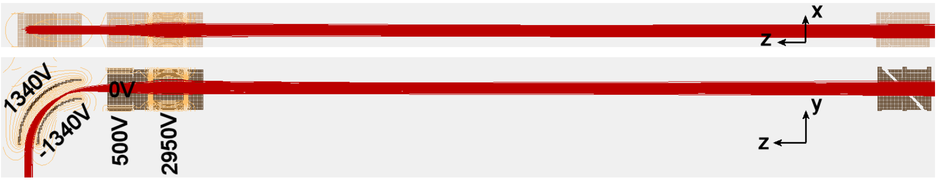

Figure 9.12: A complete optimised setup for a 90 degree deflection and recollimation of ions towards the trap. Ion flight trajectories are shown in red and potential contours in orange.

9.3.2.4 Deflector

The recollimated beam as shown in Fig.9.12 passes through the deflector and into the final einzel lens (#1). The deflector is a device for repointing ions towards the trap. This is only useful however if the ion optics are not physically aligned properly. For the deflector to correct the angle of propagation, the ions must be approximately centred on the deflector so that the output will feed in line with the remaining elements (as shown in Fig.9.8). If this condition is not met, the angle is corrected for, but the offset from the centre remains and ions are lost to the walls (Fig.9.13). In the simulation, the ion optics are aligned perfectly along the trap axis. The bender only changes the deflection angle assuming the beam is recollimated properly. As the deflector is in the far field of the bender, the maximum angular deviation is small but the tangential offset can be as large as the device. Therefore the deflector does not improve the ion throughput to the trap centre. In the experiment there is a bellows between the bender and deflector. Therefore a small misalignment is likely and the device should help. In the simulation however, the deflector is not strictly necessary and so remains grounded. For a conservative estimate of the power supply requirements for this device, an exaggerated 30 degree deflection of the ions is made for a potential difference of approximately 1500V between the deflector electrodes.

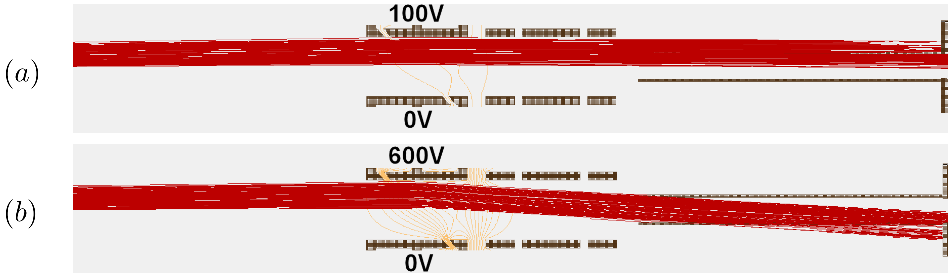

Figure 9.13: (a) cross-sectional views of the deflector showing how the ion bunch is made parallel to the trap axis, and (b) how the ions are deflected to maximise injection into the succeeding drift tube. The bender is setup with $V^{+}_{bender} = 1400$V and $V^{-}_{bender} = -1340$V to feed the deflector with a maximum angular error without ion loss to the electrodes of the deflector.

9.3.2.5 Einzel Lens #1

The final einzel lens (#1) potential (E_1)is now set to optimise injection of the ions into the trap. Between this lens and trap, there is a series of drift tubes. From inside the very first (grounded) drift tube, the effects of the magnetic field can be observed. In the tangential or radial plane, the tell-tale signs of cyclotron motion can be seen (see Fig. 9.14). The axial magnetic field helps to radially confine the ions from inside the pulsed drift tubes where $B_z > 1000$gauss to the trap. Therefore the optimal einzel lens setup which produces the tightest beam envelope from the lens to the trap, is one where the focus of the ions is directed at or near the entrance to the pulsed drift tube.

From the simulations in Fig. 9.14, it can be seen that for a weak focus ($E_1 =$ 2300V) the ions are close to impacting the electrodes at the point of insertion

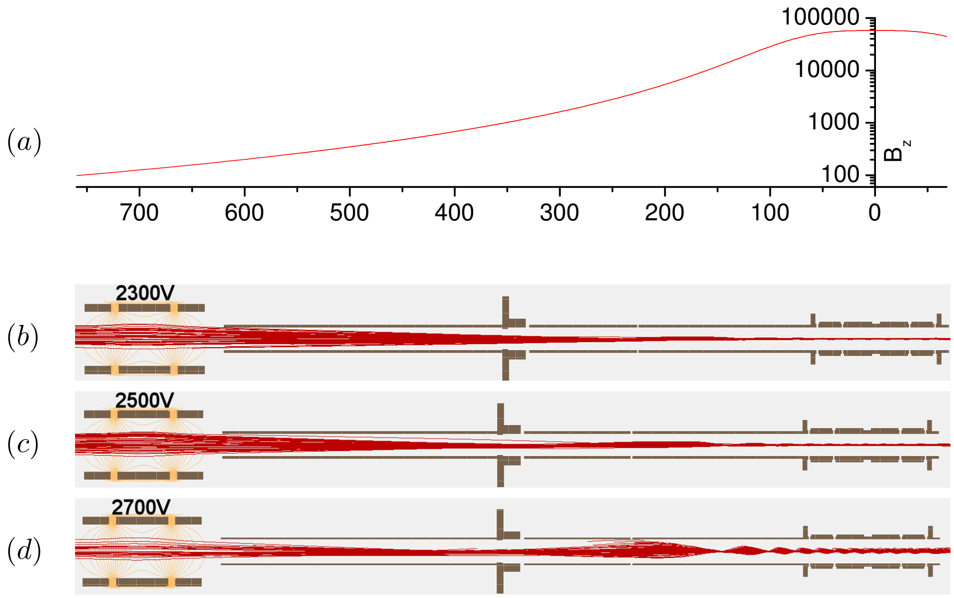

Figure 9.14: (a) axial magnetic field plot and (b-d) simulations showing how ion injection into the trap is affected by the focus of the einzel lens (#1). The modulation of the ion bunch envelope inside the pulsed drift tubes is due to the cyclotron motion.

into the grounded drift tube (Fig. 9.14b). At the other extreme where the focus is strong ($E_1 = 2700$V), the ions are close to being lost to the electrodes of the pulsed drift tube (Fig. 9.14d). Therefore the optimum setup is between these extremes. Hence the voltage of the einzel lens is set to an intermediary 2500V as shown in Fig. 9.14c. Note that with the activation of the deflector with this einzel lens, ion injection into the trap is reduced even further as expected.

9.3.3 Optimisation of Dynamic Ion Optics

The ion optics elements for which the potentials on electrodes are varied in time during the flight of ions through the system, are here referred to as the dynamical components of the system. These are the pulsed drift tubes and the ion trap. Thse are responsible for in-flight capture of ions.

9.3.3.1 Pulsed Drift Tubes

Most of the ion transport energy will be removed by the pulsed drift tubes. Although there are two separate sections, they will be electrically grouped together as the length of the ion bunch is comparable to the first short tube section. As the distance between the tubes is small, it is equivalent to one continuous electrode. In the experiment, the voltage will be switched by a commercial device (Behlke HTS 51-06). This has a fixed switching time of $0.15\mu s$. Although the voltage is not switched linearly, the switching speed is fast enough that the ions will still be inside the tube where they see no electric field. Therefore the details of the switching waveform do not matter. Hence for simplicity, a linear negative voltage ramp is used in the simulation with an identical switching time. The pulsing is carried out according to the Fig. 9.15. The tube starts at some potential V^+_{pulse}, which is linearly ramped down by an amount ΔV_{pulse}, to a potential of V^-_{pulse}. The switching time is denoted δt.

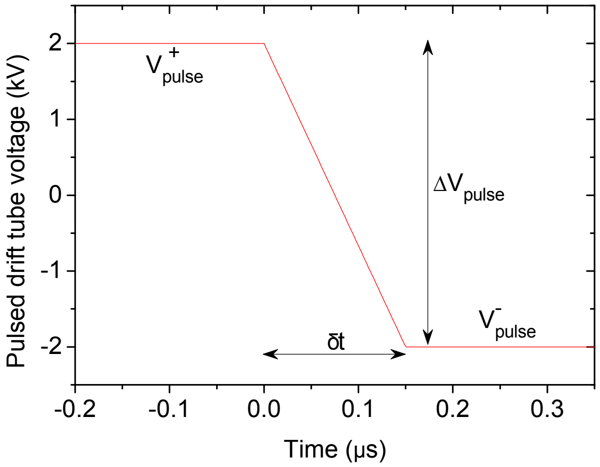

Figure 9.15: Readout of the pulsed drift tube voltage as it is switched in the simulation.

There are essentially two variables that need to be optimised, V^+_{pulse} and ΔV_{pulse}. V^+_{pulse} and V^-_{pulse} control not only how much energy is removed on entry and exit of the tube(s), but also the focusing of the ions, as the ends of the tube can be seen as two electrostatic immersion lenses. The pulsing needs to be optimised to maximise the energy removal (ΔV_{pulse}) and minimise the bunch length (l). This should lead to a high trap capture efficiency of cold ions. Where the magnitude of either V^+_{pulse} or V^-_{pulse} is large, focusing will be strong. This is not desirable because ions can be lost to the walls. The magnetic field will help prevent this to some degree, but as energy or velocity is transferred from the axial to the radial direction, the bunch length will increase. Therefore as the magnetic field decreases away from the trap, it is predicted that the optimum pulsed drift tube setup will be asymmetric with an emphasis on the magnitude of V^{-}_{pulse} over V^{+}_{pulse}.

9.3.3.2 Pulsed Tube Optimisation

In the simulation the voltage switching starts when the centre of the ion bunch crosses a predefined longitudinal position. This is set to approximately 2/3 of the way into the tube, so switching occurs well inside the region of zero electric field (as shown in Fig. 9.16). Switching starts from a fixed position rather than a fixed time as the latter changes with the energy of the ions inside the tube. The time of flight data is important in the experiment as the hardware switch is activated by a TTL pulse in a sequence. Therefore in this simulation, the ion time of flight is recorded when switching starts. Fig. 9.16a shows the position of the ions as the voltage is ramped down (coloured blue during this period). Fig. 9.16b shows that the ions leave the drift tubes having lost the right amount of kinetic energy amounting to $\mathrm{e}\Delta \mathrm{V}_{pulse}/\mathrm{u}$. This confirms the operation of the code written for switching the electrode voltages in SIMION[2].

The ion energy and bunch length are measured at the end of the ion trap at $z = -60$mm. This is done because for in-flight ion capture, ions would be reflected at the capture electrode at $z = -30$mm, and have a round trip back to the centre of the trap of 60mm. Hence this provides an estimate of the bunch parameters when the capture electrode at $z = +30$mm would be switched closing the trap. The CM coordinates, average ion energy and bunch length are all taken from the central 90% of ions about the CM in space. An ion register is also employed to count the number of ions at the measurement position. This gives an ion number transport efficiency for the beamline.

Theoretically, if the ion bunch diameter was small, the approximation could be made that all ions pass through the same (axial) potential 1D profile, conserving the temporal bunch length. In such a case, this gives the scaling relation

$$\frac{l'}{l} = \frac{v'}{v} = \sqrt{\frac{KE'}{KE}} = \sqrt{\frac{KE(\mathrm{keV/u}) - \Delta V_{pulse}(\mathrm{kV})}{KE(\mathrm{keV/u})}} \tag{9.3.3}$$

where v is the velocity of the ions and the unprimed and primed variables represent the values before and after, for example, the pulsing of the drift tubes.

---

[2] Dynamic switching of electrode voltages in SIMION is not built into the software as standard. Addition program scripts must be written by the user for such purposes.

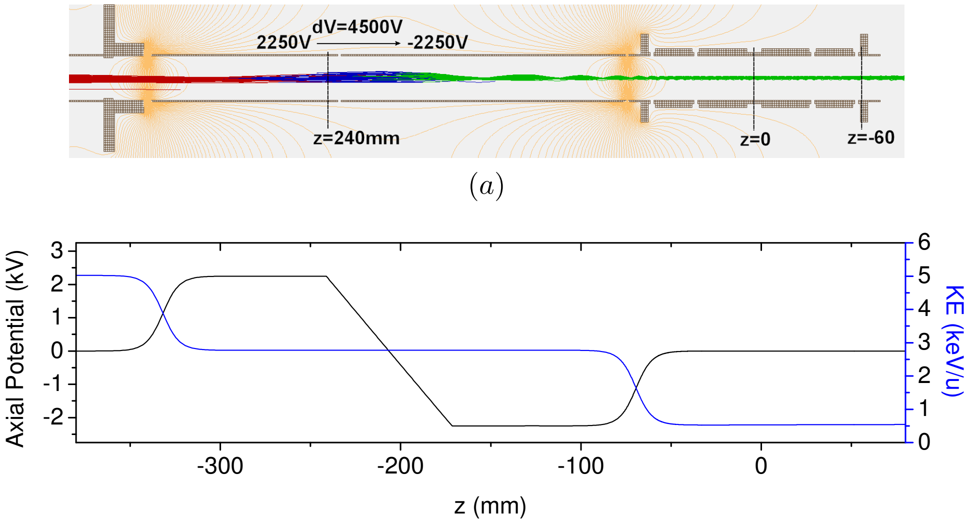

(a)

(b)

Figure 9.16: A simulation showing the switching of the pulsed drift tube(s) from 2250V to −2250V when the ion bunch (CM) crosses $z = 240$mm. The switching period is 0.15μs and the trap remains grounded. Ion flight trajectories are shown in (a), and the axial potential about the ions and their kinetic energy as they travel down the beamline is shown in (b). Before, during and after voltage switching, the ions are coloured red, blue and green respectively. The modulation of the ion bunch envelope from inside the pulsed drift tubes through the trap is due to the cyclotron motion.

This can be used to give a minimum bound to the bunch length achievable post-switching the drift tubes.

9.3.3.3 Pulsing the Tubes

Fig. 9.17 shows how the bunch length varies with ΔV_{pulse}. The simulations show a good agreement with the theoretical predictions using equation (9.3.3) for ΔV_{pulse} up to approximately 3000V. For higher ΔV, that is lower energy ions, electrostatic lensing and the magnetic field transfer ever more velocity from the axial into the radial plane, leading to an increase in bunch length. Furthermore, as more energy is transferred away from the axial direction, some ions no longer have enough energy to overcome the potential barrier on exit of the tube and are reflected back towards the bender. This causes the $2\sigma_z$ spatial width of the ion bunch to blow up for $\Delta V_{pulse} > 4700$V. There is an optimum in ΔV_{pulse} of 4400V±50V which gives a minimum in bunch length of 55 ± 5mm, a low ion kinetic energy of 0.6keV/u and a 100% $2\sigma_{x,y,z}$ transport efficiency. For ΔV_{pulse} up to 4700V, another 200eV/u of energy can be removed without ion loss, but at the expense of returning the bunch length to the original input value of 100mm. As this is still within the capture length of the trap, this setup is fully supported.

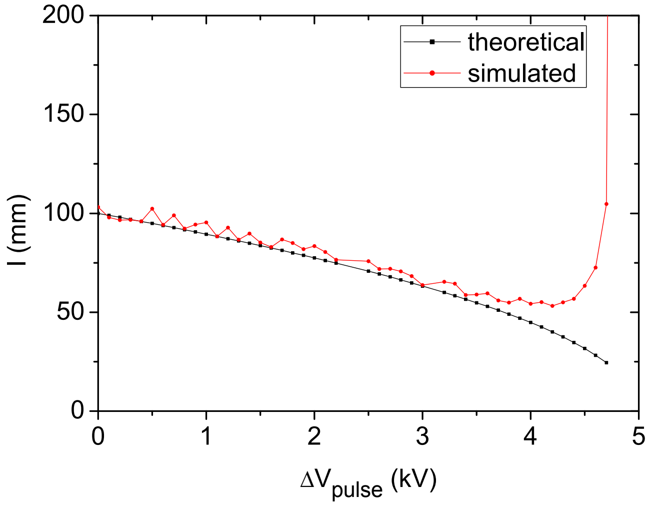

Figure 9.17: A graph showing how the ion bunch length l varies with increasing potential switched by the pulsed drift tubes ΔV_{pulse} for a fixed initial value of $V^{+}_{pulse} =$ 3kV. The simulated bunch length diverges from the theoretical expectations above $\Delta V_{pulse} \sim$ 4kV as an increasing fraction of ions are reflected at the output of the pulsed drift tubes. This occurs because the magnetic field transfers longitudinal kinetic energy into the radial direction via the cyclotron motion.

Fig. 9.18 shows how the bunch length varies with V^{+}_{pulse} for constant $\Delta V =$ 4500V. The flat broad minimum up to $V_{pulse} \approx$ 4000V shows that the bunch length is not strongly dependent on the pulsed tube starting voltage. It was expected that due to electrostatic lensing, a close to symmetric setup would be optimum but this is not the case as there is no particular minimum in l around $V^{+}_{pulse} =$ +2250V (i.e $\Delta V_{pulse}/2$). The most likely reason for this is that in this voltage range, the lensing is sufficiently weak that it is suppressed by the guiding effects of the magnetic field in the region.

9.3.3.4 In-Flight Ion Capture

As the ion bunch propagates through the trap, it is very well radially confined by the strong magnetic field ($\sim$ 6tesla). The bunch diameter measured at the centre of the trap is $<$ 1.5mm which is much less than the inner diameter of

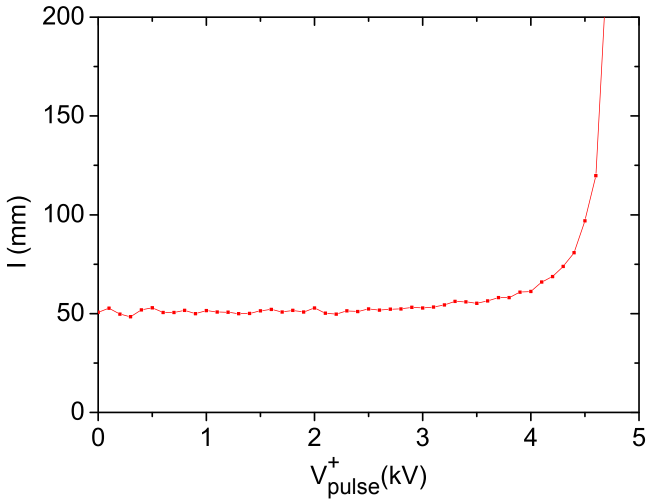

Figure 9.18: A graph showing show the ion bunch length varies as a function of the initial pulsed drift tube potential V^{+}_{pulse} for a fixed switching value of $\Delta V_{pulse} = 4$kV.

the trap electrodes of 21.2mm. For in-flight ion capture, the bunch will first be trapped between the capture electrodes. The ions will then be localised between the endcaps by raising their potentials. It is only at this stage that resistive cooling can begin to remove energy from the ions. An important question is, how high can the electrode potentials be for a stable Penning trap? This can be answered by looking at the Penning trap stability criteria in terms of the maximum harmonic potential curvature. Along the axis, this is given by

$$\frac{q_{ion}B^2}{4m_{ion}} = \frac{1}{2}\frac{d^2V_z}{dz^2} \tag{9.3.4}$$

which in the SPECTRAP trap for $^{207}\mathrm{Pb}^{81+}$ ions in the maximum supported magnetic field of 5.8tesla, gives 21.7V/mm^2. Analysis of the axial trap potential for the setups described above is presented in Fig. 9.19.

Fig. 9.19a and Fig. 9.19c show the axial potential per volt for the localised harmonic trap and for the larger trap that will initially capture the ions respectively. The maximum potential curvature for the localised trap is 0.006V/mm^2 per volt of U_0 (Fig. 9.19b), and therefore at this maximum magnetic field, this sets a theoretical upper limit of 3.6kV on the endcap electrodes for stable trapping. For capturing the ions, the limit of stability is reached for 7.2kV on the

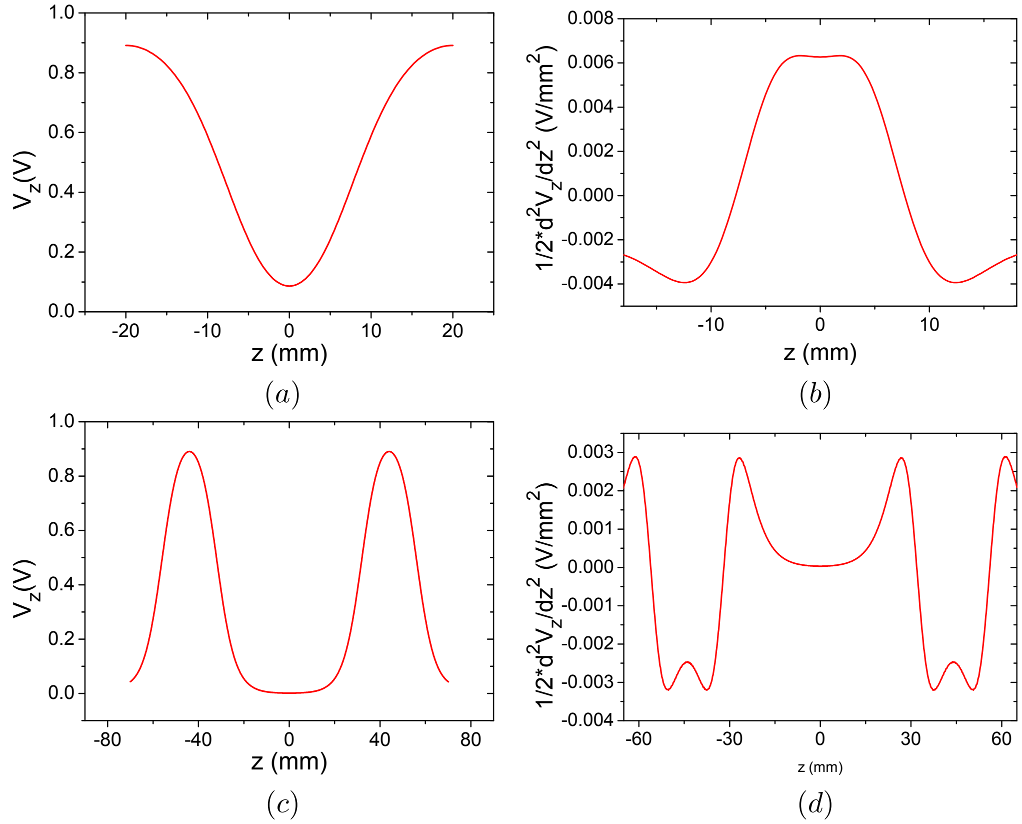

(a) (b) (c) (d)

Figure 9.19: (a) and (b) show the axial potential and curvature for $1V$ on the end-caps and -1.768V on the compensation electrodes, and (c) and (d) show the axial trap potential and curvature for 1V on the capture electrodes respectively while all other trap electrodes are grounded. The latter setup is for the more harmonic and orthogonalised trap which is required for resistive cooling.

capture electrodes as the curvature is approximately a factor of 2 smaller. In the experiment however, the electrode voltages have to be limited to 1.2kV due to the attached electronics. Therefore this sets a fundamental upper limit on the ion energy at the trap of 1keV/u, set by the potential barrier height along the axis at the position of the capture electrodes. This also implies that a minimum potential of $\Delta V_{pulse} = 4$kV must be switched by the pulsed drift tubes to remove the required kinetic energy.

For a conservative estimate of the switching speed required to close the trap potential, ^{207}Pb^{81+} ions with $KE = 1$keV/u, and a bunch length of 100mm are taken as the worst case scenario inside the trap. This implies for H-like lead ions, the velocity will be 274kms^{-1}, and therefore the switching needs to

Device	Minimum bunch length	Maximum energy removal
Einzel lens #1	500V	
Bender-outer electrode,V^{+}_{bender}	1340V	
Bender-inner electrode,V^{-}_{bender}	-1340V	
Quadrupole	500V	
Einzel lens #2	2950V	
Deflector	0V	
Einzel lens #3	2500V	
Pulsed drift tubes		
V^{+}_{pulse}	$2000(0 < V^{+}_{pulse} < 4000)$	$2000(0 < V^{+}_{pulse} < 4000)$
ΔV_{pulse}	4400V±50V	4700V±50V
δt	0.15μs	0.15μs
switch time	-0.47μs	-0.52μs
In trap		
Ion kinetic energy	600eV/u	300eV/u
$2\sigma_{x,y,z}$ bunch length	55mm±5mm	100mm±5mm
switch time	0.54μs	0.87μs
Maximum HITRAP ion bunch period for 0.15μs trap switching	4.7μs	6.6μs
Transport and capture efficiency	100% of $2\sigma_{x,y,z}$	

Table 9.1: A table showing a summary of the optimised SPECTRAP ion optics parameters for transport and in-flight capture of ^{207}Pb^{81+} HCI from the HITRAP facility.

be completed in a length of 20mm. This gives a maximum switching time of 0.7μs to capture all the ions inside $2\sigma_{x,y,z}$. This should easily be achievable with the current electronics. The hardware switch used for the pulsed drift tubes has two independent outputs and so can also be used for the trap. With a round trip of approximately 160mm between the capture electrodes, for this conservative estimate, HITRAP must provide bunched ions in a pulse of up to 3.6μs.

In the experiment, an ion-time-of-arrival detector will be made from a Schottky signal pickup from the upper capture electrode. This will be used to calibrate the switching time of the pulsed drift tubes and the closure of the trap with respect to a HITRAP ion ejection TTL pulse. From the simulation, the switching times have been recorded with respect the the ion bunch (CM) passing this virtual detector position at the centre of the upper capture electrode. These results along with a complete summary of the ion optics setup for optimised maximum compression of the ion bunch length and for maximum energy removal at the trap is shown in table 9.1.

9.3.4 Conclusion

These simulations have shown how $^{207}\mathrm{Pb}^{81+}$ ions can be transported and captured into the SPECTRAP ion trap at GSI with high efficiency. HITRAP should aim to deliver HCI ions according to their early (2009) specifications outlined in section 9.3.1.1 or to the limits set out in table 9.1. In addition to defining an exact set of optimum parameters for this system, the work reported here provides a qualitative understanding of best practices for each of the ion optics elements should any changes be implemented. The simulation of the entire system in SIMION further provides, although idealised, an off-line test of the system which is particularly useful as both the time when the magnet is energised ($\sim$ 1 week LHe hold time) and when HITRAP beam time is available ($\sim$ 1 week), is very limited.

9.4 Progress Report

The RETRAP superconducting magnet is an essential component of the SPECTRAP experiment. In 2007, during transport of RETRAP to GSI, the magnet suffered extensive damage that took (colleagues) a further two years to repair. In addition to this, delays in commissioning the HITRAP facility have meant that no HCI will be available to the SPECTRAP experiment until at least 2012. To allow preliminary tests to be made of the SPECTRAP sysem, local ion sources, namely $^{24}\mathrm{Mg}^{+}$ and $^{40}\mathrm{Ar}^{2+}$, were built. The ion sources are external to the magnet and thus allow testing of the final section of beamline. $^{24}\mathrm{Mg}^{+}$ was chosen because laser cooling and spectroscopy is relatively simple requiring only one laser, and $^{40}\mathrm{Ar}^{2+}$ was chosen because it can be abundantly produced and is also more likely to be detectable via the electronics due to the higher charge state. Later the $^{24}\mathrm{Mg}^{+}$ ions will also provide the ability to sympathetically cool HCI much more quickly and to lower temperatures than those achievable with resistive cooling. Photographs of the current setup are shown in Fig. 9.20. In order to use both ion sources simultaneously, the 90 degree (mono-directional) bender was replaced with a 2D (bi-direction) quadrupole bender. A Mg^{+} Doppler cooling laser was setup by R. Cazan in a laser laboratory constructed under the SPECTRAP platform and provides axial cooling. The 280nm induced fluorescence can be detected radially by a PMT provided by R. Jühren (Münster).

The magnet was energised to a conservative 4tesla in January 2011 for a period of approximately 2 weeks during which Z. Andjelkovic, R. Cazan and I attempted, for the first time, to load and detect ions in the trap. Ion transport through the system had already been optimised without the magnetic field with the aid of an MCP in the horizontal, and a Channeltron along the vertical, beamline above the magnet. The pressure measured in a room temperature region of the vacuum system was around 10^{-8}mbar, which implies around the cold-bore, it should have been at least two orders of magnitude lower and within acceptable limits for long ion lifetimes in the trap. All trap electrodes are attached to low-pass filter boards in the cryogenic environment and via large resistors to ground. The resistors provide a continuity check up to that position in the vacuum. After ramping the magnetic field and turning on the power supplies for the trap electronics, it was found that the electrical connection for the upper capture electrode was grounded. This meant that the

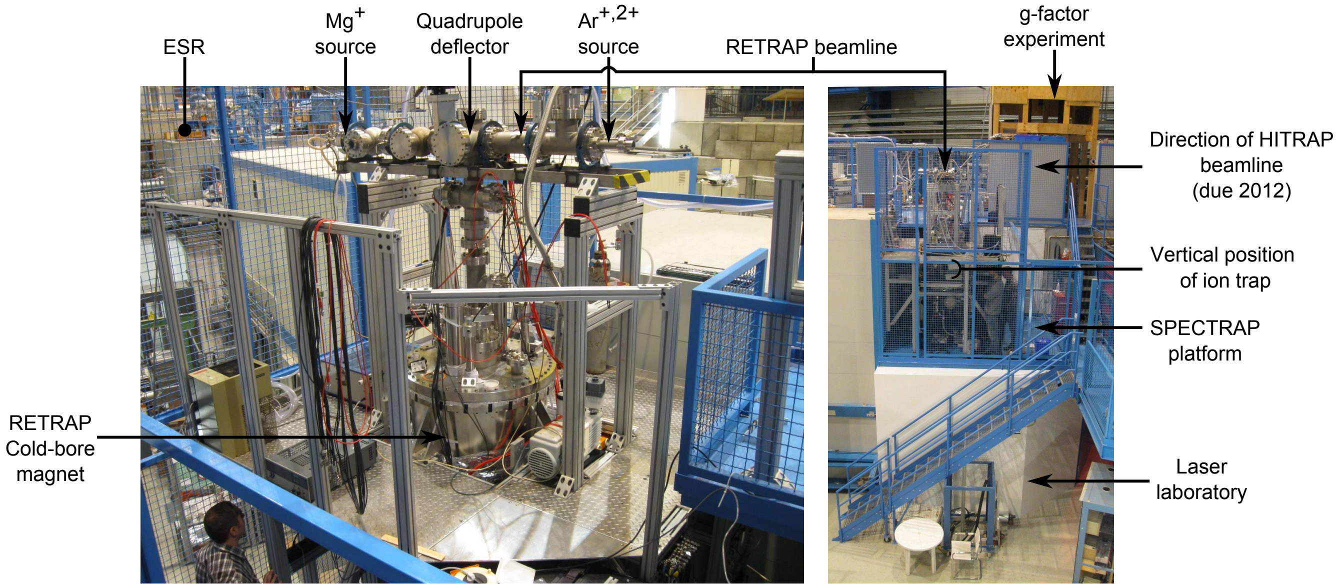

Figure 9.20: Photos showing the current status of the SPECTRAP experiment at GSI.

electrode itself was either grounded or floating and hence not able to perform its function. Attempts were made to capture the ions between the endcap electrodes, but no ions were electronically (^{40}Ar^{2+} or ^{24}Mg$^+$) or optically (^{24}Mg$^+$) detected. In the strong magnetic field, ions could not be deflected to the trap electrodes and so there was no real means of knowing whether ions were actually passing through the trap after energisation. The voltages on the ion optics and time of switching the trap and pulsed drift tube electrodes were also varied, with no success.

After this initial test, the system was opened and the electrical connection repaired. The MCP was then installed under the magnet in-line with the trap on a translation stage allowing throughput for the laser beam when required. The magnet was next energised in March 2011 after I had returned to the UK. During this period, again no trapped ions were detected. However the MCP under the magnet detected a large count rate after applying high voltages to the trap electrodes. This is believed to be a result of ions produced by electron impact ionisation of residual gas atoms from electrons produced by field emission from sharp features on the trap electrode surfaces and thereabouts.

A number of further changes were then made for the next stage of tests currently under way. Namely the electrode surfaces were polished, the vacuum system was pumped and baked for longer to reduce the residual gas pressure, an einzel lens was installed under the magnet to focus more ions onto the MCP, the possibly leaky Ar gas source was removed and a manual shutter was installed above the trap to stop the ballistic trajectory of residual gas atoms to the trap. Early results are very promising and show that $^{24}\mathrm{Mg}^{+}$ ions have been trapped, laser cooled to sub-kelvin temperatures and optically detected (as shown in Fig. 9.21). The major hindrance to progress has been the magnet. Because it has a cold-bore, each time the system is tested, the magnet must be cooled from room temperature and hence the time ($\sim$ 1 week) and financial cost ($\sim$ 2000 euro) is large. Therefore this process cannot be readily repeated. The trap and magnet coils are also mounted from the top large diameter ($\sim$ 1m) vacuum flange, and hence this must be removed with a crane for access. These factors result in a turn-around time between energisations of typically 1 month if changes inside the magnet need to be made. At this stage, the collaboration already has the detectors and laser system built (off-site) for spectroscopy of the much needed H-like Bismuth, but ultimately this must wait for the HITRAP facility to be commissioned in 2012. More detailed information on the overall progress of the SPECTRAP experiment can be found in the GSI annual reports [28] [78] [7] and the presentations of the annual collaborators' meetings [79]. The preliminary results reported here will be well documented in the theses of Z. Andjelkovic and R. Cazan to be published later this year.

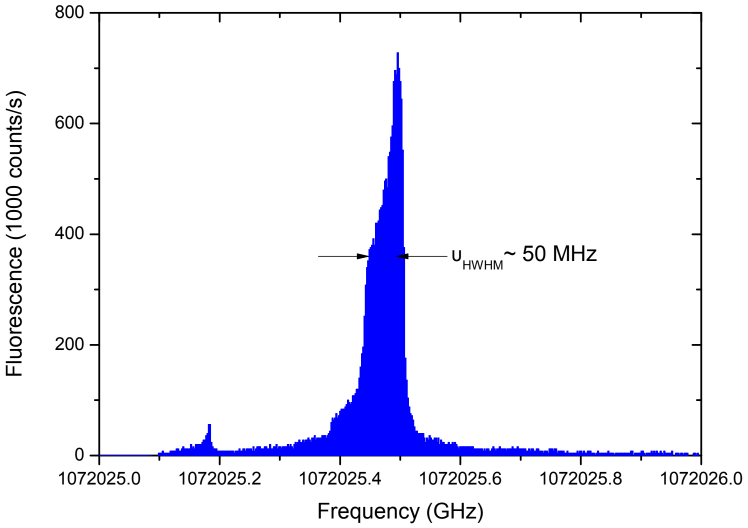

Figure 9.21: PMT fluorescence trace from $^{24}\mathrm{Mg}^{+}$ ions in the SPECTRAP at GSI as the Doppler cooling laser is scanned across the transition. The smaller peak in fluorescence is due to the Doppler width of the cloud momentarily being equal to the detuning of the laser.

Chapter 10

Closing Remarks and Suggestions for Further Work

The main motivation behind this thesis was to work towards performing laser spectroscopy of the ground-state HFS of HCI in the SPECTRAP experiment at GSI, as a test of certain bound-state QED calculations.

A prototype SPECTRAP ion trap was successfully operated as a Paul and Penning trap at Imperial College London. Paul trap operation proved very valuable in optimising the system without the physical constraints of the magnet, and the more complicated laser cooling scheme in the presence of Zeeman splitting inherent in the Penning trap. This is the first superconducting magnet Penning trap experiment in the group at Imperial College London, where fluorescence from Ca^+ ions has been observed. This is most likely due to the 'in-vacuum' spherical mirror and lens confocal arrangement which provided an effective way to align the imaging system without (first) seeing fluorescence from ions. This was critical because of the complexity in using a fibre optic bundle to relay wide-field fluorescence images of an ion cloud out of the magnet bore.

The experiments in London on a cloud of laser cooled $^{40}Ca^+$ ions showed that the rotating wall technique can compress an ion cloud without the need to ramp the frequency of the rotating wall drive from low values up to $\omega_c/2$. This answered one of the main open questions from the outset of this investigation, and will greatly simplify the application of the rotating wall technique at GSI.

On scanning the rotating wall drive from low frequencies up to $\omega_c/2$, heating resonances were observed and identified as being associated with the axial motion of ions in the trap potential, and the $\omega_{21}^{(1)}$ plasma mode. The width of the $\omega_{21}^{(1)}$ heating resonance, as observed via the fluorescence intensity, gives a clear indication of the persistent effects of this mode at low trap frequencies. A plot of these heating resonances (with widths) as a function of trap frequency can be used to optimally set the trapping and rotating wall parameters to avoid these ubiquitous heating effects at GSI, thus achieving maximum fluorescence for the spectroscopy of the weak HFS transitions in HCI. The rigid rotation frequency of an ion cloud about the axial magnetic field, has been shown to have an (unforeseen) effect on the application of radial laser cooling. Namely, the transition of ions is increasingly Doppler shifted away from the centre of the trap, across the width of the laser beam. This implies much of the laser beam cross-section (and power) in these experiments was not resonant with the transition of all ions in the beam, and so was wasted. Therefore in the future where possible, the fluorescence to background laser scatter ratio can be optimised by using an appropriately (smaller in this case) sized laser beam waist.

Simulations were conducted of ion transport and in-flight capture in the SPECTRAP ion trap at GSI, that provide: (i) a set of optimum ion optics parameters for one of the first spectroscopic candidates of interest (^{207}Pb^{81}); (ii) a qualitative understanding of the flight of ions through the complex system; (iii) upstream requirements for the bunched HCI for the HITRAP facility. During attempts at trapping at GSI, this (SIMION) simulation was used several times to test various assumptions and particular experimental parameters that gave high count rates on the particle detectors. The recent experimental results presented here have demonstrated loading ^{24}Mg^{+} ions from an external source, laser cooling to sub-kelvin temperatures and optical detection. There are several routes the experiment can take now, before the HITRAP facility delivers HCI in 2012, and this will be decided at the next SPECTRAP collaborators meeting.

Finally some very interesting effects were seen during trapping in London at low rotating wall frequencies ($\approx \omega_m$). Radially discontinuous fluorescence images of ion clouds were observed for particular Doppler cooling laser frequencies.

An example of such an image is shown in Fig. 10.1. Time did not permit the further investigation of this effect, but a possible explanation could be a non-uniform radial cloud rotation frequency which would produce a Doppler shift in the transition of ions along the direction of the laser beam. At low ion number densities expected around $\omega_r \sim \omega_m$, the Deybe length could become comparable to the cloud dimensions and so the density and cloud rotation frequency would vary across much of the ion cloud. These observations were quite repeatable and rather robust. They are therefore rather left to colleagues to investigate further.

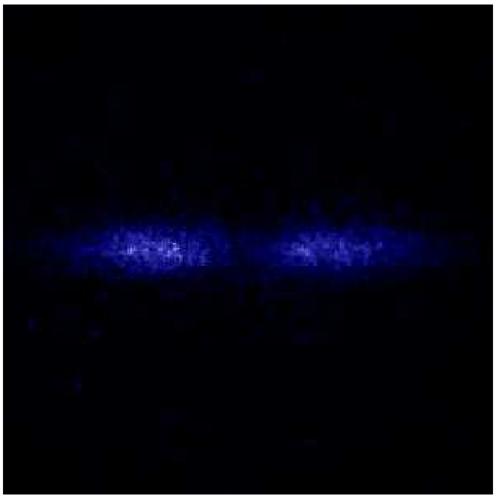

Figure 10.1: A image of a cloud of ^{40}Ca^{+} ions in the London SPECTRAP operating as a Penning tap with $B = 1.75$T, $U_0 = 130$V, $V_{rot} = 1.5$V and $\omega_{rot} \approx \omega_m$. The laser frequencies or detunings relative to maximum fluorescence were not recorded at the time.

Appendix A

SPECTRAP Feedthrough Wiring Diagram

A wiring schematic diagram for the Imperial College London SPECTRAP ion trap vacuum vessel.

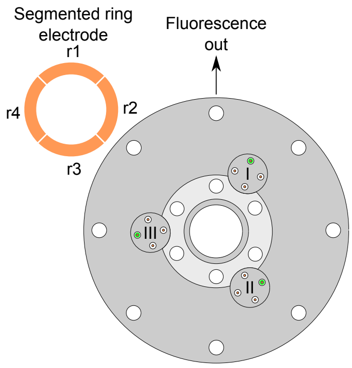

Feedthrough Connection		Electrode
Group	Pin	
I	I	Ring segment, r1
	II	Ring segment, r3
	III	Ring segment, r2
	IV	Ring segment, r4
II	I	Filament
	II	Upper compensation, c1
	III	Lower compensation, c2
	IV	Oven
III	I	Filament
	II	Lower endcap, e2
	III	Upper endcap, e1
	IV	Oven

Figure A.1: SPECTRAP feedthrough wiring diagram. The illustration (left) shows three groups of four pins and their internal connections (right) on the 80mm diameter top vacuum flange. Pin one in each group is highlighted in green and the numbers increment in a clockwise fashion when viewed from above.

Appendix B

SPECTRAP Experimental Setup

A photograph of the Imperial College London SPECTRAP experiment outside the superconducting magnet. The lasers are prepared on the adjacent optical table and transported to the SPECTRAP platform via optical fibres.

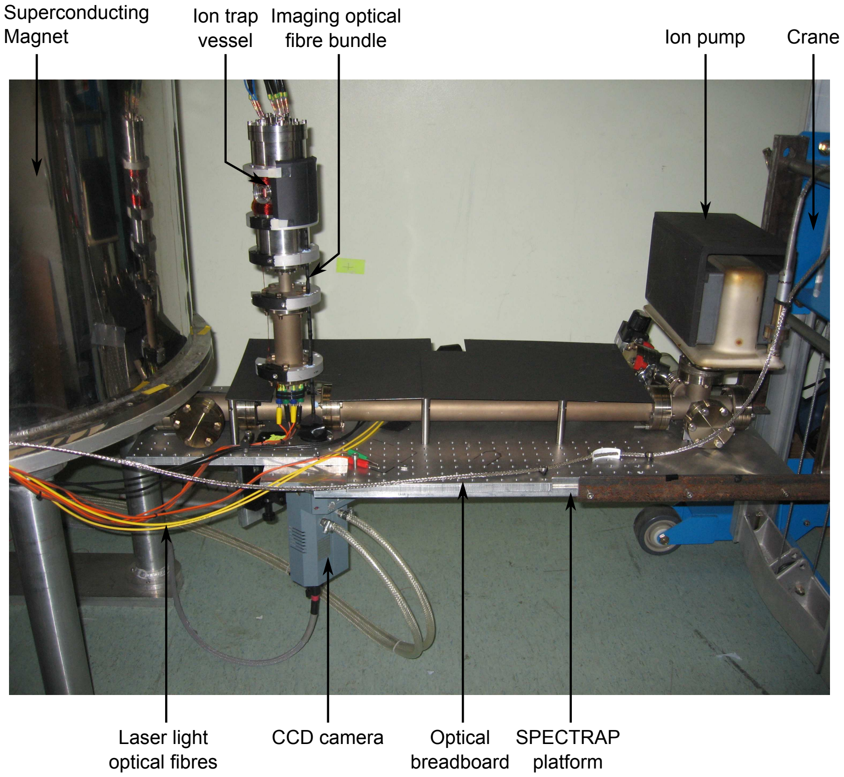

Figure B.1: A photograph of the Imperial College SPECTRAP ion trap in vacuum, with a CCD camera detector attached as it would be when installed inside the bore of the superconducting magnet.

Appendix C

Rotating Wall Results Error Analysis

The noise on the calculated fluorescence intensity (I_γ) from each recorded image was dominated by the small number of photoelectrons emitted from the photocathode ($\mu_{CCD} \times I_\gamma$) before amplification of the charge by the MCP. Therefore the noise in the fluorescence intensity δI_γ scales with the total number of photons per second per pixel I_γ (including the laser scatter), the length of the exposure time t_{expo}, the number of pixels averaged over N_{pixel} and the number of accumulated frames per image N_{accum} according to

$$\delta I_\gamma = \frac{\sqrt{I_\gamma}}{\sqrt{\mu_{CCD} \times t_{expo} \times N_{pixels} \times N_{accum}}} \tag{C.0.1}$$

where the $1/\sqrt{\mu_{CCD}}$ factor comes from the conversion of photoelectrons to photons. The errors according to equation (C.0.1) were automatically calculated using the Matlab program for each data point measured and have been included in the following results.

For graphs where intensity profiles along a line (line-profiles) are measured, a line of best fit is obtained by Fourier filtering the data signal to remove fluctuations (noise) with a spatial periodicity smaller than 0.1mm or approximately one third the dimensions of the smallest typical ion cloud. For these graphs, the data points are dense due to the resolution of the camera. Therefore an error bar is only displayed at the extreme values in fluorescence intensity to give the reader an indication of the level of noise.

For graphs where an average fluorescence intensity (inside the FWHM) is measured across an ion cloud, a line of best fit is obtained by calculating a moving average over 2-3 data points, except over a region where there is a sharp feature such as a resonance where the line is forced to go through the data points unless otherwise stated.

In order to avoid hysteresis effects from heating resonances, the rotating wall frequency is always abruptly changed from a resonance free region (typically at or above $\omega_{rot} = \omega_c/2$) to the frequency required for measurement.

Appendix D

SPECTRAP Confocal Imaging

A diagram illustrating the confocal imaging system employed inside the vacuum system around the SPECTRAP ion trap at Imperial College London. Rays are traced from a laser beam with an exaggerated axial offset on a prolate ion cloud showing how the CCD camera images are (in principle) produced.

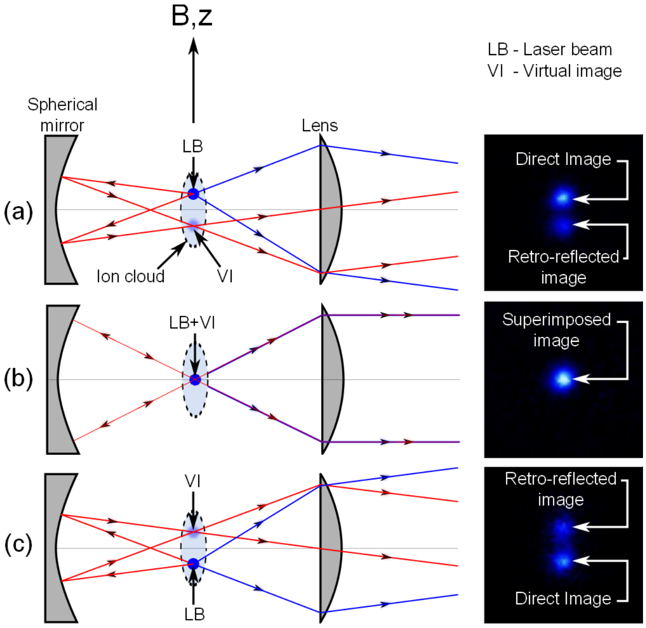

Figure D.1: (left) a race trace diagram showing the 'in-vacuum' confocal arrangement of the spherical mirror and lens with three different axial positions of the laser beam through a prolate ion cloud, with the corresponding (right) CCD camera images of such a setup with the trapping parameters of $U_0 = 5\text{V}$, $\omega_{rot} = \omega_c/2$ and $V_{rot} = 1.5\text{V}$.

Appendix E

Matlab Script to Analyse ICCD Camera Images

A Matlab script to rotate, remove background laser scatter, produce radial and axial line profiles, and calculate an average fluorescence intensity across an image of an ion cloud captured using the Andor intensified CCD camera. The shot noise is also calculated for the above fluorescence measurements. More detailed information can be obtained by reading the comments in the script.

```
clear all;close all
set(0,'DefaultTextInterpreter','none')
files = dir('*.sif');
g=[];
ctsperphoton=3780*0.96*0.14*2.44;     %3780 counts per photon at 0A
      mag field , 0.96 window transmission , 0.14 photocathode
    transmission at 397 and x2.44 gain enhancement at 70A mag field
    .
file_1=fopen('rot_wall_amplitude_scan_integrated_intensity.csv','w
    ');        %file to save integrated fluorescence output.
file_3=fopen('rot_wall_FWHM.csv','w');
%Gaussian_psf=fspecial('Gaussian',100,12.0/2);    %point spread
    function of the aberrations in the system.
%decon_iterations=12;    % should be 12 number of iterations of the
      blind deconvolution algorithm to perform properly - tested on
    2D Gaussian image.
image_rotation=-37;     % rotation angle of the image to make cloud
      (r,z) axis align with (x,y) axis.
deconv_flag=0;          %flag to perform deconvolution.
```

```
pixel_area=0.013*0.013;     %pixel area is mm squared.

centre_column_index=243;    %manually entered centre coordinates
    of the cloud for background scatter removal....
centre_row_index=245;       %this should be checked for each sif
    data set in case the camera capture pixel area was changes.

scatter_centre_column_index=230;    %centre of the background
    laser scatter image....
scatter_centre_row_index=265;       %this is static as the same
    saved scatter image is loaded each time.
ext_image_size=110;                 %half length of the image to
    be cut-out of the background scatter removed oversized image.
load scatter.mat                    %loads background scatter
    image.
scatter_sum=0;
norm_singlet=0;
sum_radius=90;      %radius of circular aperture boundary around
    the centre of the cloud to sum inside i.e. restricts the
    integration of fluorescence inside the FWHM region inside the
    boundary of the fibre.


for aa=1:1:38
    for bb=1:1:54
        scatter_sum=scatter_sum+scatter(scatter_centre_row_index
            -88+bb,scatter_centre_column_index-78+aa);     %sums an
            isolated area of the scatter image for scaling
            background removal.
    end
end

for lmn=1:length(files)
    a(2)=sifread(files(lmn).name);
    if length(a(2).imageData(1,1,:))==1
        if max(max(a(2).imageData(:,:,1)/((a(2).exposureTime)*
            ctsperphoton*a(2).accumulateCycles)))>norm_singlet
            norm_singlet=max(max(a(2).imageData(:,:,1)/((a(2).
                exposureTime)*ctsperphoton*a(2).accumulateCycles)))
                ;    %this number is used to scale the colormap for
                single sif file image sets.
        end
    end
end
```

```
for i=1:length(files)
a(1)=sifread(files(i).name);

figwidth=900;
figheight=310;
fig1=figure(1);
load('MyColormaps','mycmap');
set(fig1,'Colormap',mycmap);
set(fig1,'Color',[1 1 1]);
set(fig1,'Position',[5 5 figwidth figheight]);
set(fig1,'NextPlot','replacechildren');

figwidth2=300;
figheight2=300;
fig2=figure(2);
load('MyColormaps','mycmap');
set(fig2,'Colormap',mycmap);
set(fig2,'Color',[1 1 1]);
set(fig2,'Position',[5 395 figwidth2 figheight2]);
set(fig2,'NextPlot','replacechildren');

figwidth3=300;
figheight3=300;
fig3=figure(3);
load('MyColormaps','mycmap');
set(fig3,'Colormap',mycmap);
set(fig3,'Color',[1 1 1]);
set(fig3,'Position',[400 395 figwidth2 figheight2]);
set(fig3,'NextPlot','replacechildren');



if length(a(1).imageData(1,1,:))>1      % this loop runs for a sif "
    movie" file.
figure(1);
file_2=fopen(strcat(sprintf(files(i).name,i),'.frame.','
    rot_wall_amplitude_scan_integrated_intensity.csv'),'w');
numframes=length(a(1).imageData(1,1,:));
winsize = [50 2 900 310];
winsize(1:2) = [0 0];
A=moviein(numframes,fig1,winsize);

norm=max(max(max(a(1).imageData(:,:,:))));
for l=1:length(a(1).imageData(1,1,:))
```

```
subplot(1,3,1);
p=get(subplot(1,3,1), 'pos');
p(1)=((p(1)*figwidth)-68)/figwidth;
p(2)=p(2)*1.1;
p(3)=p(3)*1.2;
p(4)=p(3)*figwidth/figheight;
set(subplot(1,3,1), 'pos', p);
b=imrotate((a(1).imageData(:,:,1)),image_rotation);    %extracts
    the image data from the andor sif file and rotates.
if deconv_flag==1
  b=deconvblind(b,gaussian_psf,decon_iterations);    %deconvolutes
       to remove defocus.
end
%%%
ee=0;
b_sum=0;
for aa=1:1:38
    for bb=1:1:54
        b_sum=b_sum+b(centre_row_index-88+bb,centre_column_index
            -78+aa);    %integrates a patch of background laser
            scattered in the ion image.
    end
end
ee=b;
for cc=1:1:290    %row
    for dd=1:1:290    %column
        ee(centre_row_index+cc-145-1,centre_column_index+dd-145-1)
            =abs(b(centre_row_index+cc-145-1,centre_column_index+dd
            -145-1)-(b_sum/scatter_sum)*scatter(
            scatter_centre_row_index+cc-145-1,
            scatter_centre_column_index+dd-145-1));    %removes
            laser background scatter from image but only around the
             fibre bundle.
    end
end

ff=[];
for ccc=1:1:ext_image_size*2
    for ddd=1:1:ext_image_size*2
        ff(ccc,ddd)=ee(centre_row_index+ccc-ext_image_size-1,
            centre_column_index+ddd-ext_image_size-1);    %extracts
             the background laser scatter removed image of the ions
             around the fibre bundle.
    end
end
```

```
b=ee;
%%%
subplot(1,1,1);
imagesc(ff, [ 0 norm ]);
set(gca, 'visible', 'off')
p=get(subplot(1,1,1), 'pos');
p(1)=0;
p(2)=0;
p(3)=p(3)*1.29;
p(4)=p(3);
set(subplot(1,1,1), 'pos', p);

figure(3);
subplot(1,1,1);
imagesc(b, [ 0 norm ]);
set(gca, 'visible', 'off')
p=get(subplot(1,1,1), 'pos');
p(1)=0;
p(2)=0;
p(3)=p(3)*1.29;
p(4)=p(3);
set(subplot(1,1,1), 'pos', p);

figure(1);
imagesc(ff, [ 0 norm ]);
title_handle = title(strcat(sprintf(files(i).name,i),'.',num2str(l
    )),'FontSize',8);
t=get(title_handle,'position');
t(2)=t(2)*3.5;
t(1)=t(1)*3;
set(title_handle,'position',t);
subplot(1,3,2);
p=get(subplot(1,3,2), 'pos');
p(1)=((p(1)*figwidth)-30)/figwidth;
p(2)=p(2)*1.1;
p(3)=p(3)*1.2;
p(4)=p(3)*figwidth/figheight;
set(subplot(1,3,2), 'pos', p);
[S1,I1]=max(sum(b,1));    %finds the column index with maximum
    fluorescence and returns the index I1 or x-pixel centre.
%
offset=0;
cumalative=cumsum(b(:,I1));    %now dealing with the z-profile
    data of the cloud.
for n=1:1:length(b(:,I1))
```

```
    if (cumalative(n)>cumalative(length(b(:,I1)))/2) && offset==0
            %finds the middle of the fluorescence distribution by
        looking for 50% of integrated intensity index.
    offset=n;
        end
end
for m=1:1:length(b(:,I1))
    zmm(m)=(m- offset)*13/1000;       %creates z axis which is
        centred on the middle of the fluorescence distribution.
end
%get(gca)
c=0;
for k=1:1:3
    c=c+b(:,I1-2+k);    %for line profile plots, data over 3 lines
         is summed to reduce noise.
end
plot(zmm,c/((a(1).exposureTime)*ctsperphoton*a(1).accumulateCycles
    *3));       % plots the line profile with the fluorescence in
    units of photons/s/pixel.
%plot(xmm,b(:,I1))
title(strcat('axial␣line␣profile␣through␣column␣index␣=␣', num2str
    (I1)),'FontSize',8);
xlabel('z␣(mm)');
ylabel('Fluorescence␣(photons/s)');
set(gca,'XLim', [-1.8 1.8]);
set(gca,'xtick', [-1.5 -1.0 -0.5 0 0.5 1.0 1.5]);


%


subplot(1,3,3);
p=get(subplot(1,3,3), 'pos');
p(1)=((p(1)*figwidth)+10)/figwidth;
p(2)=p(2)*1.1;
p(3)=p(3)*1.2;
p(4)=p(3)*figwidth/figheight;
set(subplot(1,3,3), 'pos', p);
[S2,I2]=max(sum(b,2));      %finds the row index with maximum
    fluorescence and returns the index I2 or z-pixel centre.
%

offset2=0;
cumalative=cumsum(b(I2,:));      %now dealing with the r-profile
    data of the cloud.
for p=1:1:length(b(I2,:))
```

```
    if (cumalative(p)>cumalative(length(b(I2,:)))/2) && offset2==0
            %finds the middle of the fluorescence distribution by
        looking for 50% of integrated intensity.
        offset2=p;
    end
end
for q=1:1:length(b(I2,:))
    rmm(q)=(q- offset2)*13/1000;     %creates r axis which is
        centred on the middle of the fluorescence distribution.
end
%get(gca)
d=0;
for q=1:1:3
    d=d+b(I2-2+q,:);     %for line profile plots, data over 3 lines
         is summed to reduce noise.
end
plot(rmm,d/((a(1).exposureTime)*ctsperphoton*a(1).accumulateCycles
    *3));       % plots the line profile with the fluorescence in
    units of photons/s/pixel.
%plot(ymm,b(I2,:));

title(strcat('radial␣line␣profile␣through␣row␣index␣=␣', num2str(
    I2)),'FontSize',8);
xlabel('r␣(mm)');
ylabel('Fluorescence␣(photons/s)');
set(gca,'XLim', [-1.8 1.8]);
set(gca,'xtick', [-1.5 -1.0 -0.5 0 0.5 1.0 1.5]);
%
set(fig1, 'Visible', 'on');
    frame = getframe(fig1);
    %set(fig1,'Visible','off');
    imagen = frame.cdata;
    imwrite(imagen, strcat(sprintf(files(i).name,i),'.frame.',
        num2str(1),'.tif'));

A(:,1)=getframe(fig1,winsize);     %adds the image to an array
    which will contain all files in the "movie"


flu_sum=0;
flu_area=0;
flu_boundary=0.5*max(max(b));
for qq=-sum_radius-1:1:sum_radius+1
    for kk=-sum_radius-1:1:sum_radius+1
```

```
            if (qq^2+kk^2<=sum_radius^2) && (b(centre_row_index+qq,
                centre_column_index+kk)>flu_boundary)
                    flu_sum=flu_sum+b(centre_row_index+qq,
                        centre_column_index+kk);    %this sums the
                        counts and number of pixels that are inside
                        the fibre bundle and within 50% of the peak
                        counts.
                    flu_area=flu_area+1;

            end
        end
end
flu_intensity=flu_sum/((a(1).exposureTime)*ctsperphoton*a(1).
    accumulateCycles*flu_area);
flu_noise=sqrt(flu_intensity+3)/sqrt(((0.134*a(1).exposureTime)*a
    (1).accumulateCycles*flu_area));
fprintf(file_2,'%s, %5.3e,%5.3e,%5.3e, %5.3e, %5.3e, %5.3e\r\n',
    sprintf(files(i).name,i),flu_sum/((a(1).exposureTime)*
    ctsperphoton*a(1).accumulateCycles),flu_area,a(1).exposureTime,
    a(1).accumulateCycles, flu_intensity, flu_noise);    %the
    integrated fluorescence and integrated fluorescence normalised
    by the associated pixel area is saved to file.

end
fclose(file_2);
end


if length(a(1).imageData(1,1,:))==1   %script for single sif data
    files.
figure(1);
subplot(1,3,1);
p=get(subplot(1,3,1), 'pos');
p(1)=((p(1)*figwidth)-68)/figwidth;
p(2)=p(2)*1.1;
p(3)=p(3)*1.2;
p(4)=p(3)*figwidth/figheight;
set(subplot(1,3,1), 'pos', p);
b=imrotate((a(1).imageData(:,:,1)),image_rotation);    %extracts
    the image data from the andor sif file and rotates.
%colorscale=(max(max(b))/norm_singlet);
%%%
ee=0;
b_sum=0;
for aa=1:1:38
```

```
    for bb=1:1:54
        b_sum=b_sum+b(centre_row_index-88+bb,centre_column_index
            -78+aa);    %integrates a patch of background laser
            scattered in the ion image.
    end
end
ee=b;
for cc=1:1:290    %row
    for dd=1:1:290    %column
        ee(centre_row_index+cc-145-1,centre_column_index+dd-145-1)
            =abs(b(centre_row_index+cc-145-1,centre_column_index+dd
            -145-1)-(b_sum/scatter_sum)*scatter(
            scatter_centre_row_index+cc-145-1,
            scatter_centre_column_index+dd-145-1));    %removes
            laser background scatter from image but only around the
             fibre bundle
    end
end

ff=[];
for ccc=1:1:ext_image_size*2
    for ddd=1:1:ext_image_size*2
        ff(ccc,ddd)=ee(centre_row_index+ccc-ext_image_size-1,
            centre_column_index+ddd-ext_image_size-1);    %extracts
             the background laser scatter removed image of the ions
             around the fibre bundle.
    end
end
b=ee;
%%%
if deconv_flag==1
  b=deconvblind(b,gaussian_psf,decon_iterations);    %
      deconvolutes to remove defocus.
end
imagesc(ff/((a(1).exposureTime)*ctsperphoton*a(1).accumulateCycles
    ), [ 0 norm_singlet*1.2 ]);

figure(2);
subplot(1,1,1);
imagesc(ff/((a(1).exposureTime)*ctsperphoton*a(1).accumulateCycles
    ), [ 0 norm_singlet*1.2 ]);
set(gca, 'visible', 'off')
p=get(subplot(1,1,1), 'pos');
p(1)=0;
p(2)=0;
```

```
p(3)=p(3)*1.29;
p(4)=p(3);
set(subplot(1,1,1), 'pos', p);

figure(3);
subplot(1,1,1);
imagesc(b/((a(1).exposureTime)*ctsperphoton*a(1).accumulateCycles)
    , [ 0 norm_singlet*1.2 ]);
set(gca, 'visible', 'off')
p=get(subplot(1,1,1), 'pos');
p(1)=0;
p(2)=0;
p(3)=p(3)*1.29;
p(4)=p(3);
set(subplot(1,1,1), 'pos', p);

figure(1);
xlabel('pixel');
ylabel('pixel');
title_handle = title(sprintf(files(i).name,i),'FontSize',8);
t=get(title_handle,'position');
t(2)=t(2)*3.5;
t(1)=t(1)*3;
set(title_handle,'position',t);
subplot(1,3,2);
p=get(subplot(1,3,2), 'pos');
p(1)=((p(1)*figwidth)-30)/figwidth;
p(2)=p(2)*1.1;
p(3)=p(3)*1.2;
p(4)=p(3)*figwidth/figheight;
set(subplot(1,3,2), 'pos', p);
[S1,I1]=max(sum(b,1));      %finds the column index with maximum
    fluorescence and returns the index I1 or x-pixel centre.
%
offset=0;
cumalative=cumsum(b(:,I1));     %now dealing with the z-profile
    data of the cloud.
for n=1:1:length(b(:,I1))
    if (cumalative(n)>cumalative(length(b(:,I1)))/2) && offset==0
            %finds the middle of the fluorescence distribution by
        looking for 50% of integrated intensity.
        offset=n;
    end
end
for m=1:1:length(b(:,I1))
```

```
    zmm(m)=(m- offset)*13/1000;    %creates z axis which is
        centred on the middle of the fluorescence distribution.
end
%get(gca)
c=0;
for k=1:1:3
    c=c+b(:,I1-2+k);    %for line profile plots, data over 3 lines
         is summed to reduce noise.
end
plot(zmm,c/((a(1).exposureTime)*ctsperphoton*a(1).accumulateCycles
    *3));    % plots the line profile with the fluorescence in
    units of photons/s/pixel.
%plot(zmm,b(:,I1))
title(strcat('axial␣line␣profile␣through␣column␣index␣=␣', num2str
    (I1)),'FontSize',8);
xlabel('z␣(mm)');
ylabel('Fluorescence␣(photons/s/pixel)');
set(gca,'XLim', [-1.8 1.8]);
set(gca,'xtick', [-1.5 -1.0 -0.5 0 0.5 1.0 1.5]);
u=0;
for f=1:1:3
    u=u+b(:,centre_column_index-2+k);    %records z-profile
        through fixed column index to compare multiple images with
        various z-position beam offsets.
end
g(:,i)=u; %array that contains z-profiles of images to measure the
     axial extent of the cloud.
%

subplot(1,3,3);
p=get(subplot(1,3,3), 'pos');
p(1)=((p(1)*figwidth)+10)/figwidth;
p(2)=p(2)*1.1;
p(3)=p(3)*1.2;
p(4)=p(3)*figwidth/figheight;
set(subplot(1,3,3), 'pos', p);
[S2,I2]=max(sum(b,2));    %finds the row index with maximum
    fluorescence and returns the index I2 or z-pixel centre.
%

offset=0;
cumalative=cumsum(b(I2,:));    %now dealing with the r-profile
    data of the cloud.
for p=1:1:length(b(I2,:))
```

```
    if (cumalative(p)>cumalative(length(b(I2,:)))/2) && offset==0
            %finds the middle of the fluorescence distribution by
        looking for 50% of integrated intensity.
        offset=p;
    end
end
for q=1:1:length(b(I2,:))
    rmm(q)=(q- offset)*13/1000;      %creates r axis which is
        centred on the middle of the fluorescence distribution.
end
%get(gca)
d=0;
for q=1:1:3
    d=d+b(I2-2+q,:);      %for line profile plots, data over 3 lines
         is summed to reduce noise
end

plot(rmm,d/((a(1).exposureTime)*ctsperphoton*a(1).accumulateCycles
    *3));      % plots the line profile with the fluorescence in
    units of photons/s/pixel.
%plot(rmm,b(I2,:))
title(strcat('radial␣line␣profile␣through␣row␣index␣=␣', num2str(
    I2)),'FontSize',8);
xlabel('r␣(mm)');
ylabel('Fluorescence␣(photons/s/pixel)');
set(gca,'XLim', [-1.8 1.8]);
set(gca,'xtick', [-1.5 -1.0 -0.5 0 0.5 1.0 1.5]);




set(figure(1), 'Visible', 'on');      %script to save figure to file
    frame = getframe(figure(1));
    %set(fig1,'Visible','off');
    imagen = frame.cdata;
    imwrite(imagen, strcat(sprintf(files(i).name,i),'.tif'));
saveas(figure(1),strcat(sprintf(files(i).name,i),'.fig'),'fig')

set(figure(2), 'Visible', 'on');
    frame = getframe(figure(2));
    %set(fig1,'Visible','off');
    imagen = frame.cdata;
    imwrite(imagen, strcat(sprintf(files(i).name,i),'.raw.tif'));
saveas(figure(2),strcat(sprintf(files(i).name,i),'.raw.fig'),'fig'
    )
```

```
flu_sum=0;
flu_area=0;
flu_boundary=0.5*max(max(b));
for qq=-sum_radius-1:1:sum_radius+1
    for kk=-sum_radius-1:1:sum_radius+1
        if (qq^2+kk^2<=sum_radius^2) && (b(centre_row_index+qq,
            centre_column_index+kk)>flu_boundary)
                flu_sum=flu_sum+b(centre_row_index+qq,
                    centre_column_index+kk);    %this sums the
                    counts and number of pixels that are inside
                    the fibre bundle and within 50% of the peak
                    counts.
                flu_area=flu_area+1;

        end
    end
end
flu_intensity=flu_sum/((a(1).exposureTime)*ctsperphoton*a(1).
    accumulateCycles*flu_area);
flu_noise=sqrt(flu_intensity+3)/sqrt(((0.134*a(1).exposureTime)*a
    (1).accumulateCycles*flu_area));
fprintf(file_1,'%s␣,␣%5.3e,%5.3e,␣%5.3e,%5.3e,%5.3e,␣%5.3e\r\n',
    sprintf(files(i).name,i),flu_sum/((a(1).exposureTime)*
    ctsperphoton*a(1).accumulateCycles), flu_area, a(1).
    exposureTime,a(1).accumulateCycles, flu_intensity, flu_noise);
        %the integrated fluorescence and integrated fluorescence
    normalised by the associated pixel area is saved to file.

%%
d_width=0;
for qqq=1:length(d)
        if d(qqq)>d_boundary
            d_width=d_width+1;

        end
end

c_boundary=0.5*max(max(c));
c_width=0;
for kkk=1:length(c)
        if c(kkk)>c_boundary
            c_width=c_width+1;
```

```
        end
end

fprintf(file_3,'%s␣,␣%5.3e,␣%5.3e\r\n',sprintf(files(i).name,i),
    d_width*0.013,c_width*0.013);
%%%
rrr=0;
zzz=0;
rmm_extract=[];
zmm_extract=[];
for rmmi=1:length(rmm)
    if abs(rmm(rmmi))<1.5
        rrr=rrr+1;
        rmm_extract(rrr)=rmm(rmmi);
        radial_extract(rrr)=d(rmmi)/((a(1).exposureTime)*
            ctsperphoton*a(1).accumulateCycles*3);     %extracts
            radial profile data across the centre of the cloud.
    end
end
for zmmi=1:length(zmm)
    if abs(zmm(zmmi))<1.5
        zzz=zzz+1;
        zmm_extract(zzz)=zmm(zmmi);
        axial_extract(zzz)=c(zmmi)/((a(1).exposureTime)*
            ctsperphoton*a(1).accumulateCycles*3);     %extracts
            axial profile data across the centre of the cloud.
    end
end
radialprofile(:,1)=rmm_extract;
radialprofile(:,2)=radial_extract;
radialprofile(:,3)=sqrt(radial_extract+3)/sqrt((a(1).exposureTime)
    *3*0.134*a(1).accumulateCycles);

axialprofile(:,1)=zmm_extract;
axialprofile(:,2)=axial_extract;
axialprofile(:,3)=sqrt(axial_extract+3)/sqrt((a(1).exposureTime)
    *3*0.134*a(1).accumulateCycles);

cellwrite(strcat(sprintf(files(i).name,i),'.z_profile','.csv'),
    axialprofile);
cellwrite(strcat(sprintf(files(i).name,i),'.r_profile','.csv'),
    radialprofile);
%%%
clear zmm rmm offset;
end
```

```
if length(a(1).imageData(1,1,:))>1 && length(A)==length(a(1).
    imageData(1,1,:))
     framerate=5;
%movie(fig1,A,1,framerate,winsize)
%save(strcat(sprintf(files(i).name,i),'.movie.mat'), 'A', '-mat')
for e=1:length(A)
     for f=1:1:2
          Z(f-2+(e*2))=A(e);        %creates an mpg movie.
     end
end

%mpgwrite(Z,mycmap,strcat(sprintf(files(i).name,i),'.mpg'));




end




end
% code to superimpose axial line-profiles
% the relative offset positions of all line-profiles are
    maintained
aaa=0;
for q=1:length(g(1,:))
     if max(g(:,q))> aaa;
                    aaa=max(g(:,q));
                    qq=q;
     end
end

offsetq=0;
cumalative=cumsum(g(:,qq));        %now dealing with the r-profile
    data of the cloud.
for p=1:1:length(g(:,qq))
     if (cumalative(p)>cumalative(length(g(:,qq)))/2) && offsetq==0
             %finds the middle of the fluorescence distribution by
         looking for 50% of integrated intensity.
          offsetq=p;
     end
end
for q=1:1:length(g(:,qq))
     zqmm(q)=(q- offsetq)*13/1000;      %creates r axis which is
          centred on the middle of the fluorescence distribution.
end
```

```
figure(4)
plot(zqmm, g(:,:)/((a(1).exposureTime)*ctsperphoton*a(1).
    accumulateCycles*3))
xlabel('z␣(mm)');
ylabel('Fluorescence␣(photons/s/pixel)');
set(gca,'XLim', [-1.8 1.8]);
set(gca,'xtick', [-1.5 -1.0 -0.5 0 0.5 1.0 1.5]);
%%%%

fclose(file_1);
```

Bibliography

[1] S. Bharadia, M. Vogel, D. M. Segal, R. C. Thompson, Dynamics of laser-cooled Ca^+ ions in a Penning trap with a rotating wall, *Accepted for publication in Appl. Phys. B* (2011).

[2] B. Odom, D. Hanneke, B. D'Urso, and G. Gabrielse, New measurement of the electron magnetic moment using a one-electron quantum cyclotron, *Phys. Rev. Lett.*, **97**, 030801 (2006).

[3] D. Hanneke, S. Fogwell, and G. Gabrielse, New measurement of the electron magnetic moment and the fine structure constant, *Phys. Rev. Lett.*, **100**, 120801 (2008).

[4] T. Beier, The g_j factor of a bound electron and the hyperfine structure splitting in hydrogenlike ions, *Phys. Rep.*, **339**, 79–213 (2000).

[5] M. P. Stockli, R. M. Ali, C. L. Cocke, M. L. A. Raphaelian, P. Richard, and T. N. Tipping, The KSU-CRYEBIS: A unique ion source for low-energy highly charged ions, *Rev. Sci. Instrum.*, **63**, 2822 (1992).

[6] R. E. Marrs, S. R. Elliot, and D. A. Knapp, Production and trapping of hydrogen like and bare uranium ions in an electron-beam ion-trap, *Nuc. Inst. and Meth. in Phys. Research A*, **357**, 110–114 (1994).

[7] Z. Andjelkovic, C. Geppert, J. Krämer, W. Nörtershäuser, M. Vogel, V. Hannen, C. Weinheimer, D. F. A. Winters, D. Church, D. Schneider, S. Bharadia, D. M. Segal, and R. Thompson, Development of the SPECTRAP experimental setup for laser spectroscopy of cold and trapped HCI, *GSI scientific report*, page 291 (2007).

[8] W. Quint, J. Dilling, S. Djekic, H. Häffner, N. Hermanspahn, H. J. Kluge, R. Moore G. Marx, D. Rodriguez, J. Schönfelder, G. Sikler, T. Valenzuela, J. Verdú, C. Weber, and G. Werth, HITRAP: A facility for experiments with trapped highly charged ions, *Hyperfine Interactions*, **132**, 453–457 (2006).

[9] I. Meshkov and A. Sidorin, Electron cooling, *Nuc. Inst. and Meth. in Phys. Research A*, **532**, 19–25 (2004).

[10] J. Marriner, Stochastic cooling overview, *Nuc. Inst. and Meth. in Phys. Research A*, **532**, 11–18 (1990).

[11] W. E. Lamb and R. C. Retherford, Fine structure of the hydrogen atom by a microwave method, *Phys. Rev.*, **72**, 241–243 (1947).

[12] H. F. Beyer, *Introduction to the Physics of Highly Charged Ions*, 1st edition, Taylor and Francis (2002).

[13] A. Gumberidze, Experimental studies of the ground state QED corrections in H- and He-like uranium, *Ph.D. thesis, Johann Wolfgang Goethe-University* (2003).

[14] A. Gumberidze, T. Stöhlker, D. Banas, K. Beckert, P. Beller, H. F. Beyer, F. Bosch, S. Hagmann, C. Kozhuharov, D. Liesen, F. Nolden, X. Ma, P. H. Mokler, M. Steck, D. Sierpowski, and S. Tashenov, Quantum electrodynamics in strong electric fields: The ground-state Lamb shift in hydrogen-like uranium, *Phys. Rev. Lett.*, **94**, 223001 (2005).

[15] T. Stöhlker, H. F. Beyer, A. Gumberidze, A. Kumar, D. Liesen, R. Reuschl, U. Spillmann, and M. Trassinelli, Ground state Lamb-shift of heavy hydrogen-like ions: Status and perspectives, *Hyperfine Interactions*, **172**, 135–140 (2006).

[16] T. Stöhlker, P. H. Mokler, F. Bosch, R. W. Dunford, F. Franzke, O. Klepper, C. Kozhuharov, T. Ludziejewski, F. Nolden, H. Reich, P. Rymuza, Z. Stachura, P. Swiat M. Steck, and A. Warczak, 1s Lamb shift in hydrogenlike uranium measured on cooled, decelerated ion beams, *Phys. Rev. Lett.*, **85**, 3109–3112 (2000).

[17] V. A. Yerokhin, P. Indelicato, and V. M. Shabaev, Two-loop self-energy correction in high-Z hydrogen-like ions, *Phys.Rev.Lett.*, **91**, 073001 (2003).

[18] V. M. Shabaev, A. N. Artemyev, V. A. Yerokhin, O. M. Zherebtsov, and G. Soff, Towards a test of QED in investigations of the hyperfine splitting in heavy ions, *Phys. Rev. Lett.*, **86**, 3959 (2001).

[19] J. E. Rosenthal and G. Breit, The isotope shift in hyperfine structure, *Phys. Rev.*, **41**, 459–470 (1932).

[20] M. F. Crawford and A. L. Schawlow, Electron-nuclear potential fields from hyperfine structure, *Phys. Rev.*, **76**, 1310–1317 (1949).

[21] M. Vogel, D. F. A. Winters, D. M. Segal, and R. C. Thompson, Proposed precision laser spectrometer for trapped, highly charged ions, *Rev. Sci. Instrum.*, **76**, 103102 (2005).

[22] S. M. Schneider, W. Greiner, and G. Soff, The transition time for the ground state hyperfine splitting of $^{209}\mathrm{Bi}^{82+}$, *Z. Phys. D*, **31**, 143 (1994).

[23] A. Bohr, The influence of nuclear structure on the hyperfine structure of heavy elements, *Phys. Rev.*, **77**, 94 (1950).

[24] P. Beiersdorfer, Testing QED and atomic-nuclear interactions with high-Z ions, *Phys. Rev.*, **77**, 94 (2010).

[25] I. Klaft, S. Borneis, T. Engel, B. Fricke, R. Grieser, G. Huber, T. Kühl, D. Marx, R. Neumann, S. Schröder, P. Seelig, and L. Völker, Precision laser spectroscopy of the ground state hyperfine splitting of hydrogen like $^{209}\mathrm{Bi}^{82+}$, *Phys. Rev. Lett.*, **73**, 2425–2427 (1994).

[26] P. Forck, Beam instrumentation and diagnostics, *Joint University Accelerator School Lecture Notes* (2003), `http://www-bd.gsi.de/conf/juas/juas.html`.

[27] A. G. Nörtershäuser, Laser spectroscopy on lithium-like bismuth, July 15, 2009, `http://www.uni-mainz.de/FB/Chemie/AK-Noertershaeuser/experiments/li-like-bismuth/index.html`.

[28] Z. Andjelkovic, R. Cazan, W. Nörtershäuser, M. Vogel, V. Hannen, R. Jöhren, D. Church, S. Bharadia, C. Weinheimer, R. Thompson, and G. Birkl, Development of the spectrap experiment, *GSI scientific report*, page 350 (2010).

[29] A. A. Elizarov, V. M. Shabaev, N. S. Oreshkina, I. I. Tupitsyn, and T. Stoehlker, The hyperfine structure of heavy hydrogen-like ions: Calculation based on experimental data on muonic atoms, *Optics and Spectroscopy*, **100**, 361 (2006).

[30] G. Breit, The magnetic moment of the electron, *Nature*, **122**, 649 (1928).

[31] M. Vogel, J. Alonso, S. Djekić, H. J. Kluge, W. Quint, S. Stahl, J. Verdú, and G. Werth, Towards electronic g-factor measurements in medium-heavy hydrogen-like and lithium-like ions, *Nucl. Instr. and Meth. in Phys. Res. B*, **235**, 7 (2005).

[32] S. Sturm, A. Wagner, B. Schabinger, J. Zatorski, Z. Harman, W. Quint, G. Werth, C. H. Keitel, and K. Blaum, g factor of hydrogenlike $^{28}\mathrm{Si}^{13+}$, *Phys. Rev. Lett.*, **107**, 023002 (2011).

[33] A. Wagner, S. Sturm, W. Quint, G. Werth, J. Zatorski, Z. Harman, C. H. Keitel, and K. Blaum, GSI scientific report, *PNI-AP-06*, page 332 (2010).

[34] V. A. Yerokhin, P. Indelicato, and V. M. Shabaev, Self-energy correction to the bound-electron g factor in H-like ions, *Phys. Rev. Lett.*, **89**, 143001 (2002).

[35] J. Verdú, S. Djekić, S. Stahl, T. Valenzuela, M. Vogel, and G. Werth, Electronic g factor of hydrogenlike oxygen $^{16}\mathrm{O}^{7+}$, *Phys. Rev. Lett.*, **92**, 093002 (2003).

[36] N. W. McLachlan, *Theory and application of Mathieu functions*, Clarendon Press (1947).

[37] F. G Major, V. N. Gheorghe, and G. Weth, *Charged Particle Traps*, Springer (2004).

[38] L. S. Brown and G. Gabrielse, Precision spectroscopy of a charged particle in an imperfect Penning trap, *Phys. Rev. A*, **25**, 2423–2425 (1982).

[39] P. Paasche, C. Angelescu, S. Ananthamurthy, D. Biswas, T. Valenzuela, and G. Werth, Instabilities of an electron cloud in a Penning trap, *Eur. Phys. J. D*, **22**(2), 183–188 (2002).

[40] D. F. A. Winters, M. Vogel, D. M. Segal, and R. C. Thompson, Electronic detection of charged particle effects in a Penning trap, *J. Phys. B: At. Mol. Opt. Phys.*, **39**, 3131–3143 (2006).

[41] L. R. Brewer, J. D. Prestage, J. J. Bollinger, W. M. Itano, D. J. Larson, and D. J. Wineland, Static properties of a non-neutral ^{9}Be$^+$-ion plasma, *Phys. Rev. A*, **38**, 859–873 (1988).

[42] X. P. Huang, F. Anderegg, E. M. Hollmann, C. F. Driscoll, and T. M. O'Neil, Steady-state confinement of non-neutral plasma by rotating electric fields, *Phys. Rev. Lett.*, **78**, 875–878 (1997).

[43] D. H. E. Dubin and T. M. O'Neil, Trapped non-neutral plasmas, liquids, and crystals (the thermal equilibrium states), *Rev. Mod. Phys.*, **71**, 88–172 (1999).

[44] J. J. Bollinger, D. J. Heinzen, F. L. Moore, W. M. Itano, and D. J. Wineland, Electrostatic modes of ion-trap plasmas, *Phys. Rev. A*, **48**, 525–542 (1993).

[45] D. J. Heinzen, J. J. Bollinger, F. L. Moore, W. M. Itano, and D. J. Wineland, Rotational equilibria and low-order modes of a non-neutral ion plasma, *Phys. Rev. Lett.*, **66**, 2080–2083 (1991).

[46] X. P. Huang, J. J. Bollinger, T. B. Mitchell, W. M. Itano, and D. H. E. Dubin, Precise control of the global rotation of strongly coupled ion plasmas in a Penning trap, *Phys. Plasmas*, **5**, 1654–1663 (1998).

[47] E. Peik, J. Abel, T. Becker, J. von Zanthier, and H. Walther, Sideband cooling of ions in radio-frequency traps, *Phys. Rev. A*, **60**, 439–449 (1999).

[48] H. C. Nägerl, C. Roos, H. Rohde, D. Leibfried, J. Eschner, F. Schmidt-Kaler, and R. Blatt, Addressing and cooling of single ions in Paul traps, *Fortschr. Phys.*, **48**, 623–636 (2000).

[49] H. F. Powell, S. R. de Echaniz, E. S. Phillips, D. M. Segal, and R. C. Thompson, Improvement of laser cooling of ions in a Penning trap by use of the Axialisation technique, *J. Phys. B: At. Mol. Opt. Phys.*, **36**, 1 (2003).

[50] S. Guibal, Cooling methods in ion traps, *Université Paris-Diderot Lecture notes* (2010).

[51] F. Arbes, T. Gudjons, F. Kurth, G. Werth, F. Marin, and M. Inguscio, Lifetime measurements of the 3D3/2 and 3D5/2 metastable states in CaII, *Z. Physik D*, **25**(4) (1993).

[52] H. G. Dehmelt and F. L. Walls, Bolometric technique for the rf spectroscopy of stored ions, *Phys. Rev. Lett.*, **21**(3) (1968).

[53] *Encyclopedia of Chemical Physics and Physical Chemistry*, volume 3, Taylor and Francis (2001).

[54] W. M. Itano and D. J. Wineland, Laser cooling of atoms, *Phys. Rev. A*, **20**, 1521–1540 (1979).

[55] W. M. Itano and D. J. Wineland, Laser cooling of ions stored in harmonic and Penning traps, *Phys. Rev. A*, **25** (1982).

[56] T. M. O'Neil, Centrifugal separation of a multispecies pure ion plasma, *Phys. Fluids*, **24** (1981).

[57] L. Gruber, J. P. Holder, and D. Schneider, Formation of strongly coupled plasmas from multicomponent ions in a Penning trap, *Phys. Scr.*, **71**, 60–107 (2005).

[58] NIST, Atomic spectra database (2010).

[59] D. Cvejanovic and A. J. Murray, Single ionization of calcium by electron impact, *J. Phys. B*, **36** (2003).

[60] R. Hendricks, Spectroscopy and dynamics of laser-cooled Ca^+ ions in a Penning trap, *Ph.D. thesis, Imperial College London* (2006).

[61] H. Ohadi, Single Ca^+ ions in a Penning trap for applications of quantum information processing, *Ph.D. thesis, Imperial College London* (2008).

[62] D. Crick, Manipulation of individual laser cooled Ca^+ ions in Penning traps, *Ph.D. thesis, Imperial College London* (2009).

[63] J. Goodwin, *Private communication.*

[64] G. Gabrielse, L. Haarsma, and S. L. Rolston, Open-endcap Penning traps for high precision experiments, *Intl. J. of Mass Spec. and Ion Proc.*, **88** (1989).

[65] J. Verdú, S. Kreim, K. Blaum, H. Kracke, W. Quint, S. Ulmer, and J. Walz, Calculation of electrostatic fields using quasi-Green's functions: application to the hybrid Penning trap, *New J. Phys.*, **10**, 103009 (2008).

[66] Scientific Instrument Services Inc., Simion version 8 (2010), `http://simion.com/`.

[67] M. E. Kiziroglou, X. Li, A. A. Zhukov, P. A. J. de Groot, and C. H. de Groot, Thermionic field emission at electrodeposited Ni-Si Schottky barriers, *Solid-State Electronics*, **52**, 7 (2008).

[68] J. Orloff, *Handbook of charged particle optics, 2nd edition*, CRC Press (2009).

[69] J. F. O'Hanlon, *A user's guide to vacuum technology, 3nd edition*, Wiley (2003).

[70] P. K. Ghosh, *Ion traps*, Oxford University Press (1995).

[71] J. J. Olivero and R. L. Longbothum, Empirical fits to the Voigt line width: A brief review, *J. Quant. Spectosc. Radiat. Transfer*, **17**, 233–236 (2002).

[72] J. L. K. Koo, Laser cooling and trapping of Ca^+ ions in a Penning trap, *Ph.D. thesis, Imperial College London* (2003).

[73] J. R. Danielson and C. M. Surko, Radial compression and torque-balanced steady states of single-component plasmas in Penning-Malmberg traps, *Phys. Plasmas*, **13**, 055706 (2006).

[74] M. D. Tinkle, R. G. Greaves, and C. M. Surko, Modes of spheroidal ion plasmas at the Brillouin limit, *Phys. Plasmas*, **3**, 749 (1996).

[75] E. M. Hollmann, F. Anderegg, and C. F. Driscoll, Confinement and manipulation of non-neutral plasmas using rotating wall electric fields, *Phys. Plasmas*, **7**, 2776 (2000).

[76] B. R. Beck, J. Steiger, G. Weinberg, D. A. Church, J. McDonald, and D. Schneider, Measurement of charge exchange between H2 and low-energy ions with charge states $35 \leq q \leq 80$, *Phys. Rev. Lett.*, **77**, 1735–1738 (1996).

[77] N. Murby, Magnetic shielding with mu metal, May 27, 2009, `http://mumetal.co.uk/2009/05/27/shielding-calculation-formula/`.

[78] Z. Andjelkovic, B. Sommer, W. Nörtershäuser, M. Vogel, V. Hannen, R. Jöhren, D. Church, S. Bharadia, D. M. Segal, R. Thompson, and

G. Birkl, Development of the spectrap experimental setup, *GSI scientific report*, page 377 (2009).

[79] SPECTRAP collaboration meetings, September 20, 2011, `http://www.uni-mainz.de/FB/Chemie/AK-Noertershaeuser/experiments/spectrap/collaboration-meeting.html`.